"Nanostructured Ru/TiO2 catalysts for CO2 methanation"

Kim, Ara

Abstract

The hydrogenation of CO2 performed through heterogeneous catalysis is a pertinent strategy for mitigating CO2 emissions. This thesis aims to contribute to the understanding of the physico-chemical factors related to the catalytic performance of Ru/TiO2 catalysts at mild conditions (≤ 200 °C, 1 atm). Pre-synthesized 2 nm-RuO2 nanoparticles (NPs) are used to serve as precursors for active metallic Ru. These calibrated NPs are coupled with various tailor made TiO2 supports with different crystallinity, textural properties, stability and composition to understand parameters that dictate the activity of Ru/TiO2 catalysts. The specific RuO2-TiO2 interactions and RuO2 NPs migration phenomenon are demonstrated using various techniques including the state-of-the-art tomography and environmental transmission electron microscopy at atmospheric pressure. The important parameter for the better catalytic performance is found to be the epitaxial stabilization of RuO2 on rutile TiO2 prior to the ...

Document type : *Thèse (Dissertation)*

Universite catholique de Louvain (UCL)
Institute of Condensed Matter and Nanosciences (IMCN)
Molecules, Solids and Reactivity (MOST)

Université Pierre et Marie Curie (UPMC)
ED 397
Laboratoire Chimie de la Matière Condensée de Paris (LCMCP)

A thesis submitted in conformity with the requirements
for the degree of Doctor of Philosophy (Ph.D.)

Nanostructured Ru/TiO_2 catalysts for CO_2 methanation

Ara Kim

Promoters: Prof. Damien Debecker (UCL) – Prof. Clément Sanchez (UPMC)

Jury Members:

Dr. Capucine Sassoye (LCMCP, UPMC, Paris, France)

Prof. Eric Gaigneaux (IMCN/MOST, UCL, Louvain-la-Neuve, Belgium)

Prof. Corine Gérardin (Rapporteur - ENSCM, Montpellier, France)

Dr. Denis Uzio (Rapporteur - IFPEN, Lyon, France)

Prof. Xavier Carrier (LRS, UPMC, Paris, France)

Prof. Jacques Devaux (President - IMCN/BSMA, Louvain-la-Neuve, Belgium)

January 2016

Acknowledgements

First and foremost I thank my supervisors, Dr. Capucine Sassoye, Prof. Damien Debecker, and Prof. Clément Sanchez. Since I first arrived in France and Belgium in October 2012, they have guided my challenging journey through my PhD thesis in two laboratories not only with scientific knowledge and experience but also with perseverance, care, trust, and good humour. I thank them so much for showing their passion and confidence in whatever I have done in the laboratory and constantly encouraging me throughout my thesis even though the fields of chemistry and catalysis were new to me. I really appreciate their help and being available whenever I needed to ask questions or discuss with them. Also, I really appreciate what Capucine and Damien have done for me to adjust to a new life in France and Belgium. They have been not only scientific supervisors but also life counselors by listening to me and sharing beers.

I would like to thank my PhD thesis committee members, Prof. Eric Gaigneaux, Prof. Corine Gérardin, Dr. Denis Uzio, Prof. Xavier Carrier, and Prof. Jacques Devaux for accepting to become my jury members and providing me with valuable inputs to improve my manuscript towards the completion of my PhD degree. I would like to particularly thank Prof. Corine Gérardin and Dr. Denis Uzio for their roles as "rapporteurs", and Prof. Jacques Devaux for his role as a president of the jury.

My PhD experience in Europe couldn't have been completed without everyone I interacted on a daily basis in two laboratories, one in France and one in Belgium. I would like to thank everyone for scientific discussions, helping me with problems, translating French to English, and sharing beers, etc.

Especially, I would like to thank my colleagues at LCMCP: Laurie, Alexandre, Davide, Mikael, Benjamin, Xavier, Guillaume G., François, Virgile, Niki, Claire G., Claire V., Guillaume S., Anne-Sophie, Leslie, Marie-Anne, Gilles, Elham, Anaël, Jessie, Natacha K., and Francisco. Thanks for the great moments we have shared in lab 3.11 and teaching me French culture and food, etc. Particularly, I would like to acknowledge Cédric, Marco, Olivier, and Sophie for invaluable scientific discussions. Je remercie également sincèrement Patrick, Mohamed, et Isabelle pour avoir passé autant de temps avec moi et m'avoir aidé avec le TEM, la XRD, le SAXS, et la BET. Je remercie également Hélène et Corine pour m'avoir aidé avec tous les documents nécessaires pour rester et travailler en France.

I would like to also thank my colleagues in Louvain-la-Neuve for contributing immensely to my professional and personal time: Alejandro, Camila, Maryna, Josefine, Benjamin, Colas, Victor, Gijo, Antoine, Anna, Ludivine, Chiara, Irene and Elinana. I really appreciate scientific discussions, coffee breaks, sports, and beers we have shared. I am also grateful for the scientific help of François, Prof. Eric Gaigneaux and Prof. Patricio Ruiz. I especially thank Françoise, Nathalie, and Pascal for magically making everything work, from administration, chemicals orders, to broken everything-you-can-imagine-in-the-lab. I also wholeheartedly thank François and Pierre for their help with H_2 chemisorption, TPR, and XPS.

I would also like to acknowledge professors, colleagues, and friends involved in IDS-FunMat PhD program for providing a great international experience and inspiring scientific meetings.

Finally, I thank my family and friends in different parts of the world for their love and encouragement. I am especially grateful for the unconditional support of my mom, brother, and sister throughout my life. I thank Laurie for her effort to translate French for me and sharing great moments in Paris. I thank Maryna for the great times we shared in Louvain-la-Neuve and for cheering me up in difficult times. I thank Michelle for always being there for me to rely on. I thank Mr. B for his endless support and advice on life decisions. I thank Mr. A and Terepac team for teaching me priceless life lessons and providing me a steppingstone to reach this point of my life. To my family and friends in Korea, 엄마, 외삼촌, 외숙모, 작은큰엄마, 작은큰아빠, 이수오빠, 민수오빠, 정은언니, 상우, 예나, 어려운 시기에 응원해주시고, 기도해주시고, 조언해주시고, 기쁨을 나누워 주셔서 감사합니다. 덕분에 프랑스에서 모든일이 잘 풀려나가고 박사학위 무사히 받을수 있었습니다. 찬영아 재선아, 매년 너희들 유럽에서 만날수 있어서 너무 즐거웠고, 항상 힘이 되어주어서 너무 고마워.

My day-to-day life in Europe couldn't have been completed without Victor, Hélène, Hervé, Marion, Thony, Martin, Maceo, and Ethan. I can't thank enough for their family support in France. I deeply thank Hélène and Hervé for their kindness and openness in helping me with housing and visa issues, providing me a place to stay, food to eat, and invaluable cultural and life lessons. I equally thank Marion, Thony, and Martin for sharing great moments and being supportive. I will always remember this period of my life when my days end, I would walk on rue Mouffetard, arrive at The Local, and have a pint of beer Martin would pour for me. I also thank Maceo and Ethan for their happy spirit and laughter. And most of all, I would like to express my deepest thanks to Victor for his support, patience, and love during the final stages of this PhD thesis.

Contents

Introduction

1. Research context

The development of global economy and standard of living has fueled the growing energy demand over the past decades, leaving behind the cumulative build-up of inevitable environmental consequences. Greenhouse-gas emissions from the energy sector represent roughly two-thirds of all anthropogenic greenhouse-gas emissions [1]. In the energy sector, fossil fuels, including coal, oil, and natural gas, have been the world's primary energy source since the industrial revolution over the past century. According to the International Energy Agency (IEA), fossil fuels continue to account for more than 80% of total primary energy demand and over 90% of energy-related emissions are carbon dioxide (CO_2) from fossil-fuel combustion [1]. The abundance of CO_2 is the major contributor to the greenhouse effect which makes the planet warmer by trapping the infrared thermal radiation in the earth's atmosphere thereby raising the earth's temperature. The Intergovernmental Panel on Climate Change (ICPP) reported that the recent anthropogenic emissions of greenhouse gases are the highest in history and that recent climate changes have had widespread impacts on human and natural systems [2]. Observed changes in the climate system include the diminished amount of snow and ice, risen sea level, extreme weather as well as negative impacts on water resources, agriculture, and human health [2].

Our generation is at a critical moment of risk and opportunity as US President Obama said, "We are the first generation to feel the effect of climate change, and the last generation who can do something about it" (Press conference at the White House, August 3rd, 2015). With the increasing global awareness and pressure, policymakers aim to agree on curbing global temperature rises at United Nations Climate Change Conference in December 2015 (COP21). In realizing the objectives of mitigating global warming threats, fundamental changes in the production and usage of energy, as well as new technologies are acknowledged to be the urgent necessity and the scientific community plays an important role in providing knowledge for such changes and a basis of decisions for political community.

In recent years, there has been increasing pressure in the society to curb CO_2 emissions and develop efficient CO_2 capture, storage and utilization technologies [3-5]. The reduction of CO_2 emission is recognized as a long term task as it requires efficient use of energy and switching from fossil fuels towards less carbon intensive energy sources such as hydrogen and renewable energy [5, 6]. In regard to the reduction of CO_2 in the atmosphere, two major strategies have been proposed: CO_2 capture and storage (CCS), and usage of CO_2 [5, 7-9]. The usage of CO_2 is complementary to the carbon capture and storage but particularly promising as increasing amounts of low-cost and relatively pure CO_2 from current and planned plants for carbon capture and storage will be available at nearly zero cost [10]. As a suitable source of C1 building block, CO_2 can be used as a renewable carbon source to produce fuels and chemicals. Thus, CO_2 as a carbon source can be recycled which can lead to less consumption of fossil-fuels without producing additional CO_2 buildup in the cycle.

The usage of CO_2 as a chemical feedstock has been demonstrated in synthesis of urea, salicylic acid, carbonates, methanol and dimethyl ether (DME) [5, 7, 10]. Among different catalytic conversion processes of CO_2, hydrogenation of CO_2 to methane (CH_4), the so-called CO_2 methanation, presents several advantages over production of other chemicals; the reaction can be carried out under atmospheric pressure, the produced CH_4 can be directly injected into already existing natural gas pipelines, and it can be used as a fuel or raw material for production of chemicals [7]. Furthermore, CO_2 methanation serves as a tool for H_2 produced from renewable resources to be efficiently utilized as an energy vector since transportation of H_2 is limited due to its low volumetric energy density.

CO_2 methanation via heterogeneous catalysts has received considerable amount of attention in recent years [7]. The research focus has been the development of efficient methanation catalysts with high selectivity towards 100 %. Numerous supported metals, such as Ni, Ru, Rh, Pd, Co, and Mg on various oxide supports, including TiO_2, SiO_2, Al_2O_3, CeO_2, and ZrO_2, have been investigated. Moreover, effect of second metal or promotor to enhance the stability and catalytic activity of Ni based catalysts as well as effect of preparation method to enhance the dispersion of active sites have been addressed. The main research objective has been to obtain the best catalytic performance in terms of stability, selectivity, CO_2 conversion, and CH_4 production, especially aimed at mild reaction conditions (i.e. low reaction temperature). However, understanding of the catalysts' structures and structure-performance relationship is relatively less of a main focus.

The recurrent concept of this thesis is that studying the structure-performance relationship contributes to the key understanding of the catalysts design. Aside from the nature of the catalysts' active phase and support, the important parameters in designing nanostructured catalysts include shape and structure of the active phase and support.

In this thesis, Ru is chosen as an active metal and TiO_2 is chosen as a support for the application of CO_2 methanation. Ru/TiO_2 catalyst is already known to be 100 % selective to methane production under mild conditions. With these parameters fixed, we focus on the structure of the catalyst and understanding of the materials, employing unconventional synthesis and preparation routes to prepare Ru/TiO_2 catalysts.

The approach is initiated by synthesis of new materials (calibrated RuO_2 nanoparticles, home-made TiO_2 with different crystallinity, and advanced preparation of mesoporous TiO_2) which is then used in the application of catalysis (CO_2 methanation). This thesis attempts to combine the approaches of the materials science community and techniques of the heterogeneous catalysis community. On the one hand, the materials science community can offer new ways of catalyst preparation that can lead to new physico-chemical properties and potentially to improved performance. On the other hand, the catalysis community usually relies on preparation methods that consist of a succession of relatively simple operations. It is clearly performance oriented and this usually relies on a good understanding of the catalyst working behavior. It is believed that the combination of both approaches can lead to significant progress in materials and catalysis science, both at the fundamental and applied levels.

In the following sections, Ru- and TiO_2- based materials, their application in heterogeneous catalysis, and catalytic hydrogenation of CO_2 to CH_4 in the context of this present work are briefly reviewed.

1.1. Ruthenium (Ru) and Ruthenia (RuO_2) and their application in heterogeneous catalysis

Ruthenium (Ru) is a rare transition metal belonging to the platinum group of the periodic table. Ru can easily adopt a wide range of oxidation states from -2 to +8 in chemical bonds, thus making it a versatile metal that exhibits complex and unique properties [11-13]. Ru has given rise to several important research areas in science, including catalysis [14-17] and electrochemical energy storage devices [18].

Ru forms only one stable solid oxide phase, ruthenium dioxide (RuO_2), which crystallizes with rutile structure [11].

Any other form of simple sub-oxide is known to be thermodynamically unstable and spontaneously decomposes into RuO_2 and metallic Ru. RuO_4 is another known oxide phase of Ru, which is volatile above 313K and toxic. However, it decomposes into RuO_2 and O_2 above 373K [11]. Another oxidized phase was assigned to RuO_3 by X-ray photoelectron spectroscopy (XPS) as Ru^{6+} and Raman spectroscopy on RuO_2 surfaces [19, 20]. However, the existence of RuO_3 has been debatable since it is known that RuO_3 does not exist in a stable bulk phase [21]. A density functional theory (DFT) calculations proposed by Grillo et al. [22] showed that corundum structure of Ru_2O_3 may exist as a metastable phase. Indeed, experimental evidence showed that this metastable phase forms only when Ru (0001) is exposed to high pressure oxygen (1 mbar to 100 mbar) at temperatures <500 K [11].

Ru/RuO_2 bears a complex and unique redox surface chemistry, which makes RuO_2 a versatile oxidation catalyst [23]. Ru-supported or RuO_2-supported catalysts have shown high performance in various hydrogenation (Ru) and oxidation (RuO_2) reactions respectively, such as ammonia synthesis [24, 25], CO_2 methanation [26], and HCl oxidation [27].

RuO_2 is known to be readily reducible to Ru and re-oxidized to RuO_2, yet the reduced Ru can less easily be re-oxidized. The reduction of RuO_2 into Ru can proceed by reducing agents or thermal decomposition in vacuum. The reduced Ru forms thin surface oxide layer of 4-8 Å in atmospheric air at room temperature which can prevent further oxidation [28]. For supported Ru nanoparticles, a full oxidation in oxygen flow was reported to take place at 470 K [29], while reduction in H_2 takes place below 430 K [30]. Furthermore, it was demonstrated by in situ X-ray diffraction (XRD) that Ru nanoparticles can reversibly be reduced at about 400 K and oxidized at about 500 K [31].

Pre-synthesized nanoparticles of Ru and RuO_2 are highly attractive in the preparation of supported Ru-based catalysts, due to their relatively well-defined structures and composition. The synthesis route of Ru and RuO_2 takes advantage of their redox properties. Thus, RuO_2 nanoparticles can be prepared via oxidation of Ru nanoparticles and vice versa. For example, preparation of a core shell particles of ultrathin RuO_2 film coating with the Ru core can be obtained by oxidation of Ru particles [29]. Ru-based nanoparticles are also reported by Rossi et al. by a reaction of $NaBH_4$ with $RuCl_3$ using an ionic liquid (1-n-butyl-3-methylimidazolium

hexafluorophosphate (BMI.PF6) resulting in RuO_2 nanoparticles of 2-3 nm with a narrow size distribution [32].

Synthesis of Ru nanoparticles include impregnation [33], polyol method [34-37], metal organic chemical vapor deposition (MOCVD) [38], and barrel- sputtering method [26].

RuO_2 nanoparticles can be prepared without requiring multi-step synthesis or reducing atmosphere and can be directly used for oxidation reactions or subsequently reduced in situ for hydrogenation reaction. The synthesis of RuO_2 nanoparticles include hydrothermal synthesis [39] and wet impregnation of soluble Ru precursor. However, these synthetic pathways usually result in highly agglomerated nanoparticles with broad size distribution.

To obtain supported catalysts with well-defined nanoparticles and size distribution, catalyst preparation from colloids is advantageous [11]. The recent advancement in the preparation of colloidal RuO_2 nanoparticles include dispersed RuO_2 nanoparticles of ~ 2nm by Lin et al. [40], which have been prepared through a non-green route. More attractive preparation of colloidal RuO_2 nanoparticles via sustainable aqueous route has been developed by Sassoye et al. [41].

The control of size and shape of the supported nanoparticles is important in catalyst development of heterogeneous catalysis towards greatest reaction rate and optimal selectivity. In this regard, not only the nanoparticles (active phase) but also their support may bring an important structural effect, beside dispersion and stabilization of the nanoparticles. Therefore, the selection of support is another important parameter in the preparation of heterogeneous catalysts.

1.2. Titania (TiO_2) and its use as a support in heterogeneous catalysis

TiO_2 is best known for its properties as a pigment in sunscreens, paints, ointments, etc. The high stability, high ultraviolet absorption, and semiconductor properties allow TiO_2 to be used in different applications, ranging from photovoltaics and photocatalysis, to catalyst support in heterogeneous catalysis [42]. TiO_2 exists in three main crystal forms: rutile, anatase, and brookite. Anatase and rutile are the most common types, and brookite is a less utilized third form without any important applications [43]. The rutile phase is the most stable form of TiO_2 at high temperature and it is obtained from the metastable form of anatase TiO_2 by annealing at high temperature (above 600 °C in air), and the phase transformation is governed by numerous factors such as annealing temperature, particle size, compactness of the anatase crystallites, and grain boundary defects [44-46].

Amorphous TiO_2 initially prefers to nucleate into anatase phase since the surface Gibbs free energy of anatase phase is lower than that of rutile phase [46].

The lattice structures of anatase and rutile TiO_2 shown in Figure I-1 can be described in terms of chains of TiO_6 octahedra, where each Ti^{4+} ion is surrounded by an octahedron of six O^{2-} ions [42]. The distortion of each octahedron and the assembly pattern of TiO_6 octahedra are different in the two crystal structures. The degree of distortion of the octahedron is greater in anatase structure than rutile structure; The Ti-Ti distances are larger and Ti-O distances are shorter in anatase structure. In anatase structure, each octahedron is in contact with eight neighbors (four sharing an edge oxygen pairs and four sharing a corner oxygen atom), while, in the rutile structure, each octahedron is in contact with 10 neighbor octahedra (two sharing an edge and eight sharing a corner) [42].

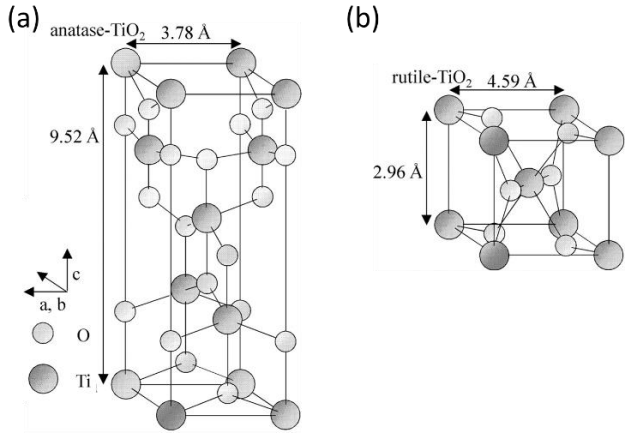

Figure I-1: Lattice structure of (a) anatase TiO_2 and (b) rutile TiO_2 [47]

The synthesis of TiO_2 uses various approaches. Nanostructured TiO_2 has been synthesized by sol-gel method via acid-catalyzed hydrolysis of titanium (IV) alkoxide, followed by condensation [42, 48-51]. The condensation kinetic of Titanium precursor is sensitive to content of water as a solvent and the hydrolysis rate. The development of three dimensional polymeric skeleton of Ti-O-Ti chains is favoured with low content of water, and low hydrolysis rate, while the formation of Ti-OH is favoured with high hydrolysis rates for less amount of water which is insufficient to develop three-dimensional polymeric skeletons [42, 50, 52]. The high reactivity of titanium alkoxide compared to silicon alkoxide is due to the lower electronegativity of Ti atom and its ability to exhibit several coordination states [49, 50]. This high reactivity towards water can be chemically controlled by using acetic acid as a

complexing agent. Addition of acetic acid prevents precipitation and increases gelation time as acetate groups OAc^- behave as complexing nucleophilic ligands and react with titanium alkoxide [49, 53, 54].

Other approaches to TiO_2 synthesis include nonhydrolytic sol-gel process, which usually involves the reaction of titanium chloride ($TiCl_4$) with a variety of different oxygen donor molecules, such as metal alkoxide or an organic ether [42, 55]. The condensation between Ti-Cl and Ti-OR leads to the formation of Ti-O-Ti bridges. Hydrothermal and solvothermal methods are another alternate route for direct synthesis of TiO_2. In hydrothermal synthesis, precipitates of titanium precursor with water are treated in steel pressure vessels (autoclaves) under controlled temperature and pressure. Solvothermal method is almost identical to the hydrothermal method but uses non-aqueous solvent. The control of size, shape, and crystallinity of TiO_2 nanoparticles is known to be better than hydrothermal method [42]. Microwave method is another synthesis route of TiO_2 nanoparticles [56-58]. High-frequency electromagnetic wave can be used as energy source to heat the solvent faster.

Mesoporous TiO_2 has gained increasing interest because of its high surface area and pore volume, which can provide high accessibility and facilitate diffusion of reactants and products in applications catalysis [59]. Mesoporous TiO_2 materials have been prepared using organic templates as structure-directing agents. Because of the high reactivity of Ti precursors which tend to hydrolyze fast and to form dense precipitates, it is difficult to enable the cooperative assembly with templates in an aqueous solution. The resultant mesoporous TiO_2 generally exhibits disordered wormhole-like mesostructure rather than ordered regularity over larger domains [59-62]. The cooperative assembly of structure-directing agent and Ti precursor was first obtained by Yang et al. via evaporation induced self-assembly (EISA) method [63], in which the hydrolysis/condensation rates can be regulated while allowing self-assembly process of the amphiphilic poly(alkylene) block copolymer simultaneously by evaporation of non-aqueous solvent. The degree of ordering and the range of the porous mesostructures have been further improved by aerosol-assisted self-assembly process, an integration of aerosol spray and evaporation-induced assembly using a structure-directing agent, first reported by Brinker et al. for silica based materials [64-66]. In this aerosol route, a solution containing metal precursors and structure-directing agents is atomized in droplets thereby confining evaporation induced self-assembly to spherical aerosol droplets. The first work on transition metal oxide was reported by Grosso et al. [67] The synthetic strategy to overcome the difficulty to couple the rapid-evaporation

nature of aerosol-spray process and the reactive sol-gel chemistry has employed chemical strategies to stabilize Ti precursor. Stucky et al. combined acetic acid mediated sol-gel system, in which metal alkoxides are dissolved in mixture solutions of acetic acid, hydrochloric acid, and ethanol (AcHE), together with the aerosol-assisted self-assembly approach [66]. The acetate ligands bonded to the metal cores of metal alkoxide form stable, nanometer-sized metal oxo-acetate particles, which serve as inorganic building blocks and rapidly co-organized with organic amphiphilic block copolymers into ordered mesostructures during the evaporation process. The control of sol-gel chemistry even allowed formation of homogeneous multicomponent mesoporous metal oxides.

TiO_2 has been widely used as a support in heterogeneous catalysis due to its chemical stability and commercial availability. Furthermore, the interaction of metal nanoparticles with TiO_2 support has been reported to strongly influence the catalytic activity and selectivity of heterogeneous catalysts [43]. The catalyst preparation step involves oxidation and/or reduction at elevated temperature which is necessary to "activate" catalysts [43]. This "activation" step generally causes morphological changes to the supported metal nanoparticles, which may or may not be beneficial to the catalytic performance. The interaction between the support and the active phase (metal nanoparticles) leading to different morphological changes include sintering, alloy formation, encapsulation and interdiffusion [43, 68]. For instance, mixed anatase and rutile crystal phases of TiO_2 increases the dispersion of Cu species as the active Cu species are being located at the interface between the anatase and rutile phases [69]. In Ru/TiO_2 system, stabilized Ru particles on rutile TiO_2 are obtained during calcination pre-treatment [70]. Similar observation was observed on RuO_2/TiO_2 system, in which stabilized and dispersed RuO_2 phase is obtained through the formation of epitaxial RuO_2 layer over rutile TiO_2 [27, 71, 72].

TiO_2 supported group 8 noble metals are also known for their strong metal support interactions (SMSI). The SMSI effect was first reported by Tauster in 1978 [73], which was demonstrated as the different behaviour of small metal particles' capacity to adsorb H_2 and CO when the catalyst is reduced at 500 °C and above compared to a low temperature reduction (200 °C). When reduced at high temperature, the H_2 and CO sorption decreased to nearly zero for well-dispersed metal particles supported on TiO_2, not due to the metal agglomeration but due to the chemical interaction between the metal and TiO_2 [73]. The underlying phenomenon for this effect was the migration of reducible oxide support onto the active metal surface. Two main models have been proposed to explain the SMSI

phenomenon; electronic perturbation of the metal function and migration of a mobile phase of the partially reduced support which encapsulates the metal particles [74, 75]. In case of TiO_2, it is now well accepted that the partial reduction of TiO_2 gives rise to TiO_x suboxide species ($x < 2$) which migrate onto the surface of metal particles [76]. Although the words "strong metal-support interactions" imply a broader concept, the use of the term "SMSI" is to solely describe the phenomenon of formation of atomic layer of TiO_2 or CeO_2 on the surface of metal particles. The SMSI effect has been reported to have both negative effect and positive effect over a range of different catalytic reactions [75].

1.3. Catalytic conversion of CO_2 to CH_4

1.3.1. Thermodynamics

The CO_2 methanation, also called the Sabatier reaction, is a reversible, exothermic, and thermodynamically favourable reaction at room temperature.

$$CO_2 + 4H_2 \rightarrow CH_4 + 2H_2O \qquad \Delta H_{298K} = -165 \text{ KJ mol}^{-1}, \Delta G_{298K} = -113.2 \text{ KJ mol}^{-1} \quad (1)$$

With the feed gas of H_2 and CO_2 at a stoichiometric H_2/CO_2 molar ratio of 4, the main products are CH_4 and H_2O at relatively low temperature (≤ 200 °C) (Figure I-2). At higher temperature, additional CO_2 is being generated as the increased energy input shifts the equilibrium to favour reverse reaction. The temperature above 450 °C, increases the formation of CO-by product due to reversed water gas shift reaction: $CO_2 + H_2 \rightarrow H_2O + CO$.

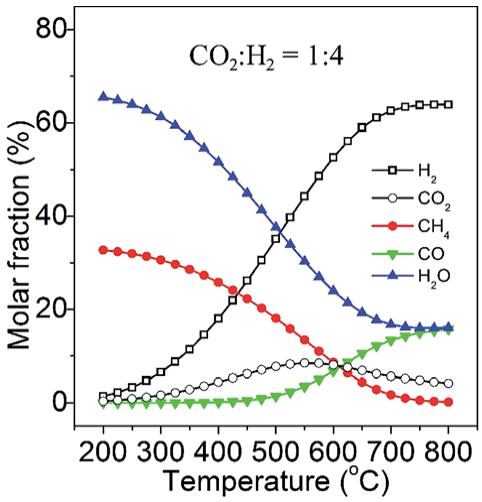

Figure I-2: Product compositions for CO_2 methanation at equilibrium at CO_2:H_2 = 1:4 and Pressure = 1 atm [77].

Although thermodynamically favourable, the reduction of the fully oxidized CO_2 to CH_4 at low temperature is difficult to achieve without enough energy input because of significant kinetic limitations [77, 78]. Thus, catalysts with high selectivity and acceptable rate are required. Supported Ni-based catalysts have been extensively studied due to their low cost and availability. Other metals such as Ru, Rh, Co, etc. on various supports have also been reported to be effective methanation catalysts.

1.3.2. Mechanism

The reaction mechanism of CO_2 methanation appears to be difficult to be established. There is no consensus on the mechanism up to date. In regard to the nature of the intermediate compound in the rate determining step and the methane formation, the ongoing arguments is whether the reaction goes through CO intermediate formation or not. There are two main mechanisms proposed (Figure I-3): (i) Conversion of gaseous CO_2 into CO_{ads} intermediate prior to methanation and (ii) direct hydrogenation of CO_2 without forming CO as intermediate [7, 78, 79]. The rate limiting step is considered to be either the formation of intermediate CH_xO and its interaction with hydrogen, or the formation of surface carbon in CO dissociation and its hydrogenation [7, 78]. Metal sites dissociate H_2 to form atomic hydrogen, which facilitates the formation of methane.

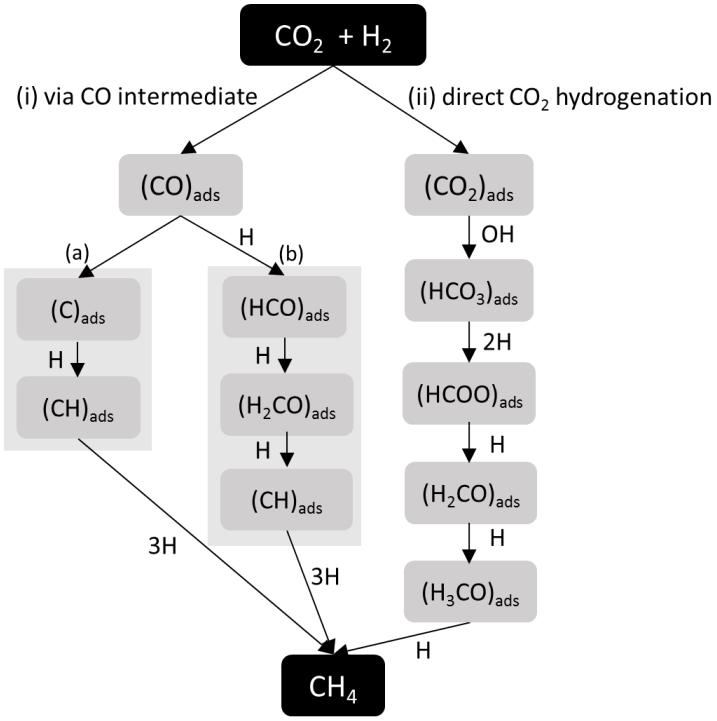

Figure I-3: Schematic of proposed mechanisms of CO_2 methanation. Reproduced from reference [79].

(i) Via CO intermediate

The reaction mechanism depends on the catalysts and reaction conditions. One suggested mechanism proposes CO as an important intermediate [80-83]. Then the subsequent reaction follows the same mechanism as CO methanation, which does not have a consensus mechanism neither [84]. The CO intermediate pathway for CO_2 methanation involves the dissociative adsorption of CO from gaseous CO_2, which is then subsequently hydrogenated to CH_4. One way of CO intermediate mechanism described by Wagner et al. [85] involves CO_2 dissociation into CO_{ads} and O_{ads}, reaction of O_{ads} with H_2 forming H_2O, while CO_{ads} is hydrogenated to CH_4. On Rh/Al_2O_3 [86], the dissociation of CO_2 into CO and O was observed by diffuse reflectance infrared Fourier transform spectroscopy (DRIFTS) analysis. Furthermore, the CO_{ads} intermediate was also reported by Marwood et al. on Ru/TiO_2 catalyst [82] on which CO_{ads} species are formed through the reaction between gaseous CO_2 with support's surface hydroxyl group to form formates ($HCO_3^- \rightarrow HCOO^-$) giving rise to CO_{ads} species. Only the interfacial formates decomposed to CO_{ads} while regenerating the surface hydroxyl group.

Concerning CO methanation, two possible pathways are suggested. First, CO_{ads} dissociates into C and O on the metal sites before further hydrogenation into CH_4 by dissociated H_2 on the metal particles [83, 87] (Figure I-3 (i)(a)). Peebles et al. showed on Ni (100) single crystal that CO_2 is first converted to CO and subsequently to C before its hydrogenation [88]. Similar observation was reported on Ni (111), on which the dissociation of CO was found to be the rate-limiting step [89]. Second, CO hydrogenation does not require the formation of Cads from CO_{ads} dissociation (i.e. associative pathway) (Figure I-3 (i)(b)). Density functional theory (DFT) studies on Ru/TiO_2 (101) showed that CO_2 transforms into CO and then the adsorbed CO is hydrogenated to HCO before CH_4 production [90]. It was further suggested that the hydrogenation of adsorbed CO and the production of CH_4 are possible rate-determining steps. Moreover, DRIFTS study on Ru/TiO_2 [91] has shown that both hydrogenation of surface carbon produced by dissociative adsorption of CO and hydrogenation of CO species adsorbed at the metal-support interface are involved. Several kinetic experiments and theoretical calculations propose that CO hydration via associative pathway assisted by H is the predominant pathway for Ru catalysts [92].

(ii) Direct CO_2 hydrogenation

The CO_2 dissociation into CO and O is not observed in all cases. Another possible mechanism involves formation of carbonates and formates which are directly hydrogenated into CH_4. Solymosi et al. reported that, on Ru/Al_2O_3 catalysts, adsorbed CO was only observed at higher temperature (> 200 °C) [93], attesting the possibility of CO_2 methanation reaction at lower temperature without dissociative adsorption of CO_2. Similarly, Ni/CeO_2 catalyst showed high CO_2 conversion at low temperature with almost 100 % selectivity to CH_4 and the high performance was attributed to the ability of CeO_2 support to adsorb CO_2 molecules [94, 95]. Furthermore, Vesselli et al. showed the direct CO_2 hydrogenation mechanism on Ni (110) where adsorbed H binds with gaseous CO_2, yielding a formate intermediate, which prevents CO formation [96]. Sharma et al. also reported that CO_2 methanation on $Ce_{0.95}Ru_{0.05}O_2$ catalyst had activity for CO_2 methanation but no activity for CO methanation, suggesting that CO is not a reaction intermediate [97].

The summary of proposed CO_2 methanation mechanisms suggests that there is no evident consensus mechanism. Different metal, support, reaction condition, preparation method, etc. can lead to compelling evidence for a different CO_2 methenation mechanism. What is clear for Ru/TiO_2 catalyst is that, according to a recent (unpublished) near-ambient-pressure XPS study (NAP-XPS), the metallic Ru

stays fully reduced in presence of the reactant mixture (CO_2 and H_2) and the fully reduced Ru is responsible during CO_2 methanation reaction.

1.3.3. Catalysts

Ni, Ru, and Rh are the most widely used metals for CO_2 methanation [7, 79]. Ni has been the most exploited metal due to its good activity, low cost, and availability. The performance of catalysts is dependent on various parameters, such as support, Ni loading, addition of a second metal, and preparation method.

Raney nickel is well known to have high activity due to its thermal and structural stability and high surface area [98]. Numerous studies reported that small metallic Ni particles dispersed on support material (i.e. Al_2O_3) with high dispersion contributes to the high activity [99, 100]. Furthermore, support with high oxygen storage capacity (CeO_2-ZrO_2) was turned out to be greatly efficient in terms of activity, stability, and ability to activate CO_2 [101, 102]. Furthermore, basic properties of support (MgO) was important to adsorb CO_2 especially when operating at higher temperature [103]. In general, Ni dispersion is thought to be an important parameter for high catalytic performance. In attempts to increase Ni dispersion and stability, a second metal can be added to prevent Ni sintering during the exothermic methanation reaction [104, 105] and various preparation methods are being explored to simultaneously enhance the reducibility of Ni.

Noble metal-based catalysts such as Ru and Rh exhibit higher selectivity towards CH_4 and higher stability during reaction compared to Ni-based catalysts [7]. Various parameters are found to affect the catalytic activity including preparation method (linked to surface reducibility [97], particle size (controlled by Ru loading) [106, 107], and metal dispersion [26, 108]. For instance, Ru nanoparticles dispersed on TiO_2 by a dry method (barrel sputtering method [26]) exhibited significantly higher activity compared to that prepared by conventional wet impregnation. Additionally, the methanation reaction proceeded at temperature as low as 300 K. It was also reported that, for high Ru dispersion, the surface-based activity (e.g. turn over frequency (TOF)) was found to be strongly affected by metal-support interactions [108].

The catalytic properties of CO_2 methanation is sensitive to the structure of the catalysts. The prevalent view of active site is the synergy between the primary metallic phase and support (or promotor). The development for the highly active catalysts directs towards high specific surface area, high dispersion of metal particles, high stability, and low temperature reaction.

2. Objectives

The research focus of most of the reported works in the literature is to develop the most active catalyst in terms of selectivity, CO_2 conversion, and CH_4 yield in CO_2 methanation. Various metal particles and support materials have been continuously explored and compared to the reported works in the field in search for the improved activities. In the process of development, several parameters have been considered such as nature of metal particle, metal particle dispersion, nature of support materials, and addition of promoters. Moreover, studies on various reaction conditions (temperature, pressure, feed composition, etc.) and reaction mechanism are ongoing. Nevertheless, understanding of catalysts' structure-performance relationship is not fully recognized. This thesis thus attempts to contribute to the understanding of parameters that influence the structure-performance relationship, fixing the nature of the metal and support materials and reaction conditions constant.

Thanks to the recent development of one-step, green synthesis of calibrated RuO_2 nanoparticles of 2 nm by Sassoye et al. [41], the system of Ru/TiO_2 catalyst has been chosen as a model to explore the effect of catalyst's structure on the catalytic performance. Ru/TiO_2 catalysts are already regarded as one of the most effective and selective towards CH_4 in CO_2 methanation [97, 109, 110]. Thus, the parameters related to the structure of the Ru/TiO_2 are viewed from pure material scientific aspect.

The approach of this work towards the understanding of the morphological factors that contribute to the catalytic performance is somewhat unconventional. Unlike a conventional approach of catalytic studies, in which the catalytic performance is the first and ultimate goal to keep in mind in developing catalysts, the first approach of this thesis is to evoke new aspects of materials first from which the catalytic performance comes as a consequence.

Overall, this study aims to understand morphological parameters that dictate the activity of Ru/TiO_2 methanation catalysts. The interactions between RuO_2 nanoparticles and TiO_2 support with different crystallinity, composition, porosity, and surface area are investigated. Furthermore, the active Ru phase formed as a result of RuO_2-TiO_2 interactions is correlated with catalytic performance to finally identify the decisive parameter. It should be viewed as a contribution from material science community to catalysis community for development of improved catalysts.

3. Strategies

A highly stable colloidal suspension of 2 nm- monodispersed RuO_2 nanoparticles is used as an initial active phase of Ru. The utilization of the preformed nanoparticles are advantageous in studying the interaction between the nanoparticles and the support, in which a better control over the noble metal nanoparticles is desired. The study on the interaction between RuO_2 and TiO_2 support is explored in four main categories; effect of TiO_2 crystal structure, effect of mixed TiO_2 crystalline phases, effect of TiO_2 textural properties, as well as the mobility of RuO_2 nanoparticle. Throughout the studies, the CO_2 methanation reaction is carried out at low temperature (≤ 200 °C) and one standard atmospheric pressure.

The first chapter focuses on studying the interaction between the-pre formed RuO_2 nanoparticles and TiO_2 supports with different crystalline phases, namely anatase and rutile. For this part, we have prepared our own home-made TiO_2 supports with definite crystal structure (rutile or anatase). We also study commercially available titania supports, as well as the very common commercially available P25 support (mixture of anatase and rutile). The morphological change of RuO_2 and TiO_2 particles are monitored at various thermal annealing temperatures (as an "activation" step) and correlated with the CO_2 methanation activity. The observation revealed that anatase- and rutile- TiO_2 interact with RuO_2 nanoparticles differently upon catalyst “activation” by annealing. When anatase- and rutile- TiO_2 crystal phases were co-present (in case of commercial TiO_2-P25 support), the catalytic performance was the highest. These results directed toward questions on any beneficial effect of the mixed anatase- and rutile- TiO_2 crystalline phases in the following study.

The second chapter is an attempt to elucidate the effect of mixture of TiO_2 crystalline phases. It is anticipated that the crucial step of catalyst preparation is annealing, during which migration, sintering, and crystallization of the active phase can occur. Support crystallinity is envisaged to impact these phenomena. Thus, the mixing of two phases, anatase and rutile, is carried out at different steps of catalyst preparation, while Ru loading and preparation conditions are kept constant. The observations showed that beneficial catalytic effect of mixing anatase- and rutile-TiO_2 crystalline phases are apparent when RuO_2 nanoparticles undergo “migration” and being stabilized onto rutile TiO_2. At this point, the possible mechanism of mobility of the initially small RuO_2 nanoparticles was questioned leading to the following study.

The third chapter focuses on the location and morphology of RuO_2 nanoparticles under heat treatment and subsequent reduction. The possible mechanism and driving force of mobility of RuO_2 nanoparticles as well as their stabilization on TiO_2 crystals are discussed through various tools including Rietveld refinement and state-of-the-art in situ environmental TEM. In an attempt to discriminate between the two main phenomena possibly leading to RuO_2 mobility (Ostwald ripening and/or local volatilization of RuO_x species depending on the experimental condition), specific annealing experiments are carried out ex situ or in situ in the environmental TEM chamber, varying the atmosphere and the temperature programs. The effect of those annealing treatments are assessed in a direct way, in environmental TEM.

The last two chapters are devoted to innovative preparation of mesoporous TiO_2 as well as mesoporous Ti-based mixed oxides using an advanced technique and chemical strategies, based on aerosol synthesis route suggested by Stucky et al. [66] The mesoporous supports are used as a tool to tune crystallinity and textural properties to serve as supports for Ru-species and study the structure-performance relationship. The low thermal stability of pure mesoporous TiO_2 support, however, led to the disrupted mesoscopic order through crystallization at relatively low temperature in presence of RuO_2. To improve the thermal stability of TiO_2 support, Si- or Al- oxide species were introduced in the sol-gel precursor to prepare mesoporous mixed oxide. The effect of improved textural properties in the RuO_2-support interactions as well as the effect of the introduction of non Ti-based oxide species on Ru-species are related to the catalytic performance. Furthermore, to assess the importance of the intimacy between RuO_x species and the support, different Ru incorporation methods are also investigated. They are compared in terms of their effect on catalysts' morphology as well as on catalytic performance.

Overall, these strategies allow us to identify the critical parameters for better catalytic performance. These are established based on the findings described in each chapter, and via correlations between performance and physico-chemical properties of the catalysts.

Experimental

1. Preparation of RuO_2 nanoparticles

Highly stable colloidal suspension of monodispersed RuO_2 nanoparticles was obtained by a dropwise addition of 15 %v/v H_2O_2 diluted in H_2O into 0.011 M $RuCl_3 \cdot xH_2O$ (x = 3–5) dissolved in H_2O so that the final concentration of [Ru] ≈ 0.007 M. The solution was heated at 95 °C for 2h. The characterization of RuO_2 nanoparticles is described in Appendix A. The catalyst preparation using these RuO_2 nanoparticles is described in the experimental summary of each chapter.

2. Catalyst characterization

2.1. Transmission electron microscopy (TEM)

Transmission electron microscopy (TEM) images were obtained with a FEI Tecnai 120 Twin microscope, operating at 120 kV and equipped with a GatanOrius CCD numeric camera. The samples were prepared by ultrasonic dispersion of the powders in water and a droplet of the dispersion was then placed onto a carbon-coated copper grid.

High-resolution analysis (HR-TEM) images were obtained by using a JEOL JEM 2010 microscope, operating at 200 kV and equipped with a Gatan camera. The sample preparation was the same as described in TEM sample preparation.

High angle annular dark field scanning transmission electron microscopy (HAADF-STEM) images were obtained by Philips CM20 “super-twin” microscope equipped with a CCD camera Megaview from Soft Imaging System, with an accelerating voltage of 200 kV. X-Ray microanalysis measurements were performed with an Inca software from Oxford instrument.

3D TEM tomography data were acquired on the JEOL 2100F electron microscope. The acquisition of bright field (BF) and dark field (DF) tilt series was carried out simultaneously in the scanning mode (STEM). A camera length of 10 cm was chosen for this experiment. It corresponds to inner and outer semiangles of 60 and 160 mrad, respectively, for the HAADF detector. A 100 µm condenser aperture was

employed, allowing one to reach a probe diameter of about 0.12 nm with a current density of 0.5 pA/Å^2. Under these conditions, the tomography series were acquired using the Digital Micrograph software (tomography plugin), giving access to an automatic increment of the tilt angles and a sharp control of the specimen drift and defocusing. A high tilt specimen holder from Gatan was employed for a tilting range of −65° to 65°, with an equal angular step of 2.5°.

The precision of these nanoscale 3D analyses greatly benefits from the DART reconstruction method [111] that minimizes the artifacts due to the missing wedge. Indeed, after a fine alignment of all projections, the 3D volume was calculated using the discrete algebraic reconstruction technique (DART). For this purpose, a preliminary simultaneous iterative reconstruction technique (SIRT) reconstruction was performed [112]. By constraining the reconstruction volume with a mask which roughly equals the particles shapes, reliable material densities can be deduced. Subsequently, the density for the gold particles is used to perform a DART reconstruction, which is discrete in terms of gray values. This means that each voxel (unit fragment of the volume) is attributed to either vacuum or gold. Consequently, DART is superior to SIRT when exact particle boundaries are to be determined.

2.2. X-ray diffraction (XRD)

X-ray diffraction (XRD) measurements were performed using Cu Kα radiation in a Bruker D8 Advance diffractometer equipped with a Lynx eye detector. The 2θ diffractograms were recorded between 24–50°with a step size of 0.04° and a step time of 20 s/step. The ICDD-PDF2 database was used to identify the crystalline phases. The Scherrer equation was used to calculate the crystallite size of particles:

$$s = \frac{K.\lambda}{\beta cos\theta}$$

s = mean size perpendicular to hkl plane (Å)

K the shape factor, 0.9 for this study

λ = the XRay wavelength (1.5419Å, the mean wavelength for Kα1 Kα2 ray)

β = the peak broadening at half maximum intensity in radian, taking into account 0.04° broadening in the used 2θ range for the instrument.

From TEM analysis, P25 particles and pure anatase particles show roughly isotropic shapes whereas pure rutile TiO_2 particle crystalize as c-axis oriented needles. Thus, TiO_2 particle sizes were calculated using Scherrer equation from rutile (110), (101),

(200) peaks and anatase (101), (103), (004) and (112) peaks for both P25 and pure anatase support. With the (001) rutile diffraction peak being forbidden, no easy estimation of the rutile needle length could be made. However, rutile needle width could be estimated from the (110) and (200) diffraction peaks; (101) and (111) diffraction peaks were excluded for this calculation because of their combined a- and c-axes influence.

When possible, TiO_2 and RuO_2 XRD peaks were deconvoluated, using WinPLOTR 2014 software (Thierry Roisnel, Juan Rodriguez-Carvajal, www.cdifx.univ-rennes1.fr/winplotr). The Scherrer equation was used to calculate the crystallite size of particles [113].

2.3. X-ray photoelectron spectroscopy (XPS)

X-ray photoelectron spectroscopy (XPS) analyses were performed on a SSX 100/206 photoelectron spectrometer from Surface Science Instruments (USA) equipped with a monochromatized micro focused Al X-ray Kα source (powered at 20 mA and 10 kV), a 30° solid angle acceptance lens, a hemispherical analyser and a position sensitive detector. The samples were pressed in small stainless steel troughs of 4 mm diameter and placed on a multi-specimen holder. The pressure in the analysis chamber was around 10^{-6} Pa. The angle between the surface normal and the axis of the analyser lens was 55°. The analysed area was approximately 1.4 mm^2 and the pass energy was set at 150 eV. Atomic concentration ratios were calculated by normalizing surface area ratios with sensitivity factors based on Scofield cross-sections. In addition, all binding energies were calculated taking as reference the C–(C, H) component of the C 1s adventitious carbon peak fixed at 284.8 eV. Peak decomposition was performed using the CasaXPS program (Casa Software Ltd., UK) with a Gaussian/Lorentzian (85/15) product function and a Shirley non-linear sigmoid-type baseline. The following peaks were used for the quantitative analysis: O 1s, C 1s, Ti 2p, and Ru 3d. The 3d Ru peak was decomposed into 3 doublets assigned to Ru^0, Ru^{4+} and the related RuO_2 plasmon species respectively [114]. Position of these species has been imposed at 280.0 ± 0.1 eV, 291.0 ± 0.1 eV and 282.8 ± 0.1 eV, respectively. The binding energy difference between the 3/2 and 5/2 contributions of each doublet was fixed to 4.17 eV. Besides, the $Ru3d_{3/2}/Ru3d_{5/2}$ ratio was fixed to 0.667. The FWHM of each component was limited at 2.5 eV.

2.4. Temperature Programmed Reduction (TPR)

H_2-TPR experiments were performed for 100 mg of each catalyst after in situ purging under inert gas (Ar) at 140 °C for one hour. The analysis was carried out

under 2.5 v/v % H_2 diluted in inert gases (2.5: 82.5: 15 v/v % H_2: He: Ar) in stream of 20 mL.min^{-1} from 20 °C to 500 °C using a 5 °C min^{-1} temperature ramp. H_2 consumption and H_2O production were measured simultaneously via a quadrupole mass spectrometer QMC 311 (Balzers) coupled in line with the reactor.

2.5. Inductively Coupled Plasma-Atomic Emission Spectroscopy

The weight percentages of Ru and Ti inside the catalysts were measured by Inductively Coupled Plasma-Atomic Emission Spectroscopy (ICP-AES) on an ICAP 6500 from Thermo Scientific.

2.6. Nitrogen (N_2) Physisorption

The specific surface area of the catalysts was obtained by nitrogen adsorption–desorption isotherm collected at −196 °C on a BELSORB-mini II (BEL Japan, Inc.). The samples were outgassed for overnight at 140 °C prior to the analysis. Specific surface area (S_{BET}) was calculated applying the Brunauer-Emmet-Teller (BET) method for N_2 relative pressure in range of $0.05 < P/P_0 < 0.30$. Total pore volume (V_p) was measured at $P/P_0 \sim 0.98$. Pore size distribution was determined by the Barret-Joyner-Halenda (BJH) method.

2.7. Hydrogen (H_2) Chemisorption

H_2 chemisorption at 100 °C was used to measure the exposed Ru atoms using ASAP 2010C apparatus from Micrometrics. Catalyst weight between 150 – 200 mg was loaded into a Pyrex tube, and subsequently degassed in He at 150 °C for 30 min. After evacuation, the sample was reduced in pure H_2 at 200 °C for 2 h (same as in situ reduction for methanation, see Section 2.3) followed by purging with He at 100 °C for 1h and adsorption of H_2. Two isotherms were measured in the range of 0.08-95 kPa. The first accounts for reversible and irreversible chemisorption. The H_2 was evacuated in vacuum at 200 °C for ~ 2 h as the sample was being cooled down to 100 °C to desorb reversibly adsorbed H_2. The second isotherm was then measured which accounts only for the reversibly adsorbed H_2. The subtraction of the linear part of the two isotherms gave the total amount of irreversibly adsorbed (chemisorbed) H_2. The amount of surface Ru atoms was calculated from the amount of chemisorbed H_2 assuming that the chemisorption stoichiometry is H:Ru = 1 [115, 116]. Dispersion is defined as surface Ru atoms divided by total Ru atoms in the catalyst.

An alternative H_2 chemisorption analysis was carried out by Micromeritics - Pulse Chemisorb 2700 apparatus. For the measurement, ~ 100 mg of samples were used

and reduced in situ under H_2 at 200 °C then purged by N_2 flow at 225 °C. After cooling down to 100 °C, the chemisorption analysis was carried out by filling a loop of a known volume (50 µL) with pure H_2 for 30s. Then H_2 was purged by N_2 on the sample. Non-adsorbed H_2 were detected by a TCD (Thermal Conductivity Detector). The signal is integrated during 150s to make sure that all of the non-adsorbing H_2 was passed through the detector. This procedure was repeated for 5 to 10 loops and the adsorbed volume of H_2 was calculated.

2.8. Small angle X-ray scattering (SAXS)

The experiment was carried out with Rigaku's S-MAX3000 3-pinhole SAXS camera with X-ray source (high brilliance MIcroMax-002) with Copper anode (λ CuKα = 1.54056 Å). The scattering radiation was collected on 2D Multiwire Area Detector (gas detector) with sample-to-detector distance of 1469 mm.

2.9. Attenuated total reflection-Fourier Transform Infrared (ATR-FTIR)

The measurement was performed on Single reflection horizontal ATR accessory from Brucker, diamond crystal plate equipped with high pressure QuickLock. The spectra was recorded with 100 scans between 400 and 4000 cm^{-1} with a resolution of 4 cm^{-1}.

3. Methanation of carbon dioxide

200 mg of catalyst with particle size between 100 and 315 µm was loaded in a continuous flow fixed bed reactor and reduced in situ at 200 °C for 2 h under 30 ml/min of H_2 prior to the catalytic reaction. The reaction was carried out at 1 atm in the temperature range of 50 to 200 °C under reaction mixture of 20 ml/min (CO_2 (10 vol. %), H_2 (40 vol. %) diluted in He). Each temperature was maintained for 52 min (+ 5 min of temperature increment) (account for 3 GC injections). The exit gases were quantified using a gas chromatograph (Varian CP3800), equipped with Hayesep Q, Molsieve 5A, and CP-Sil-5CB columns. The separated gases were detected with a flame ionization detector (CH_4) and a thermal conductivity detector (CO and CO_2). Analysis parameters were set as to allow an analysis each 19 min and to obtain measurements accurate within about 1 % (relative) for the methane production rate (mole of methane produced per gram of catalyst per second). All transfer lines were maintained at 110 °C to avoid water condensation.

Chapter 1: Unraveling the decisive role of the TiO_2 support crystal structure

1. Introduction

Supported metal nanoparticles feature important structural properties that dictate their performance in heterogeneous catalysis [117, 118]. Indeed, a structure-performance relationship is found in many metal-catalysed reactions [71, 72, 119-126]. Although the primary role of the support material is sometimes thought to be limited to physical support of intact metal nanoparticles, it has been recognized that the chemical nature of the support or the metal-support interactions can have a marked impact on catalytic activities and/or the selectivity [123, 127]. Thus, the design of tailored supports for metal-based catalysts is a topical field of research which concerns size, shape, texture, crystallinity, and redistribution process of the metal nanoparticles on their support [119, 128, 129].

The CO_2 hydrogenation to CH_4 (CO_2 methanation), also known as Sabatier reaction, is an important catalytic process of fundamental academic interest with potential commercial application [7, 77, 130, 131]. In environmental context, this reaction not only reduces exhaust CO_2 emission but produces CH_4, which can be directly transported through existing natural gas pipelines to be used as a fuel or a chemical building block, simultaneously targeting both the valorisation of CO_2 (reduction of greenhouse gas) and the vectorisation of dihydrogen via CH_4.

Although CO_2 methanation has been a topical field of research for decades, the emphasis of the development in this area has been on catalytic performance with high selectivity at thermodynamically favorable conditions (e.g. low temperature) with different types of metals and supports [95, 132].

Reducible Group VIII metal oxides have been widely used as support materials. Among them, TiO_2 is the best known for its high stability, high ultraviolet absorption, and semiconductor properties which allow its use in various applications in catalysis and photocatalysis [42]. Furthermore, the existence of various crystalline phases of

TiO_2 contributes to the tuning of catalytic performance in heterogeneous catalysis through morphologic and electronic perturbations [72, 119, 129]. For example, TiO_2 has been known as the most efficient support for noble metal catalysts including Pd, Ru and Rh in CO and CO_2 methanation [132-136]. Recently, TiO_2 supported RuO_2 nanoparticles have shown an excellent oxidation capability as a Deacon catalyst displaying different stabilities depending on the crystalline phases of TiO_2 [119].

The impact of structure-performance relationship in Ru-based catalysts has given rise to various preparation methods for well-dispersed and/or uniformly-sized nanoparticles of Ru and RuO_2 for many catalytic applications in hydrogenation and oxidation reactions [27, 71, 137, 138]. Abe et al. have developed a dry technique for modifying the surfaces of powdery materials named polygonal barrel-sputtering to prepare Ru nanoparticles loaded TiO_2 with narrow particle size distribution without the need of any heating which can cause nanoparticles sintering [26]. Balaraju et al. have shown superior catalytic performance of Ru/TiO_2 catalysts prepared by deposition-precipitation (DP) method over those prepared by conventional impregnation (IM) method in the hydrogenolysis of glycerol, which was attributed to the presence of well-dispersed nano size Ru particles on TiO_2 [139]. Also, Sassoye et al. have previously reported the synthesis of mono-dispersed 2 nm RuO_2 nanoparticles in aqueous colloidal suspension and the preparation of Ru/TiO_2 catalysts after reduction under H_2 [41]. Such catalysts demonstrated superior catalytic performance in CO_2 methanation to that prepared by IM method. A study on the crystal phase effect of TiO_2 on the structure and performance of Ru nanoparticles in CO_2 hydrogenation was recently reported [72]. However, the catalyst preparation method (IM) implied the formation of RuO_2 nanoparticles directly onto the supports and offered relatively poor control of the Ru nanoparticle size distribution.

The successful preparation of uniformly distributed 2 nm RuO_2 nanoparticles suspension and the suspected structure-performance relationship in Ru-catalysed CO_2 methanation has prompted us to study the active phase-support interaction (not to be confused by so-called “Strong metal-support interactions (SMSI)” proposed by S. J. Tauster in 1978 [73]) between pre-formed RuO_2 nanoparticles and TiO_2 supports with different crystalline phases. Indeed, starting from well-defined dispersed RuO_2 nanoparticles, TiO_2 supports with different crystalline phases might favour the stabilization of Ru in different states of dispersion, shape, structure.

In the present work, RuO_2 nanoparticles of 2 nm were initially prepared by colloidal method and supported on pure anatase, pure rutile, and P25 TiO_2. The uniform size

distribution of RuO_2 nanoparticles facilitated more accurate study of the influence of the TiO_2 crystalline phases on RuO_2 nanoparticles and the resulting catalytic behaviour in CO_2 methanation. The morphological change of the RuO_2 nanoparticles were monitored after various thermal annealing temperatures and correlated with the CO_2 methanation activity at low temperature (≤ 200 °C) and one standard atmospheric pressure.

2. Experimental summary

Pure anatase TiO_2 particles were prepared by microwave hydrothermal treatment at 200 °C for 2 h of an aqueous solution of $TiCl_4$ with the acidity adjusted to pH 6 using NaOH. The resultant precipitates were collected by centrifugation, washed with water and nitric acid [58].

Pure rutile TiO_2 particles were obtained by reflux at 120 °C for 3 days of an aqueous solution of $TiCl_4$ in 1M HCl followed by washing the resultant precipitates with water and nitric acid [140].

Highly stable colloidal suspension of monodispersed RuO_2 nanoparticles was obtained by a dropwise addition of 15 %v/v H_2O_2 diluted in H_2O into 0.011 M $RuCl_3 \cdot xH_2O$ (x = 3–5) dissolved in H_2O so that the final concentration of [Ru] ≈ 0.007 M. The solution was heated at 95 °C for 2h. Once cooled to room temperature, an appropriate amount of TiO_2 powder (P25 from Degussa, home-made pure anatase or home-made pure rutile) was added to the colloidal suspension of RuO_2 nanoparticles to yield 2.2 wt. % of Ru in the final catalyst. The mixture was put in an oven at 50 °C overnight and the excess water was removed by rotary evaporation. The resulting powder was then annealed/calcined at 150, 250, 350, or 450 °C for 16 h in static air and washed 3 times with water then dried in air. The catalysts are denoted as RuO_2/TiO_2-P25, RuO_2/TiO_2-A, and RuO_2/TiO_2-R for P25, pure anatase, and pure rutile TiO_2 supported RuO_2, respectively. After reduction under continuous flow of H_2 at 200°C (see Section 2.3), the catalysts are denoted as Ru/TiO_2-P25, Ru/TiO_2-A, and Ru/TiO_2-R, respectively. Different calcination temperatures are indicated with extended numerical notations, e.g. RuO_2/TiO_2-P25-150.

Effect of catalyst washing (with water) on chlorine content measured by XPS is summarized in Appendix B. It is shown that, although chlorine content can be lowered by repeated washing with water (centrifuge and re-dispersion), the chlorine content levels off to zero after annealing, and the resulting catalytic activity is not influenced by the washing step.

3. Results and discussions

3.1. Basic characterization of the supports and catalysts

The XRD analyses confirmed the mixed anatase and rutile phases of P25 TiO_2, pure anatase phase for the home-made anatase TiO_2, and pure rutile phase for the home-made rutile TiO_2 (Figure 1-1).

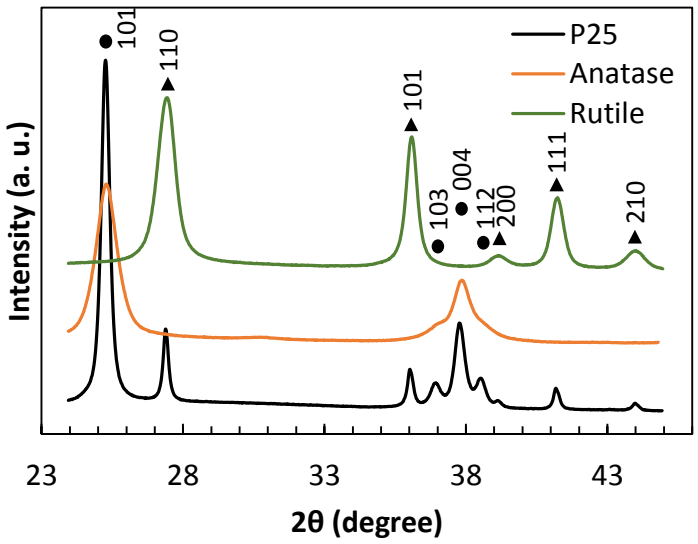

Figure 1-1: XRD patterns of P25, anatase and rutile TiO_2 supports; rutile TiO_2 (▲), anatase TiO_2 (●).

The 2D particle shapes of the three TiO_2 supports, P25, anatase, and rutile, were distinctive and well distinguishable from one another by TEM observations as shown in Figure 1-5 a-c. P25 TiO_2 particles were rounded rectangular-shaped; home-made anatase TiO_2 particles were a mixture of oval and rhombus; and home-made rutile TiO_2 particles were needle-shaped. There was no difference in the shapes of the supports before and after the deposition of RuO_2 nanoparticles with annealing at 150 °C. The particles sizes measured from TEM images were, in average, 25 – 30 nm for P25 TiO_2, 6 – 7 nm for anatase TiO_2, and 12 x 100 nm for rutile TiO_2 (see Appendix C). The RuO_2 nanoparticles of ~1.8 nm were well dispersed on all supports. 3D-TEM tomography image of well dispersed RuO_2 nanoparticles on the surface of P25 TiO_2 is shown in Figure 1-2.

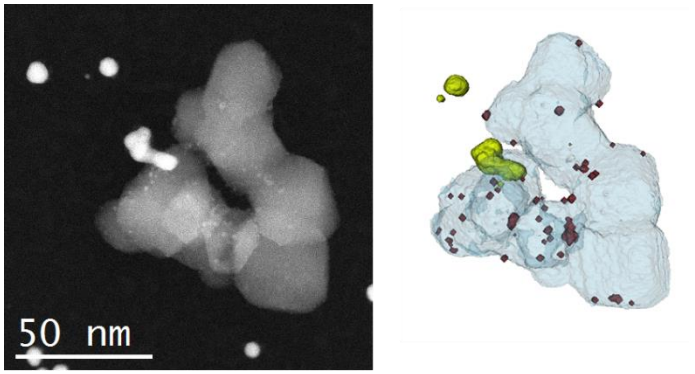

Figure 1-2: 3D-TEM tomographic analysis of RuO_2 phase decorating the surface of TiO_2 particles on RuO_2/TiO_2-P25-150; (left) STEM-HAADF image extracted from the tilt series used to calculate the reconstruction of this aggregate, (right) 3D model of the studied aggregate, with Ru nanoparticles in dark red and gold nanoparticles in light green. This 3D analysis underlines the quite uniform distribution of RuO_2 NPs on the different TiO_2 nanoparticles with annealing at 150 °C only.

After deposition of RuO_2 nanoparticles aimed at 2.2 wt. % of Ru, ICP-AES elemental analysis of the 450 °C-annealed catalysts resulted in the Ru contents of 2.35 – 2.6 wt. %, indicating no Ru loss (small variation comes from the variation in the water content in $RuCl_3.xH_2O$ (x = 3 – 5)). The specific surface areas by BET method (S_{BET}) before and after the deposition of RuO_2 followed by annealing at 150 °C were found to be consistent, as shown in Table 1-2.

3.2. CO_2 methanation activity

RuO_2/TiO_2 catalysts annealed at various temperatures were reduced in situ to obtain metallic Ru and then tested in CO_2 methanation at one atmospheric pressure and in the 50-200 °C temperature range. The specific activities of all catalysts with three supports at various annealing temperatures and reaction temperatures are summarized in Table 1-1. In these conditions, selectivity to methane and water was always 100 % for all three catalysts. The catalytic activities at 200 °C expressed in terms of CH_4 production rate were compared for the three different TiO_2 supports (Figure 1-3). The CH_4 production rate at a given reaction temperature increased with the higher annealing temperature for all three supports. As already reported previously [41], it is essential to perform an annealing treatment before reducing the catalyst; here the 450 °C-annealing appears as the most effective and thus we chose to study the effect of annealing up to 450 °C on the morphology of the catalysts.

Strikingly, even if the Ru loading is strictly the same for the three studied supports, marked differences were observed in terms of activity depending on the nature of support. The global trend (more evident as annealing temperature increases) in terms of CH_4 production rates is found to be P25 > anatase > rutile (also represented in CO_2 conversion and CH_4 yield, see Appendix D). This points to a decisive role of the TiO_2 crystal structure in the catalytic behavior of the final Ru/TiO_2 catalysts. The activation energies of the catalysts annealed at 450 °C were obtained by scanning the catalytic activities from 100 to 200 °C (Figure 1-4) and were found to be 14.3, 14.3 and 15.4 kcal/mol, for Ru/TiO_2-P25-450, Ru/TiO_2-A-450 and Ru/TiO_2-R-450 respectively. The fact that similar values of activation energies are found suggests that active species are the same in all catalysts, i.e. the TiO_2 crystal structure does not affect the reaction mechanism. The higher catalytic activity of P25 TiO_2 supported catalyst compared to anatase or rutile TiO_2 may therefore be attributed to a greater number of active sites. Thus the TiO_2 crystal structure probably plays a role in the genesis of the Ru active phase.

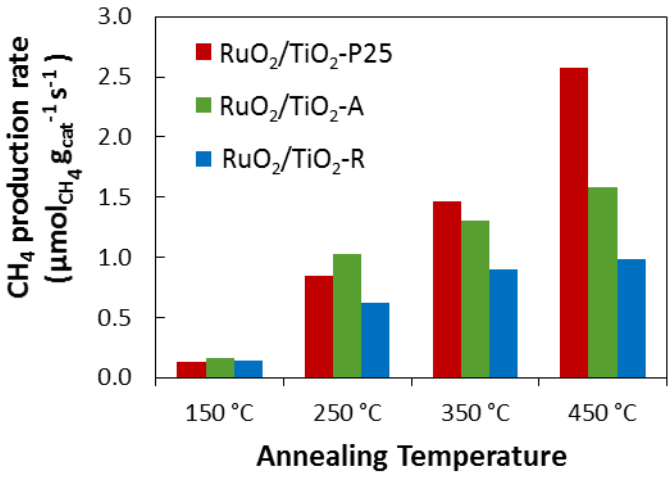

Figure 1-3: Influence of annealing temperatures on CO_2 methanation

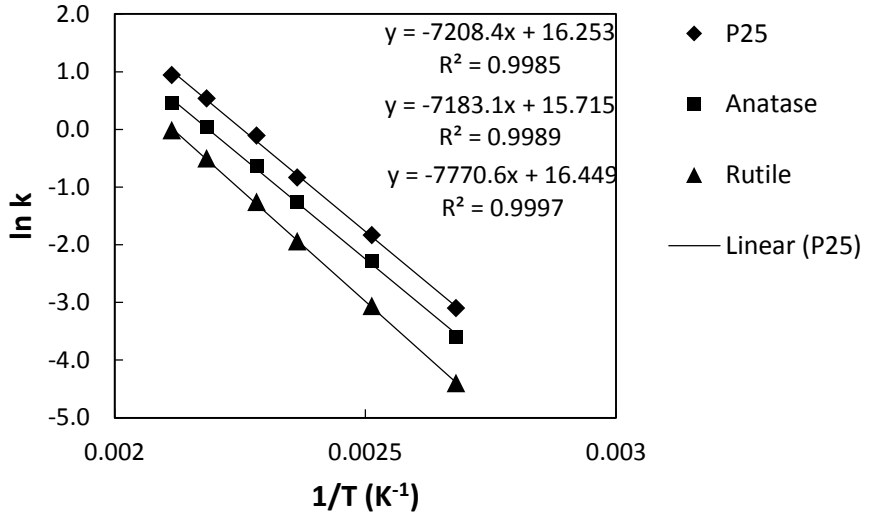

Figure 1-4: Arrhenius plot for determination of activation energy obtained from 100 to 200 °C reaction temperatures.

Table 1-1: Catalytic activities of different TiO_2 supported catalysts at various annealing temperatures and reaction temperatures.

Annealing Temperature (°C)	Reaction Temperature (°C)	CH_4 production rate ($\mu mol_{CH4}\ g_{cat}^{-1}\ s^{-1}$)		
		RuO_2/TiO_2-P25	RuO_2/TiO_2-A	RuO_2/TiO_2-R
150	50	0.000	0.000	0.000
	85	0.000	0.000	0.000
	100	0.000	0.000	0.000
	125	0.000	0.005	0.000
	150	0.016	0.023	0.013
	165	0.035	0.050	0.033
	185	0.076	0.109	0.082
	200	0.126	0.167	0.145

	50	**0.000**	**0.001**	**0.000**
	85	0.005	0.006	0.000
	100	0.017	0.019	0.006
250	125	0.069	0.075	0.030
	150	0.184	0.208	0.099
	165	0.317	0.395	0.185
	185	0.583	0.745	0.402
	200	0.848	1.025	0.619
	50	0.000	0.001	0.000
	85	0.012	0.008	0.000
	100	0.032	0.021	0.008
350	125	0.113	0.084	0.050
	150	0.316	0.256	0.155
	165	0.543	0.447	0.287
	185	1.014	0.919	0.562
	200	1.464	1.310	0.903
	50	0.000	0.000	0.000
	85	0.018	0.010	0.004
	100	0.045	0.027	0.012
450	125	0.160	0.102	0.047
	150	0.435	0.282	0.143
	165	0.898	0.532	0.283
	185	1.707	1.048	0.602
	200	2.572	1.588	0.982
	50	0.000	0.000	0.000
	85	0.013	0.006	0.000
	100	0.035	0.017	0.006
550	125	0.125	0.070	0.026
	150	0.362	0.205	0.092
	165	0.713	0.350	0.178
	185	1.436	0.594	0.419
	200	2.202	0.952	0.656

3.3. Catalyst modifications upon annealing

Drastic modifications are observed on all three catalysts after the thermal annealing. The global morphology changes from 150 to 450 °C annealing are shown in TEM images in Figure 1-5. On 150 °C annealed catalysts, RuO_2 nanoparticles of ~1.8 nm were easily observed and well dispersed on TiO_2 regardless of the crystallinity of TiO_2 supports. Upon annealing at 450 °C, the phase of RuO_2 evolved

differently depending on the crystallinity of TiO_2: difficult to be distinguished on P25 but present as large crystals on anatase support. On rutile support, white areas and thin layers of approximately 1 nm were seen (Figure 1-5 f), which was found to be Ru-depleted areas and Ru thin layers, respectively (discussed in Section 3.3.3).

It can be noted that the shape and size of the TiO_2 particles are different among RuO_2/TiO_2-P25, RuO_2/TiO_2-A, and RuO_2/TiO_2-R catalysts, before and after annealing 450 °C. The P25 particles were observed as mainly round and ill-defined pseudo cubic shape with rutile and anatase particles being impossible to distinguish. The size of the P25 particles were 25 nm in average and unchanged before and after annealing at 450 °C. On the other hand, the home-made anatase TiO_2 particles were smaller, round and ill-defined rhombus shape in the average size of 6 and 11 nm, before and after annealing at 450 °C respectively. The home-made rutile TiO_2 particles were initially well-defined thin rods of rutile crystal of thin needles of 12 x 100 nm before annealing and grown into thick rods of 23 x 100 nm after annealing at 450 °C (Table 1-3). This sintering behavior resulted in the decrease in the specific surface areas as shown in Table 1-2. The specific surface area of the RuO_2/TiO_2-P25 did not evolve with increasing annealing temperature. On the other hand, the specific surface areas of RuO_2/TiO_2-A and RuO_2/TiO_2-R were reduced by half from the calcination at 150 to 450 °C.

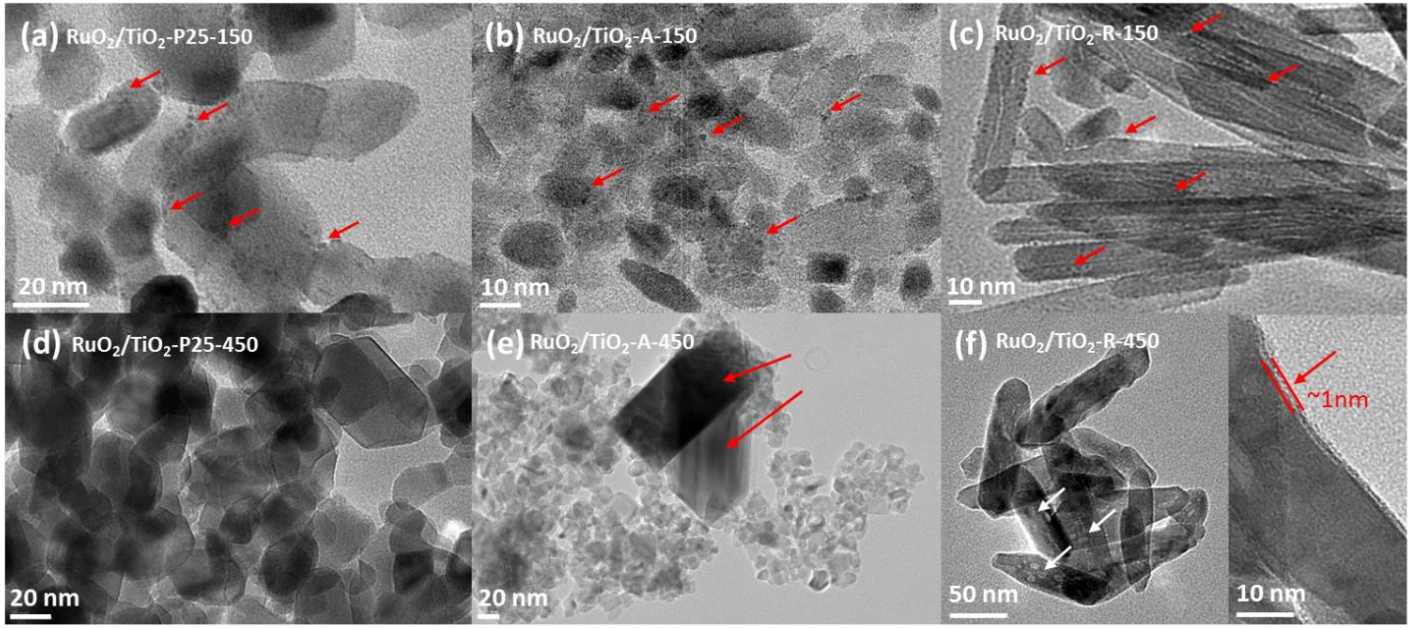

Figure 1-5: TEM micrographs of (a), (b), (c): RuO_2/TiO_2 catalysts annealed at 150 °C on P25, anatase, and rutile TiO_2, respectively; (d), (e), (f): RuO_2/TiO_2 catalysts annealed at 450 °C on P25, anatase, and rutile TiO_2, respectively. Red arrows point RuO_2 and white arrows point RuO_2- depleted areas.

Table 1-2: Summary of specific surface areas (BET).

Annealing T (°C)	Specific Surface Area ($m^2.g^{-1}$)		
	RuO_2/TiO_2-P25	RuO_2/TiO_2-A	RuO_2/TiO_2-R
Support only	50	144	71
150	52	132	64
250	45	118	60
350	50	64	41
450	46	60	32

Table 1-3: TiO_2 particle size (in nm) of RuO_2/TiO_2 catalysts measured by TEM analysis.

Annealing T (°C)	P25	Anatase	Rutile	
			width	length
150	28	6.3	11	100
250	22	7.7	10.5	105
350	-	10.5	17	95
450	25	-	24	97
550	29	-	28	96

The different sintering behavior between the anatase and rutile TiO_2 resulting from their different surface interaction with RuO_2, as well as the different particle size and shape between the rutile phase of P25 and home-made rutile TiO_2 are factors influencing the catalytic properties. More in-depth observations at each temperature are discussed below sequentially for P25, anatase, and rutile-supported catalysts with the help of HR-TEM, XRD, and XPS analyses.

3.3.1. P25

As calcination temperature increased from 150 °C to 250, 350, and 450 °C, the RuO_2 nanoparticles – initially clearly visible throughout all three samples – started to be difficult to observe in HR-TEM and HAADF-STEM.

After annealing at 250 °C, the TEM images revealed a sign of RuO_2 nanoparticles aggregation into a layer, as shown in Figure 1-6. It should be noted that the anatase and rutile particles are statistically very difficult to be distinguished due to their similar shapes in P25. Darker lines around some TiO_2 particles were measured to be around 2 – 3 nm thick. The interatomic spacing of the crystal lattice of this particle was measured to be around 3.2 Å, which is consistent with the (110) plane of rutile TiO_2 (3.24 Å) as well as (110) plane of RuO_2 (3.18 Å), meaning that RuO_2 thin layer

is seen on rutile TiO_2 particles. This RuO_2 redistribution phenomenon during thermal treatment or catalysis has also been proposed in the Deacon process as well as Volatile Organic Compound destruction [119, 138].

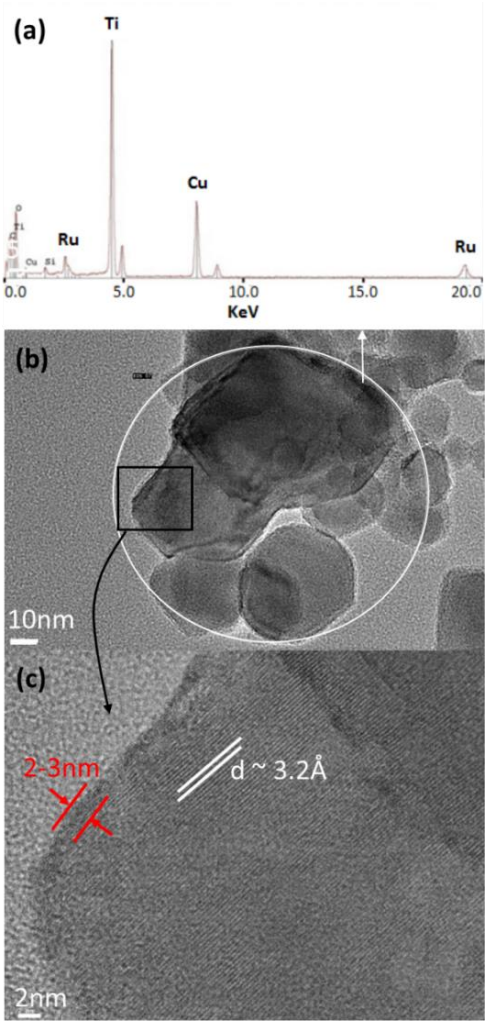

Figure 1-6: TEM images of RuO_2/TiO_2-P25-250 showing the presence of Ru on rutile TiO_2 particles. (a) EDX spectrum, (b) EDX analysis zone and certain particles surrounded by RuO_2, and (c) zoomed image of a catalyst particle corresponding to the d-spacing of rutile phase. Red arrows indicate the thickness of RuO_2 aggregates; white lines indicate d-spacing of the crystal planes; white circle indicates the EDX analysis zone in (a); black square indicates the zoomed area shown in (c).

After annealing at 450 °C, however, RuO_2 nanoparticles or agglomerates were not visible on the TEM micrographs. High-angle annular dark-field images (HAADF) were taken in scanning transmission electron microscopy (STEM) in order to obtain higher Z-contrast images of this catalyst. Figure 1-7 shows the images of TiO_2 particles taken in STEM mode, in both bright and dark field. Interestingly, the bright spots and layers found in dark field were found only on rutile TiO_2 particles. Energy dispersive X-ray spectroscopy clearly identified those bright spots as being Ru-rich. The higher atomic concentration of Ru was detected surrounding the rutile TiO_2 particles, suggesting the presence of RuO_2 layer (Figure1-7 c-d). Remarkably, the anatase TiO_2 particles, which compose 80 % of the P25 support, remained completely free of Ru (Figure 1-7 e-f).

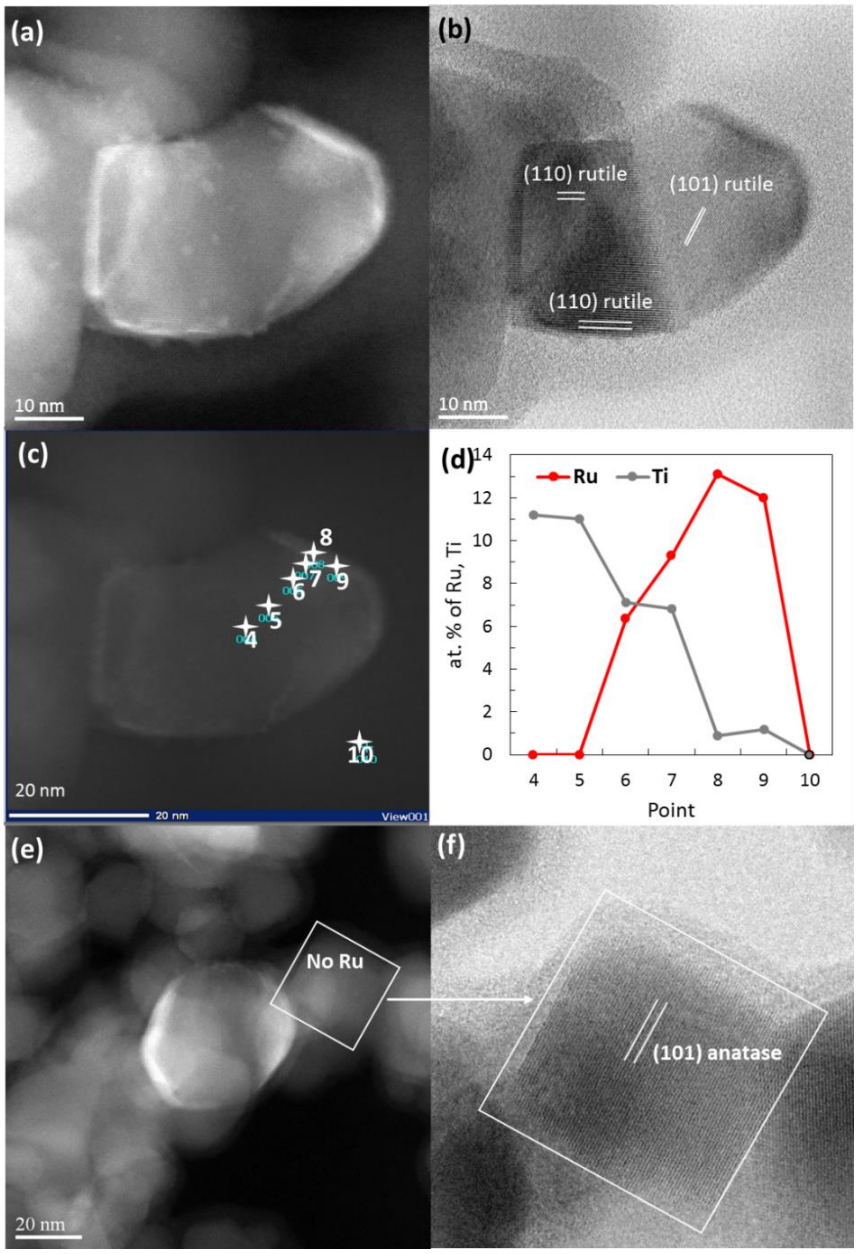

Figure 1-7: STEM images of TiO_2 anatase and rutile particles in the RuO_2/TiO_2-P25 catalyst after 450 °C calcinations; (a) HAADF image of rutile TiO_2 particles showing white spots, (b) bright field image revealing a rutile TiO_2 particle, (c) and (d) STEM-HAADF EDX analysis of rutile TiO_2 particles showing that Ru concentration is high on the white spots. (e) HAADF image of anatase TiO_2 particles free of RuO_2, (f) bright field image of a zoomed anatase TiO_2 particle.

XRD analysis and Scherrer calculations showed that the crystallinity of P25 does not evolve with the increased annealing temperature of the catalyst (Figure 1-8 and Table 1-6). The mean crystallite size calculated by Scherrer equation remained unchanged at each annealing temperature, which was consistent with the value measured from TEM observations. Also, all TiO_2 peaks (both anatase and rutile phases) remained un-shifted at all annealed temperatures. Deconvolution of RuO_2 peaks, however, showed that, with increased annealing temperature, the (110) RuO_2 and (101) RuO_2 peaks shift in opposite directions, both towards the associated rutile TiO_2 peaks (Table 1-5 and Figure 1-9); (110) RuO_2 peak was shifted towards (110) TiO_2 peak and (101) RuO_2 peak was shifted towards (101) TiO_2 peak (Figure 1-8). This observation is a clear indication of epitaxial interactions between RuO_2 and rutile TiO_2 and is supported by the fact that RuO_2 and rutile TiO_2 present the same rutile crystal structure with very close lattice parameters [PDF2-040-1290 and 070-7347]; Rutile TiO_2 with a=4.5933 Å, c=2.9592 Å and RuO_2 with a=4.4994 Å, c=3.1071 Å. The shift in RuO_2 peak positions towards rutile TiO_2 peak positions has consequences on the RuO_2 structure. The epitaxial growth of RuO_2 on rutile TiO_2 implies that the RuO_6 octahedron structure is less distorted compared to that of RuO_2 crystal alone.

The difference in cell parameters cannot be linked only with Ti^{4+} and Ru^{4+} radii (0.605 Å and 0.620 Å respectively;[141] a(RuO_2) is smaller than a(TiO_2) and c(RuO_2) is bigger than c(TiO_2). Accordingly, d_{110} (RuO_2) (3.183 Å) is smaller than d_{110} (TiO_2) (3.247 Å), and d_{101} (RuO_2) (2.558 Å) is bigger than d_{101} (TiO_2) (2.487 Å). As a consequence, the slightly distorted MO_6 octahedra are not oriented in the same way in both rutile structures: Two short Ru-O bonds (1.942 Å) propagate along the (110) direction for RuO_2 whereas this direction concerns the two long Ti-O bonds (1.978Å) for TiO_2. For RuO_2, the four remaining long Ru-O bonds (1.984 Å) are strongly governed by the c axis, whereas in case of TiO_2, the four short Ti-O bonds (1.945 Å) are restricted by the c axis. Accordingly, the significant increase of d_{110} (RuO_2) upon RuO_2 crystallization in proximity to rutile TiO_2 means an increase in length of the two short Ru-O bonds. Similarly, the decrease of d_{101} (RuO_2) contributes mostly to the decrease in the length of the long Ru-O bonds. Thus, in RuO_2/TiO_2-P25 catalyst, the shifts in the (110) and (101) RuO_2 peak positions respectively towards the (110) and (101) rutile TiO_2 peak positions indicate that RuO_2 nanoparticles are apt to crystallize adopting the rutile TiO_2 structure, which is referred to as epitaxial growth. This means that RuO_6 octahedron is globally less distorted in presence of rutile phase of P25 support than being crystallized into RuO_2 structure alone.

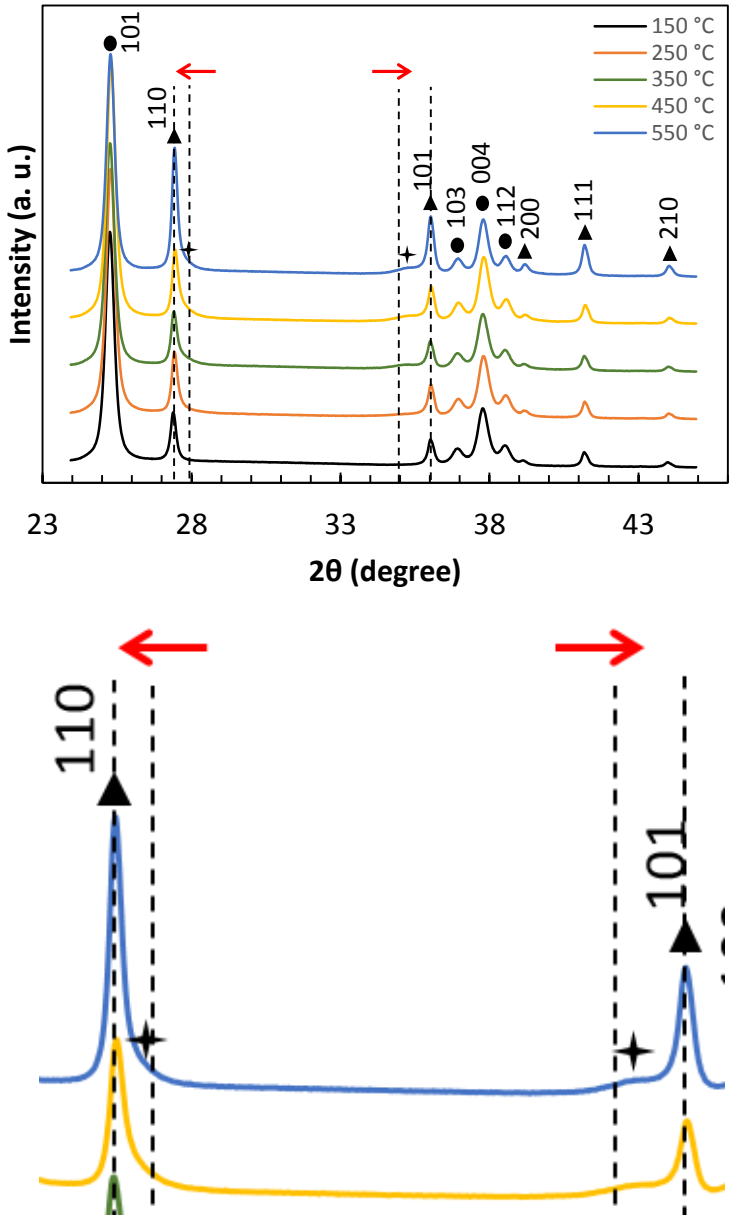

Figure 1-8: XRD patterns of RuO_2/TiO_2-P25 after annealed at 150, 250, 350, 450, and 550 °C; rutile TiO_2 (▲), anatase TiO_2 (●), shifted rutile RuO_2 (✦). Theoretical 2θ position of rutile RuO_2 and rutile TiO_2 are drawn as dotted lines (guide to the eye). Red arrows indicate the direction of RuO_2 peak position shift. Zoomed RuO_2 peaks shift is shown in the bottom image.

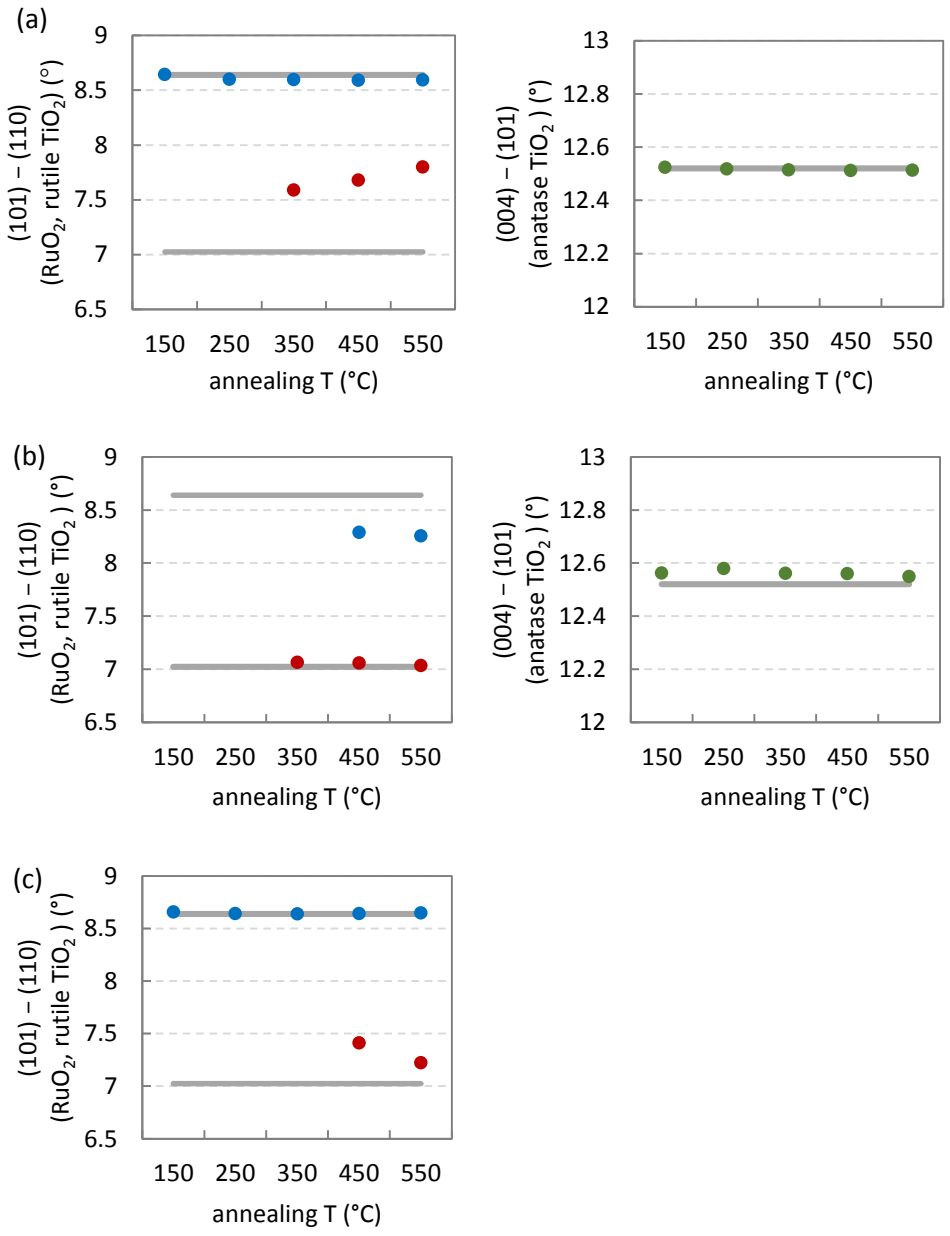

Figure 1-9: The difference between main XRD peak positions with annealing for (a) RuO_2/TiO_2-P25, (b) RuO_2/TiO_2-A, and (c) RuO_2/TiO_2-R. The main XRD peak positions used are (101) and (110) for RuO_2 (red) and rutile TiO_2 (blue), and (101) and (004) for anatase TiO_2 (green). Grey lines represent the expected values based on ICDD 01-070-2662 for RuO_2, ICDD 00-021-1276 for rutile TiO_2, and ICDD 00-021-1272 for anatase TiO_2.

XPS analysis showed a decrease in the atomic ratio of Ru/Ti with the increase in annealing temperatures while the surface atomic Ti ratio remained constant (Table 1-4). All 150 °C –annealed catalysts always had higher Ru/Ti ratios than bulk Ru/Ti ratio, 0.043, calculated based on the 2.2 wt. % of Ru in the final catalyst, indicating the good dispersion of Ru on the support surface, as seen in Figure 1-2 and 1-5a. The decrease in Ru/Ti ratio was observed with increasing annealing temperature. This could be attributed to the fact that Ru species are being concentrated only on rutile particles of P25 support, as previously demonstrated in TEM analysis. However, the link between the lower Ru/Ti ratio and the thin epitaxial layer formation phenomenon is not understood at this point.

Table 1-4: XPS analysis results of RuO_2/TiO_2 catalysts after annealing.

Reference	Ru at. %		Ti at. %	Ru/Ti (XPS)
	Ru (oxidized)	Ru (metallic)		
RuO_2/TiO_2-P25-	1.902	0.044	19.662	0.099
RuO_2/TiO_2-P25-	0.521	0.986	20.046	0.075
RuO_2/TiO_2-P25-	0.487	0.432	20.072	0.045
RuO_2/TiO_2-P25-	0.352	0.319	20.309	0.033
RuO_2/TiO_2-A-150	0.848	0.069	20.381	0.045
RuO_2/TiO_2-A-250	0.907	0.084	20.877	0.047
RuO_2/TiO_2-A-350	0.873	1.061	19.539	0.098
RuO_2/TiO_2-A-450	0.436	0.689	20.366	0.055
RuO_2/TiO_2-R-150	0.964	0.166	21.152	0.053
RuO_2/TiO_2-R-250	1.063	0.115	20.330	0.058
RuO_2/TiO_2-R-350	0.658	0.039	20.394	0.034
RuO_2/TiO_2-R-450	0.478	0.040	18.724	0.028

Table 1-5: Deconvolution of XRD peaks from 150 to 550 °C on the various support (P25, anatase and rutile). RuO_2 peaks can only be deconvoluted with reasonable width from high temperature on P25 and anatase. The proximity of the RuO_2 peaks to TiO_2 rutile prevents deconvolution of RuO_2 peak on the pure rutile TiO_2 support.

			P25 support		anatase support		rutile support	
		hkl	**2θ (°)**	**FWHM (°)**	**2θ (°)**	**FWHM (°)**	**2θ (°)**	**FWHM (°)**
150°C	**anatase**	101	25.2946	0.3419	25.2544	0.8953		
	TiO_2 rutile	110	27.4262	0.2105			27.4015	0.7226
	RuO_2	110						
	RuO_2	101						
	TiO_2 rutile	101	36.0699	0.2082			36.0602	0.4556
	anatase	103	36.9544	0.3691	36.9435	0.9111		
	anatase	004	37.8196	0.3959	37.8177	0.6631		
	anatase	112	38.5640	0.3801	38.5289	1.0937		
	TiO_2 rutile	200	39.1837	0.1927			39.2081	0.6722
250°C	**anatase**	101	25.3095	0.3412	25.2761	0.8814		
	TiO_2 rutile	110	27.4552	0.1924			27.4104	0.6663
	RuO_2	110						
	RuO_2	101						
	TiO_2 rutile	101	36.0550	0.2016			36.0518	0.4407
	anatase	103	36.9715	0.3597	37.0052	0.8381		
	anatase	004	37.8274	0.4018	37.8564	0.6431		
	anatase	112	38.5701	0.3869	38.5308	1.0354		
	TiO_2 rutile	200	39.2214	0.2512			39.1536	0.6193

	anatase	101	25.3147	0.3424	25.2918	0.7784		
	TiO_2 rutile	110	27.4642	0.2040			27.4084	0.5366
	RuO_2	110	27.7428	0.6486	27.9673	1.0202		
	RuO_2	101	35.3337	1.2289	35.0446	0.5075		
350°C	**TiO_2 rutile**	101	36.0624	0.2109			36.0466	0.3822
	anatase	103	36.9731	0.3664	36.9923	0.5518		
	anatase	004	37.8292	0.4031	37.8831	0.6769		
	anatase	112	38.5728	0.3839	38.5370	1.1692		
	TiO_2 rutile	200	39.2401	0.2883			39.1527	0.5385
	anatase	101	25.3259	0.3345	25.2678	0.5608		
	TiO_2 rutile	110	27.4777	0.1970			27.4084	0.4332
	RuO_2	110	27.7222	0.5689	27.9774	0.4925	28.0372	0.1969
	RuO_2	101	35.4020	1.1626	35.0278	0.5013	35.4491	1.3263
450°C	**TiO_2 rutile**	101	36.0676	0.2128			36.0495	0.3158
	anatase	103	36.9830	0.3520	36.9656	0.5313		
	anatase	004	37.8387	0.3930	37.8282	0.5451		
	anatase	112	38.5826	0.3726	38.5464	0.5902		
	TiO_2 rutile	200	39.2594	0.2974			39.1617	0.4659
	anatase	101	25.3196	0.3126	25.2712	0.5971		
	TiO_2 rutile	110	27.4705	0.1861	27.5005	0.4342	27.4084	0.3267
	RuO_2	110	27.6406	0.6369	27.9703	0.2840	28.0353	0.1106
	RuO_2	101	35.4398	1.0553	35.0114	0.2703	35.2582	0.2384
550°C	**TiO_2 rutile**	101	36.0656	0.2107	35.7596	0.7159	36.0560	0.2047
	anatase	103	36.9801	0.3042	36.9846	0.5841		
	anatase	004	37.8330	0.3528	37.8119	0.4861		
	anatase	112	38.5701	0.3363	38.4999	1.0359		
	TiO_2 rutile	200	39.2436	0.2729			39.1802	0.3569

3.3.2. Anatase

The S_{BET} of the RuO_2/TiO_2-A catalyst was decreasing drastically by annealing from 150 to 450 °C. This trend was well correlated with TEM observations. On home-made pure anatase TiO_2 support, the RuO_2 particles were found to be more concentrated in small areas at higher annealing temperature, while both anatase TiO_2 support and RuO_2 particles were being sintered independently. The energy dispersive X-ray analysis in TEM showed uniform atomic concentration of Ru over the support for 150 °C and 250 °C annealed catalysts from various areas analyzed. After annealing at 350 °C, a few large dark areas of highly concentrated Ru were found. Figure 1-10 shows the majority of the sample free of Ru (Figure 1-10 a) and a large crystal of RuO_2 (Figure 1-10 b) with their corresponding EDX intensity plots. Interestingly, a high Ti atomic concentration was found on the rutile-rod shaped crystal attached to the RuO_2 crystal. XRD analysis confirmed that this observation was indeed corresponding to the growth of rutile TiO_2 phase for this catalyst (Figure 1-11) at the temperature significantly below the anatase-to-rutile transformation temperature of 600 °C [44, 142, 143]. In contrary to the case of rutile phase of P25, RuO_2 does not migrate toward the newly grown rutile TiO_2 crystal in this case.

From XRD analysis, the pure anatase TiO_2 peaks became thinner with increased annealing temperature as the crystal growth resulted in the increase in the crystallite size. On the other hand, RuO_2 peaks did not shift when supported on pure anatase TiO_2. This is in correlation with TEM images where large RuO_2 crystallites were observed clearly separated from the anatase TiO_2 support. Since no evidence of epitaxial growth of RuO_2 was found, RuO_6 octahedron is not modified by anatase TiO_2. Deconvolution of the RuO_2 peaks was only possible at annealing temperature above 350 °C (Table 1-5). The d_{110} and d_{101} of RuO_2 did not evolve with increasing annealing temperature. Surprisingly, at 350 °C and 450 °C, the appearance of (110) and (101) rutile TiO_2 peaks were observed as shown in Figure 1-11. Interestingly, these peaks were identified as shifted- (110) and (101) TiO_2 rutile peaks respectively towards (110) and (101) RuO_2 peaks, as opposed to what was observed on rutile phase of TiO_2 P25. This observation indicates the occurrence of rutile TiO_2 crystallization starting at 350 °C through the epitaxial lattice matching mechanism from RuO_2 to TiO_2, as also confirmed in Figure 1-10.

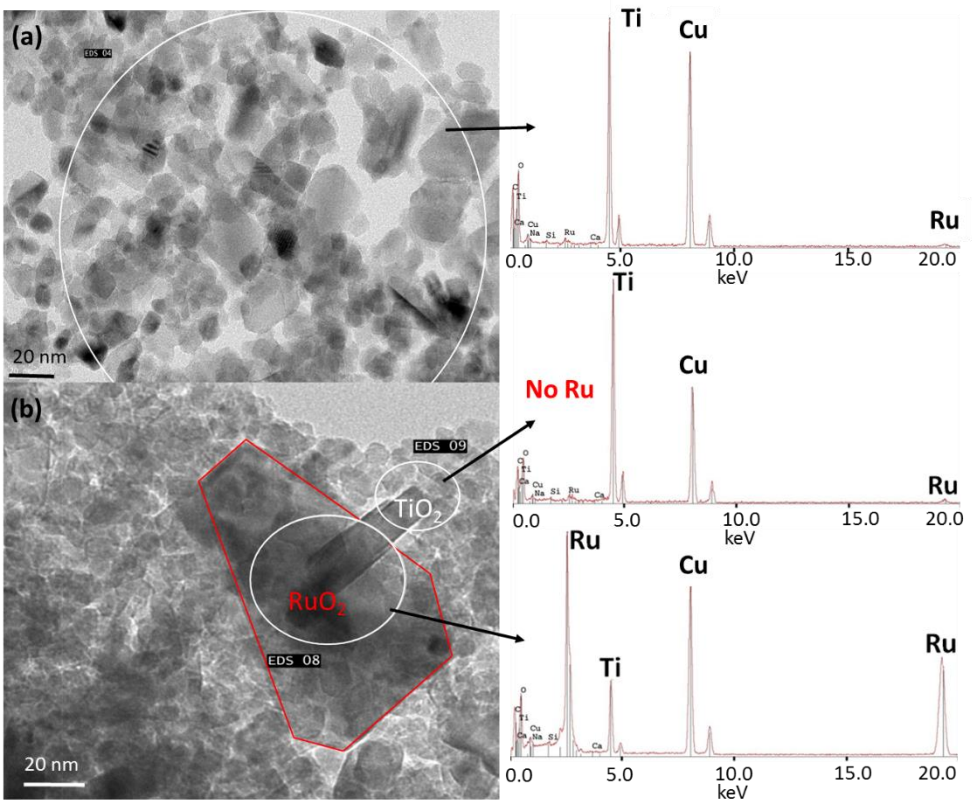

Figure 1-10: TEM images and EDX intensities of RuO_2/TiO_2-A after annealing at 350 °C; (a) anatase particles free of Ru and (b) large RuO_2 nanocrystal onto which rutile TiO_2 phase has crystallized.

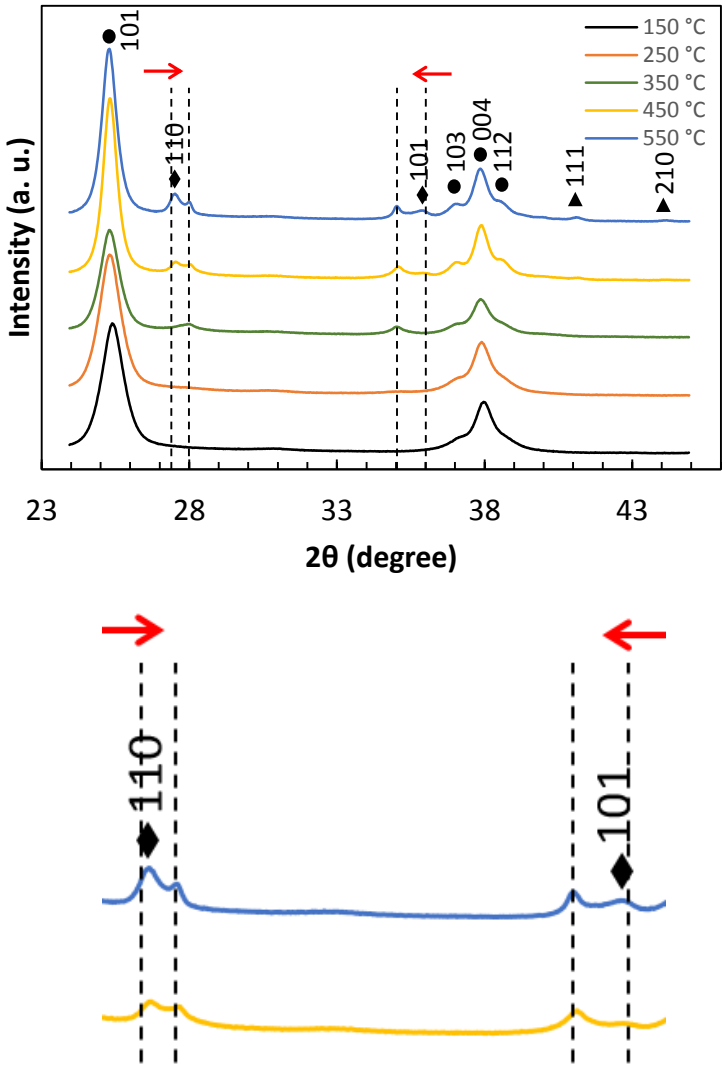

Figure 1-11: XRD patterns of RuO_2/TiO_2-A after annealed at 150, 250, 350, 450, and 550 °C; rutile TiO_2 (▲), anatase TiO_2 (●), rutile RuO_2 (★), shifted rutile TiO_2 (◆), theoretical 2ϑ position of rutile RuO_2 and rutile TiO_2 are drawn as dotted lines (guide to the eye). Red arrows indicate the direction of rutile TiO_2 peak position shift. Zoomed rutile TiO_2 peaks shift is shown in the bottom image.

Ru/Ti ratios determined by XPS analysis at various annealing temperatures (Table 1-4) do not agree with sintered Ru species observed by TEM or XRD analysis. Due to the sintering of both support and Ru species on pure anatase support, extraction of a trustworthy trend at various annealing temperatures becomes delicate.

3.3.3. Rutile

TEM observations showed a gradual shape evolution of RuO_2/TiO_2-R catalysts at elevated annealing temperatures from 150 to 450 °C (Figure 1-14). After 150 °C annealing, RuO_2 nanoparticles were well distributed on the intact rod-shaped rutile TiO_2 particles (Figure 1-12). Starting from 250 °C annealing, the nanoparticles started to "disappear" to form thin RuO_2 layers. With increasing annealing temperature, the layer around the rutile TiO_2 rods became better defined and the thickness was measured to be approximately 1 nm. This phenomenon is in accordance with the RuO_2 nanoparticles transforming into a thin layer on the rutile particles of P25 support. The thin layer was verified to have d-spacing of 3.2 Å, which corresponds to the (110) plane of rutile RuO_2 (3.18 Å) (Figure 1-13). This is an indication that the (110) RuO_2 plane is oriented parallel to the (110) rutile TiO_2 plane of the support, forming the so-called epitaxial layer [119]. Unlike the case of P25 support, the thin RuO_2 layer covering the rutile TiO_2 particles exhibits Ru-depleted areas, as shown in white areas in bright field TEM images in Figure 1-14 d-e. These Ru-depleted areas are believed to be generated by the low content of RuO_2 which is not sufficient to fully cover the surface of rutile TiO_2 particles.

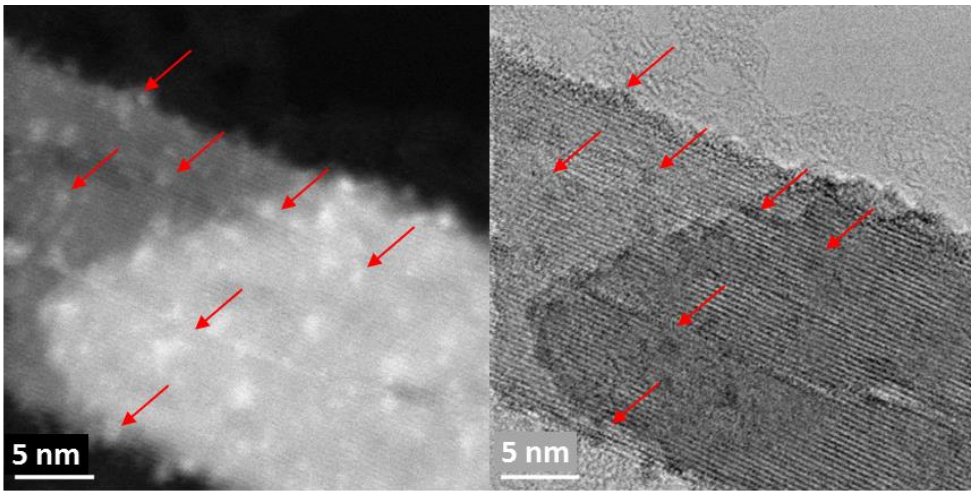

Figure 1-12: HRTEM images of RuO_2/TiO_2-R-150, dark field (left) and bright field (right). Red arrows point some of the RuO_2 nanoparticles.

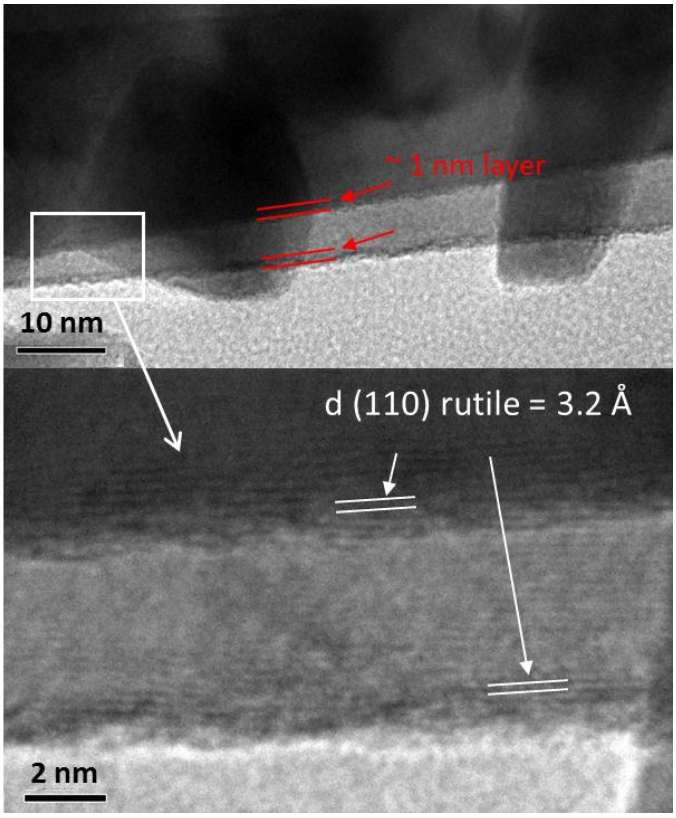

Figure 1-13: RuO_2 layer of ~ 1 nm on (110) plane of rutile TiO_2 on RuO_2/TiO_2-R-450.

The TiO_2 support itself was clearly affected by the thermal treatment (Figure 1-14). The TiO_2 rutile average particle dimensions in width and length were measured based on TEM images. The width of the support particles was found to be approximately doubled from 150 °C to 450 °C (Also confirmed by Scherrer calculations, shown in Table 1-6), while the length remained constant. It suggests stacking of the rod- shaped rutile TiO_2 particles in direction of the (110) facet, as depicted in Figure 1-15. STEM images and their corresponding HAADF images revealed the presence of white lines of RuO_2 layers every ~ 12 nm in average, which corresponds to the initial width of the rutile TiO_2 rod (Figure 1-15 c). This evidences that RuO_2 epitaxial layers on (110) facet of rutile TiO_2 thus act as "cement" between the 12 nm-wide TiO_2 rutile rods, resulting in the "sandwiching" of the RuO_2 layers between TiO_2 rods.

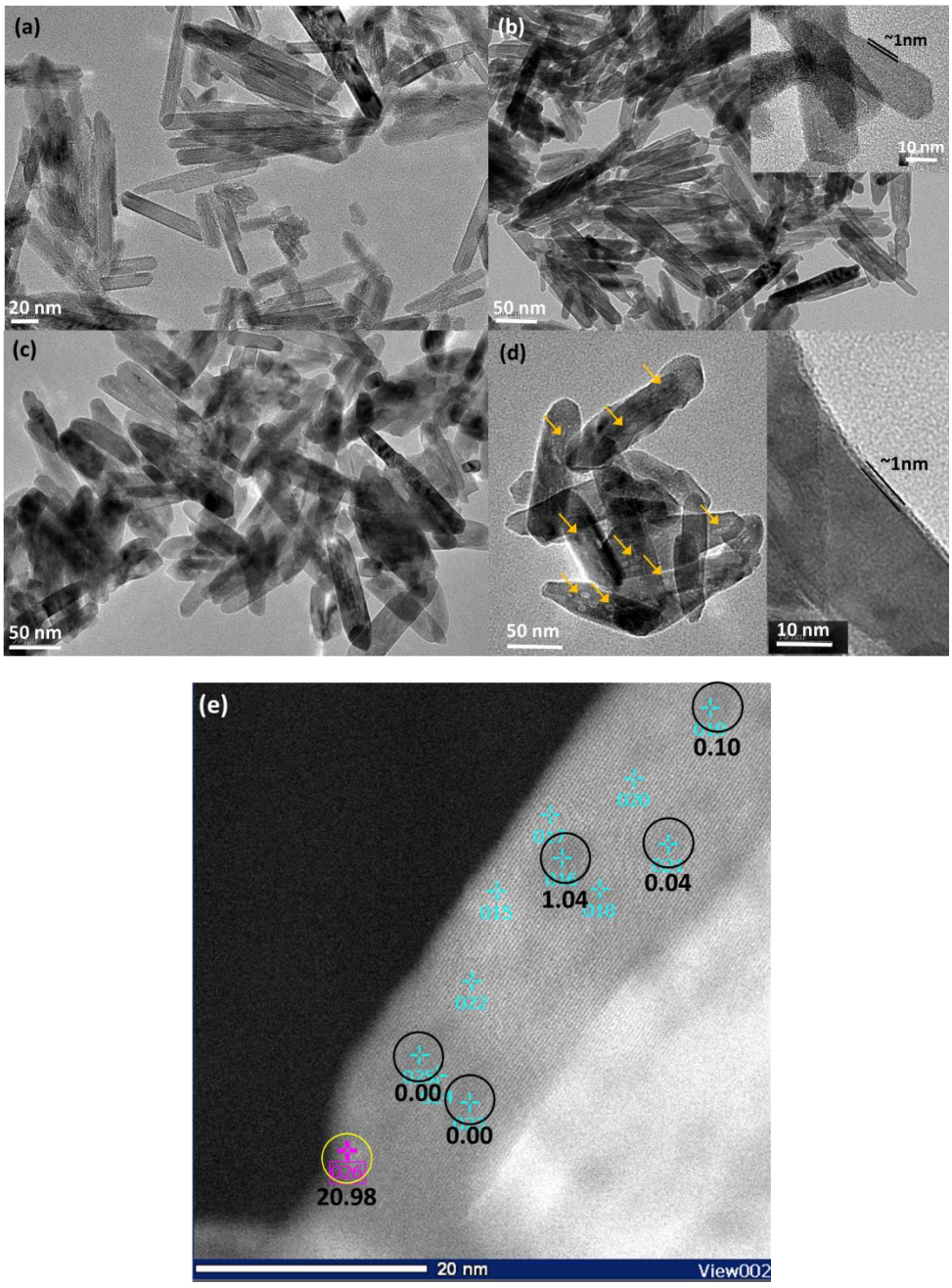

Figure 1-14: TEM images of RuO_2/TiO_2-R after annealing at (a) 150°C, (b) 250 °C, (c) 350 °C, (d) 450 °C, and (e) STEM-HAADF EDX analysis on Ru depleted spots (black circles) and Ru-concentrated spot (yellow circle), and corresponding atomic concentration of Ru in numerical values (%). Arrows point white spots corresponding to Ru depleted spots.

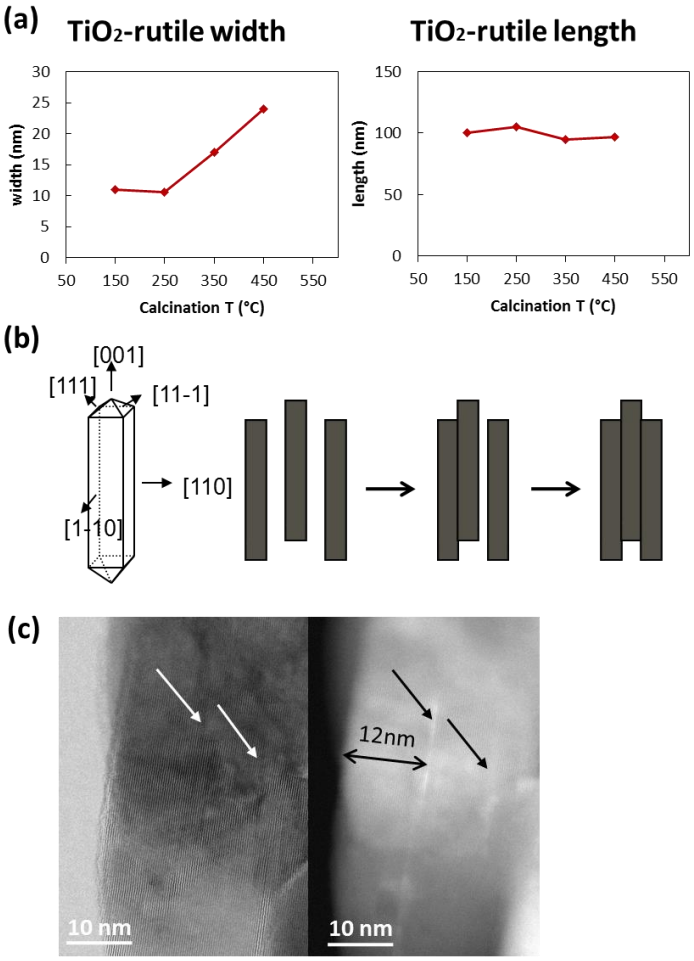

Figure 1-15: (a) TiO_2-rutile particle size measurement; (b) Schematic drawing of TiO_2-rutile growth in the direction of (110) facet; (c) STEM images of rutile RuO_2/TiO_2-R-450 particle and the corresponding dark field image. Arrows indicate RuO_2 layer in-between irutile TiO_2 particles and double arrow indicates the initial width of rutile TiO_2 particle.

Upon heating, the crystallinity of pure rutile TiO_2 evolves due to sintering and growth. The XRD peaks are clearly becoming thinner as shown in Figure 1-16. Due to the broad and high intensity of the pure rutile peaks as well as RuO_2 crystallization into the epitaxial layer over the rutile TiO_2 crystals as discussed earlier, the RuO_2 peaks were difficult to be seen. The degree of mismatch between pure RuO_2 and pure rutile TiO_2 stands as 1.8% for (110) surface and 2.7% for (101) surface, largely below the reported 5% limit authorizing epitaxial layer growth [116, 119].

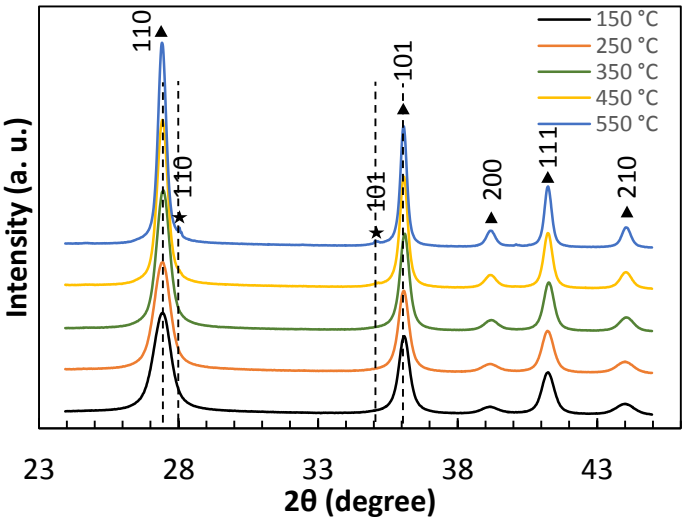

Figure 1-16: XRD patterns of RuO_2/TiO_2-R; rutile TiO_2 (▲), rutile RuO_2 (★), theoretical 2ϑ position of rutile RuO_2 and rutile TiO_2 are drawn as dotted lines (guide to the eye).

Table 1-6: TiO_2 support particle sizes calculated from the Scherrer equation. In case of pure rutile TiO_2 support, only the widths of the needle are calculated.

		rutile			anatase				mean size (Å)
	(°C)	110	101	200	101	103	004	112	
P25	150	47.5	49.2	54.6	26.7	25.2	23.4	24.5	35.9
	250	53.1	51.2	39.5	26.8	25.9	23.0	24.0	34.8
	350	49.4	48.4	33.6	26.6	25.4	22.9	24.2	32.9
	450	51.6	47.9	32.4	27.4	26.6	23.5	25.0	33.5
	550	43.5	47.8	42.5	29.6	31.0	26.3	28.1	35.5
anatase	150				9.4	9.5	13.3	7.9	10.0
	250				9.6	10.4	13.8	8.4	10.5
	350				10.9	16.2	13.1	7.4	11.9
	450				15.5	16.9	16.5	15.1	16.0
	550				14.5	14.0	17.0	15.9	15.3
rutile	150	11.9		13.2					12.5
	250	12.9		14.4					13.7
	350	16.3		16.7					16.5
	450	20.6		19.6					20.1
	550	23.8		23.9					23.9

XPS analysis on RuO_2/TiO_2-R catalysts showed the decrease in both metallic Ru and oxidized Ru species resulting in the decrease in Ru/Ti ratios with the increased annealing temperature (Table 1-4). Unlike RuO_2/TiO_2-A catalysts, the decrease in Ru/Ti is clearly identified despite of sintering of the support. This is attributed to the "sandwich" structure described above in which RuO_2 is strongly attached to the rutile TiO_2 support and then embedded in larger particles.

3.4. Catalyst modifications upon reduction

The close observation of the morphology of RuO_2 phase at different temperature increment indicated unambiguously that the nature of the support dictates the behavior of the RuO_2 nanoparticles and this was correlated with different catalytic performance. Yet, the actual active species in the methanation reaction is the reduced states of Ru over TiO_2 obtained after an in situ thermal treatment under H_2 at 200°C. The three most active catalysts for each support, annealed at 450 °C, were analyzed by TPR. As shown in Figure 1-17, the peaks of H_2 consumption for the three catalysts were not exactly overlapping which indicate that the oxidized catalysts on different TiO_2 supports do not present the same reduction pattern. For P25 supported catalyst, two close reduction events were observed, both below 200 °C. On the other hand, for anatase TiO_2 supported catalyst, one main reduction event was observed at 200 °C with another slight reduction event of broader temperature range centered around 366 °C and for rutile TiO_2 supported catalyst, two well-defined main reduction events were observed. These two reduction events for rutile TiO_2 supported catalysts provide an insight of more (exposed) and less (trapped) accessible RuO_2 layers corresponding to the lower and higher reduction temperatures, respectively. As discussed in the previous section, the support structure has a strong impact on the morphology of RuO_2 in the oxidized catalysts and this appears to result in different reducibility. To gain further insight on the impact of the support structure on the catalytic performance, the post-methanation catalysts (annealed at 450 °C) were observed by TEM and XPS.

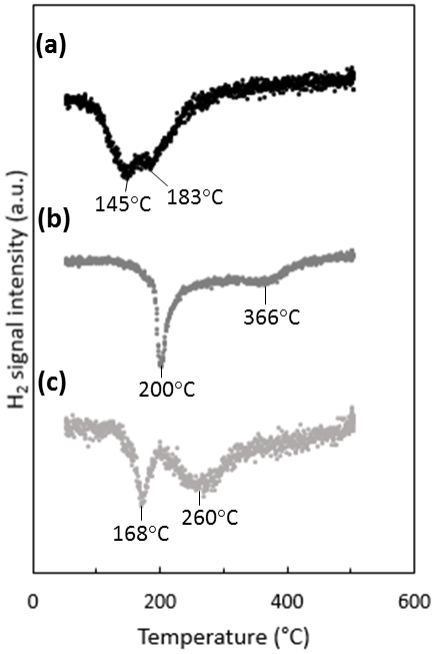

Figure 1-17: TPR results of (a) RuO_2/TiO_2-P25-450, (b) RuO_2/TiO_2-A-450, and (c) RuO_2/TiO_2-R-450.

In Ru/TiO_2-P25-450 post methanation, as the RuO_2 reduces into metallic Ru, the epitaxial lattice matching over rutile TiO_2 is suppressed. As a result, the TEM image contrast between metallic Ru and TiO_2 becomes higher than between RuO_2 and rutile TiO_2. This allows to clearly distinguish metallic Ru patches that are non-homogeneously dispersed on TiO_2 P25 particles. Most TiO_2 particles remain "naked" (Ru-free) and a few particles are covered by Ru nanoparticles (Figure 1-18 a). Energy dispersive X-ray analysis on various areas of the TEM grid confirmed the presence of Ru on the TiO_2 particles that appear "decorated" and the absence of Ru where TiO_2 particles appear naked. HR-TEM images clearly showed (110) TiO_2 rutile plane underneath Ru particles (Figure 1-18 b-c). These observations are ultimately confirmed by 3-D TEM tomography analysis shown in Figure 1-19.

Ru nanoparticles mostly appear closely packed at the rutile TiO_2 surface, resulting in clustered Ru particles with mean size of 2.8 ± 1.0 nm as well as in Ru layers. Anatase TiO_2 particles of P25, on the other hand, always appear to be Ru-free. This unambiguously confirms that the Ru that accumulated specifically onto rutile TiO_2 particles in the form of RuO_2 epitaxial layers during annealing remain localized over the same TiO_2 rutile particles upon reduction.

As observed previously during the thermal annealing treatment, the mean particle size of TiO_2 P25 has not been affected by the catalytic test and remained at 25 ± 14 nm.

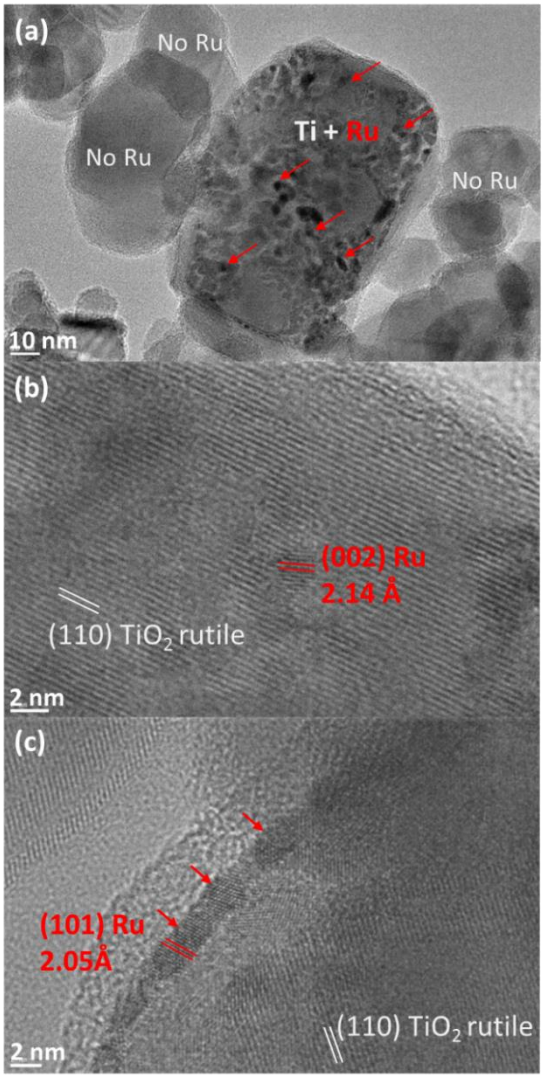

Figure 1-18: TEM image of Ru/TiO_2-P25-450 post methanation; (a) Ru-free anatase TiO_2 and Ru-covered rutile TiO_2 particles, HRTEM images of (b) crystal planes of metallic Ru and rutile TiO_2 and (c) rutile TiO_2 surrounded by Ru particles showing (002) and (101) Ru planes.

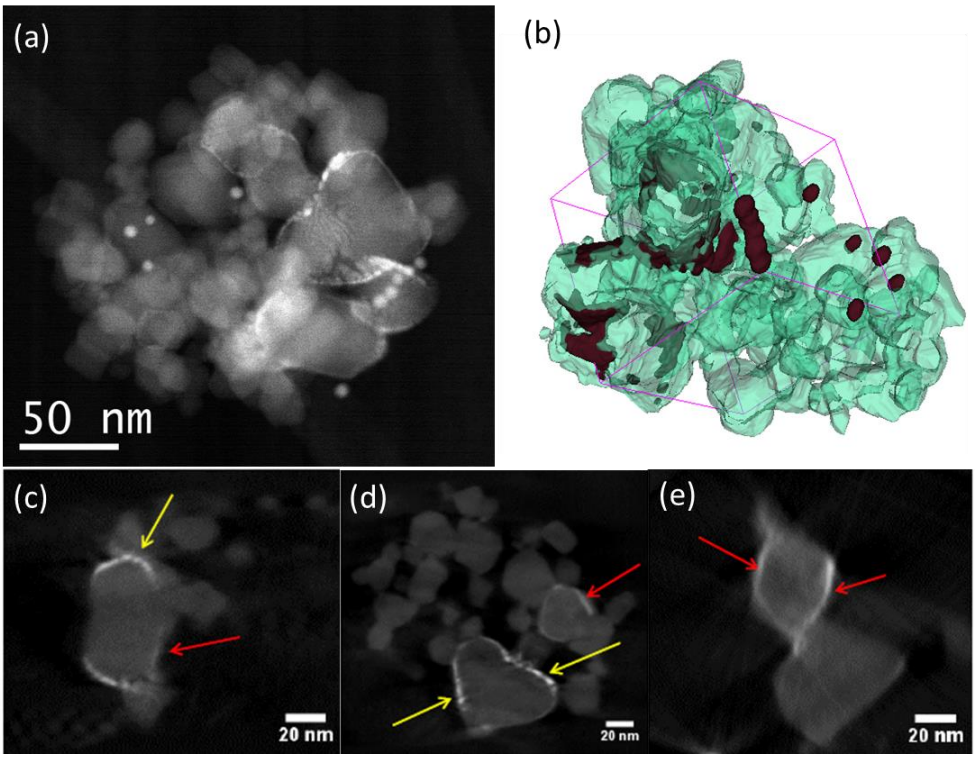

Figure 1-19: 3D-TEM tomographic analysis of Ru/TiO_2-P25-450 showing the presence of Ru on the surface of rutile TiO_2 particles after reduction and methanation; (a) STEM-HAADF image extracted from the tilt series used to calculate the reconstruction of this aggregate, (b) 3D model of the studied aggregate, with Ru nanoparticles in dark red, and (c), (d) and (e) representative slices extracted from the reconstruction, showing the presence of Ru on some of TiO_2 nanoparticles as individual particles (yellow arrows) or as a continuous thin layer (red arrows). This 3D analysis underlines the preferential localization of the Ru after reaction on only some TiO_2 nanoparticles (rutile particles as proven by HRTEM). The Ru is present as individual nanoparticles or as a thin layer covering a given facet.

On the anatase support, metallic Ru particles appear as agglomerates of smaller particles as shown in Figure 1-20 a. The approximate sizes of these agglomerates are in the same range as the RuO_2 crystal prior to reduction and catalytic test (50 to 100 nm) and the global shape of the biggest agglomerates remains close to the initial RuO_2 crystals. Their thickness however is too big to allow the electronic beam to go through (Figure 1-20 b). Only the smaller agglomerates allow the observation of separate Ru particles. It is suggested that RuO_2 has undergone fragmentation

during reduction, but no significant re-dispersion, leaving most of the anatase particles uncovered. Ru particles appear crystalline ((100), (002) and (101) planes of metallic Ru) (Figure 1-20 c-d), with a mean size of 3.8±1.0 nm. As observed on the non-reduced sample, a few rutile TiO_2 crystals could be seen; systematically decorated with Ru particles (Figure 1-20 c), again attesting the absence of Ru mobility during reduction and methanation. The size of anatase TiO_2 particles remains unchanged after reduction and methanation (11.5±2.6 nm).

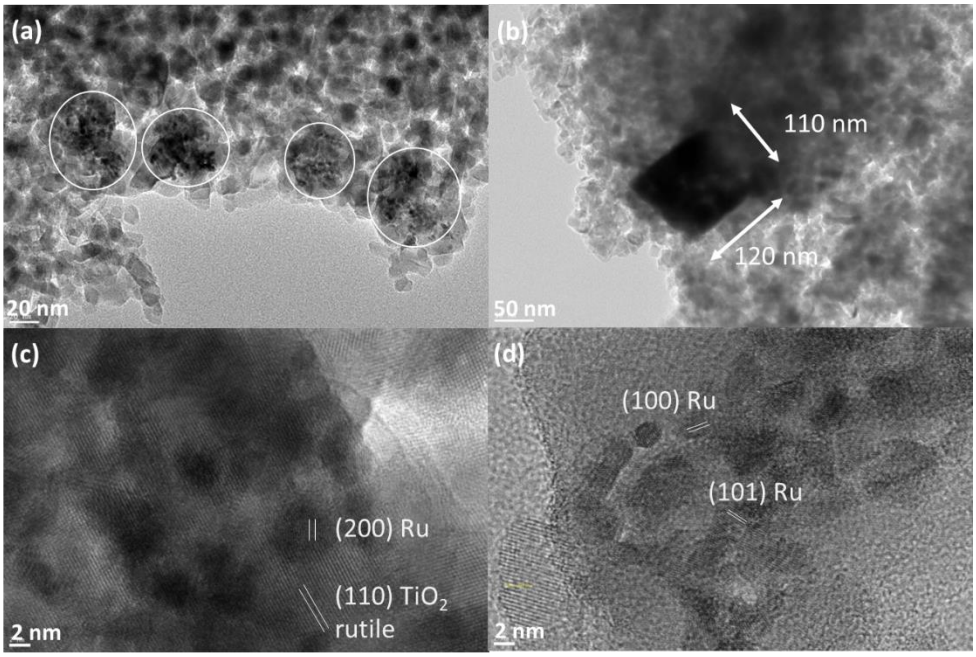

Figure 1-20: TEM images of Ru/TiO_2-A-450 post methanation; (a) fragmented and agglomerated Ru particles (indicated by white circles) (b) a large Ru agglomerate, (c) crystalline planes of Ru over rutile TiO_2 particles in HRTEM, (d) crystalline Ru particles in HRTEM.

On pure rutile TiO_2, metallic Ru particles can be easily seen after methanation; they are mainly localized close to the tip of the TiO_2 rutile needles (Figure 1-21 a). Their mean size is 3.5±1.0 nm. TiO_2 needles have not sintered during reduction or reaction (length of 96±17 nm and width of 24±5 nm). Ru particles, however, appears scarce on the numerous images that were taken, in comparison with P25 and anatase supports. Instead, STEM HAADF images show trapped Ru-containing

layers in between the rutile TiO_2 crystals (Figure 1-21 b-c), indicating that the "sandwiching" of RuO_2 is maintained upon reduction.

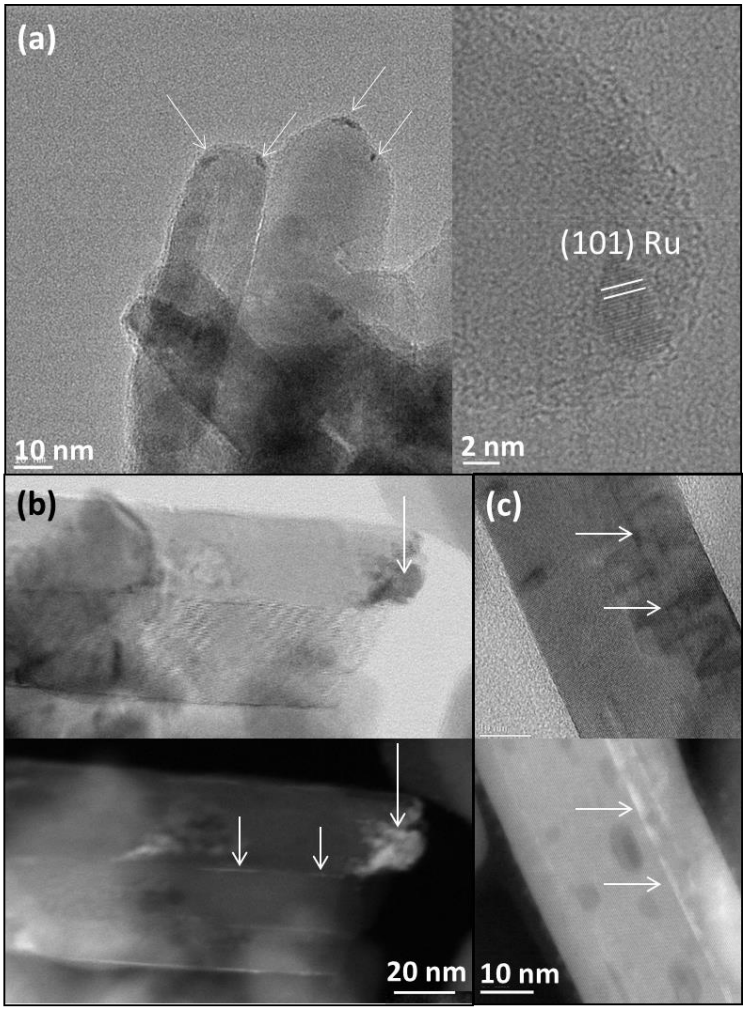

Figure 1-21: TEM images of Ru/TiO_2-R-450 post methanation; (a) Ru particles at the tip of the rutile TiO_2 needles, (b) and (c) STEM images of sintered rutile TiO_2 particles; bright field (top) and dark field (bottom).

XPS analysis after methanation revealed that Ru/Ti ratios remained similar to the values obtained before methanation for all three supports (Table 1-7), indicating that the catalysts were barely modified after reduction and methanation.

For all three supports, the proportion of surface metallic Ru increased after reduction and methanation. It is, however, important to note that the metallic Ru proportions on rutile support were significantly lower compared to P25 and anatase support as shown in Figure 1-22, due to the "sandwiched" RuO_2 layers described above. This fraction of ruthenium is not subjected to reduction. On the P25 support, the proportion of oxidized and metallic Ru in the spent catalysts was always around 40% oxidized and 60% metallic Ru species (after being exposed to air) regardless of the annealing temperatures (Figure 1-22 a-b). This indicates that the beneficial effect of high annealing temperature is exerted through the morphology changes observed for the active phase and not through a change in reducibility of the RuO_2 phase.

H_2 chemisorption resulted in the Ru dispersion values of 24 %, < 5 %, and 13 % for Ru/TiO_2-P25-450, Ru/TiO_2-A-450, and Ru/TiO_2-R-450, respectively. A lower Ru dispersion suggests sintering of Ru nanoparticles. Based on the fact that the P25 and rutile supports follow the same pattern of RuO_2 modification through epitaxial layer formation, the lower Ru dispersion value of Ru/TiO_2-R-450 compared to Ru/TiO_2-P25-450 is clearly attributed to the loss of Ru in between the rutile TiO_2 particles. On the other hand, the lowest Ru dispersion value of Ru/TiO_2-A-450 is due to the high degree of sintering of RuO_2 resulting in highly agglomerated Ru after reduction. In conclusion, dispersion is strongly affected by the modifications that occur during annealing as described above.

Table 1-7: Comparison of Ru/Ti ratios before and after reduction and methanation for catalysts annealed at 450 °C.

Support	**Ru/Ti (XPS)**	
	Before reduction	After methanation
P25	0.033	0.036
Anatase	0.055	0.068
Rutile	0.028	0.031

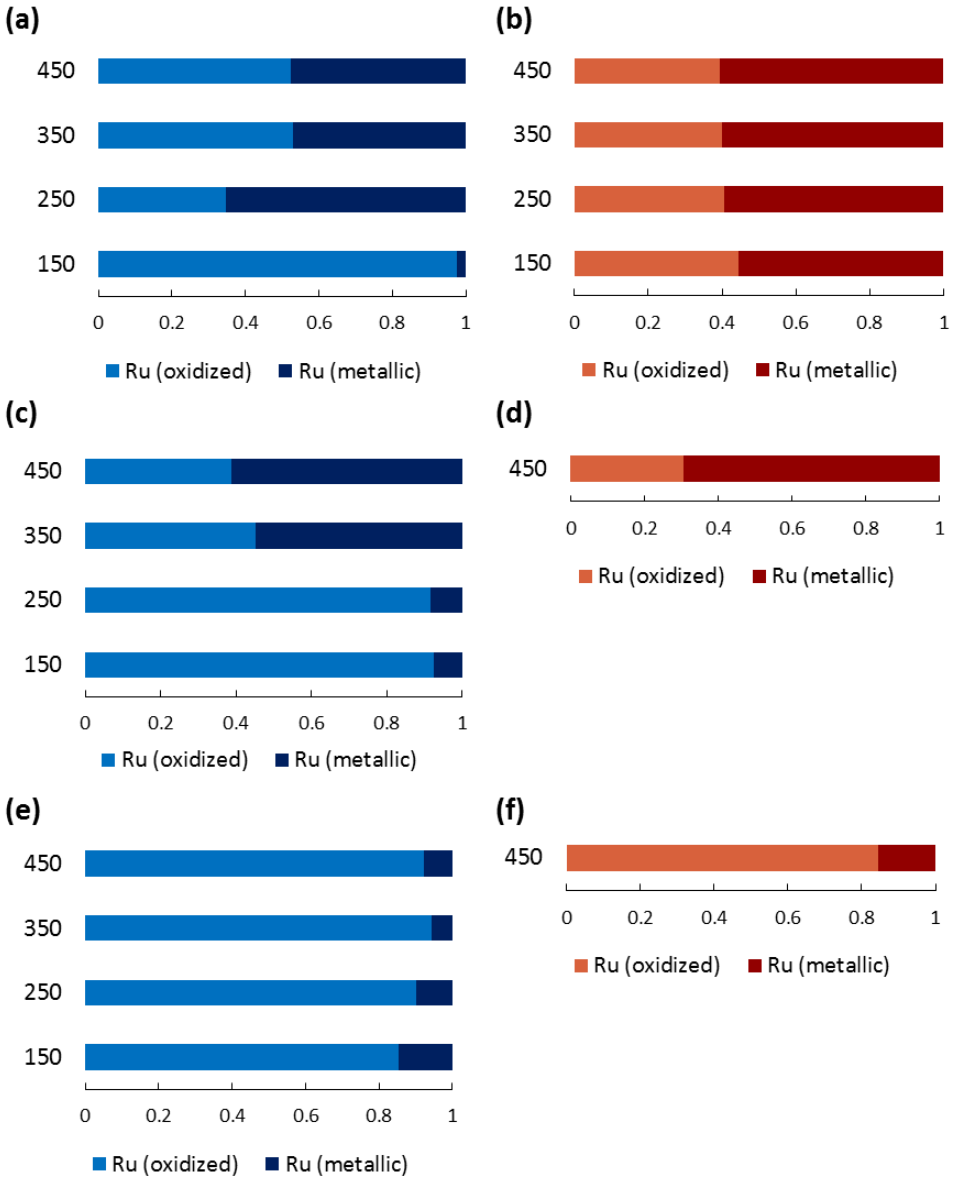

Figure 1-22: Proportions of oxidized and metallic Ru species by XPS; (a) RuO_2/TiO_2-P25 (before reduction), (b) Ru/TiO_2-P25 (after methanation), (c) RuO_2/TiO_2-A (before reduction), (d) Ru/TiO_2-A (after methanation), (e) RuO_2/TiO_2-R (before reduction), and (f) Ru/TiO_2-R (after methanation).

3.5. Decisive factors dictating methanation activity

The catalysts prepared on different crystalline TiO_2 supports show distinctive behaviors in the catalytic reaction of CO_2 methanation. Although the selectivity to CH_4 was 100 % for all catalysts, the level of activity was markedly affected by the crystallinity of the TiO_2 support used. As a general trend, the P25 supported catalysts showed the best CH_4 production rate, followed by anatase- and then rutile-supported catalysts. Taking into account the dispersion data, a turn over frequency (TOF) can be calculated. At 200°C, the TOF (expressed as mole of CH_4 produced per mole of surface-accessible Ru per second) reached very close values for Ru/TiO_2-P25-450 (~0.11 s^{-1}) and for Ru/TiO_2-R-450 (~0.16 s^{-1}). This indicates that the specific activity of P25 and rutile-supported catalysts is directly related to the dispersion of the Ru phase. The TOF is found to be much higher for Ru/TiO_2-A-450 (about 0.59 s^{-1}). This has to be related to the high degree of RuO_2 sintering after annealing (poor dispersion). Moreover, this suggests that different Ru surface species exist on anatase TiO_2 support, having distinct intrinsic activities compared to those stabilized onto P25 or rutile TiO_2 supports. This indicates that Ru atoms present at the surface of more agglomerated particles as those formed on anatase have higher intrinsic activity than the Ru atoms present at the surface of less agglomerated particles stabilized onto rutile. Similarly, different physical states of active species have been reported to have different intrinsic activities. The importance of the optimum size and distribution of the active nanoparticles has been proven in the case of ammonia synthesis [144] (Ru particles) and CO_2 methanation [107] (Rh particles) under mild conditions. Moreover, the importance of the exposed active face, as well as the presence of defects, steps or terraces on the catalyst surface has been widely discussed for TiO_2 and metallic ruthenium [145, 146]. This discussion, however, is beyond the scope of this current study and has to be tempered by mechanistic studies and the fact that CO_2, and not only H_2, plays a major role in the CO_2 methanation reaction. Independently from the proposed pathways for CO_2 methanation (mainly formate intermediates versus direct CO_2 dissociation into CO_{ads} and O_{ads}), the dissociation of CO_{ads}, assisted or not by hydrogen, is indeed generally recognized to be the rate-determining reaction [132, 147, 148].

The detailed inspection of the catalyst morphology at various annealing temperatures by TEM provided a link between the morphology and the resulting catalytic behaviour. In summary, on anatase and rutile TiO_2 crystalline phases, two main phenomena occurs with regards to the shape of the RuO_2 species after annealing at 450 °C as presented in Figure 1-23. The weak interaction between

RuO_2 and anatase TiO_2 results in the growth of large rutile structured RuO_2 crystals which do not interact with the support. After reduction, the resulting large metallic Ru aggregates have high intrinsic activity but the proportion of surface Ru is so low that only modest levels of activity are obtained. Strong interaction between RuO_2 and rutile TiO_2 promotes the formation of continuous epitaxial layer, dominantly over (110) facet, and to a sandwiching phenomenon that results in loss of Ru species, embedded between TiO_2 rods. For P25-supported catalysts, the same epitaxial interaction is observed between RuO_2 and rutile TiO_2 particles but the co-existence of rutile and anatase particles gives rise to better dispersed RuO_2 with anatase TiO_2 acting as a diluent to separate the RuO_2/rutile-TiO_2 particles. Thus, the co-existence of anatase and rutile phase in P25 is proven to be the reason for the high CO_2 methanation activity.

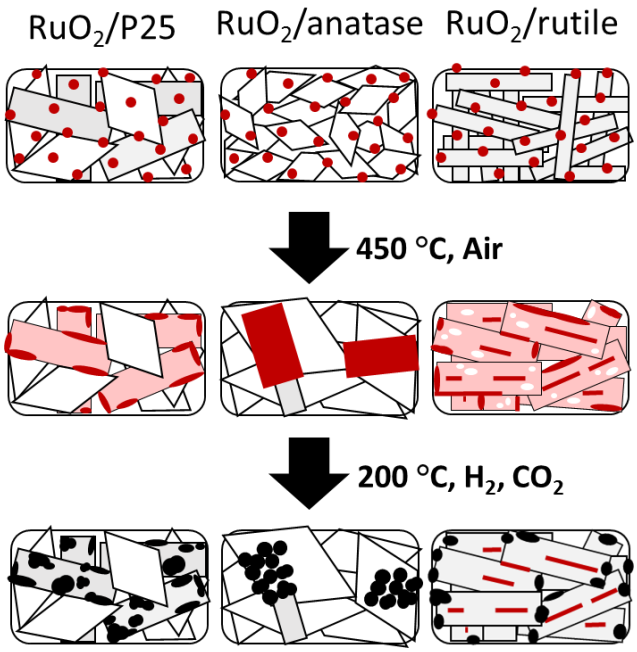

Figure 1-23 Graphical illustration of the shape evolution of the RuO_2/TiO_2 catalysts; after RuO_2 nanoparticles deposition, after thermal annealing at 450 °C, and after reduction and methanation. Red indicates RuO_2, Pink indicates thin RuO_2 layer, white indicates Ru depleted area, and black indicates metallic Ru.

4. Conclusion

Ru/TiO_2 methanation catalysts were studied systematically, starting from calibrated RuO_2 nanoparticles as precursor for active Ru species, which are subsequently supported on anatase, rutile, and mixture of the two crystal structures of TiO_2 (commercial P25 from Degussa).

This strategy using different crystalline TiO_2 as supports for RuO_2 nanoparticles provides an insight in the nature of the interactions between RuO_2 and the respective crystalline structures of the support. Despite having the same chemical composition, these catalysts exhibited different methanation activity. This demonstrates the impact of the support crystallinity on the catalytic performance. The catalyst based on the P25 material was significantly more active.

Characterization showed that, starting from a calcination temperature of 350 °C, the weak interactions between the RuO_2 and anatase TiO_2 cause sintering and a dramatic growth of RuO_2 crystals. On the contrary, the strong interactions (i.e. lattice-matched interfacial structure) between the RuO_2 and rutile TiO_2 crystal phases lead to a transformation of nanoparticles to epitaxial layers over the rutile TiO_2. Importantly, this phenomenon also appeared to trigger the formation of "sandwich-like" structures into which RuO_2 remains trapped and unavailable for catalysis. On the surface of P25 TiO_2, the intimate mixing of anatase and rutile phases resulted in the modulation of the interactions between the RuO_2 nanoparticles and the support. The drastic sintering observed on pure anatase was not observed. Instead a phenomenon of RuO_2 migration – from anatase toward rutile TiO_2 support particles – was clearly demonstrated by advanced electron microscopy (tomography) techniques. At the same time, the sandwiching phenomenon was not observed.

The results obtained on these well-defined RuO_2/TiO_2 catalysts demonstrate that drastic morphological changes occur during thermal annealing and that these directly have a great impact on the catalytic performance of the reduced catalysts.

Chapter 2: On the beneficial effect of mixing anatase- and rutile-TiO_2 as supports for Ru/TiO_2 catalysts

1. Introduction

As shown in chapter 1, the crystal structure of TiO_2 support plays an important role that dictates the morphology of Ru species, thereby affecting the catalytic performance in CO_2 methanation. It was revealed that Ru/TiO_2 catalyst supported on TiO_2-P25, which is composed of 20% rutile and 80% anatase phases, presents the highest catalytic performance compared to Ru/TiO_2 catalysts supported on home-made anatase TiO_2 or rutile TiO_2. The high catalytic performance was found to be correlated to the high Ru dispersion thanks to the absence of support sintering which prevented the loss of exposed Ru species through agglomeration or trapping in-between the support particles. Our observations were in accordance with the previously reported studies in which highly dispersed and stable RuO_2 species were formed owing to the lattice matching with rutile TiO_2 support in HCl oxidation [27, 71, 119] and CO_2 methanation [72]. Yet, several questions remain:

(i) Can we discriminate between the effect of the crystal structure (anatase versus rutile) and the potential effect of support sintering (size and shape of the particles)?
(ii) Is there a true synergistic effect of the co-presence of anatase and rutile phases in the formation of a more active catalyst?
(iii) Can we reproduce the good performance of TiO_2-P25 with mechanical mixtures of anatase and rutile?
(iv) Is the co-presence of the two phases important only during the reaction or at specific steps of the catalyst preparation?

In this chapter, we study the effect of mixture of anatase and rutile TiO_2 crystal phases. Ru/TiO_2 catalysts were prepared by deposition of pre-synthesized RuO_2 NPs on mixtures of rutile and anatase TiO_2 with various mixing ratios while keeping

other parameters constant (Ru loading and annealing condition). Rutile and anatase phases were mixed at three different stages of catalyst preparation as described in the following experimental section. Both home-made and commercial rutile and anatase TiO_2 are exploited in an attempt to separate the crystalline structural effect from the sintering one. First, home-made rutile and anatase TiO_2 were investigated (expecting sintering phenomena of TiO_2 as in Chapter 1). Second, non-sintering commercial rutile and anatase TiO_2 supports were investigated to eliminate the sintering parameter towards further interpretation and definitive conclusions.

The catalysts were characterized by N_2 physisorption, H_2 chemisorption, ICP-AES, and XRD, and the catalytic performances were evaluated in CO_2 methanation.

2. Experimental summary

The catalysts were prepared by deposition of pre-synthesized RuO_2 nanoparticles of 2 nm in colloidal suspension (2.2 wt. % of Ru in the final catalysts). The general catalysts preparation steps follow the same details described in the experimental section in chapter 1, (Pg. 31), but an additional step of mixing rutile and anatase TiO_2 components was introduced at three different stages of the preparation. The schematics of catalyst preparation involving the mixing of anatase and rutile TiO_2 phases are shown in Figure 2-1. All mixing is done manually using mortar and pestle by grinding dry powders containing anatase and rutile TiO_2 phases for at least 5 min.

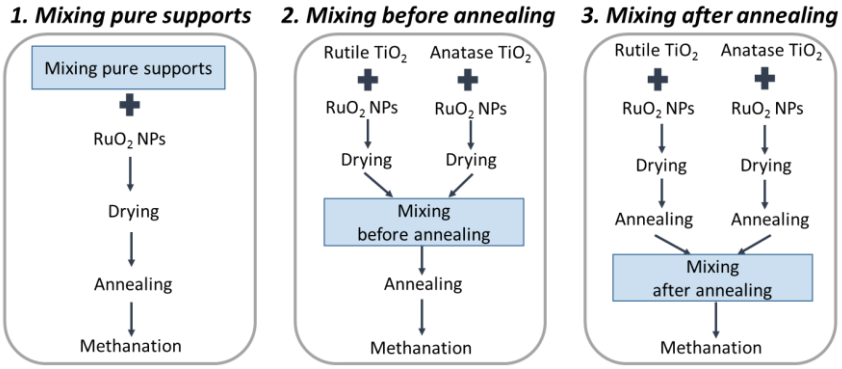

Figure 2-1: Schematics of mixing anatase and rutile TiO_2 phases at different stages of catalyst preparation. Methanation step include in-situ reduction of RuO_2 into Ru.

First, pure rutile and anatase supports were mixed in various mass ratios (rutile to anatase = 5:5, 3:7, 2:8, 1:9 for home-made TiO_2 supports and rutile to anatase = 5:5, 2:8 for commercial TiO_2 supports) followed by the deposition of RuO_2 NPs by

immersing the mixed powder in colloidal suspension of RuO_2 nanoparticles, evaporation of water, annealing at 450 °C for 16 hours in static air, and washing 3 times with water then dried in air. These catalysts are denoted as (R+A)55, (R+A)37, (R+A)28, and (R+A)19 for home-made TiO_2 supports and C(R+A)55 and C(R+A)28 for commercial TiO_2 supports respectively, where the numbers indicate the anatase-to-rutile mass ratio and "C" indicates the commercial origin of the supports. The commercial TiO_2 nanopowder was obtained from Sigma-Aldrich; anatase nanopowder (99.7% trace metal basis, particle size <25 nm) and rutile nanopowder (99.5% trace metal basis, particle size <100 nm).

Second, RuO_2 NPs were deposited by immersing rutile and anatase supports in the colloidal suspension of RuO_2 NPs and dried separately then mixed in various ratios right before annealing at 450 °C for 16 hours in static air. The annealed catalysts were washed 3 times with water and dried in air. These catalysts were noted (R+A)55-BA, (R+A)37-BA, (R+A)28-BA, and (R+A)19-BA for home-made TiO_2 supports and C(R+A)55-BA and C(R+A)28-BA for commercial TiO_2 supports, where "BA" stands for "before annealing".

Third, RuO_2 NPs were deposited by immersing rutile and anatase supports in the colloidal suspension of RuO_2 NPs and dried separately, annealed separately at 450 °C for 16 hours in static air (full final catalyst preparation), washed 3 times with water, dried in air and then mixed in various ratios. These catalysts were noted (R+A)55-AA, (R+A)37-AA, (R+A)28-AA, and (R+A)19-AA for home-made TiO_2 supports and C(R+A)55-AA and C(R+A)28-AA for commercial TiO_2 supports, where "AA" stands for "after annealing".

Finally, for comparison, pure anatase supported catalysts and pure rutile supported catalysts were prepared and denoted as A100 and R100 for home-made anatase- and rutile- supported catalysts respectively and CA100 and CR100 for commercial anatase- and rutile- supported catalysts respectively. Table 2-1 summarizes the catalysts discussed in this chapter.

Table 2-1: Summary of catalysts discussed in the chapter.

Rutile content	Anatase content	Home-made TiO_2			Commercial TiO_2		
		Mixing 1	Mixing 2	Mixing 3	Mixing 1	Mixing 2	Mixing 3
0%	**100%**	A100 (no mixing)			CA100 (no mixing)		
10%	**90%**	(R+A)19	(R+A)19 -BA	(R+A)19 -AA			
20%	**80%**	(R+A)28	(R+A)28 -BA	(R+A)28 -AA	C(R+A)28	C(R+A)28 -BA	C(R+A)28 -AA
30%	**70%**	(R+A)37	(R+A)37 -BA	(R+A)37 -AA			
50%	**50%**	(R+A)55	(R+A)55 -BA	(R+A)55 -AA	C(R+A)55	C(R+A)55 -BA	C(R+A)55 -AA
100%	**0%**	R100 (no mixing)			CR100 (no mixing)		

The catalysts were reduced in situ prior to catalytic test, as described in detail in the experimental section (Pg. 27).

3. Results and discussion

3.1. Mixture of home-made anatase- and rutile-TiO_2

3.1.1. Catalytic activity

3.1.1.1. Mixing final catalysts after annealing (Mixing 3)

The selectivity to methane for all catalysts was 100% and the catalytic activities are expressed in methane production rates. The activities of the different ratios of mixing are shown as a function of anatase content in the catalysts (Figure 2-2). The catalytic activities are presented in both per gram of catalyst and per mole of Ru according to the real Ru content determined by ICP-AES. Since there was no discrepancy between the theoretical and real Ru contents, all catalysts have very similar Ru loading and both plots show the same trends.

The dotted lines in Figure 2-2 represent the weighted average activity of 100% rutile TiO_2 supported catalyst and 100% anatase TiO_2 supported catalyst. For the catalysts mixed after being prepared (and annealed) separately on rutile- and anatase- TiO_2 supports, the catalytic activity of each mixing ratio corresponded to the weighted average of the pure rutile supported- and anatase supported- catalysts. This suggests that there is no beneficial impact of mere co-presence of rutile and anatase TiO_2 particles in the formation of reduced Ru particles on CO_2 methanation activity.

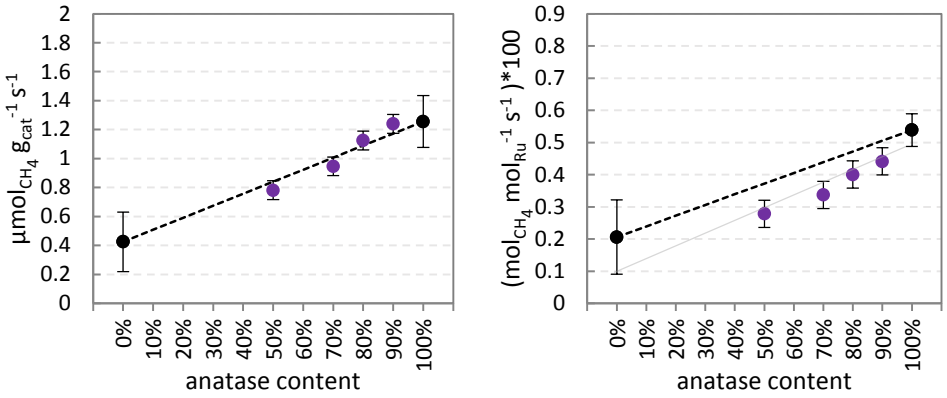

Figure 2-2: Methanation rate per gram of catalyst (left) and per mole of Ru determined by ICP-AES (right) for the mixing 3 series. R100 and A100 are shown in black dots, the dotted line indicates the weighted average of R100 and A100 activities as if they were mixed at various ratios, and the experimental catalytic activities of (R+A)55-AA, (R+A)37-AA, (R+A)28-AA, and (R+A)19-AA are shown in purple dots. The grey line on the right plot is drawn to guide eyes to show that the experimental points are still within the acceptable error range. The error bars represent the statistic error (repeatability) of the catalytic testing procedure. For R100 and A100, the error bar ranges also take account for the reproducibility of a same catalyst; the catalytic activities of two same catalysts prepared with different batches of pure home-made TiO_2 were averaged and the two spread values were taken into the error range.

3.1.1.2. Mixing catalysts before annealing (Mixing 2)

When the RuO_2 nanoparticles were deposited separately on rutile- and anatase-TiO_2 supports and then mixed before annealing, the catalytic activities were found to be above the calculated weighted average activity line, as shown in Figure 2-3. More precisely, it was observed that the higher the anatase content is, the greater the catalytic activity above the weighted average activity line. This suggests that there is a beneficial cooperation between the two mixed parts which indicates a catalytic synergy.

Here, the synergy is defined as the result of the greater methane production rate from catalysts prepared by mixing the rutile and anatase TiO_2 phases compared to the weighted average methane production rate of the pure rutile TiO_2- and anatase TiO_2-supported catalysts at a chosen ratio of rutile to anatase phases.

The synergistic effect of (R+A)28-BA and (R+A)19-BA was evident. However, the catalytic activities of (R+A)55-BA and (R+A)37-BA did not show any obvious synergy. Since the catalytic activities of these catalysts were on the calculated weighted

average activity line or within the error ranges of R100 and A100, any possible synergy is considered negligible.

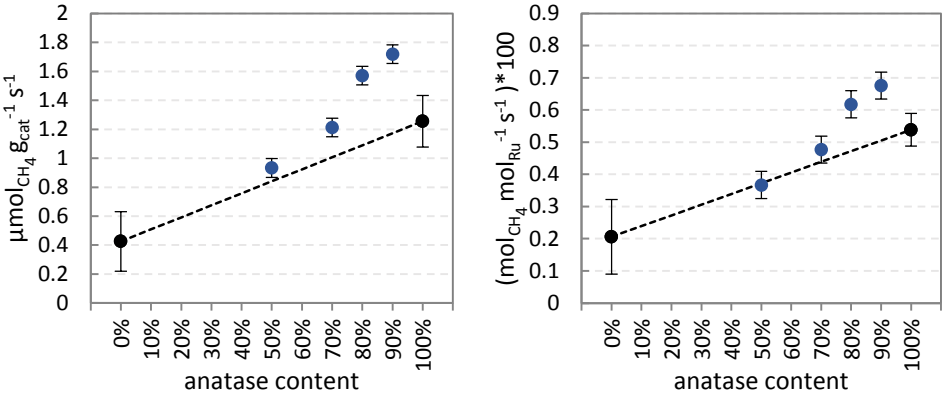

Figure 2-3: Methanation production rate per gram of catalyst (left) and per mole of Ru determined by ICP-AES (right) for the mixing 2 series. R100 and A100 are shown in black dots, the dotted line indicates the weighted average of R100 and A100 activities as if they were mixed at various ratios, and the experimental catalytic activities of (R+A)55-BA, (R+A)37-BA, (R+A)28-BA, and (R+A)19-BA are shown in blue dots. The determination of error ranges is described in the caption of Figure 2-2.

3.1.1.3. Mixing pure supports before RuO_2 deposition (Mixing 1)

When the catalysts were prepared by mixing rutile- and anatase TiO_2 supports prior to RuO_2 nanoparticles deposition, the synergistic effect was observed in a similar manner as in the case of catalysts in mixing 2 series (Figure 2-4). In this case also the 2:8 and 1:9 mixing ratios give rise to a clear synergistic effect. Interestingly, the synergy was more marked for (R+A)19 as compared to (R+A)19-BA.

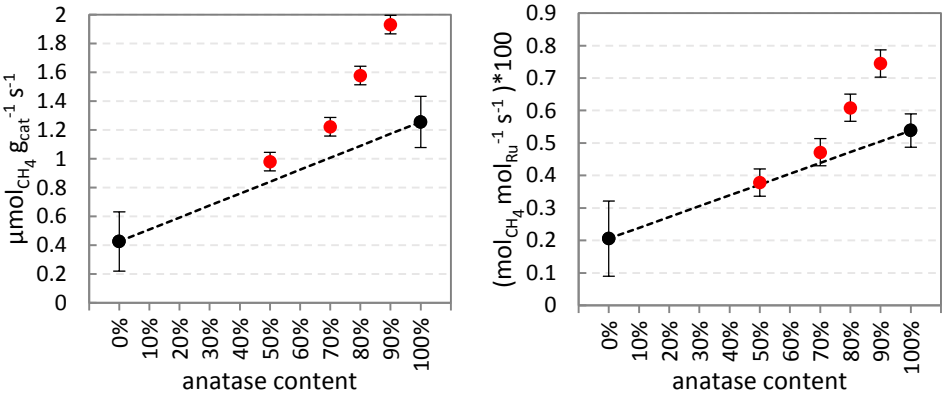

Figure 2-4: Methanation production rate per gram of catalyst (left) and per mole of Ru determined by ICP-AES (right) for the mixing 1 series. R100 and A100 are shown in black dots, the dotted line indicates the weighted average activity of R100 and A100 activities as if they were mixed at various ratios. The catalytic activities measured for (R+A)55, (R+A)37, (R+A)28, and (R+A)19 are shown in red dots. The determination of error ranges is described in the caption of Figure 2-2.

3.1.2. Catalyst characterization

The catalysts are characterized after annealing in static air at 450 °C, prior to the methanation test.

The textural properties of the catalysts analyzed by N_2 physisorption are summarized in Table 2-2.

The texture of the starting anatase and rutile supports (specific surface areas of ~ 140 $m^2 \cdot g^{-1}$ and 80 $m^2 \cdot g^{-1}$, respectively) is affected by the catalyst preparation, as discussed in Chapter 1, leading to the corresponding Ru/TiO_2 catalysts with specific surface areas of ~60 $m^2 \cdot g^{-1}$ and ~30 $m^2 \cdot g^{-1}$, respectively. The mixing of both catalysts after annealing (AA) is expected to produce catalysts with specific surface areas corresponding to the weighted averages of the specific surface areas of the separate catalysts. This trend is indeed verified in the third series of samples (mixing after annealing). It is noteworthy, however, that two other series of samples (mixing pure supports first and mixing before annealing) show similar specific surface areas, pointing to an absence of impact of the mixing stage to the TiO_2 sintering behaviour.

On the other hand, it is notable that, while the pore volumes are similar for the catalysts mixed before annealing (BA) and after annealing (AA), the catalysts prepared by mixing the pure supports prior to the RuO_2 NPs deposition systematically present smaller pore volumes. We put forward that a better degree of mixing of rutile and anatase particles is obtained in case of mixing the pure supports prior to the RuO_2 NPs deposition, where the mixed phases are first immersed in aqueous colloidal suspension of RuO_2 NPs, as compared to the dry mixtures after RuO_2 NPs deposition separately on each support. The immersion of mixed dry supports in the aqueous colloidal suspension of RuO_2 NPs could have led to a tighter contact among particles, resulting in smaller pore volumes.

Table 2-2: N_2 physisorption results of (a) home-made anatase and rutile TiO_2 supports and their corresponding catalysts, A100 and R100, and (b) catalysts of mixed phases based on home-made rutile and anatase TiO_2.

(a)	Rutile		Anatase	
	Support only	**R100**	**Support only**	**A100**
Surface area (BET) ($m^2 \cdot g^{-1}$)	79	27	144	59
Pore volume ($cm^3 \cdot g^{-1}$)	0.19	0.14	0.15	0.17
(b)	Mixing pure supports first (Mixing 1)			
Catalysts	**(R+A)55**	**(R+A)37**	**(R+A)28**	**(R+A)19**
Surface area (BET) ($m^2 \cdot g^{-1}$)	48	48	60	62
Pore volume ($cm^3 \cdot g^{-1}$)	0.16	0.13	0.14	0.12
	Mixing before annealing (BA) (Mixing 2)			
Catalysts	**(R+A)55-BA**	**(R+A)37-BA**	**(R+A)28-BA**	**(R+A)19-BA**
Surface area (BET) ($m^2 \cdot g^{-1}$)	47	51	55	61
Pore volume ($cm^3 \cdot g^{-1}$)	0.19	0.20	0.19	0.21
	Mixing after annealing (AA) (Mixing 3)			
Catalysts	**(R+A)55-AA**	**(R+A)37-AA**	**(R+A)28-AA**	**(R+A)19-AA**
Surface area (BET) ($m^2 \cdot g^{-1}$)	44	49	50	64
Pore volume ($cm^3 \cdot g^{-1}$)	0.18	0.19	0.19	0.21

A possible factor influencing catalytic activity is the Ru dispersion, namely the proportion of Ru atoms effectively accessible on the surface of the catalyst and thus potentially active in the reaction. Ru dispersion has been measured by H_2 chemisorption for the catalysts made from pure anatase and rutile TiO_2 supports as well as for the mixtures (Fig. 2-5).

As discussed in Chapter 1, the anatase-supported Ru catalyst displayed a much lower dispersion than the corresponding catalyst prepared from pure rutile. This was explained by a heavy sintering of RuO_2 when supported on anatase. On rutile, it was shown that RuO_2 was in part highly dispersed at the surface of rutile rods (stabilized through epitaxial interactions) and in part trapped ("sandwiched") between rutile rods that tend to sinter during annealing. Both phenomena are expected to have opposite effect on the dispersion value. Yet the dispersion value

for rutile-supported catalyst reached ~14%, significantly higher than that of the anatase supported catalyst.

For catalysts obtained with mixed supports, the repeatability of the measurement was much lower than for R100 and A100. Large error bars are tentatively attributed to an inhomogeneous sampling or preparation for the measurement. Catalysts from the mixing 3 series tend to exhibit Ru dispersion in the vicinity of the value expected for a simple mechanical mixture of R100 and A100, yet sometimes higher. Catalysts from mixing 2 and mixing 3 series tend to exhibit higher dispersion. It is reasonable to consider that the "sandwiching" effect discussed in Chapter 1 for R100 would be reduced in the case of an intimate mixture between anatase and rutile. Also, the migration of Ru towards rutile, as discussed in Chapter 1 and further demonstrated in Chapter 3, is expected to occur in these samples, which is expected to favor a better dispersion.

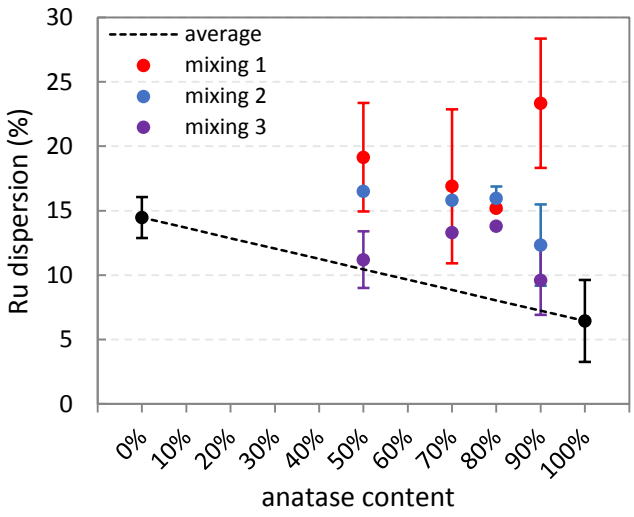

Figure 2-5: Ru dispersion (%) obtained by number of surface Ru atoms probed by H_2 chemisorption divided by total number of Ru atoms in bulk catalyst determined by ICP-AES. A100 and R100 are shown as references with error ranges determined from several reproduced catalysts.

XRD patterns of all catalysts are presented in Figure 2-6, 2-7 and 2-8. As expected, the intensities of the rutile and anatase TiO_2 peaks consistently follow the increasing or decreasing contents of each phase in orderly manner.

As described in chapter 1, XRD peaks associated with RuO_2 are too small in intensity to be refined using a pattern matching method. However, it is possible to

deconvolute the main TiO_2 and RuO_2 peaks, and observe their widths and positions. Results are reported in table 2-3.

Overall, TiO_2 peak positions and widths (2θ and FWHM) do not evolve significantly when the mixing order or the anatase/rutile ratio is changed; mixing order or anatase/rutile ratio do not drastically influence the TiO_2 sintering in comparison to what already occurs on pure home-made TiO_2 supported RuO_2 catalysts, nor do they influence the crystal structure (cell parameters) of the TiO_2 supports.

On the other hand, the RuO_2 peak positions appear to evolve. For a better visualization of the shifts in RuO_2 peak positions, the (110) 2θ positions were subtracted from the (101) 2θ positions and compared with the expected value ($2\theta_{101}$-$2\theta_{110}$=7.024° from ICDD 01-070-2662), as shown in Figure 2-9 (a). The mixing 3 series of catalysts (mixing of the catalysts after separate annealing) show values close to 7.024° (although slightly higher from 7.045° to 7.065°), whereas the mixing 2 and 1 series clearly show significantly higher values, attesting a change in the RuO_2 structure. As seen in chapter 1, both RuO_2 peaks are shifted towards the associated rutile TiO_2 peaks, which confirms the epitaxial growth of RuO_2 over rutile TiO_2, for series of catalysts from mixing 1 and 2. In comparison, Figure 2-9 (b) shows the values of the difference in $2\theta_{101}$ and $2\theta_{110}$ positions of rutile TiO_2, which remain constant.

This is consistent with the fact that RuO_2 nanoparticles are able to migrate from anatase to rutile during annealing in mixing 1 and 2 scenarios. In the case of mixing 3, two different populations of RuO_2 are expected: one on anatase TiO_2 support and one on rutile TiO_2 support. Upon separate annealing prior to mixing, the RuO_2 nanoparticles grow into larger RuO_2 crystals independently from the support on anatase TiO_2, while they transform into epitaxial layer over rutile TiO_2 in interaction with the support. As a result, when these two catalysts were mixed (mixing 3) two RuO_2 peaks are expected; one which is broader and shifted toward TiO_2 rutile peak positions, and the other one which is thinner and non-shifted. The resulting RuO_2 peaks are broad and un-shifted ((110) and (101)), as shown in Figure 2-6.

The shift in (110) and (101) RuO_2 peak positions towards (110) and (101) rutile TiO_2 peak positions is of more considerable extent for mixing 1 than mixing 2. We hypothesize that this results from the better degree of mixing with higher proximity between rutile and anatase particles at the wet step of the preparation, which may have contributed to the kinetics of RuO_2 nanoparticles' mobility and transformation.

The size of RuO_2 is difficult to evaluate due to the low peak intensity, their overlapping with rutile TiO_2 peaks, as well as the fact that RuO_2 is well known to present numerous defects which enlarge the XRD peaks by itself [149]. It is, however, possible to discuss tendencies; it appears that the epitaxial growth of RuO_2 on (110) rutile TiO_2 is preferred stronger than on (101) rutile TiO_2. This can be related to the fact that rutile TiO_2 (110) facets are the most exposed and well-defined surfaces.

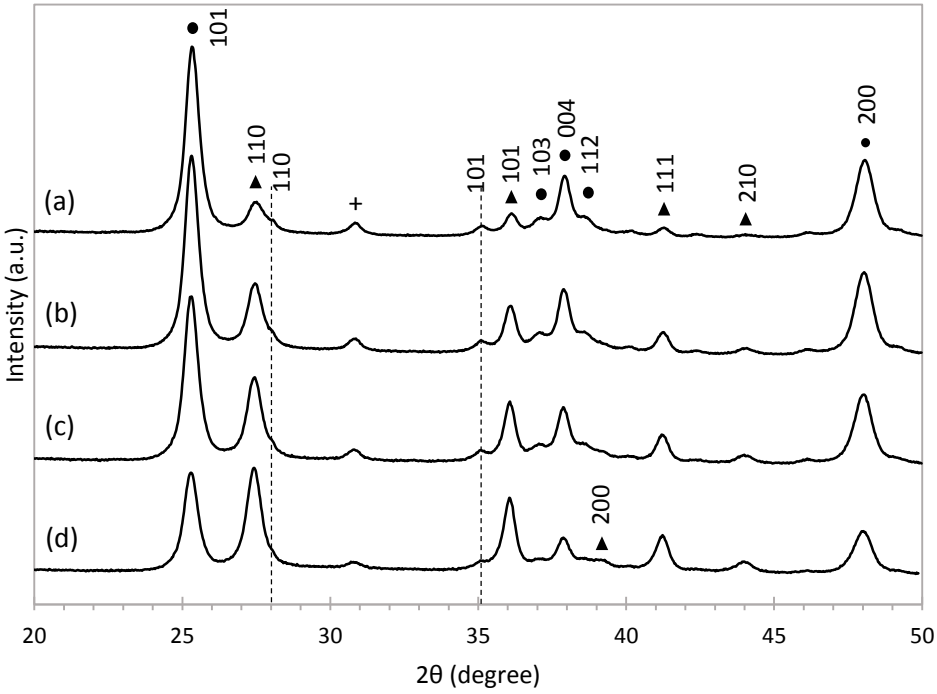

Figure 2-6: XRD patterns of (a) (R+A)19-AA, (b) (R+A)28-AA, (c) (R+A)37-AA, and (d) (R+A)55-AA; rutile TiO_2 (▲), anatase TiO_2 (●), brookite TiO_2 (+) impurity, and rutile RuO_2 (drawn as dotted lines) peak positions.

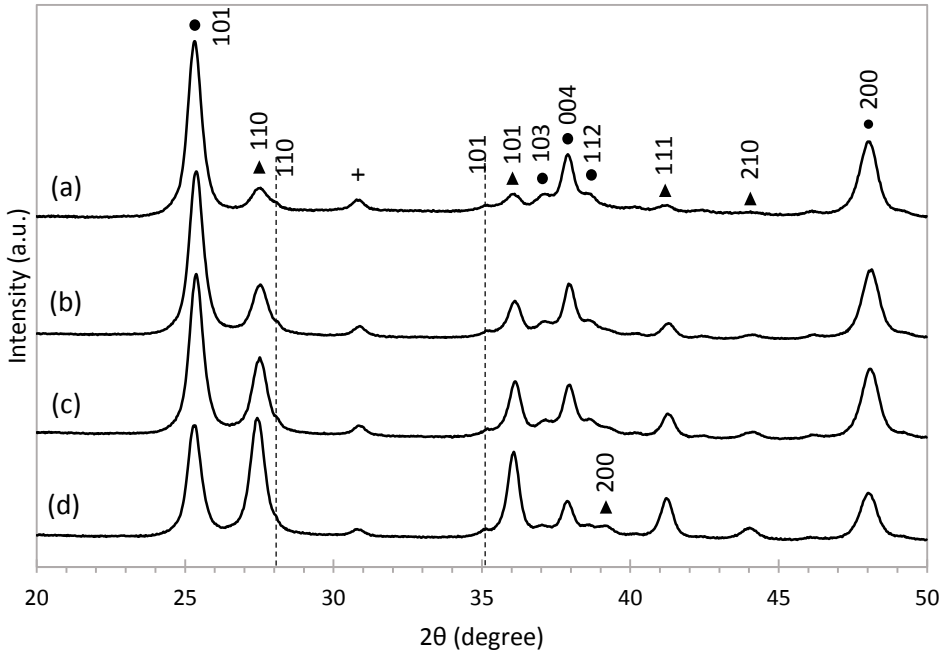

Figure 2-7: XRD patterns of (a) (R+A)19-BA, (b) (R+A)28-BA, (c) (R+A)37-BA, and (d) (R+A)55-BA; rutile TiO_2 (▲), anatase TiO_2 (●), brookite TiO_2 (+), and rutile RuO_2 (drawn as dotted lines) peak positions.

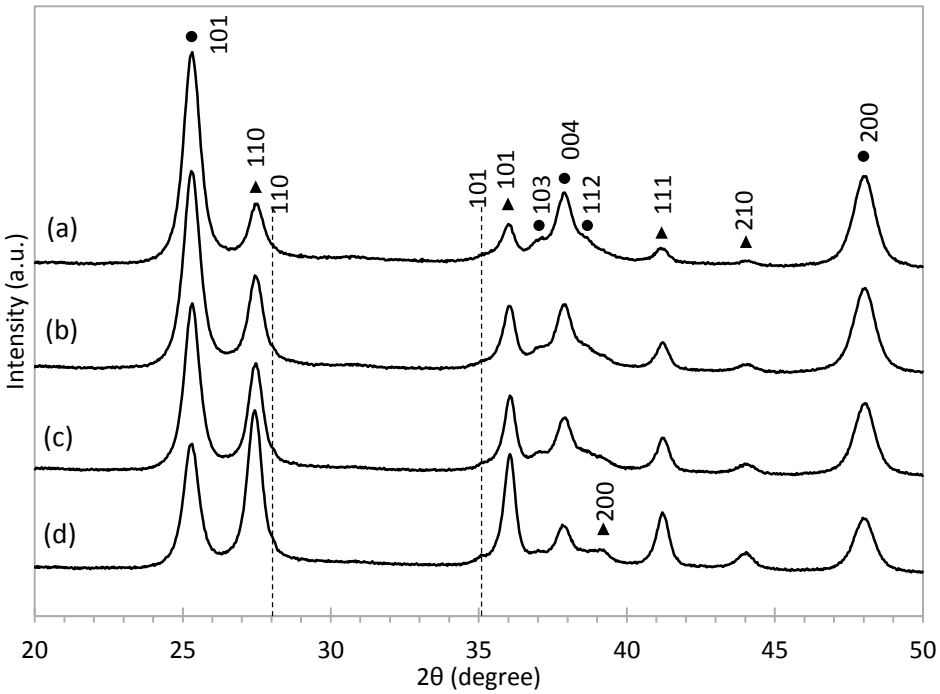

Figure 2-8: XRD patterns of (a) (R+A)19, (b) (R+A)28, (c) (R+A)37, and (d) (R+A)55; rutile TiO_2 (▲), anatase TiO_2 (●), and rutile RuO_2 (drawn as dotted lines) peak positions.

Table 2-3: Position (2θ) and width (FWHM) of the main TiO_2 and RuO_2 peaks obtained after deconvolution, and corresponding crystal size calculated from Scherrer equation; (a) Mixing 3, (b) Mixing 2, and (c) Mixing 1.

(a)		(A+R)55-AA			(A+R)37-AA			(A+R)28-AA			(A+R)19-AA		
	hkl	2 θ (°)	FWHM (°)	Size (nm)	2 θ (°)	FWHM (°)	Size (nm)	2 θ (°)	FWHM (°)	Size (nm)	2 θ (°)	FWHM (°)	Size (nm)
anatase	**101**	25.273	0.562	14.5	25.283	0.556	14.6	25.303	0.548	14.9	25.323	0.546	14.9
rutile	**110**	27.402	0.586	14.0	27.417	0.584	14.0	27.437	0.583	14.0	27.471	0.617	13.2
RuO_2	**110**	28.033	0.176	47.6	28.019	0.310	26.7	28.018	0.367	22.5	28.027	0.380	21.7
RuO_2	**101**	35.078	0.486	17.2	35.071	0.569	14.6	35.094	0.578	14.4	35.092	0.535	15.6
rutile	**101**	36.024	0.458	18.3	36.036	0.451	18.6	36.056	0.456	18.4	36.087	0.464	18.0
anatase	**103**	37.056	0.564	14.9	37.035	0.601	13.9	37.051	0.618	13.5	37.061	0.615	13.6
anatase	**004**	37.846	0.509	16.5	37.850	0.486	17.3	37.869	0.468	18.0	37.889	0.463	18.2
anatase	**112**	38.528	0.529	15.9	38.559	0.605	13.9	38.573	0.605	13.9	38.603	0.587	14.3
rutile	**200**	39.108	0.567	14.9	39.147	0.637	13.2	39.183	0.720	11.7	39.246	0.741	11.4

(b)		(A+R)55-BA			(A+R)37-BA			(A+R)28-BA			(A+R)19-BA		
	hkl	2 θ (°)	FWHM (°)	Size (nm)	2 θ (°)	FWHM (°)	Size (nm)	2 θ (°)	FWHM (°)	Size (nm)	2 θ (°)	FWHM (°)	Size (nm)
anatase	**101**	25.295	0.533	15.3	25.356	0.538	15.2	25.338	0.637	12.8	25.304	0.546	14.9
rutile	**110**	27.420	0.567	14.4	27.492	0.597	13.7	27.487	0.723	11.3	27.482	0.649	12.6
RuO_2	**110**	28.051	0.178	47.1	28.115	0.166	50.5	28.140	0.173	48.6	28.024	0.412	20.0
RuO_2	**101**	35.143	0.700	11.9	35.280	0.835	10.0	35.344	0.900	9.2	35.198	0.823	10.1
rutile	**101**	36.035	0.452	18.5	36.089	0.485	17.3	36.070	0.583	14.3	36.029	0.590	14.2
anatase	**103**	37.048	0.595	14.1	37.118	0.666	12.6	37.182	0.950	8.8	37.086	0.710	11.8
anatase	**004**	37.855	0.469	17.9	37.916	0.477	17.6	37.915	0.520	16.2	37.869	0.460	18.3
anatase	**112**	38.553	0.554	15.2	38.618	0.558	15.1	38.556	0.568	14.8	38.557	0.656	12.8
rutile	**200**	39.147	0.637	13.2	39.226	0.702	12.0	39.074	0.905	9.3	39.281	0.699	12.0

(c)		(A+R)55			(A+R)37			(A+R)28			(A+R)19		
	hkl	2 θ (°)	FWHM (°)	Size (nm)	2 θ (°)	FWHM (°)	Size (nm)	2 θ (°)	FWHM (°)	Size (nm)	2 θ (°)	FWHM (°)	Size (nm)
anatase	**101**	25.264	0.615	13.2	25.289	0.592	13.7	25.281	0.663	12.3	25.287	0.666	12.2
rutile	**110**	27.405	0.578	14.2	27.437	0.552	14.8	27.443	0.598	13.7	27.463	0.599	13.6
RuO_2	**110**	28.045	0.094	92.1	28.061	0.155	54.2	28.078	0.173	48.6	28.079	0.699	11.7
RuO_2	**101**	35.463	1.223	6.8	35.514	1.101	7.5	35.528	1.217	6.8	35.373	0.980	8.5
rutile	**101**	36.015	0.434	19.3	36.026	0.429	19.5	36.003	0.456	18.3	35.975	0.478	17.5
anatase	**103**	37.005	0.572	14.6	37.004	0.553	15.1	37.018	0.659	12.7	37.000	0.676	12.4
anatase	**004**	37.828	0.615	13.6	37.852	0.649	12.9	37.848	0.632	13.3	37.852	0.633	13.2
anatase	**112**	38.483	0.488	17.3	38.563	0.465	18.1	38.533	0.497	17.0	38.554	0.455	18.5
rutile	**200**	39.058	0.861	9.7	39.028	1.042	8.0	38.948	1.272	6.6	38.774	1.553	5.4

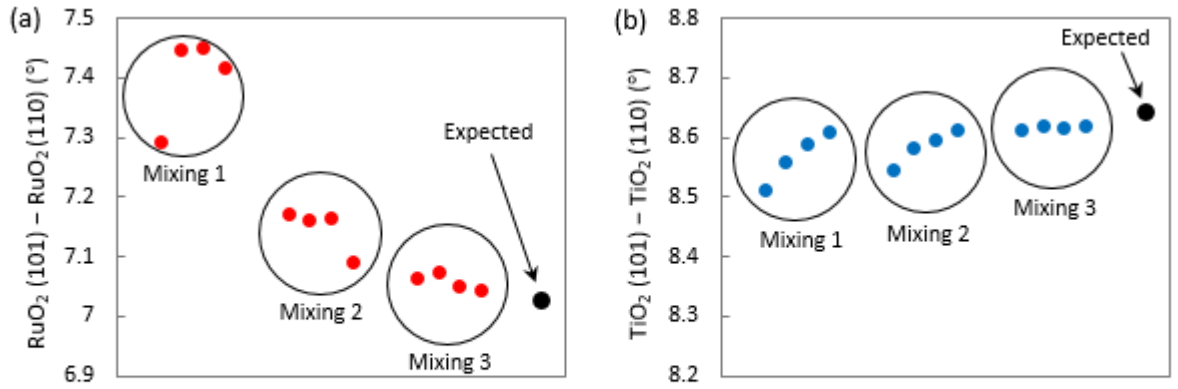

Figure 2-9: The difference in the XRD 2ϑ peak positions, 101 and 110, for (a) RuO_2 and (b) rutile TiO_2. Expected values are taken from ICDD 01-070-2662 for RuO_2 and ICDD 00-021-1276 for rutile TiO_2. The grouped four data points represent rutile to anatase mixing ratios, 1:9, 2:8, 3:7, 5:5, from left to right.

3.1.3. Interpretation of the synergistic effect

It should be noted that both of the home-made anatase and rutile TiO_2 are prepared without high temperature treatment and are subjected to sintering and further crystallization during the catalyst preparation (annealing step). As shown previously by N_2 physisorption analysis, the mixing of anatase and rutile phases at different stages of catalyst preparation did not significantly affect the degree of sintering of the catalysts as the specific surface areas of all catalysts were similar to the catalysts prepared separately on anatase and rutile TiO_2 respectively and mixed afterwards. Based on the catalytic activities of the (R+A)-AA series that fall on the weighted average activity of the R100 and A100 with different mixing ratios, the synergy in the catalytic activities of (R+A) and (R+A)BA series clearly does not simply come from the co-existence of the two different TiO_2 phases in the reaction. Rather, it is envisaged to be the result of the effect of the co-existence of the two different TiO_2 phases on the morphology of the RuO_2 nanoparticles that are stabilized prior to the reduction (i.e. during annealing).

In an attempt to explain the performance of the catalysts by the dispersion of the active phase, the methanation activity has been normalized by the amount of surface accessible Ru atoms (probed by H_2-chemisorption). This provides the apparent TOF, here defined as the number of methane molecules produced per surface Ru atom and per second (Fig. 2-10). A100 has a specific activity 3-times higher than R100 and its dispersion is 3 times lower. Thus, the TOF of A100 is about 1 order of magnitude higher than that of R100. This shows that activity is not simply governed by dispersion. Indeed, in such case, TOF values would be the same for both catalysts. Instead, such marked difference in TOF value points to a marked difference in the speciation of surface Ru atoms in both catalysts. In plain words, it means that, for a given surface of Ru atoms, those that are found on the large Ru aggregates formed on anatase supported catalysts are either 10 times more abundant or 10 times more active than those found on the smaller Ru particles formed on rutile supported catalysts.

It must be recalled that the rate limiting step in CO_2 methanation is believed to be the activation of CO_2 or CO and their subsequent hydrogenation, not the dissociation of H_2 [7, 78, 150]. The activation energies for both catalysts (and for the other catalysts obtained from mixed supports) are similar (~15 kcal) which indicates that the rate determining pathway of the catalytic reaction was the same for all catalysts (Table 2-4). Thus the factor limiting the activity of the catalysts is

the number of sites able to catalyze the CO_2 or CO dissociation and their subsequent hydrogenation. While H_2 chemisorption is a good way to probe the proportion of surface Ru, it cannot be seen as a measurement of the proportion of active sites (able to catalyse the dissociation of CO_2). The latter may tentatively be related to Ru particle size [108] or to the formation of specific sites at the interface between the metallic particles and the support (e.g. oxygen vacancy located at the metal-support interface, which are often proposed to take an active part in the rate limiting step [151, 152]). Data presented here do not, however, allow depicting the precise nature of these active sites. What can be concluded from the comparison between R100 and A100, is that the "configuration" (size, shape, interaction with the support) of the Ru phase is different in the Ru/TiO_2 catalysts with different TiO_2 crystal phase, giving rise to drastically different catalytic behavior.

As a matter of fact, obtaining a high TOF (as defined here) should not be seen as the ultimate goal for applied research. A high TOF obtained with a very low dispersion can mean a very low methane production rate. What should be maximized is the methane production, expressed per gram of catalyst or per mole of Ru (taking into account the total Ru loading).

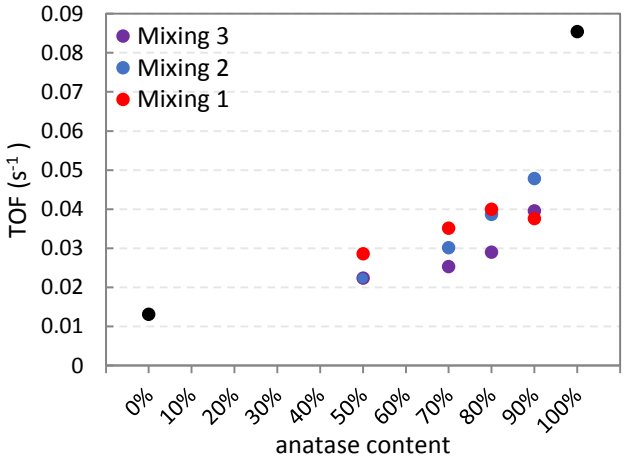

Figure 2-10: Turn over frequencies (TOF) or methane production rates normalized per surface Ru probed by H_2 chemisorption for all catalysts concerned in this section.

Table 2-4: Summary of activation energies (Ea) of the catalysts (units in kcal·mol^{-1}).

rutile:anatase ratio	Mixing 1 (R+A)	Mixing 2 (R+A)-BA	Mixing 3 (R+A)-AA
5:5	16.2	15.5	15.0
3:7	16.5	15.5	15.1
2:8	15.2	14.9	15.2
1:9	15.3	15.1	15.1

In Chapter 1, the migration of Ru from anatase particles to rutile particles was demonstrated. Here, the same phenomenon of migration was expected (as further discussed in Chapter 3). Consistently, TOF values were systematically found in the interval between the extremes values of R100 and A100. TOF tends to increase as the anatase content increases. No clear delineation can be drawn between the catalysts from the three mixing series. The TOF values tend to land in the same area, not far from the theoretical line, but systematically lower (closer to R100 than A100). Within the hypothesis that all the Ru migrates towards rutile and forms identical rutile-supported Ru nanoparticles, in all catalysts prepared by support mixing, one should expect a constant TOF, close to that obtained for R100. However, as mentioned above, it is clear that the intrinsic activity of surface Ru is also affected by other factors like the particle size or the nature of the interaction with the support. As Ru concentrates on rutile particles (especially in anatase-rich mixtures), the Ru particles size is expected to be affected, potentially leading to a different TOF. Also, if a fraction of the Ru did not migrate and still formed large Ru chunks as those formed in A100, the measured dispersion (and the corresponding TOF) should be an average of both types of active species. Finally, let us remember that rutile rods stacking with the sandwiching of RuO_2 was clearly evidenced in Chapter 1. It is possible that mixed support tend to minimize this phenomenon, even if this is not clearly reflected by textural analysis (which is not surprizing taking into account the low Ru loading).

Taking into consideration the broad experimental error in dispersion measurement and the absence of clear trend in this set of data, no hasty conclusion should be drawn on the TOF. Instead, the specific activity data are direct measurements of the catalyst activity. At this point, we conclude that Ru does migrate from anatase to rutile support particles during the annealing step. Simultaneously, the loss of Ru through the TiO_2-RuO_2-TiO_2 particle stacking on the (110) facets may be partly prevented by the mixing of rutile and anatase TiO_2 particles, especially when diluting rutile in large proportions of anatase. Thus, the superior activity of catalysts

based on mixed supports may be explained by a higher amount of surface Ru as compared to R100. However, it is not excluded that more active (larger) Ru metallic particles are formed due to the accumulation of higher Ru content on rutile particles.

The super-imposed sintering behaviour of the home-made TiO_2 supports further complicates the conclusion. In order to eliminate the sintering parameter, non-sintering commercial rutile and anatase TiO_2 were used as supports and their effect is discussed in the next section.

3.2. Mixture of commercial anatase- and rutile-TiO_2

3.2.1. Catalytic activity

Prior to discussing catalytic activity data, let us note that the non-sintering behaviour of supports and catalysts made thereof was confirmed by textural analysis (see Section 3.2.2.).

3.2.1.1. Mixing final catalysts after annealing (Mixing 3)

It should be noted that the catalytic activities of the catalysts prepared from the commercial anatase and rutile supports (CA100 and CR100) show completely opposite trend from what we have observed for A100 and R100. When sintering of the TiO_2 supports do not occur, the catalytic activity of the catalyst based on rutile TiO_2 is much higher than that based on anatase TiO_2 (Figure 2-11). CR100 was also more active than the catalyst based on the commercial P25 support (studied in details in Chapter 1).

As expected, when the fully annealed rutile TiO_2 supported and anatase TiO_2 supported Ru catalysts were mixed, the catalytic activities of the mixed catalysts corresponded to the weighted average activity of the two separately prepared CR100 and CA100. This is the same trend seen in case of home-made TiO_2 supports and it indicates that the co-presence of rutile and anatase phases during reaction does not have any effect on the activity.

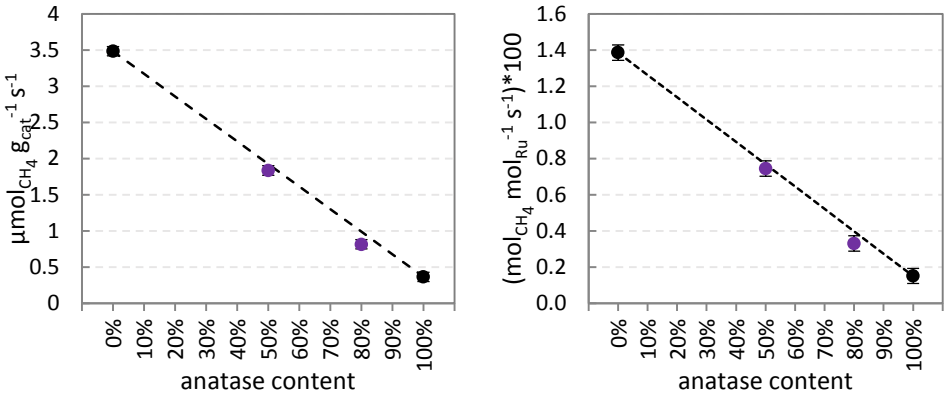

Figure 2-11: Methanation production rate per gram of catalyst (left) and per mole of Ru determined by ICP-AES (right). CR100 and CA100 are shown in black dots, the dotted line indicates the weighted average of CR100 and CA100 activities as if they were mixed at various ratios, and the experimental catalytic activities of C(R+A)28-AA and C(R+A)55-AA are shown in purple dots. The error bars are added based on the repeatability of the catalytic testing apparatus. Reproducibility of the catalysts were not taken into account since the TiO_2 supports were commercial, based on the conclusion that the reproducibility of the P25 (commercial) supported catalysts which has always fallen within the error of the repeatability of the catalytic testing apparatus (thus negligible).

3.2.1.2. Mixing catalysts before annealing (Mixing 2)

When the catalysts were prepared separately and mixed right before annealing, the effect of synergy in the catalytic activity was present for both mixing ratios as shown in Figure 2-12. This again points to a beneficial effect of the co-presence of rutile and anatase during the annealing step. The absolute methane production rates, however, remained below the activity of CR100.

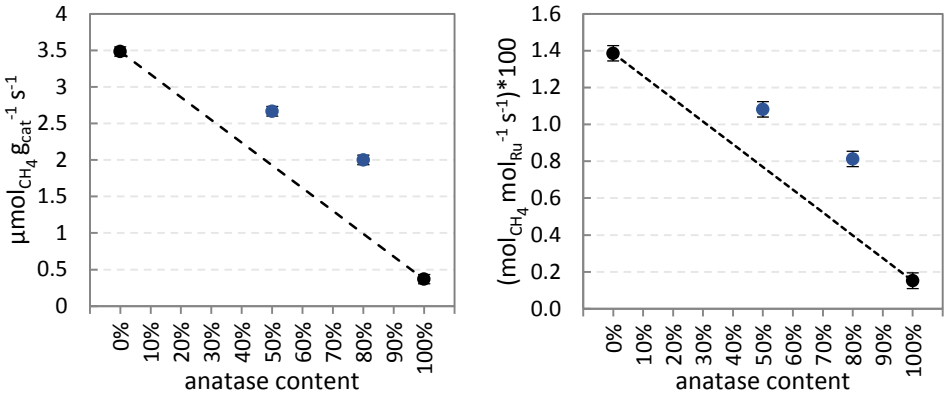

Figure 2-12: Methanation production rate per gram of catalyst (left) and per mole of Ru determined by ICP-AES (right). CR100 and CA100 are shown in black dots, the dotted line indicates the weighted average of CR100 and CA100 activities as if they were mixed at various ratios, and the experimental catalytic activities of C(R+A)28-BA and C(R+A)55-BA are shown in blue dots. The justification of the error bar determination is described in the caption of Figure 2-11.

3.2.1.3. Mixing pure supports before RuO_2 deposition (Mixing 1)

The synergistic effect was again present when the catalysts were prepared with mixing the pure rutile and anatase TiO_2 supports prior to the deposition of RuO_2 NPs (Figure 2-13) It is remarkable that the synergy was greater when the mixture contained higher rutile content. The catalytic activity reached the same activity as CR100 when the mixing ratio was 50% rutile to 50% anatase (C(R+A)55), significantly higher than the value expected for a simple mechanical mixture.

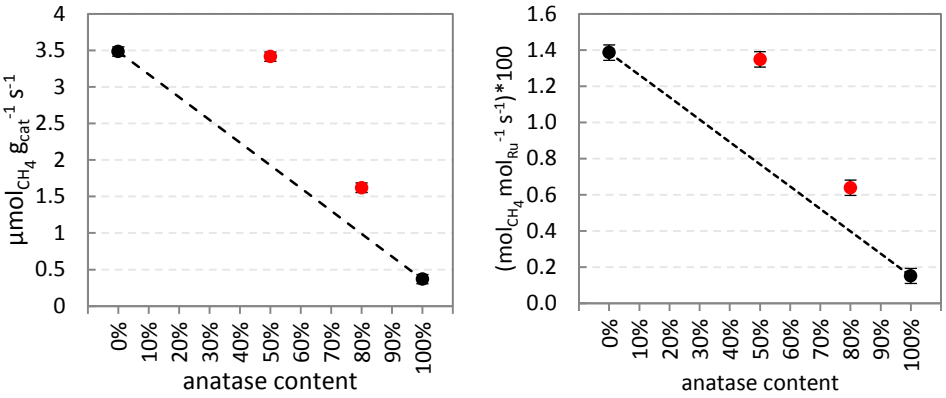

Figure 2-13: Methanation production rate per gram of catalyst (left) and per mole of Ru determined by ICP-AES (right). CR100 and CA100 are shown in black dots, the dotted line indicates the weighted average of CR100 and CA100 activities as if they were mixed at various ratios, and the experimental catalytic activities of C(R+A)28 and C(R+A)55 are shown in red dots. The justification of the error bar determination is described in the caption of Figure 2-11.

In summary, the catalytic activities of the commercial non-sintering TiO_2 supported catalysts showed a complete opposite trend from the home-made TiO_2 supported catalysts. On the one hand, the catalytic activity of the commercial anatase TiO_2 supported catalyst was significantly lower than home-made anatase TiO_2 supported catalyst. On the other hand, the activity of the commercial rutile TiO_2 supported catalyst was significantly higher than home-made rutile TiO_2 supported catalyst. This latter observation tends to validate our previous hypothesis (from chapter 1) that the home-made rutile TiO_2 supported catalyst performs lower than P25 supported catalyst only because of the loss of accessible Ru due to sintering in the annealing step ("sandwiching" of RuO_2 between rutile rods).

3.2.2. Catalyst characterization

N_2 physisorption analysis confirmed that both commercial anatase and rutile TiO_2 particles are not subjected to sintering upon annealing at 450 °C, with or without the presence of RuO_2 NPs, as shown in Table 2-5 (a). The specific surface areas of the mixture of rutile and anatase phases at different catalyst preparation stages were unaffected and remained similar to the weighted averages of 50%/50% mixture (33 m^2 g^{-1}) and 20%/80% mixture (38 m^2 g^{-1})(Table 2-5(b)). Pore volumes were also unaffected by mixing at different stages, and it was anticipated to be due to the surface properties of the TiO_2 nanoparticles which prevented sticking or sintering of the particles.

Table 2-5: Textural properties of (a) commercial anatase and rutile TiO_2; pure TiO_2, pure TiO_2 annealed at 450 °C, and after deposition of RuO_2 and annealing at 450 °C, and (b) catalysts of mixed commercial anatase and rutile TiO_2.

(a)		Pure support	TiO_2-450	RuO_2/TiO_2-450
Anatase TiO_2	Surface area (BET) ($m^2 \cdot g^{-1}$)	48	48	42
	Pore volume (BJH) ($cm^3 \cdot g^{-1}$)	0.25	0.25	0.21
Rutile TiO_2	Surface area (BET) ($m^2 \cdot g^{-1}$)	21	23	24
	Pore volume (BJH) ($cm^3 \cdot g^{-1}$)	0.08	0.08	0.09

(b)	Mixing 1		Mixing 2		Mixing 3	
Catalysts	**C(R+A)55**	**C(R+A)28**	**C(R+A)55 -BA**	**C(R+A)28 -BA**	**C(R+A)55 -AA**	**C(R+A)28 -AA**
Surface area (BET) ($m^2 \cdot g^{-1}$)	34	40	37	41	35	41
Pore volume ($cm^3 \cdot g^{-1}$)	0.29	0.26	0.27	0.27	0.29	0.27

The Ru dispersion on the commercial rutile TiO_2 is much higher than on the commercial anatase TiO_2 (Figure 2-14). This again points to the heavy sintering of RuO_2 on anatase while a much better dispersion is obtained on rutile, thanks to the epitaxial stabilization effect. For mixed supports, the same observation can be made concerning the relatively large experimental error in dispersion measurements. Dispersion for the mixing 3 series expectedly falls close to the values expected (weighted average) for simple mechanical mixtures of CR100 and CA100. The mixing 1 series appears to exhibit relatively high dispersion, clearly above that expected for mechanical mixture. Again, this points to a better dispersion when RuO_2 has the opportunity to migrate towards rutile during the annealing phase, while it sinters heavily when the only available support surface is anatase. Note that the dispersion obtained for C(R+A)55 is similar to that of R100. In the case of a quantitative migration of Ru towards rutile, this suggests that similar Ru particles, with similar size are stabilized.

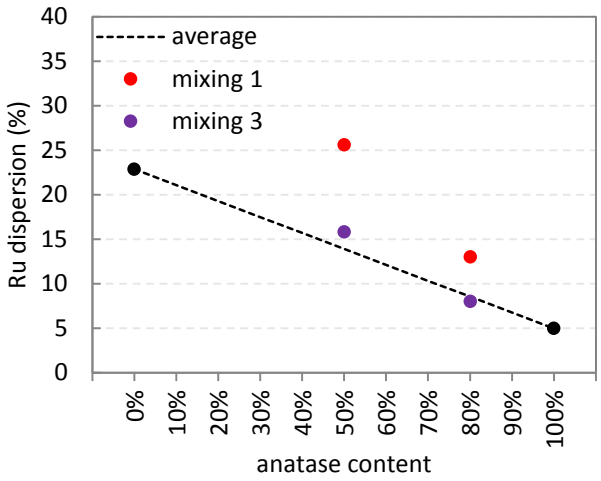

Figure 2-14: Ru dispersion (%) of catalysts prepared with non-sintering commercial TiO_2. CA100 and CR100 are shown as references. Mixing 2 series is not plotted due to technical difficulty with H_2 chemisorption apparatus.

The XRD patterns of CR100 and CA100 are shown in Figure 2-15. Similar behaviour as the home-made TiO_2 supports was observed. On rutile TiO_2 support, RuO_2 peaks are not easily seen but only slight broadening at each shoulder of rutile TiO_2 (110) and (101) peaks can be seen. On the other hand, on anatase TiO_2 support, RuO_2 (110) and (101) peaks are clearly visible, confirming the crystal growth of RuO_2 as on the home-made anatase TiO_2. The anatase-to-rutile transformation of the TiO_2, shown in chapter 1, can be seen to a lesser extent; only a broadening of the RuO_2 (110) peak towards rutile TiO_2 (110) peak position is observed (red arrow in Figure 2-15). This can be attributed to the already-sintered and fully crystalline commercial anatase TiO_2 which is more difficult to transform into rutile, even with the presence of RuO_2 as a promoter.

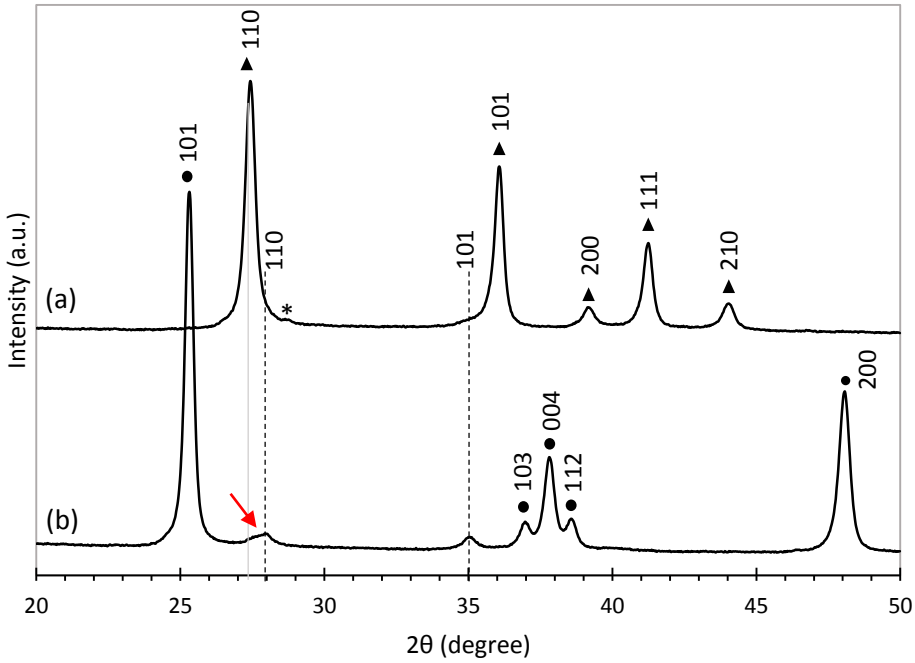

Figure 2-15: XRD patterns of (a) CR100 and (b) CA100; rutile TiO_2 (▲), anatase TiO_2 (●), TiC_2 impurity (*), rutile RuO_2 (drawn as dotted lines), and rutile TiO_2 (110) (drawn in solid grey line) peak positions.

The XRD patterns of all commercial TiO_2 supported catalysts mixed at different stages of mixing in various ratios are shown together in Figure 2-16 and the corresponding deconvolution results of the main TiO_2 peaks and RuO_2 peaks are summarized in Table 2-6. The difference in the (110) and (101) RuO_2 as well as rutile TiO_2 peak positions are distinguished as represented in Figure 2-17. The same tendency as in the previous section with the home-made TiO_2 supports was observed; the (110) and (101) rutile TiO_2 peak positions stay constant regardless of the mixing order while the shift in (110) and (101) RuO_2 peak positions towards 110 and 101 rutile TiO_2 peak positions are apparent for mixing 1 and 2.

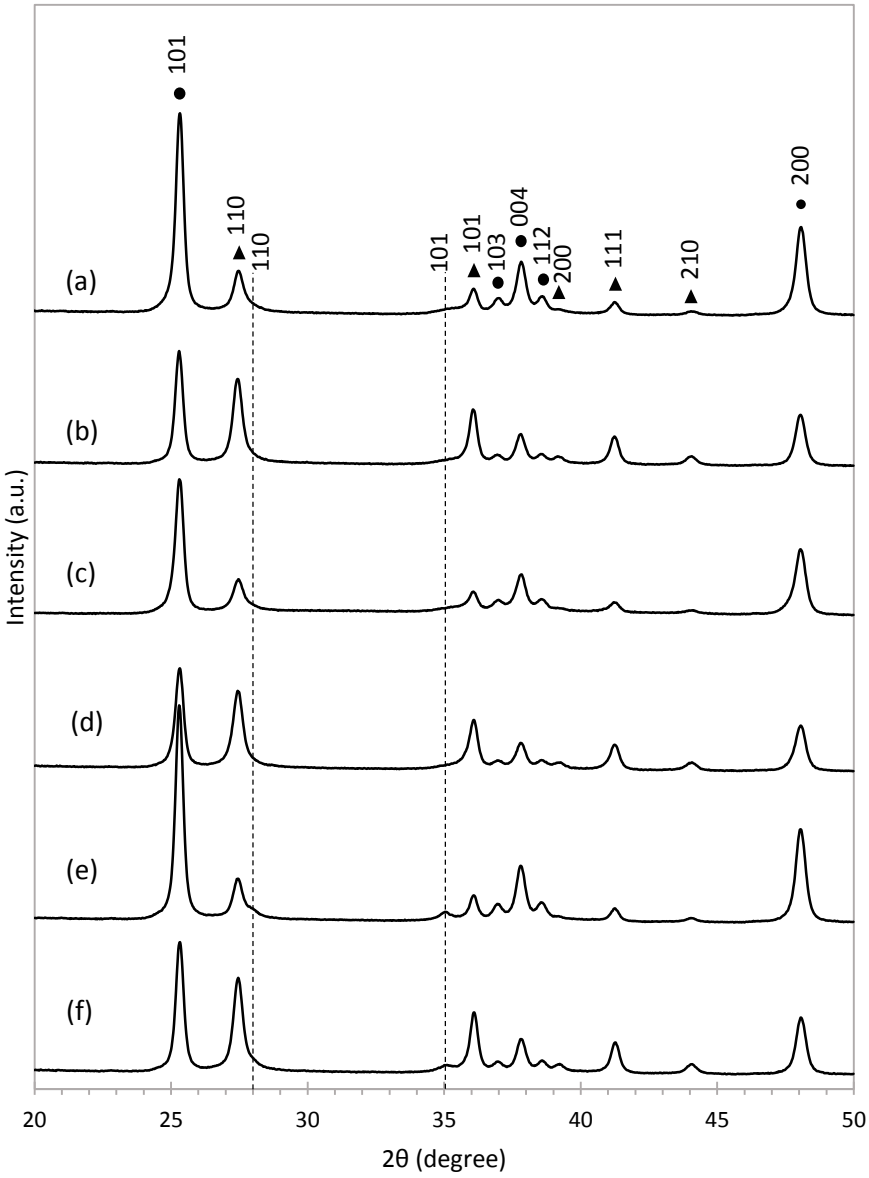

Figure 2-16: XRD patterns of (a) C(R+A)28, (b) C(R+A)55, (c) C(R+A)28-BA, (d) C(R+A)55-BA, (e) C (R+A)28-AA, and (f) C(R+A)55-AA; rutile TiO_2 (▲), anatase TiO_2 (●), and rutile RuO_2 (drawn as dotted lines) peak positions.

Table 2-6: Deconvoluted main TiO_2 and RuO_2 peaks presenting their positions (2ϑ), widths (FWHM), and sizes calculated from Scherrer equation; (a) Mixing 3, (b) Mixing 2, and (c) Mixing 1.

(a)		C(A+R)55-AA			C(A+R)28-AA		
	hkl	2 θ (°)	FWHM (°)	Size (nm)	2 θ (°)	FWHM (°)	Size (nm)
anatase	**101**	25.291	0.316	25.5	25.276	0.318	25.3
rutile	**110**	27.428	0.395	20.5	27.415	0.410	19.7
RuO_2	**110**	27.975	0.604	13.4	27.942	0.551	14.7
RuO_2	**101**	35.082	0.807	10.2	35.020	0.609	13.5
rutile	**101**	36.058	0.312	26.5	36.040	0.328	25.2
anatase	**103**	36.944	0.326	25.4	36.925	0.352	23.6
anatase	**004**	37.789	0.368	22.6	37.772	0.362	22.9
anatase	**112**	38.554	0.313	26.6	38.544	0.334	24.9
rutile	**200**	39.189	0.575	14.5	39.149	2.660	3.1

(b)		C(A+R)55-BA			C(A+R)28-BA		
	hkl	2 θ (°)	FWHM (°)	Size (nm)	2 θ (°)	FWHM (°)	Size (nm)
anatase	**101**	25.278	0.339	23.7	25.276	0.349	23.1
rutile	**110**	27.421	0.424	19.1	27.431	0.435	18.6
RuO_2	**110**	27.927	1.813	4.5	27.865	1.536	5.3
RuO_2	**101**	35.585	1.138	7.3	35.421	1.269	6.5
rutile	**101**	36.043	0.333	24.8	36.032	0.332	24.9
anatase	**103**	36.956	0.365	22.7	36.950	0.422	19.6
anatase	**004**	37.774	0.412	20.2	37.773	0.402	20.6
anatase	**112**	38.547	0.370	22.5	38.548	0.322	25.9
rutile	**200**	39.173	0.561	14.9	38.953	2.468	3.4

(c)		C(A+R)55			C(A+R)28		
	hkl	2 θ (°)	FWHM (°)	Size (nm)	2 θ (°)	FWHM (°)	Size (nm)
anatase	**101**	25.267	0.323	24.9	25.288	0.324	24.9
rutile	**110**	27.408	0.400	20.2	27.440	0.386	21.0
RuO_2	**110**	27.909	0.669	12.1	27.737	1.090	7.4
RuO_2	**101**	35.372	1.299	6.3	35.338	1.337	6.2
rutile	**101**	36.031	0.313	26.4	36.042	0.312	26.5
anatase	**103**	36.920	0.323	25.6	36.947	0.383	21.6
anatase	**004**	37.764	0.381	21.8	37.787	0.387	21.5
anatase	**112**	38.526	0.350	23.8	38.555	0.323	25.7
rutile	**200**	39.165	0.549	15.2	39.156	1.445	5.8

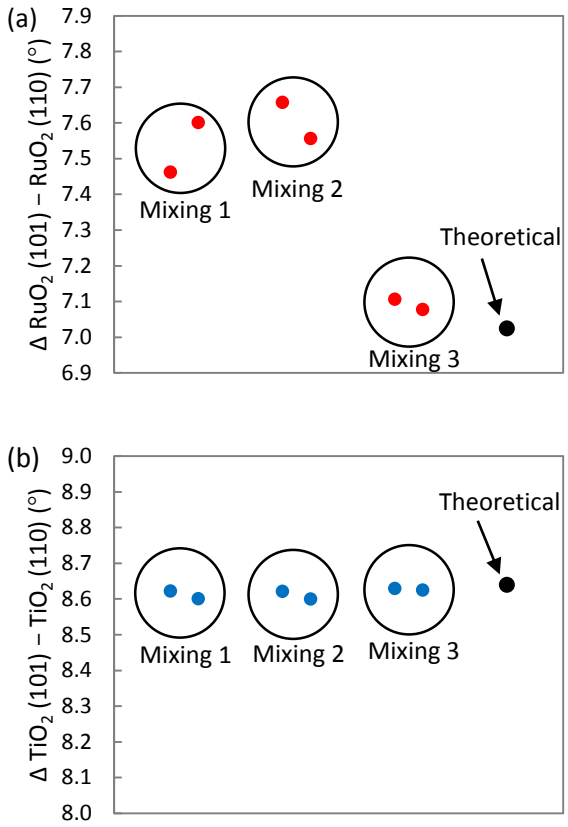

Figure 2-17: The difference in the XRD 2ϑ peak positions, 101 and 110, for (a) RuO_2 and (b) rutile TiO_2. Expected values are taken from ICDD 01-070-2662 for RuO_2 and ICDD 00-021-1276 for rutile TiO_2.

3.2.3. Interpretation of the synergistic effect

Synergy is clearly evidenced: when a mixture of anatase and rutile is present during annealing, the specific activity is much higher than the expected value for simple mechanical mixtures. This again points to an effect of the migration of Ru towards rutile particles. This is clearer in the present case because no support sintering is occurring. So the beneficial effect of support blending is not merely related to the absence of Ru "sandwiching". Instead, it is proposed to be the effect of two phenomena that are related to the migration of Ru from anatase to rutile.

Firstly, when rutile is present, Ru can migrate towards it, be stabilized via epitaxial interactions and remain highly dispersed after reduction. Secondly, the concentration of Ru on the rutile particles can lead to particles having different

(larger) size. In this way, the intrinsic activity of surface Ru can be affected. So even if dispersion is lower than in R100, the activity can in principle be as high or even higher, simply because the morphology of the stabilized particles is different.

In attempt to discriminate between both effects, the apparent TOF was also calculated by normalizing the activity by the amount of surface Ru. It is noteworthy that the TOF for the pure commercial support is markedly different from that reported for the pure home-made supports. While this observation is not fully understood at this stage, it again points to an influence of the interaction of the Ru nanoparticles with the TiO_2 supports (which can be linked to the generation of active sites). It would not be surprizing that the nature of such interactions is totally different in the catalysts which undergo severe support modifications (sintering) vs. in the catalysts based on very stable supports. Nevertheless, the activation energies of the catalysts supported on commercial TiO_2 (Table 2-7) were similar to the catalysts supported on home-made TiO_2 (Table 2-4) at all different ratios of mixing at different steps. This indicates that the rate determining pathway of the catalytic reaction is the same for all catalysts.

For the catalysts prepared by mixing the final catalysts (Mixing 3), the TOF was close to the expected value for a simple mechanical mixture (as expected). For the catalyst prepared by mixing the pure supports before RuO_2 deposition and annealing (Mixing 1), the TOF values were very close to those catalysts from Mixing 3. This suggests that the main effect of synergy is related to the fact that Ru species that migrate towards rutile is simply better dispersed. Furthermore, the active Ru nanoparticles are not strongly modified in terms of shape, morphology, and interaction with the support, thus the synergistic effect is mainly explained by a dispersion effect.

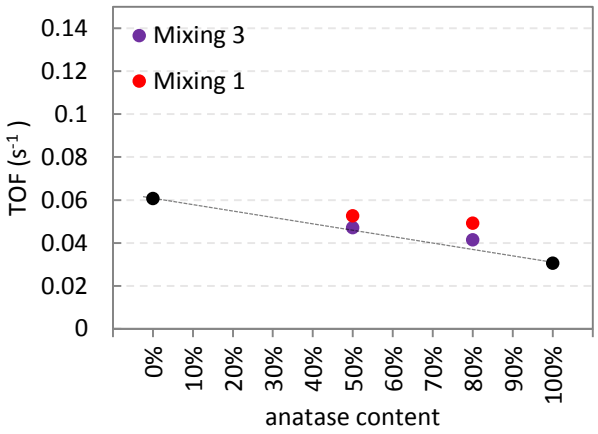

Figure 2-18: Turn over frequencies (TOF) or methane production rates normalized per surface Ru probed by H_2 chemisorption for all catalysts concerned in this section. Mixing 2 series is not plotted due to technical difficulty with H_2 chemisorption apparatus.

Table 2-7: Summary of activation energies (Ea) of the catalysts (units in kcal·mol^{-1}).

rutile:anatase ratio	Mixing 1 C(R+A)	Mixing 2 C(R+A)-BA	Mixing 3 (CR+A)-AA
5:5	14.6	15.6	15.0
2:8	14.6	15.1	14.4

4. Conclusion

RuO_2 nanoparticles supported TiO_2 catalysts were prepared by mixing the rutile and anatase TiO_2 phases in various ratios at different stages of catalyst preparation. The mixed crystalline phases were found to affect the morphology of the RuO_2 and location of metallic Ru-species which resulted in synergy in catalytic performance. The main contributor to the synergy was found to be related to the high Ru dispersion. Furthermore, the co-existence of rutile and anatase TiO_2 crystal phases itself do not affect the catalytic performance. Rather, it is the migration phenomenon of RuO_2 nanoparticles towards rutile TiO_2 phase during annealing which facilitates the dispersion of Ru-species through epitaxial stabilization of RuO_2 over rutile TiO_2. The stabilized RuO_2 phase is thus transformed into reduced Ru species without gaining mobility to move away or sinter. The scheme in Figure 2-19 represents this general observation.

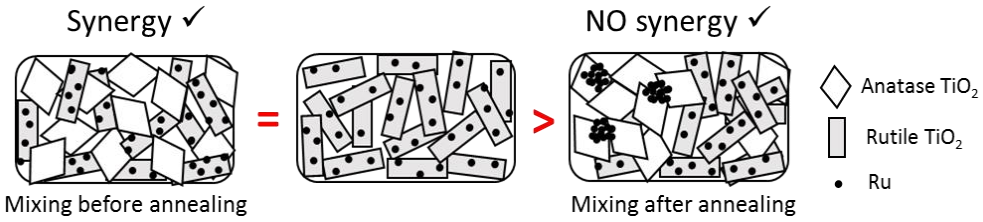

Figure 2-19: Graphical representation of Ru/TiO_2 catalysts; red signs represent the comparative catalytic performance.

This study was first performed using home-made rutile and anatase TiO_2. Both supports are however prone to sintering and further crystallization upon thermal treatment. This complicated the full understanding of the performance enhancement in catalysts based on mixed supports. Therefore, the study was also conducted on commercial non-sintering (or fully-sintered) rutile and anatase TiO_2. The synergy in CO_2 methanation activity was confirmed.

Ultimately, the non-sintering rutile TiO_2 was found to be the best support to contribute to the high Ru dispersion thus high methane production rate, due to the stabilized Ru species over rutile phase.

Chapter 3: Towards a better understanding of RuO_2 migration and its consequences

1. Introduction

Following the observations in chapter 1 and 2, this chapter focuses on the study of RuO_2 nanoparticles migration under heat treatment or annealing and during the subsequent reduction process, leading to the active phase for CO_2 methanation. While the migration of small RuO_2 nanoparticles toward rutile TiO_2 is documented in the literature and also discussed in chapter 1, several specific questions remain. In particular, while the driving force for the dislocation of RuO_2 is said to be related to the gain in energy obtained in the epitaxial interaction between rutile phases, the actual migration mechanism is not fully understood. Thus, it arises the question whether it is a surface diffusion phenomenon or the displacement of a solid/gas equilibrium leading to the formation of volatile species.

Moreover, while the occurrence of the migration is demonstrated, the consequence of the phenomenon on the shape and structure of the RuO_2 crystals ultimately stabilized at the surface of rutile TiO_2 support is also not fully understood. It can be questioned whether the stabilized RuO_2 present anisotropy governed by the rutile TiO_2 crystal structure.

To answer such questions, some specific experimental set-up that would allow observing the migration phenomenon in situ would be beneficial, rather than investigating the catalyst before and after thermal treatments (annealing or reduction).

This chapter is divided in three parts and the results are presented and discussed together with the experimental details of the respective experiments. Firstly, the consequences of epitaxy between TiO_2 rutile and RuO_2 for the RuO_2 crystalline patches are evaluated with respect to the shape of the crystallites, exposed facets

and evolution of the Ru-O distances. Secondly, the possible mechanism for migration is discussed; both experimental results from chapter 1 and 2, and literature investigation are gathered to propose the most likely scenario. Finally, in situ TEM experiment is presented with the final goal of witnessing the migration to confirm the proposed mechanical hypothesis.

Environmental TEM was utilized to observe the catalyst's behaviour during annealing (catalyst activation), reduction and reaction, in situ. Environmental TEM is a state of the art setup that allows observation of particles with high resolution scanning transmission electron microscope (STEM) in situ, during their transformation at ambient pressure and at temperature up to 1000 °C. Yet, creating the real representation of the environment of catalyst treatment in presence of gas flow and electron beam is challenging. Therefore, attempts to establish experimental conditions as close as possible to the reality was demonstrated in series of experiments towards the conclusion of the migration phenomenon.

2. Experimental summary

XRD patterns were recorded using a Bruker D8-Advance Diffractometer with Cu-Kα radiation (λ1= 1.54056 Å, λ2= 1.54439 Å) equipped with a LynxEye detector operating at 40 kV and 40 mA.

A sample of RuO_2 nanoparticles deposited on TiO_2-P25 (prepared by deposition of pre-synthesized RuO_2 nanoparticles (See experimental section in chapter 1)) containing Ru = 7 wt.% after annealing at 450 °C for 16 h in static air was used for XRD analysis.

All powder patterns were refined using the Rietveld method [153] (G. Rousse, IMPMC, UPMC) as implemented in the FullProf program [154].

Theoretical RuO_2 XRD patterns were calculated for specific plate shapes of RuO_2 crystallites using the IFPEN software SIMWAX (O. Durupty, LCMCP, UPMC).

Environmental TEM experiment is performed at IPCMS (Institut de Physique et Chimie des Matériaux de Strasbourg) by Simona Moldovan and Pr. Ovidiu Ersen. Environmental TEM images were acquired on the JEOL 2100F electron microscope, using the MEMS-based gas-cell heating specimen holder which allows in situ TEM observation of the catalyst powder during the catalytic reaction [155] at gas pressure of 1 atm, and various temperatures up to 1000 °C. The specimen holder has shown to allow recording of both bright-field and high-angle annular dark field TEM (HAADF-TEM) images in scanning mode. As described in Figure 3-1 and 3-2,

the holder incorporates an Aduro heating device into a “closed-cell” configuration. Current can be passed through the heater membrane onto which a thin film of SiN is placed and onto which the catalytic powder in deposited. This system prevents gas leaks.

Environmental TEM allows direct in situ observation of nanostructural evolution at the solid surface under gas reactions, which is particularly interesting to understand structure-property relationship and reaction mechanism in heterogeneous catalysis. The pioneering development of in situ atomic-resolution environmental TEM was by Gai and Boyes at DuPont USA in 1995 [156]. The gas-solid reaction at the atomic resolution was possible at gas pressure of a few milibars. Furthermore, Benavidez et al. reported the observation of Pt nanoparticles sintering by environmental TEM in 560 Pa at 550 °C in O_2 [157]. The reported environmental TEM studies have been demonstrated at higher pressure, although still below atmospheric pressure. What makes the current study in this chapter innovative is that the demonstration state-of-the-art environmental TEM analysis was carried out at 1 atm.

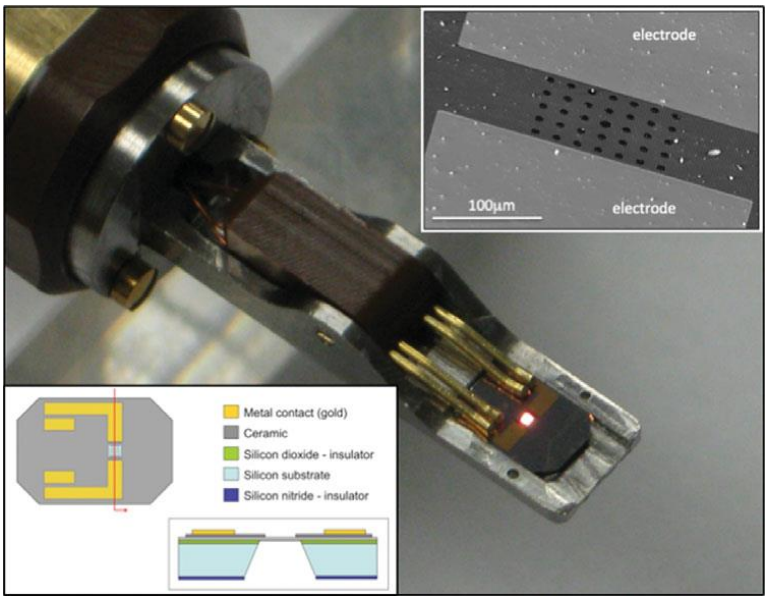

Figure 3-1: Standard AduroTM heater device (picture taken from ref [155]). The cross-section schematic inset illustrates the components of the MEMS device, and the top view shows the configuration of Au electrodes on the upper surface of the device that provide contacts for current to flow through the heater membrane. The SEM image inset shows a typical pattern of holes in the heater membrane, which support the SiN thin film that in turn supports deposited catalyst.

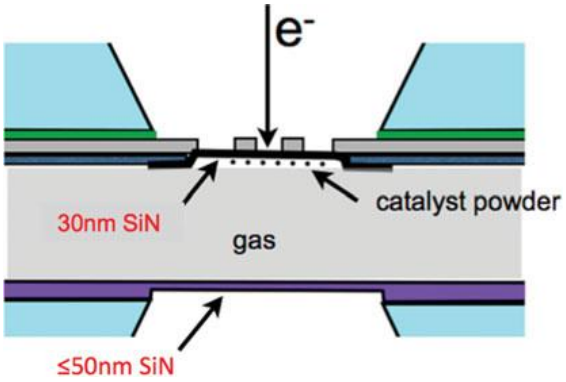

Figure 3-2: Cross-section drawing that illustrates schematically the structure of the cell in the gas-cell holder. The upper "window" of the cell is an Aduro device with a 30-nm amorphous SiN film deposited over the heater membrane. The catalyst is dispersed on that film. A lower SiN window serves to confine the reaction gas inside the cell. (picture taken from [155])

A sample of RuO_2 nanoparticles deposited on mechanical mixture of home-made 80% anatase and 20% rutile TiO_2 (prepared by deposition of pre-synthesized RuO_2 nanoparticles (See experimental section in chapter 1 and chapter 2)) containing Ru = 2.2 wt.% after annealing at 150 °C, for 16 h in static air was used for environmental TEM analysis.

To prepare the sample for environmental TEM studies, the RuO_2/TiO_2 powder was ground and dispersed in ethanol. Several drop of the suspension were then deposited on the Aduro chip as seen on figure 3-3.

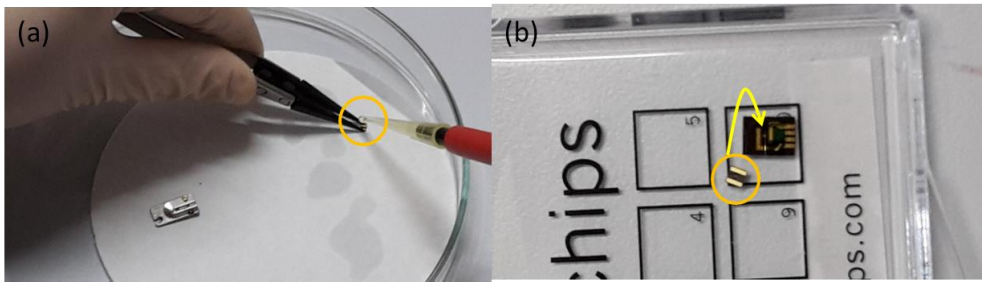

Figure 3-3: (a) Drops of the catalyst suspension are deposited on the Aduro chip that constitutes the upper window of the cell. (b) The chip is then inserted into the device.

3. Investigation of RuO_2 migration phenomenon

3.1. X-Ray experiments for a better understanding of the RuO_2 phase morphology

Following observations made in chapter 1, the changes in the RuO_2 structure and shape upon annealing in air are investigated more specifically. The consequences of these modifications are discussed in terms of Ru-O bond length and active phase reducibility.

One of the first questions concerns the link that could be established between the sizes of RuO_2 thin patches observed by TEM and the measured RuO_2 XRD peak intensities.

To address the issue, theoretical RuO_2 XRD patterns were calculated for specific plate shapes of RuO_2 crystallites. The typical dimensions observed in TEM for the RuO_2 patches located at the surface of rutile particles (think patches of about 10 nm diameter and 1 nm thickness) were converted into a number of RuO_2 unit cells to recreate thin plates; 2 to 3 cells for the thickness, and around 20 cells for the diameter were arbitrarily chosen. Stacked cell parameters into thin layers consisting a x b x c = 2 x 20 x 20, 20 x 20 x 2, and 20 x 20 x 3 were used to generate theoretical XRD patterns, addressing [101] and [110] scattering directions. For (110) plane, both 2 and 3 cell parameter thickness were chosen.

These theoretical structures were used as inputs for the calculation of expected diffraction patterns. It was revealed that in order to reproduce the situation that can prevail in P25-RuO_2 catalysts, RuO_2 plates with several orientations are required. It appears clearly (Figure 3-4) that, for such thin RuO_2 plates, the diffraction peak corresponding to the direction of the thickness will produce very broad – probably indistinguishable XRD peaks.

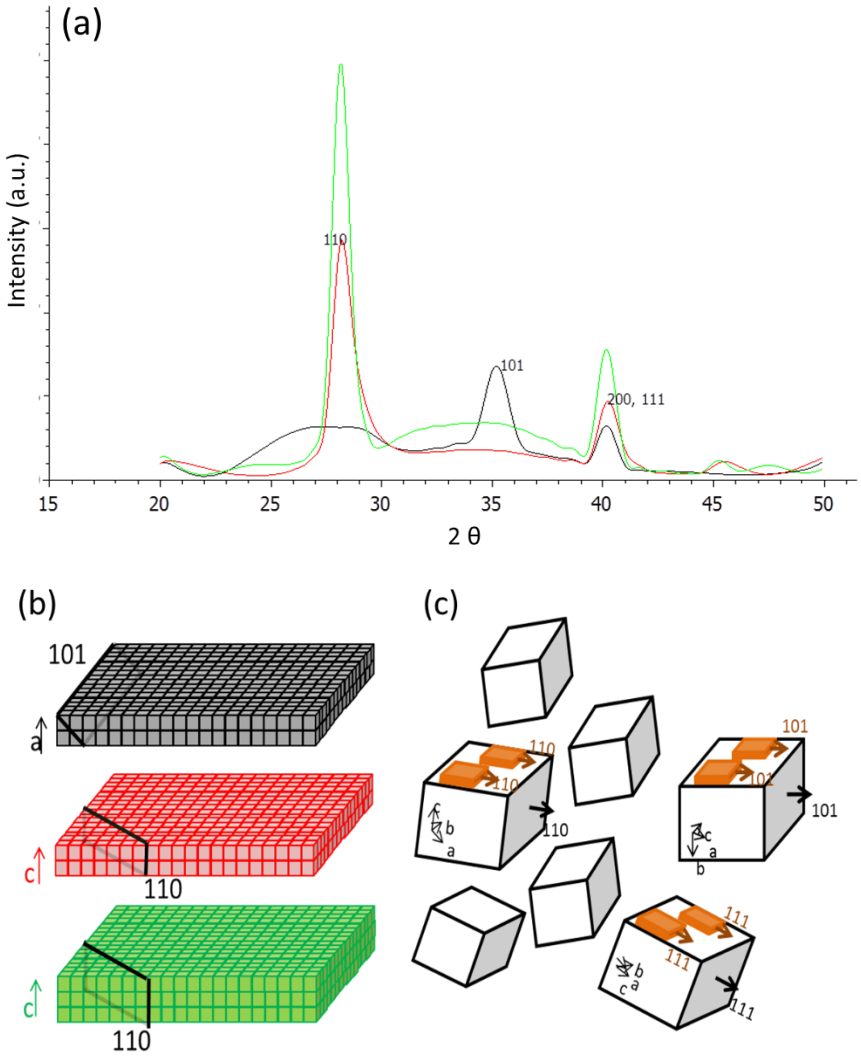

Figure 3-4: (a) SIMWAX calculated XRD patterns (b) of anisotropic models of RuO_2 crystallites, and (c) Interpretation for the P25 supported catalyst; black XRD pattern corresponds to black model consisting stacked cell parameters (a x b x c = 2 x 20 x 20), red XRD pattern corresponds to red model consisting stacked cell parameters (a x b x c = 20 x 20 x 2), and green XRD pattern corresponds to green model consisting stacked cell parameters (a x b x c = 20 x 20 x 3).

Ru content was increased up to 7 wt.% in the RuO_2/TiO_2 catalyst, in order to gain resolution in the XRD patterns as compared to the actual catalysts studied in other chapters of the thesis. This allows us to perform Rietveld refinements on all the implied phases instead of just peak deconvolutions and fittings as in chapter 1.

Rietveld calculations are shown in Figure 3-5 and Table 3-1. Among all the parameters that have been allowed to vary, we focused our attention on the cell parameters, as well as anisotropy parameters. It should be mentioned that the atomic positions have not been refined; most were on spatial positions (Ru on (0;0;0) and O on (0.30469; 0.30469;0)).

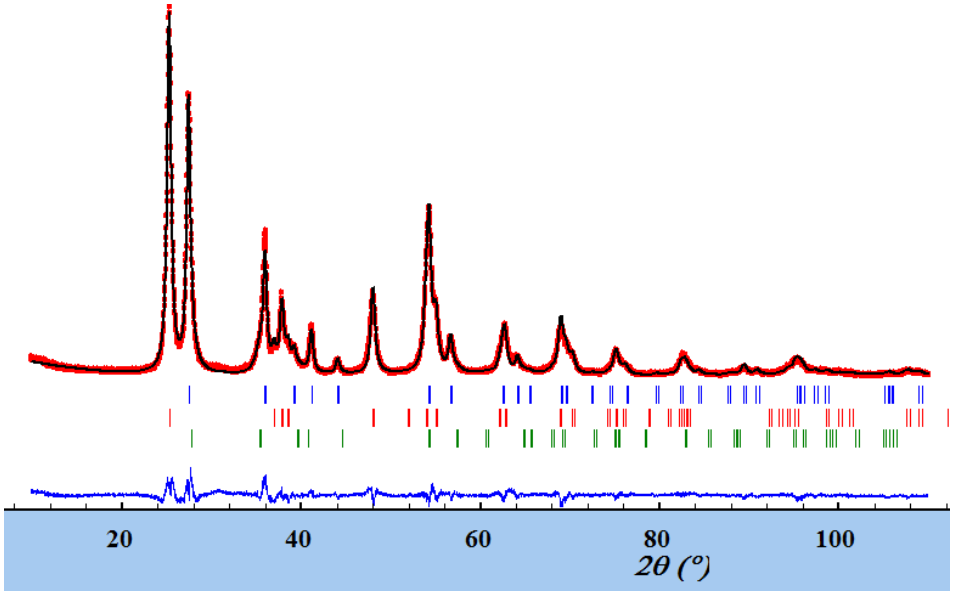

Figure 3-5: Rietveld refinement of 7% RuO_2/TiO_2-P25 catalyst. Vertical blue lines represent Bragg peaks from rutile TiO_2, green lines, RuO_2 Bragg peaks and red lines the anatase ones. The red dots represent the experimental data. The black pattern stands for the Rietveld calculated pattern. The blue line represents the difference between the experimental and the calculated pattern.

Table 3-1: Rietveld refinement results of 7% RuO_2/TiO_2-P25 catalyst.

	a(Å)	c(Å)	Long Ru-O (Å)	Short Ru-O (Å)
RuO_2 reference (ICDD 043-1027)	4.4919	3.1060	1.989	1.939
RuO_2 on P25	4.5444	3.0500	1.978	1.958
Rutile reference (ICDD 070-7347)	4.5930	2.9610		
Rutile from P25	4.5907	2.9702		
Anatase reference (ICDD 021-1272)	3.7852	9.5139		
Anatase from P25	3.7869	9.4959		

As seen in chapter 1, it appears that RuO_2 particles crystallized on the rutile particles of P25 present shifted cell parameters, closer to TiO_2 rutile ones. The consequences is that the RuO_6 octahedra that are stabilized at the surface of TiO_2 rutile are less distorted than the RuO_6 octahedra normally found in undisturbed RuO_2. The pattern was refined with no sign of preferred orientation effects nor anisotropic broadening. The calculated mean RuO_2 size stands at 5.2 nm which is compatible with the TEM observed patches of 10 nm in diameter and around 1 nm in thickness.

3.2. On the possible RuO_2 migration mechanisms

The redistribution process of RuO_2 during heat treatment from anatase TiO_2 particles to rutile TiO_2 particles appears to play a major role into the catalyst activation. As previously observed by Xiang et al [158], this phenomenon only occurs for small sub-2 nm RuO_2 particles. In this range of size, it is well known that surface tension dominates most physicochemical properties of nanomaterials, especially the interface behaviors and surface stability. When energy (heat) is applied, the small RuO_2 particles can overcome the constraints from the bulk network in order to minimize global free energy, either by diffusion to grow into bigger particles or undergoing shape change.

The shape transformation (from sphere to thin layer) is driven by the surface relaxation due to epitaxy stabilization at the interface of rutile TiO_2 and RuO_2.

The mechanism of departure of the ruthenium atom from anatase TiO_2 surface remains less clear. Two possible phenomena can be proposed: (i) RuO_2 local volatilization followed by re-deposition and (ii) RuO_2 nanoparticle diffusion.

Indeed, RuO_2 vaporization/condensation phenomena have been addressed in the fabrication of α-Al_2O_3 at 1000 °C with RuO_2 crystals trapped in the matrix,

presenting a Ru gradient from the core of the sample to the surface [159]. Upon heating in oxidative atmosphere, the two following equilibrium can be considered:

$RuO_2(s) + O_2 = RuO_4(g)$ (1)

$RuO_2(s) + ½\ O_2 = RuO_3(g)$ (2)

This way, during heat activation, RuO_2 (s) on TiO_2 support could be locally vaporized as RuO_x gas and randomly redeposited as RuO_2 on other TiO_2 surface. When deposited on rutile TiO_2, stabilization and fixation would occur through epitaxy. Vaporization would occur again for RuO_2 deposited on anatase TiO_2, until RuO_2 could be redeposited on rutile TiO_2.

However, the amount of ruthenium gas in equilibrium with RuO_2 usually remains very low. Equation suggested by Garisto [160] using reports of Bell [161] and Schaefer [162] can be used:

From equation (1), $P(RuO_4)=exp(20.002-2.2867*lnT-15562.5/T+ln*P(O_2))$

From equation (2), $P(RuO_2)=exp(37.939-3.0590*lnT-32488.1/T+0.5*ln\ P(O_2))$

(T in Kelvin and P in standard atmosphere)

It shows, for example, that under pure oxygen static atmosphere (1 atm), RuO_x vapors pressure stands at $0.2*10^{-3}$ atm at 1000 °C. A short calculation at 450 °C leads to $0.2*10^{-5}$ atm of gas above $RuO_{2(s)}$. According to Le Chatelier's principle, both equilibrium can be displaced: towards volatilization under high oxygen gas flow, or towards RuO_2 deposition from RuO_3/RuO_4 rich atmosphere [163]. This explain why the rare studies published concerning pure bulk (unsupported and unstabilized) RuO_2 catalyst in automotive for NO_x reduction report that, under extremely high gas flow (100000 h^{-1} space velocity, meaning 28 total changes of the entire gas volume of the chamber per second), a drastic increase of the loss rate of ruthenium over time occurs [164, 165]. Of course, our static conditions of heat treatment at 450 °C in air do not favor this general volatilization of RuO_4 and RuO_3, even if local volatilization followed by rapid re-deposition cannot be totally excluded [159].

To solidify the idea, RuO_2/TiO_2-P25 catalysts were prepared and annealed separately in a flow of pure N_2 as well as dry air. As shown in Figure 3-6, the RuO_2 nanoparticles are migrated selectively to rutile TiO_2 particles in both inert and oxidizing environments. This means that RuO_2 migration indeed can occur without the oxidation/volatilization phenomenon.

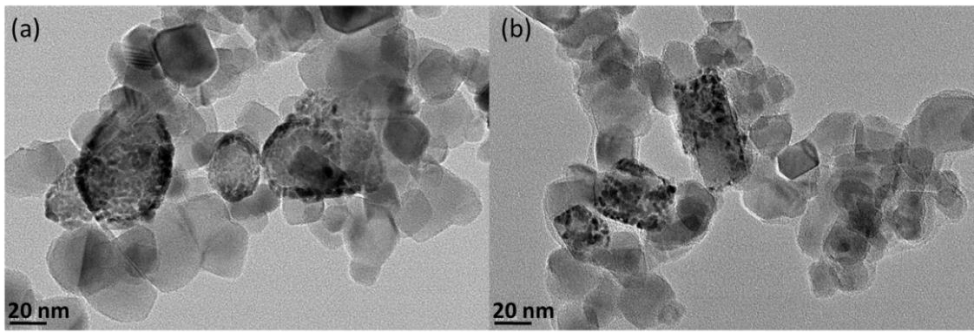

Figure 3-6: TEM images of Ru/TiO_2-P25 catalyst (a) annealed in N_2 and (b) annealed in dry air, at 450 °C, 4 hours.

Small RuO_2 nanoparticles, on the other hand, have already been proven to be able to diffuse at the surface of particles. For example, at temperature as low as 300 °C, small RuO_2 nanoparticles embedded into amorphous silica matrix were shown to diffuse and grow at the surface of the RuO_2/SiO_2 composite in the generated porosity path [166]. Larger RuO_2 particle (above 4 nm) lose their ability to diffuse and remain trapped.

The driving force of this diffusive sintering can be understood in terms of two operative mechanisms: Ostwald ripening (OR) or particle migration and coalescence (PMC) [167]. OR involves interparticle transport of mobile molecular species (or clusters), driven by differences in free energy and local adatom concentrations on the support surface. In contrast, PMC involves the mobility of particles in a Brownian-like motion on the support surface, with subsequent coalescence when particles come in close proximity to each other [167]. In the early stage of diffusive sintering, the evidence from recent in situ studies [157, 167-169] suggests that OR dominates the diffusion of nanoparticles towards sintering when particles are very small.

In our experimental conditions, the diffusion driven by OR explains the migration of RuO_2 nanoparticles at the surface of TiO_2 particles. It is possible that traces of chlorine residue may contribute to formation of highly mobile metal chloride compounds. The diffusion of RuO_2 nanoparticles subsequently leads to two different phenomena in terms of sintering: isotropic growth of RuO_2 crystals on anatase TiO_2 (or sintering) and epitaxial growth of RuO_2 layer on rutile TiO_2.

3.3. Environmental TEM

Environmental TEM was performed with the idea to observe the migration phenomenon in conditions as close as possible to those of annealing. It is clear indeed – by looking at the catalyst before and after annealing – that migration occurs during annealing. To do that, transmission electron microscopy is carried out in a specific cell that features a very small dead volume that can be kept up to atmospheric pressure, equipped with an in situ heating system, and delimited by electron-transparent windows. In this section, three experiments are described and discussed sequentially to show that the strategy is not straightforward and that the conditions chosen for performing these measurements have a great influence on the outcome.

Given the fact that anatase and rutile particles in P25 are not easily distinguishable on TEM images, it was decided to use a mechanical mixture of 20% home-made rutile and 80% home-made anatase TiO_2 to mimic the composition of P25. Home-made anatase and rutile particles have different shapes and can be distinguished easily: rutile TiO_2 consists of long needles (11 x 100 nm) and anatase TiO_2 consists of smaller isotropic particles (~ 6 nm in average diameter).

3.3.1. Experiment 1:

To avoid contamination, the chip is usually heated under argon in order to remove all adsorbed organic molecule from the air. Thus we chose to perform such purge under Ar at 250°C and then to replace Ar by pure O_2 before heating up (Scheme 3-1).

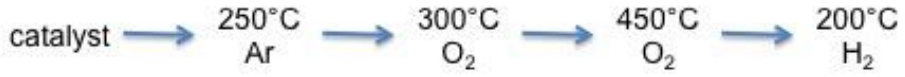

Scheme 3-1: Heating scheme for Experiment 1.

Under Ar, at 250°C, images obtained allow the clear observation of rutile TiO_2 needles and of isotropic anatase particles, along with small RuO_2 particles dispersed throughout the sample, at the surface of both types of TiO_2 crystals. After this first treatment, an oxygen flow is applied, and the chip is heated up to 300°C, while maintaining the TEM electron beam over the areas under observation. Two zones have been selected and observed: one showing rutile particles and another showing anatase particles. Our observations are focused into seeing RuO_2 particles "moving from" anatase, and in the meantime RuO_2 "arriving to" TiO_2 rutile. Given

the epitaxy between RuO_2 and TiO_2 rutile, we can assume that this last observation on rutile will be more difficult than the disappearance from anatase.

At 300°C, it appears that RuO_2 particles remain located on both anatase and rutile in such conditions, even after one hour.

When the experiment is continued at 450°C under oxygen flow, it clearly appears that the migration has not occurred; RuO_2 particle remained both on anatase and rutile surfaces. RuO_2 particles clearly appear to have grown in size on both supports, (initially bellow 2nm, up to a mean diameter of 2.4 nm at 450°C under the electron beam).

After several purges with argon and a decrease of temperature down to 200°C, the sample is flowed with hydrogen under 1 atm. Metallic Ru nanoparticles are immediately distinguished with higher contrast than with RuO_2. It appears that Ru has not migrated: both anatase and rutile are covered with Ru nanoparticles. As seen in Figure 3-7 and 3-8, metallic Ru particles appears larger on anatase than on rutile (mean diameter of 3.1 nm on anatase and 2.4 nm on rutile).

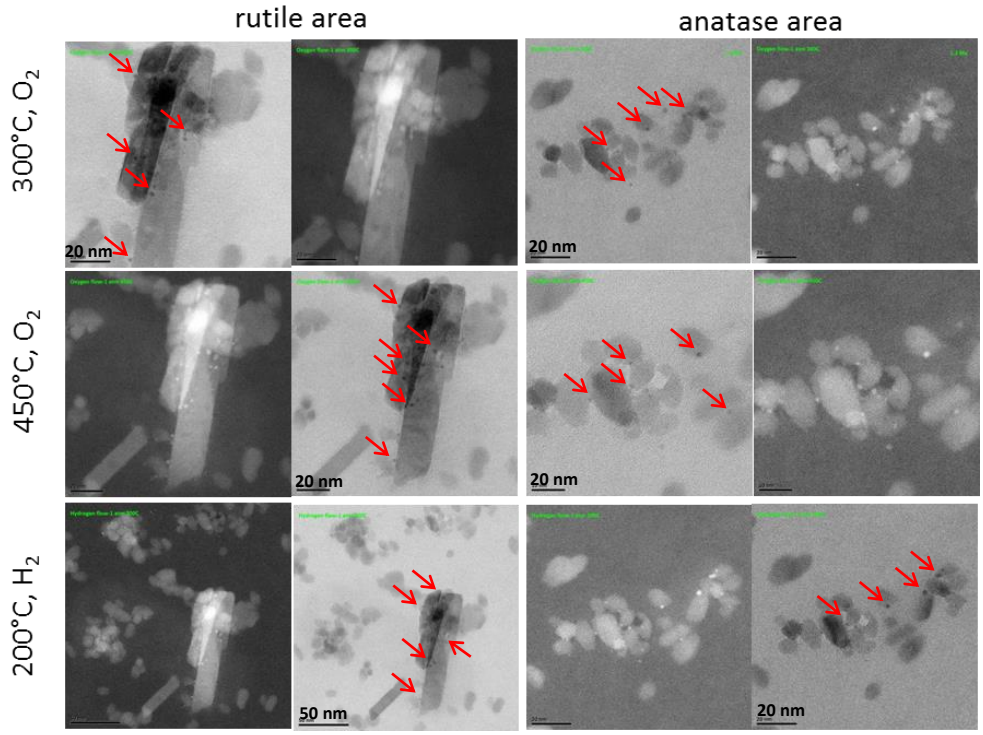

Figure 3-7: STEM images of RuO_2 and Ru particles on both anatase and rutile at 300°C and 450°C under oxygen flow, and 200°C under hydrogen flow. The images had carefully been taken on the same selected anatase and rutile areas. Red arrows indicate Ru species (only shown in bright field images).

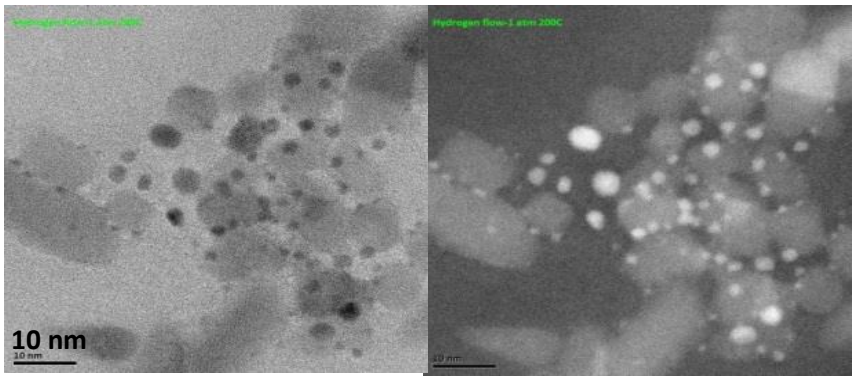

Figure 3-8: STEM images of bigger Ru particles on anatase at 200°C under H_2 atmosphere.

The fact that no migration of RuO_2 have been observed during this experiment, and that bigger RuO_2 particles are observed compared to initial RuO_2 particles, raises several questions concerning the RuO_2 migration:

- Would the electron beam interfere with the migration phenomenon? And in this case, knowing that the electron beam could be seen as a reductive source, would that mean that the oxidation of RuO_2 into RuO_3 or RuO_4 is prevented solely due to the electron beam, thereby implying a volatilization mechanism to explain RuO_2 migration in the actual catalytic preparation step in static air?
- Should the temperature be raised to higher temperature to provoke the migration under the electron beam?
- Would the initial heating of the sample overnight in air at 150°C be responsible for a better anchoring of RuO_2 to the TiO_2 support? Once the RuO_2 particles have sintered and grown up to several nanometers, their stability is higher, and part of the driving force of migration is lost, according to Xiang et al. The stabilization/attachment question can also be raised regarding the 250°C argon treatment inside the TEM chamber.
- What would be the catalytic activity of such a powder presenting Ru particles, distributed both on anatase and rutile?

3.3.2. Experiment 2:

A second set of experiment is thus performed taking into account the questions we had; the degassing pre-treatment is performed at lower temperature in argon, and the temperature is then raised up to 600 °C in oxygen, as shown in Scheme 3-2:

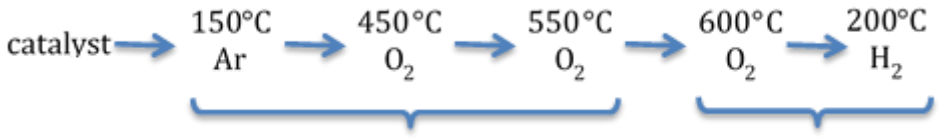

Scheme 3-2: Heating ramp for Experiment 2.

Several areas are selected depending on the crystallite morphology, and are continuously observed during the heat treatment (Figure 3-9).

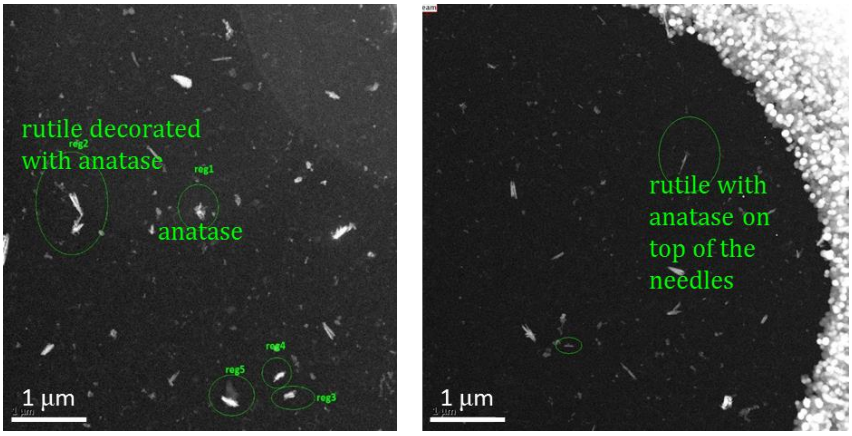

Figure 3-9: Global observation of one window of the grid, crystallites phases are attributed to anatase or rutile TiO_2 depending on their morphology.

RuO_2 nanoparticles are well observed at 150°C under argon, both on anatase and rutile. The distinguishable RuO_2 particles on rutile particles decorated with anatase particles are shown in Figure 3-10.

Upon heating at 450°C under oxygen RuO_2, numerous RuO_2 particles can still be observed on anatase, on the separated selected area as well as on the anatase surrounding rutile particles. Sintering of anatase is clearly observed from 450°C, which resulted in thicker particles thereby lowering the contrast between RuO_2 and TiO_2 particles making the RuO_2 particles difficult to be well-distinguished.

At 550°C under oxygen, the same tendencies are observed: RuO_2 particles are still observed on anatase (both anatase around rutile and anatase alone).

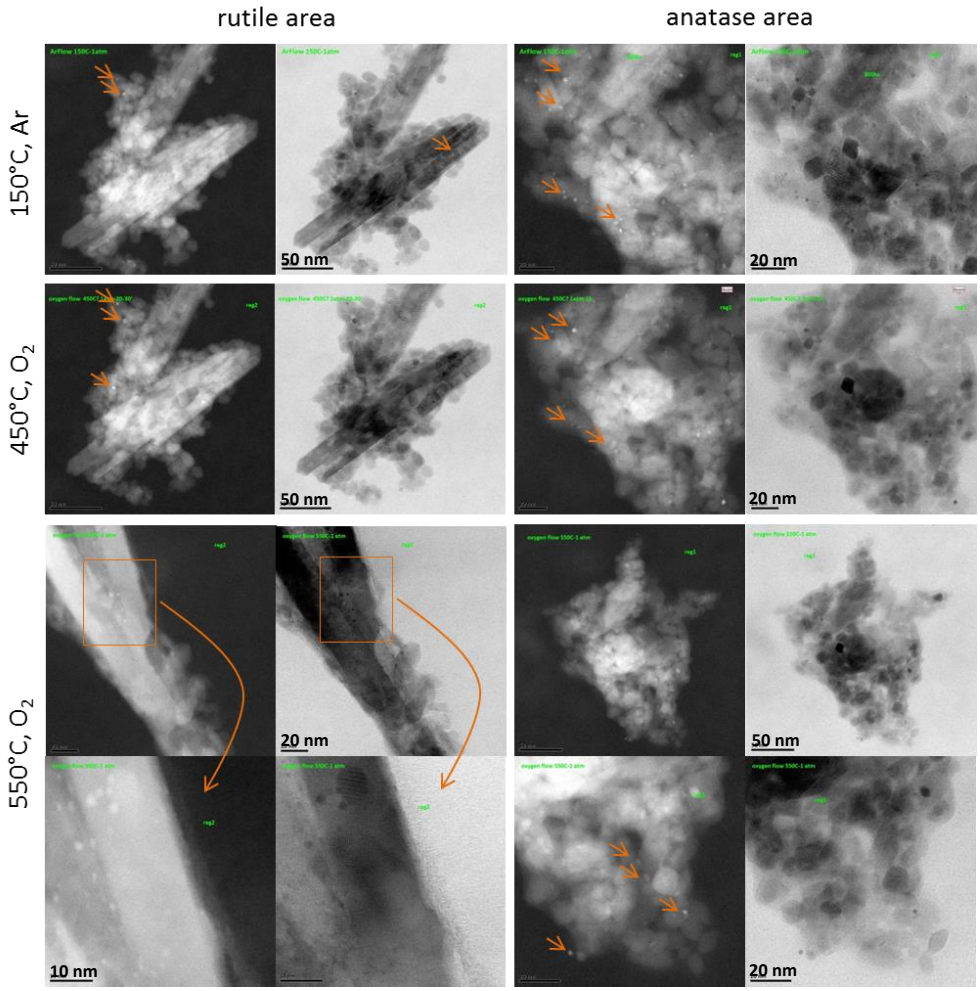

Figure 3-10: STEM images of RuO_2 particles on both anatase and rutile at 150°C, 450°C and 550°C under oxygen flow. The images had carefully been taken on the same selected anatase and rutile areas. Orange arrows point the RuO_2 nanoparticles.

Due to sintering of the particles and electron beam damages, the images at 600°C were taken on different particles from the particles shown in Figure 3-10, where both anatase and rutile TiO_2 are present (Figure 3-11). As expected, once the sample is reduced at 200°C under hydrogen, metallic Ru nanoparticles can be observed on both anatase and rutile (Figure 3-12).

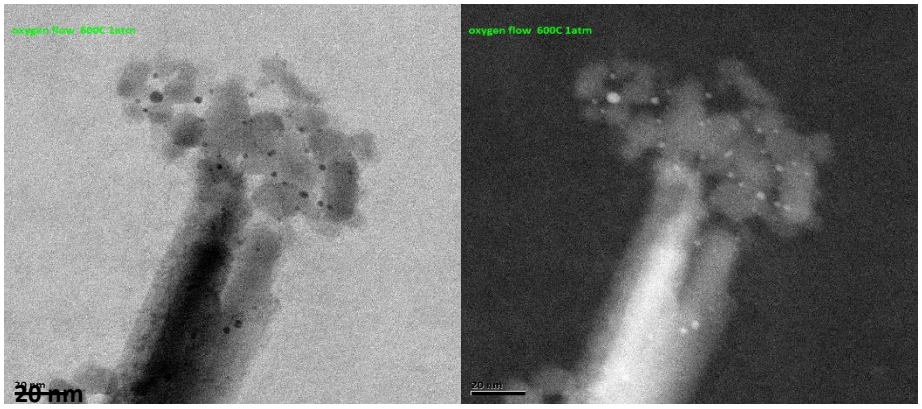

Figure 3-11: STEM image taken under oxygen at 600 °C showing RuO_2 particles both on anatase and rutile.

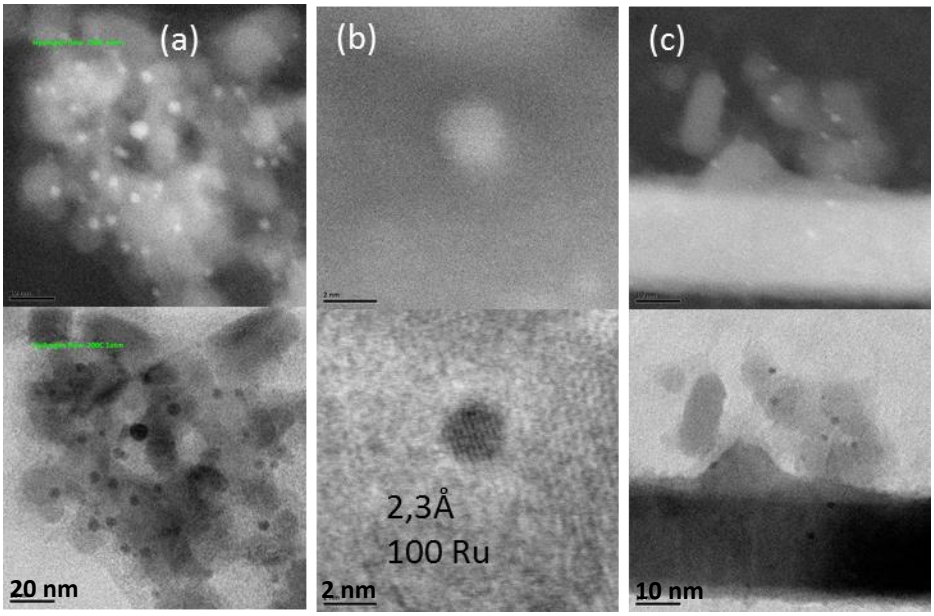

Figure 3-12: STEM images at 200 °C under hydrogen (1 atm) showing Ru nanoparticles (b) clearly present on anatase (a) and (c) rutile particles.

This second test allows us to disregard the calcination temperature criterion: Indeed, even at 600 °C, RuO_2 particles are located on anatase. Ex situ, migration occurs at 450 °C in air.

3.3.3. Experiment 3:

The third experiment aims at varying the degassing conditions as well as studying the possible impact of the electron beam over time. The degas condition was chosen to heat the sample only at 150 °C, and under oxygen instead of argon. Several sample areas are chosen based on their morphology as shown in Figure 3-13.

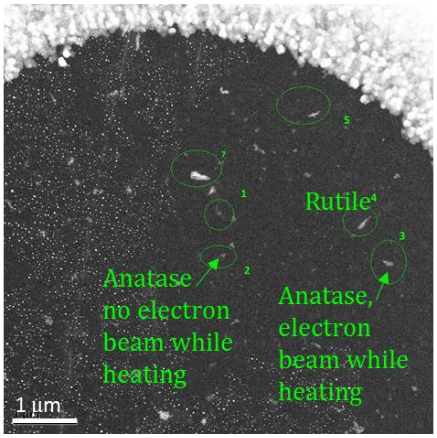

Figure 3-13: Global observation of one window of the grid at 150 °C, which allows to select crystallite phases attributed to anatase or rutile TiO_2 depending on their morphology.

After degassing, the sample was heated gradually with an increment of 50°C, up to 450°C. During this gradual temperature increment, the electron beam was focused on one area where anatase phase was present and images were taken at every 50°C increment. The first image was taken two minutes after the desired temperature was reached, and a second one was taken 10 minutes later in order to examine whether RuO_2 mobility is time-dependent. Once the temperature was reached to 450°C, the anatase area was observed regularly for one hour. Another separated anatase and rutile areas were observed only after being heated at 450°C for an hour (not exposed to electron beam). The results are shown in Figure 3-14.

After one hour at 450°C RuO_2 nanoparticles have totally disappeared from the anatase particles which were not exposed to the electron beam, whereas RuO_2 nanoparticle are still present on the anatase particles exposed to the electron beam.

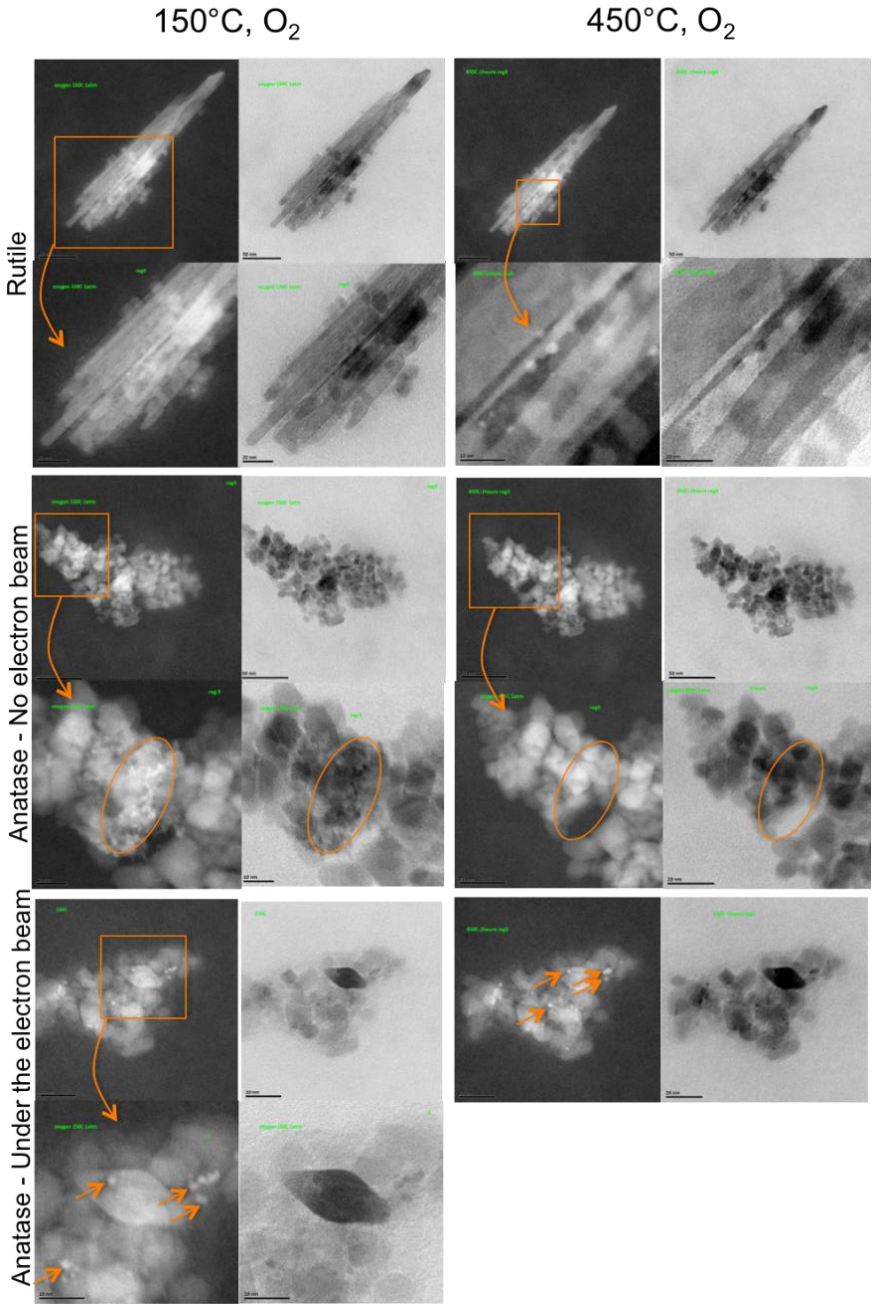

Figure 3-14: STEM images of RuO_2 particles on both anatase (with and without electron beam) and rutile (without electron beam) at 150°C and 450°C under oxygen flow. Orange arrows point the RuO_2 nanoparticles. The orange circled area shows RuO_2 nanoparticles that have disappeared at 450°C after one hour.

The series of these preliminary observations definitely show the difficulties of in situ studies to mimic the reality. In fact, our preliminary observations with the environmental TEM setup are biased by several factors: the presence of electron beam, the high dispersion of the powder on a TEM grid in comparison to the compact catalyst powder used during catalyst preparation and test, the use of pure oxygen vs. thermal treatment in (static) air, and the use of gas flow vs. static air, etc.

The influence of the electron beam on RuO_2 mobility raises several questions. Considering that the electron beam is reductive, do the electrons prevent the oxidation of RuO_2 into the volatile RuO_4? If electron beam prevents the migration of RuO_2 under one-hour time frame, would that mean that only the volatilization of RuO_2 (and further redeposition on rutile TiO_2) is responsible for the migration within the first hour?

As calculated in the beginning of this chapter, for pure static oxygen environment, $P(RuO_3 + RuO_4) = 0.2*10^{-5}$ atm. This very low value by itself attests that it is diffusive sintering and not RuO_2 volatilization that can be accounted for the RuO_2 migration in our ex situ static air annealing conditions. However, during the environmental TEM analysis, pure oxygen flow is estimated to be 0.00012 Torr*L/s, which is equivalent to 0.00948 standard cubic centimeter per minute (sccm). If we take into account that the TEM cell (containing sample) volume measures 1.2 μL, we can estimate a space velocity of $0.13s^{-1}$, meaning that the entire cell volume is renewed every 8 seconds. Even if this is 215 times slower than in the NOx study (28 renewal per second[164]), volatilization and redeposition of RuO_2 is highly likely in the actual chosen environmental setup. Preventing this volatilization would restore the diffusive sintering mechanism and allow in situ observation of the mobility of RuO_2 nanoparticles.

To better understand the RuO_2 migration phenomenon, further experiment would be necessary. Based on the environmental TEM analysis, several experimental improvements can be suggested.

- Catalyst sample with higher Ru loading (e.g. Ru = 7 wt. %) in order to localize RuO_2 nanoparticles more easily.
- In situ analysis under air, not oxygen to prevent any possible displacement of RuO_2-RuO_4 equilibrium.
- Minimum gas flow, or static gas atmosphere during in situ analysis.

4. Conclusion

This chapter discusses the hypothesis concerning the migration of RuO_2 nanoparticle – from anatase TiO_2 particles to rutile TiO_2 particles – during thermal annealing and further reduction process.

Thanks to the crystallographic study and TEM images, it has been proved that the RuO_2 nanoparticles, once migrated from anatase to rutile TiO_2, would sinter and crystalize. The crystallization is driven by epitaxial lattice matching to the rutile TiO_2 structure. On P25 support, the relative isotropic shape of the rutile particles leads to numerous exposed rutile TiO_2 facets. As a consequence, crystalline RuO_2 patches on the facets of the TiO_2 rutile, expose various crystallographic planes. The epitaxially grown RuO_2 is composed of RuO_6 octahedra that are less distorted compared to that of bulk RuO_2 reference structure.

Rietveld refinements can be performed on pure anatase supported RuO_2 catalysts, pure rutile supported RuO_2 catalysts, as well as mechanical mixture of the anatase and rutile supported RuO_2 catalysts. On pure anatase support, large isotropic RuO_2 crystallites of non-disturbed RuO_2 structure (=distorted RuO_6 octahedra), presenting numerous faces are expected. On the contrary, pure rutile TiO_2 needles with highly exposed (110) facets are expected to present aligned, non-isotropic RuO_2 patches of highly disturbed RuO_2 structure (=less distorted RuO_6 octahedra). Furthermore, a careful comparison with the mechanical mixtures of home-made anatase and rutile TiO_2 particles as well as pure commercial anatase and rutile TiO_2 particles may give an insight to the most exposed plane, and establish a possible link between crystallographic planes and catalytic activities.

The shape transformation of RuO_2 nanoparticles is driven by the surface relaxation due to epitaxy stabilization during thermal annealing at the interface of rutile TiO_2 and RuO_2. The mechanism of RuO_2 migration involves two possible phenomena: RuO_2 local volatilization followed by redeposition and RuO_2 nanoparticle diffusion. We propose that these 2 phenomena co-exist, but with one being predominant over the other one depending on the calcination conditions and probably sample history.

At our classical annealing conditions (450°C in static air), RuO_2 nanoparticles diffusion via Ostwald ripening is considered to be the most predominant. Yet, environmental TEM studies performed under pure oxygen flow also suggests that the RuO_2-RuO_4 equilibrium could be displaced at 450°C toward the volatilization.

Our attempts to observe the RuO_2 migration phenomenon by environmental TEM experiments have shown some difficulties of in situ studies to mimic the reality. On the other hand, exciting potential to observe RuO_2/TiO_2 catalysts in situ from catalyst activation to catalytic reaction condition could be envisaged with further adjustments of the in situ analysis conditions.

Chapter 4: Preparation of mesoporous TiO_2 and its application as a support for Ru-based catalyst

1. Introduction

Our previous investigation on the active phase-support interaction in the RuO_2-TiO_2 system showed that the crystallinity of TiO_2 support enables the transformation of the shape of the RuO_2. Consequently, the different interactions based on the TiO_2 support crystallinity influenced the catalytically active Ru-species after in situ reduction and methanation reaction, resulting in different catalytic activities. This observation led to further explore a different aspect of the TiO_2 properties as a support for Ru-species. Mesoporous TiO_2 with high surface area and lower crystallinity was chosen to investigate the interaction of the support with Ru-species using the pre-synthesized RuO_2 nanoparticles as an initial active phase.

Mesoporous material as a support for small metal particles is of great interest because of their high specific surface area and calibrated pore structures [79]. Sol-gel chemistry is recognized as a powerful toolbox for the preparation of such solids, often allowing to respond to strict specifications in terms of texture, composition, homogeneity, surface chemistry, etc. [49, 50, 170, 171]. On the other hand, the design and synthesis of porous materials remain more challenging than the synthesis of non-porous dense materials [172]. Especially, the preparation of non-silicate transition metal oxides is not as extensively studied as silica-based mesostructured materials [173, 174]. This is attributed to the different sol-gel condensation kinetics of silicate and non-silicate precursors. It was demonstrated by Fan et al. [54] that silicon alkoxides are quite stable in ethanol exposed to atmospheric moisture and the particle growth rate of the oxide precursor is slow enough to control. However, many metal oxides are highly reactive toward water due to coordination expansion and rapid condensation [54]. As a consequence, several strategies are developed for the stabilization of inorganic precursor in solution including the use of reactivity-modifiers that are complexing agents [53,

54, 175], the implementation of non-hydrolytic conditions [55], as well as coupling of acetic acid mediated sol-gel chemistry with aerosol-assisted self-assembly process [66].

Aerosol-assisted self-assembly (AASA), an integration of aerosol spray and evaporation-induced assembly, has been proposed for a simple and rapid production of high surface area-nanostructured materials with well-defined pore size and controllable texture [64, 173]. In its process, a stable colloidal dispersion of precursor sol is atomized into droplets (aerosol) and undergoes the evaporation of the solvent and condensation of the non-volatile solute into solid particles. The material preparation with AASA, however, has been mainly focused on silica-based mesostructured materials. Due to the very different sol-gel condensation kinetics, non-silicate inorganic precursors require chemical strategies to form stable sol. In this regard, the use of acetic acid in metal alkoxides solubilized in a sol-gel solution consisting of acetic acid, hydrochloric acid, and ethanol (AcHE system) have been demonstrated by Doeuff et al. [53] and Fan et al. [54] The strong acid (HCl) serves as a catalyst for the esterification of acetic acid with ethanol to produce water. It was demonstrated that the acetate ligands are directly bonded to the metal cores of metal alkoxide in a bidentate and bridging fashion to form stable, nanometer-sized metal oxo-acetate particles [66], which slows down the hydrolysis process, thereby increasing the time of gelation.

In the present study, we have combined the acetic acid-mediated sol-gel chemistry system with the aerosol-assisted self-assembly technique in order to synthesize mesoporous TiO_2 with high surface area and porosity. Porosity is then released through a thermal treatment step designed as to remove the organic template. The properties of obtained mesostructured TiO_2 was studied at various calcination conditions. The resulting mesoporous TiO_2 was used as a support for RuO_2 nanoparticles in the catalytic CO_2 methanation. The effects of specific surface areas, support crystallinity and active phase-support interaction were investigated using various characterization techniques and related to the catalytic performance in CO_2 methanation.

2. Experimental summary

2.1. Aerosol assisted preparation of mesoporous TiO_2

The synthesis of mesoporous TiO_2 via aerosol-assisted self-assembly process was adapted from Tsung et al. [66]. The setup for the aerosol-assisted self-assembly process is illustrated in Figure 4-1. An aerosol generator from TSI was employed; vacuum was used to carry the aerosol towards the collection of dried powder.

The precursor solution was prepared by dissolving Titanium (IV) butoxide precursor, acetic acid, and hydrochloric acid (37 wt.%) in ethanol. The molar ratio of the components was $Ti(OBu)_4$: acetic acid : HCl : EtOH : F127 = 1 : 4 : 1.2 : 40 : 0.01 (water from concentrated HCl gives metal to water ratio of 1 to 4). To form nanometer-sized stable metal oxo-acetate precursor particles, amphiphilic block copolymer F127 ($EO_{106}PO_{70}EO_{106}$, Mw=12000 $gmol^{-1}$) was added after stirring for 2 h. The solution was stirred vigorously for at least one more hour to obtain a clear solution and transferred to a closed container attached to the aerosol generator. During the aerosol spray process, the aerosol droplets were allowed to dry and start the surfactant-directed assembly gradually across the heating zone at 400 °C inside a 1 m-long quartz tube with a diameter of 8 cm. The dried powder was collected on a membrane filter with pore size of 0.2 µm. The flow was kept constant throughout the process by an oil bubbler, which gave an indication of the pressure drop increase throughout the process. When the bubbling was about to cease, which indicated the blocking of the filter due to the sample collection, the dried powder was scraped from the filter and this sample collection was repeated for ~2 h from the first time the precursor solution was atomized. The collected powder was carefully spread out in a shallow crucible(s) with larger bottom as a very thin layer and calcined at various calcination temperatures (325, 350, 375, 400, 425, or 450 °C) for 5 h with 1 °C/min heating rate in static air to obtain mesoporous spheres. One aerosol process yielded about 1 g of sample after calcination. In order to prepare enough amount of samples for characterization and catalyst preparation, the aerosol process was repeated until at least 2 g (up to 12 g) of sample was prepared in total; different batches of identical sample were combined after checking their textural properties to confirm the reproducibility.

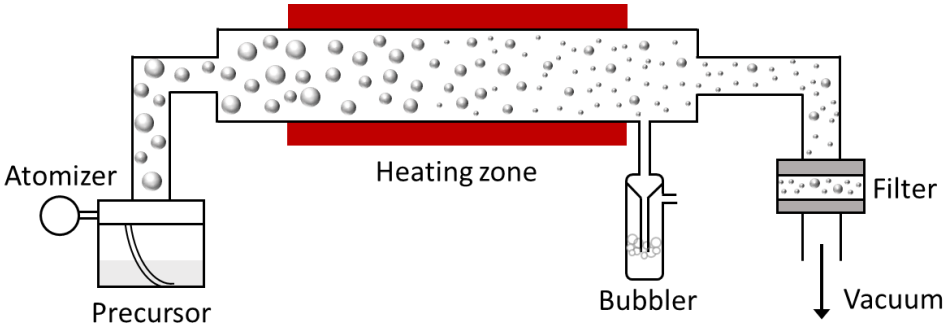

Figure 4-1: Schematic of aerosol process.

2.2. Catalyst preparation

To prepare Ru-based catalysts, selected samples were deposited with pre-synthesized RuO_2 nanoparticles, as detailed in the general experimental section (Pg. 23 and Pg. 31). First, certain amount (2 g to 12 g) of mesoporous TiO_2 was added to a calculated volume of RuO_2 nanoparticles colloidal suspension to yield 2.2 wt. % of Ru in the final catalyst, then the mixture was put in an ultrasonic bath for 30 minutes operating at 40 kHz at room temperature. This step was introduced in attempt to separate highly agglomerated mesoporous spheres as well as to favor the diffusion of RuO_2 nanoparticles inside the pores. The annealing of support containing RuO_2 nanoparticles suspension at 50 °C for 16 h was omitted, after confirming that there is no difference in catalytic activity with or without this annealing step.

After ultrasonification, water was evaporated by rotary evaporation under vacuum at 50° C. The resulting dried powder was annealed at various temperatures (250, 350, 400, 450, 500, 550, 650 °C) for 4 h with heating ramp of 10 °C/min. The samples are not washed by water as it was previously shown that chlorine content levels off to zero after annealing with or without washing and that no impact on catalytic activity was observed on P25 supported catalysts (see Appendix B).

The samples discussed in this chapter are summarized in Table 4-1.

The catalyst preparation by deposition of RuO_2 nanoparticles is compared with wet impregnation of $RuCl_3$ solution and incipient wetness impregnation of aqueous solution of $RuCl_3$ followed by microwave treatment.

For wet impregnation, $RuCl_3$ were dissolved in water at [Ru] = 0.007 M (same concentration as RuO_2 NPs in suspension) and support was added to yield 2.2 wt. %

of Ru in the final catalyst. The dried powder was obtained after rotary evaporation under vacuum at 50° C and annealed at 450 °C for 4 h with heating rate of 10 °C/min.

For microwave treatment, $RuCl_3$ were dissolved in water at [Ru] = 0.6 M. Then, 0.35 ml of the concentrated $RuCl_3$ solution was added to 1 g of TiO_2-P25 or mesoporous TiO_2 (Ti350) powder (V_{pore}(Ti350) ~ 0.36 cm^3g^{-1}) drop by drop by vigorously mixing with TiO_2 powder to obtain sticky (TiO_2-P25) or dry (Ti350) texture. The resulting powder is added to a Teflon tube containing 15 ml of Toluene and a SiC bar was dropped inside the sample. The sample was then treated under microwave (Synthos 3000 Multiwave) at 600 W set at 100% power at 200 °C for 30 min with a heating rate of ~ 6 °C/min and the pressure ramped from atmospheric to ~40 bar.

Table 4-1 summarized all samples discussed in this chapter.

Table 4-1: Samples discussed in this chapter

System	Sample	Calcination [a] T (°C)	Annealing[b] T/t (°C/h)
Pure mesoporous TiO_2	Ti325	325	N/A
	Ti350	350	N/A
	Ti375	375	N/A
	Ti400	400	N/A
	Ti425	425	N/A
	Ti450	450	N/A
RuO_2 supported catalysts	Ti350Ru250	350	250
	Ti350Ru350	350	350
	Ti350Ru400	350	400
	Ti350Ru450	350	450
	Ti350Ru500	350	500
	Ti350Ru550	350	550
	Ti350Ru600	350	600
	Ti450Ru350	450	350
	Ti450Ru450	450	450
	Ti350Ru450-WI	350	450
	Ti350Ru450-MW	350	450
	Ti350Ru350-MW	350	350
	Ti350Ru-MW	350	N/A

[a] Removal of structure-directing agent

[b] Annealing of catalyst after RuO_2 nanoparticles deposition

3. Results and discussion

3.1. Effect of calcination temperature on pure mesoporous TiO_2

The removal of the structure-directing triblock copolymer, F127, is important to obtain both mesostructured and mesoporous TiO_2 spheres. This is, however, a very delicate process due to the amorphous nature of TiO_2 at atomic level of the initially obtained mesostructured TiO_2 spheres by the aerosol process. Due to the replacement of hydrolyzable alkoxy groups by acetate groups, the degree of cross-linking of the metal gel network as well as the density of the gel network is lower than that of the pure oxide frameworks [54]. As a result, the fresh mesostructured TiO_2 is less-condensed and sustaining the mesoscopic order after removal of the organic template by thermal treatment requires a strategic approach. The temperature of the heating during the aerosol process, the residence time of the aerosol droplets across the heating zone, the amount of sample per crucible for calcination, as well as the calcination temperature and heating rate directly influence the yield of the mesoporous mesostructured TiO_2. In our system, the temperature of the heating during the aerosol process was fixed at 400 °C and the residence time of the aerosol droplets was kept constant under vacuum.

The decomposition of the F127 was analyzed by TGA (Figure 4-2). The pure F127 was mostly decomposed before 400 °C and almost completely decomposed at 600 °C (Figure 4-2 (a)). The fresh mesostructured sample was analyzed at two different conditions; up to 600 °C with heating rate of 5 °C/min and up to 350 °C with heating rate of 1 °C/min which was kept constant for 10 hours, same as the calcination condition. The decomposition temperature of F127 was observed to be shifted towards a lower temperature with a decreased heating rate. This confirmed the better efficiency of organic template removal with 1 °C/min heating rate for calcination. The total weight loss of the fresh sample was about 60 % which is consistent with the amount composition of the solution that was used in the aerosol-assisted sol-gel process. The relatively high amount of organic template allows the production of samples with high porosity. Interestingly, when the fresh sample was heated to 350 °C with 1 °C/min and kept at 350 °C for 10 hours, further weight loss was observed for 4.5 hours (Figure 4-2 (b)). This shows that slow heating rate (1 °C/min) is more efficient at removing the organic template. It further suggests that the calcination duration of 5 hours is enough to remove the organic template at maximum at a given calcination temperature.

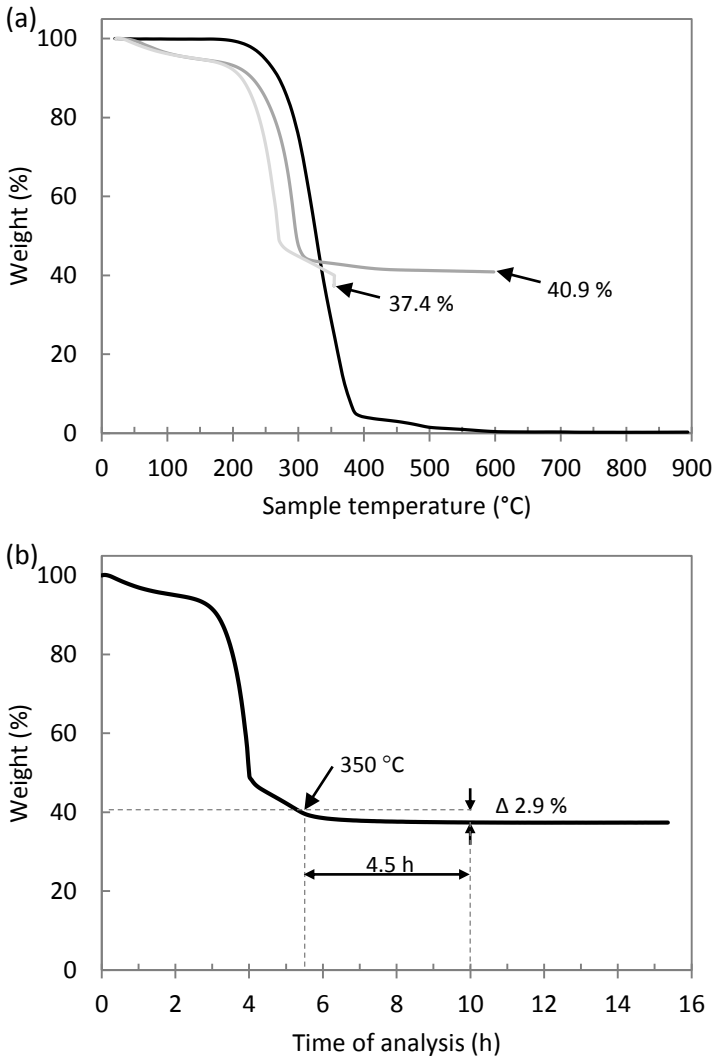

Figure 4-2: TGA curves showing sample weight loss; (a) F127 with heating rate of 10 °C/min (black), fresh sample with heating rate of 5 °C/min (grey) up to 600 °C and 1 °C/min up to 350 °C, which was kept constant for 10 h (lighter grey), and (b) fresh sample with heating rate of 1 °C/min showing the weight loss with time of analysis.

FTIR-ATR analysis was performed on selected samples: Ti350, Ti375, Ti425, and Ti450. It confirmed the removal of F127 after calcination at 350 °C and higher temperatures as the stretching vibration of C-H and C-O-C of PEO and PPO blocks at 2880 cm^{-1} and 1105 cm^{-1} disappeared (Figure 4-3) [176]. These bands are present

in non-calcined fresh mesostructured sample (Figure 4-3 (b)), as expected. The very weak peak at 2980 cm^{-1} is related to C-H asymmetric stretching [177] and can be attributed to the presence of organic residue or carbon impurity as it was also observed for commercial TiO_2-P25. The broad band around 3300 cm^{-1} and 1630 cm^{-1} are assigned to bending vibration of adsorbed water molecules [178].

The bands for Ti-O and Ti-O-Ti bonds are present in the 800 – 400 cm^{-1} region, the former being observed at a higher wavenumber than the latter [179, 180]. The broad band centered around 715 cm^{-1} and a weak band at 410 cm^{-1} are associated to Ti-O-Ti vibrations [178, 181, 182]. These bands, however, are slightly shifted towards higher wavenumber for Ti350 at 790 cm^{-1} and 440 cm^{-1}. The peak around 800 cm^{-1} is assigned to Ti-O vibration, where the oxygen atom is in the non-binding condition [183]. This can be associated with the lower degree of TiO_2 lattice formation after calcination at 350 °C compared to higher temperature-calcined samples [178, 180]. No other obvious trend was observed across the different calcination temperatures from 350 to 450 °C. However, the colour of the samples were slightly different; when Ti350 was compared to Ti425 or Ti450, Ti425 or Ti450 was whiter than Ti350 and no difference in colour was seen between Ti425 and Ti450. This suggests that 350 °C was not enough to remove the residual carbon completely.

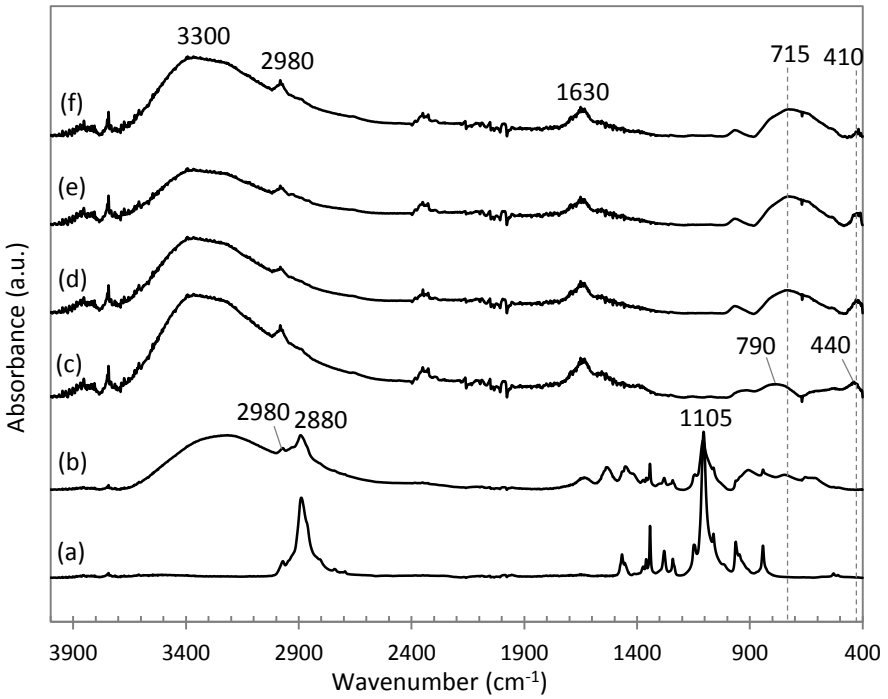

Figure 4-3: FTIR-ATR spectra of (a) F127, (b) fresh mesostructured sample, and 5x amplified spectra of (c) Ti350, (d) Ti375, (e) Ti425, and (f) Ti450; dotted lines are guide to the eyes.

The textural properties of the mesoporous TiO_2 calcined at various temperatures are summarized in Table 4-2. The calcination temperature has an important effect on the specific surface area; the specific surface area decreases with higher calcination temperature. The pore volume follows the same trend. Interestingly, the calcination temperature and specific surface area exhibited a linear correlation up to the calcination temperature of 425 °C, as shown in Figure 4-4. This demonstrates that the textural properties of the aerosol processed TiO_2 is tunable with relatively high precision. Surprisingly however, the specific surface area and pore volume are similar after calcination at 425 °C and 450 °C.

Table 4-2: Textural properties of mesoporous TiO_2 prepared by aerosol process.

Sample	SSA_{BET} (m^2g^{-1})	D_{pore} (nm)	V_{pore} (cm^3g^{-1})
Ti325	313	5.4	0.43
Ti350	262	5.4	0.36
Ti375	214	5.5	0.30
Ti400	159	6.4	0.25
Ti425	129	6.8	0.22
Ti450	132	6.8	0.23

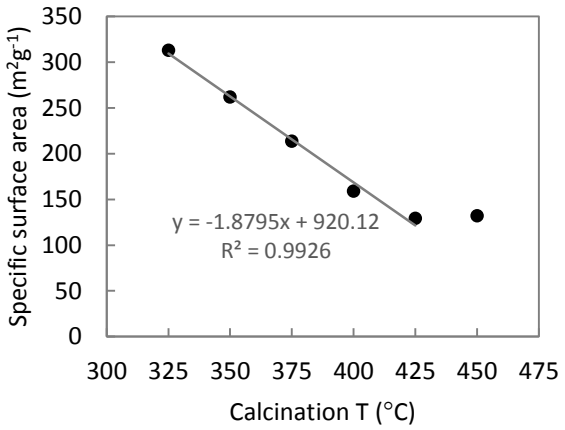

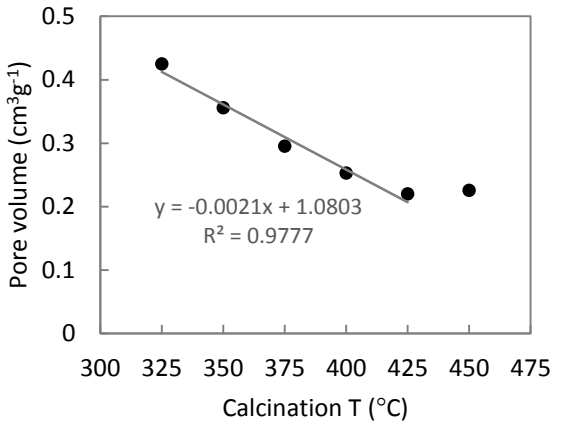

Figure 4-4: Specific surface area vs. calcination temperature (top) and total pore volume vs. calcination temperature (bottom).

The N_2 physisorption isotherms of all samples belong to type IV [184], with a characteristic hysteresis associated with the presence of open mesopores (Figure 4-5). The size of the hysteresis decreases with higher calcination temperature, as the pore volume decreases. The shape of the hysteresis loop obtained shows an

intermediate between type H1 and H2. H1 type hysteresis loop has almost vertical and parallel adsorption and desorption branches, which is associated with narrow pore size distribution. H2 type hysteresis is asymmetrical with a steeper desorption branch than the adsorption branch, which is explained as a consequence of less well-defined pore size and shape or interconnectivity of pores [185, 186].

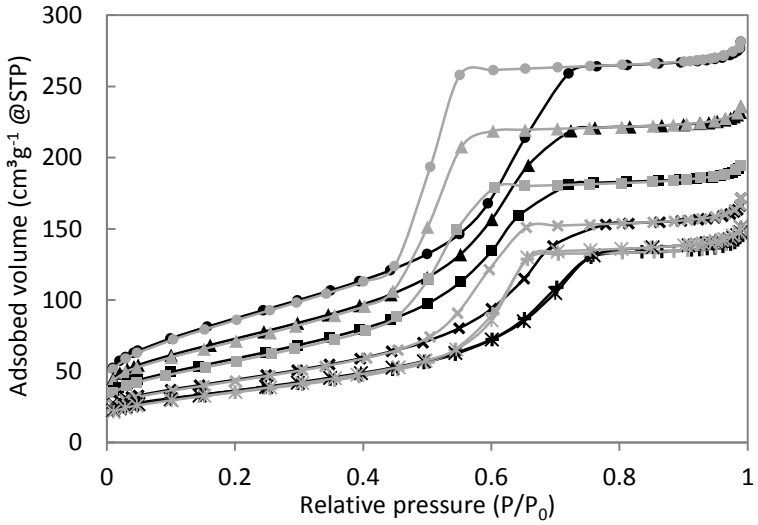

Figure 4-5: N_2 isotherms of Ti325 (●), Ti350 (▲), Ti375 (■), Ti400 (✖), Ti425 (✚), and Ti450 (✳). Adsorption isotherm is in black and desorption isotherm is in grey.

Pore size distribution was centered around 3-5 nm for the support calcined at relatively low temperature, namely between 325°C and 375°C (Figure 4-6). This size is consistent with the expected size of the micelles formed by F127. Pore volume however decreases when calcination temperature increases. The pore size distribution starts to become broader and to shift to larger size after calcination at 375 °C and higher. The pore size distribution shifts towards larger pore diameter after calcination at 400 °C and above, while the 425 °C and 450 °C stay constant, as discussed in case of the specific surface area and pore volume. This is attributed to the possible disruption of mesoscopic order in the calcination temperature range of 375 °C and 425 °C.

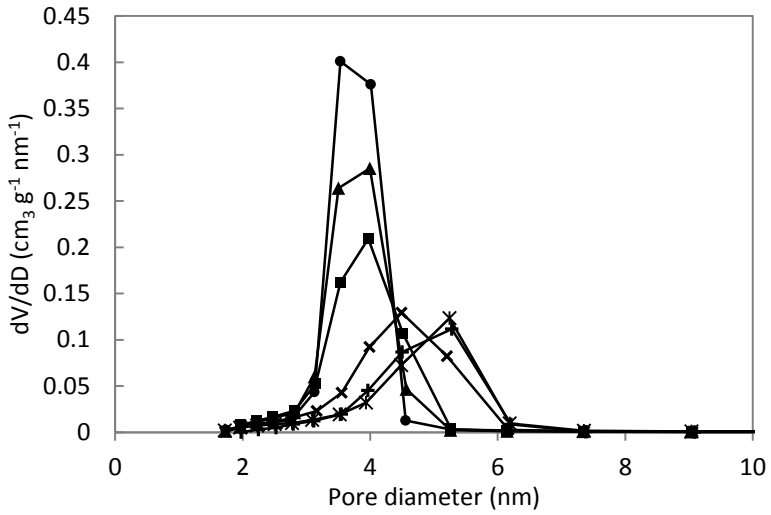

Figure 4-6: Pore size distribution of Ti325 (●), Ti350 (▲), Ti375 (■), Ti400 (✖), Ti425 (✚), and Ti450 (✳).

The TEM image of Ti350 confirmed perfectly spherical mesostructured TiO_2 particles with uniform pore size of 5 nm, thus in good agreement with N_2-physisorption measurements (Figure 4-7 (a)). The pore shape is considered to be spherical as the circular pattern of the pores from TEM images were better defined around the edges of the particles, while the pattern in the core of the particles was resembling overlapped circles. Furthermore, no specific organization of the pores was observed, but the pores were rather fully packed inside the aerosol particles, which could explain the shape of the hysteresis in N_2 physisorption isotherm. The spherical shape of the aerosol droplets was also preserved. On the other hand, Ti450 exhibited the growth of TiO_2 grains and destruction of the mesostructure, although the global shape of the aerosol droplets was fairly well-preserved (Figure 4-7 (b)). This observation is well in agreement with the textural properties.

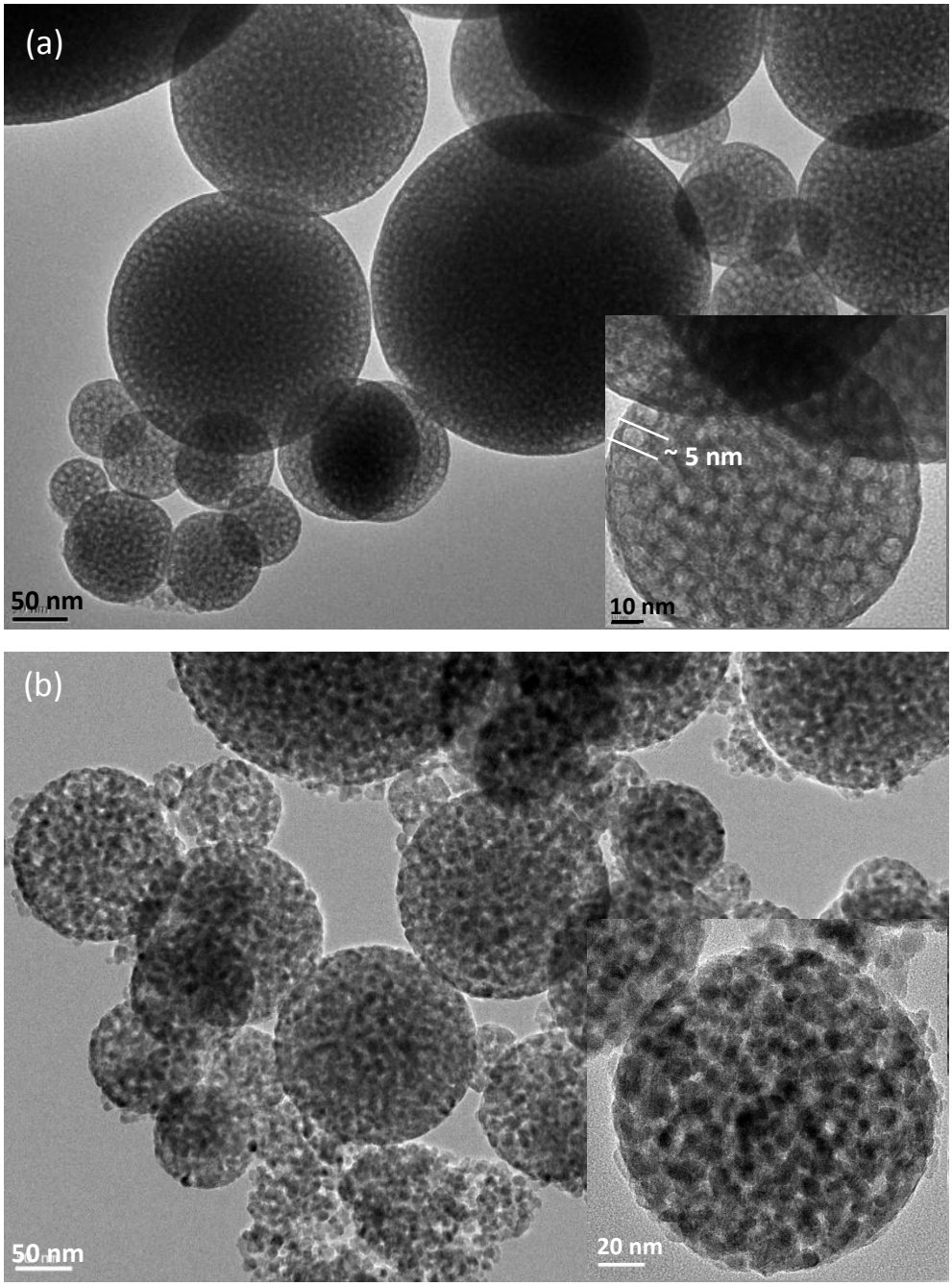

Figure 4-7: (a) TEM image of Ti350. The inset shows a zoomed-in image showing the pore size of 5 nm. (b) HRTEM image of Ti450. The inset shows a zoomed-in image showing the TiO_2 crystallites.

The XRD analysis revealed the growth of anatase phase starting at the calcination temperature of 350 °C (Figure 4-8). The crystal growth was continued up to the calcination temperature of 425 °C and stabilized at 450 °C, confirming the FTIR analysis interpretation. This could be attributed to the greater sensitivity of amorphous TiO_2 network to the thermal treatment and crystallization compared to already crystallized anatase to a certain degree, although it is anticipated that the crystallization process would be further continued towards anatase-to-rutile phase transformation at higher temperature.

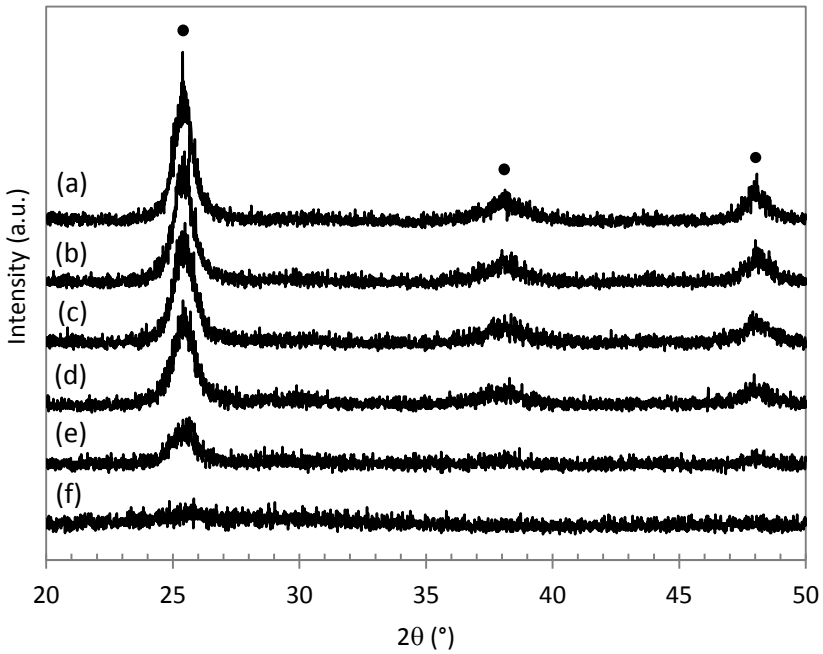

Figure 4-8: XRD patterns of (a) Ti450, (b) Ti425, (c) Ti400, (d) Ti375, (e) Ti350, and (f) Ti325. Black dots indicate anatase TiO_2 crystal planes; black dot (●) indicates anatase TiO_2 phase.

From SAXS analysis, a correlation peak which indicates the mesoscopic order in the sample was found in case of the fresh and 350 °C calcined samples, as shown in Figure 4-9. The d-spacing, which corresponds to the distance between the repeating unit, pore-to-pore or wall-to-wall distance in this case, was calculated ($d = 2\pi/q$) to be 11.4 nm and 8.4 nm for the fresh sample and Ti350, respectively. The decrease in the d-spacing after calcination is attributed to the shrinkage due to the increased density of the TiO_2 network. Based on the pore diameter observed by TEM and N_2 physisorption analysis for Ti350 (approximately 5 nm), the TiO_2 wall

thickness is estimated to be approximately 3 nm. On the other hand, no correlation peak was observed after calcination at 375 °C up to 450 °C. This indicates the destruction of the mesostructure due to the growth of anatase phase.

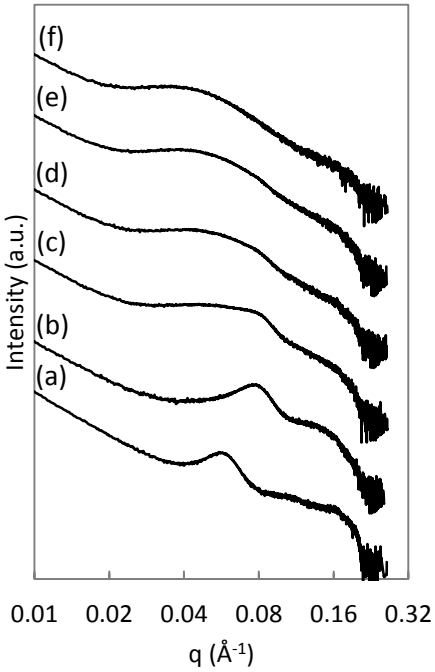

Figure 4-9: SAXS patterns of (a) fresh sample, (b) Ti350, (c) Ti375, (d) Ti400, (e) Ti425, and (f) Ti450. The wave vector, q, is defined as (4π*sinϑ)/λ, where 2ϑ is the scattering angle.

Overall, the employed process leads to spherical TiO_2 particles with mesopores released by the efficient removal of the surfactant. The calcination temperature can be seen as a tool to tune both the textural properties and the crystallinity of the support, and this can be tentatively exploited in the study of Ru/TiO_2 methanation catalysts.

3.2. Effect of surface area of mesoporous TiO_2 on RuO_2 supported catalysts

The mesoporous TiO_2 with two distinct specific surface areas (Ti350 and Ti450) were chosen as supports for RuO_2 nanoparticles. In order to activate the catalysts in CO_2 methanation, the resulting catalysts were further annealed at two different temperatures, 350 °C and 450 °C.

The textural properties of starting mesoporous TiO_2 and the RuO_2 supported catalysts are presented in Table 4-3. After RuO_2 deposition and annealing, the

specific surface areas and pore volumes of the catalysts decreased compared to the starting TiO_2. This implies that the presence of RuO_2 nanoparticles or the presence of RuO_2 nanoparticles in aqueous medium combined with further annealing affects the mesoscopic order of the starting TiO_2, even when the annealing temperature of the catalysts was the same as the calcination temperature of the pure mesoporous TiO_2. As the change in the textural properties is significant, this disruption is not only due to the presence of the RuO_2 nanoparticles but also attributed to further crystallization of the TiO_2 network.

Indeed, the decrease in the specific surface area and pore volume, as well as the change in the pore diameter were greater when the calcination temperature of the mesoporous TiO_2 was lower than the annealing temperature of the catalyst. This relation is also shown in the N_2 physisorption isotherms in Figure 4-10 and 4-11. The cumulative volume of adsorbed N_2 as well as the size of the hysteresis loop were decreased to a greater degree for the annealing temperature higher than the calcination temperature. The shape of the hysteresis loop did not show any significant evolution before and after RuO_2 deposition with annealing, which shows that the shape of the pores is somewhat preserved.

Table 4-3: Textural properties of starting mesoporous TiO_2 as a support and RuO_2 supported catalysts; (a) catalysts annealed at 350 °C and (b) catalysts annealed at 450 °C.

(a) **Sample**	**Calcination[a] T (°C)**	**Annealing[b] T (°C)**	**SSA_{BET} (m^2g^{-1})**	**V_{pore} (cm^3g^{-1})**	**D_{pore} (nm)**
Ti350	350	N/A	262	0.36	5.4
Ti350Ru350	350	350	166	0.28	6.7
Ti450	450	N/A	132	0.23	6.8
Ti450Ru350	450	350	108	0.17	6.2

(b) **Sample**	**Calcination[a] T (°C)**	**Annealing[b] T (°C)**	**SSA_{BET} (m^2g^{-1})**	**V_{pore} (cm^3g^{-1})**	**D_{pore} (nm)**
Ti350	350	N/A	262	0.36	5.4
Ti350Ru450	350	450	112	0.24	8.7
Ti450	450	N/A	132	0.23	6.8
Ti450Ru450	450	450	94	0.17	7.2

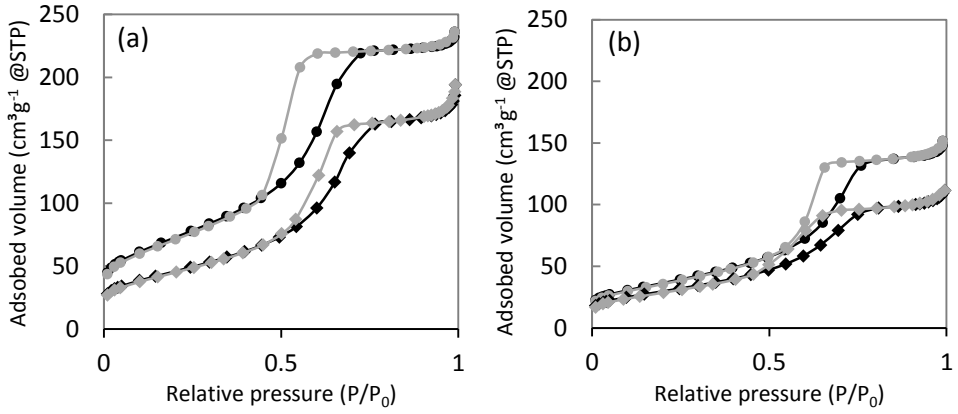

Figure 4-10: N_2 physisorption isotherms of (a) Ti350 (●) and Ti350Ru350 (◆), and (b) Ti450 (●) and Ti450Ru350 (◆). Adsorption isotherm is in black and desorption isotherm is in grey.

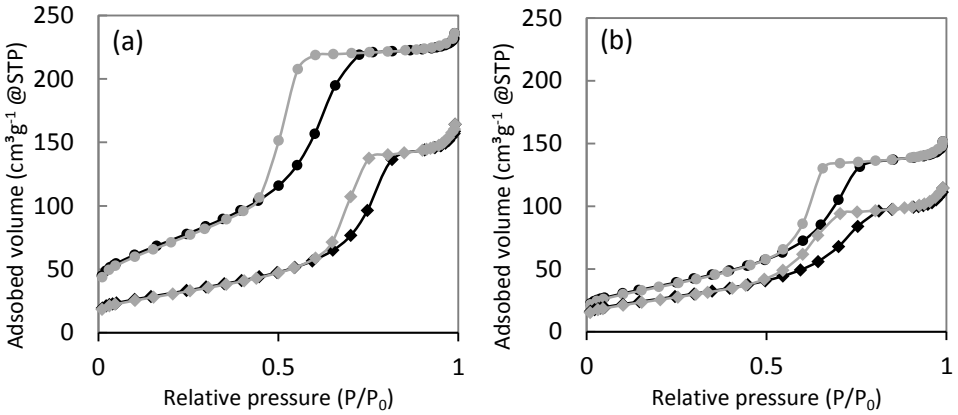

Figure 4-11: N_2 physisorption isotherms of (a) Ti350 (●) and Ti350Ru450 (◆), and (b) Ti450 (●) and Ti450Ru450 (◆). Adsorption isotherm is in black and desorption isotherm is in grey.

The methane production rates, expressed in both per gram of catalyst and per mole of Ru (measured by ICP-AES), are shown in Figure 4-12 for 350 °C annealing and Figure 4-13 for 450 °C annealing. For both annealing temperatures, there was no impact of the specific surface area of the starting mesoporous TiO_2. The extent of surface area decrease from 262 m^2g^{-1} (Ti350) to 166 m^2g^{-1} (Ti350Ru350) and 132 m^2g^{-1} (Ti450) and 108 m^2g^{-1} (Ti450Ru350) resulted in the same methane production rate. As discussed in previous chapters, annealing at 450 °C resulted in higher catalytic activity compared to 350 °C. Again, the same methane production rate was obtained for the catalysts annealed at 450 °C but based on supports calcined

at different temperature (thus with different specific surface area (from 262 m^2g^{-1} (Ti350) to 112 m^2g^{-1} (Ti350Ru450) and 132 m^2g^{-1} (Ti450) to 94 m^2g^{-1} (Ti450Ru450)). This suggests that the high surface area is not a decisive or limiting factor in the studied catalysts. This is not surprizing considering the low (2.2 wt. %) Ru loading, and it appears reasonable that not all the surface is utilized to disperse the Ru nanoparticles, even on the supports with the lowest surface area (94 m^2g^{-1} in this case).

For reference, the catalytic activities of the mesoporous TiO_2 supported catalysts are compared with P25 supported catalyst; P25 supported catalyst still shows higher catalytic activities (at 200 °C, 2.6 $\mu mol_{CH4}\ g_{cat}^{-1}\ s^{-1}$ and 1.1 $\mu mol_{CH4}\ \mu mol_{Ru}^{-1}\ s^{-1}$ (x100). This suggests that high surface area and porosity of TiO_2 support is not a decisive factor for an improved catalytic activity of Ru-based catalysts.

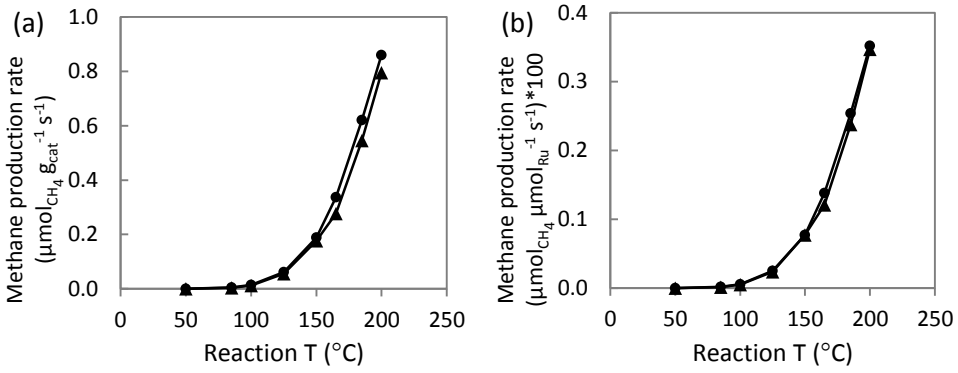

Figure 4-12: Comparison of methane production rate after annealing at 350 °C; (a) Ti350Ru350 (●) and Ti450Ru350 (▲) per gram of catalyst, and (b) Ti350Ru350 (●) and Ti450Ru350 (▲) per mole of Ru determined by ICP-AES.

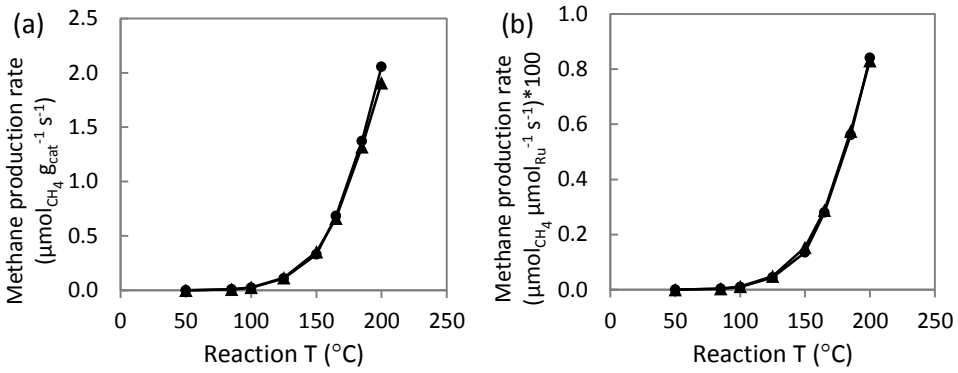

Figure 4-13: Comparison of methane production rates after annealing at 450 °C; (a) Ti350Ru450 (●) and Ti450Ru450 (▲) per gram of catalyst, and (b) Ti350Ru450 (●) and Ti450Ru450 (▲) per mole of Ru determined by ICP-AES.

On the other hand, the Ru dispersions of Ti350Ru450 (10.1%) and Ti450Ru450 (4.2%) were found to be divergent. This means that the starting mesoporous TiO_2 with higher surface area with defined pore size (5 nm) and less crystalline was better at dispersing the Ru-species and that the Ru-species are more likely to be inside the pores. Given that the two catalysts with different specific surface areas (262 m^2g^{-1} vs. 132 m^2g^{-1}) of the starting TiO_2 support gave the same methanation activity with the same activation energy (16.4 kcal), the higher dispersion did not help improve the specific catalytic activity; i.e. methanation production rate normalized per surface Ru atom or TOF is higher for less dispersed Ru. Yet, the fact that catalysts with the difference in Ru dispersion by 2 folds have the same specific catalytic activity could be questioned. As a matter of fact, the H_2 chemisorption measurement was only done once thus one should keep in mind the possible large error bars. With that in mind, the deviation in Ru dispersion values may come closer. However, the difference in Ru dispersion values could be qualitatively related to XRD analysis. The XRD patterns for Ti350Ru450 and Ti450Ru450 before in situ reduction and methanation are shown in Figure 4-14. The shifted RuO_2 (110) and (101) peaks are observed for Ti350Ru450 which is attributed to the formation of epitaxial RuO_2-rutile TiO_2 phase. On the other hand, distinguished (110) and (101) peaks of RuO_2 and rutile TiO_2 are observed for Ti450Ru450. Specifically, the peak positions of (110) and (101) RuO_2 peaks were un-shifted, which indicates sintered and crystallized RuO_2. These observations qualitatively prove the lower Ru dispersion of Ti450Ru450 as it was obtained by H_2 chemisorption analysis. On the other hand, XPS analysis of the catalyst before reduction and methanation reaction showed higher Ru/Ti ratio for Ti450Ru450 compared to Ti350Ru450 (Table 4-4).

This could be attributed to the more exposed surface Ru species of Ti450Ru450 although crystalline RuO_2 is present. The epitaxial RuO_2-rutile TiO_2 present in the Ti350Ru450 is possibly inside the pores, giving rise to the less exposed surface Ru species. However, XPS analysis on porous material may contain artifacts which make the interpretation non-conclusive.

It should be noted that the XRD and XPS analysis were carried out on catalysts prior to reduction and methanation. Indeed, it was demonstrated in Chapter 1 from TEM analysis that the RuO_2 crystals are being transformed into smaller Ru particles after reduction and methanation. Nevertheless, the XPS analysis in Chapter 1 confirmed that the Ru/Ti ratios before and after reduction and methanation were similar. These results indicates that the Ru species after reduction and methanation stay agglomerated although the RuO_2 particles go through shape and size transformation to be reduced. It further suggests that the Ru dispersion is qualitatively higher for Ti350Ru450 than Ti450Ru450.

On the basis of these results, several possible conclusions can be drawn. First, the better dispersed Ru particles converts more CO_2 to produce CH_4. Second, the lower Ru dispersion means more agglomerated Ru particles and these localized Ru particles convers CO_2 to produce CH_4 at a higher rate. Third, the degree of TiO_2 support crystallinity and pore volume in forming more or less dispersed Ru particles should not be ignored.

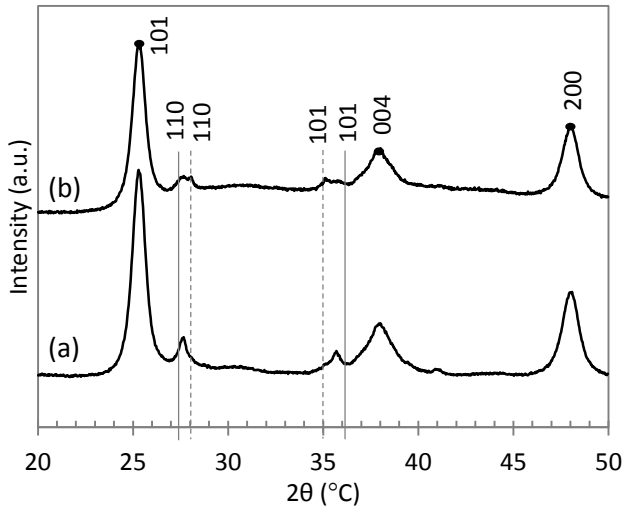

Figure 4-14: XRD patterns of (a) Ti350Ru450 and (b) Ti450Ru450; black dot (●) indicates anatase TiO_2 phase, solid grey line indicates rutile TiO_2 phase, and dotted line indicates RuO_2 phase.

Table 4-4: XPS analysis results displaying surface mole fraction (%) of elements.

Sample	O 1s	Ti $2p_{3/2}$	C 1s	Ru $3d_{5/2}$	Ru/Ti
Ti350Ru450	55.6	19.7	24.1	0.5	0.026
Ti450Ru450	57.0	20.3	21.8	0.9	0.045

3.3. Effect of catalyst annealing temperature

The mesoporous TiO_2 obtained after calcination at 350 °C (Ti350) was chosen as a starting support for RuO_2 nanoparticles since it maintained the mesostructure with well-defined pore size without significant crystal growth after calcination. The methane production rates for the catalysts annealed at various temperatures are shown in Figure 4-15. The methanation production rate reached its maximum after annealing of the catalysts at 400 °C and 450 °C (the difference is negligible), and decreased after annealing at 500 °C or higher temperature (The same behaviour is seen with different crystalline TiO_2 supports in chapter 1).

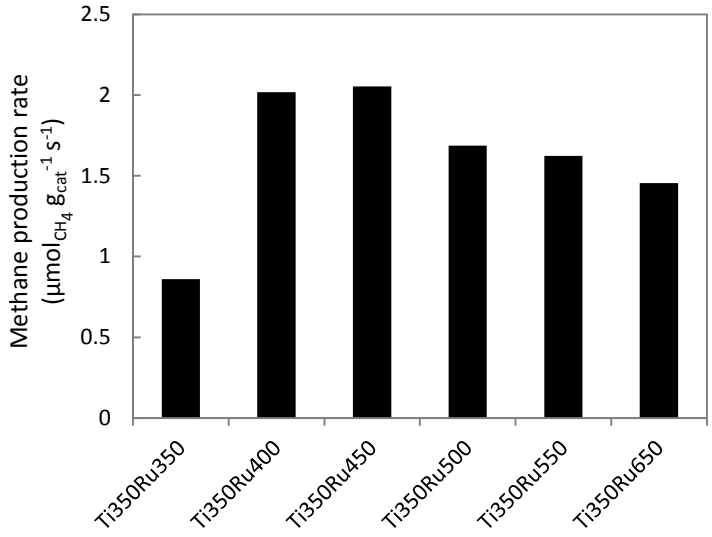

Figure 4-15: Comparison of methane production rates of Ru-supported mesoporous TiO_2 annealed at various temperatures.

The textural properties of the catalysts annealed at various temperatures were modified, as shown in Table 4-5 and Figure 4-16. As expected, the surface area and the pore volume decreased with higher annealing temperatures, whereas the average pore diameter was increased which indicates the progressive destruction of the mesoscopic order. All catalysts presented type IV isotherms characteristic of

mesoporous materials, maintaining the shape of the hysteresis loop, although the specific surface area decreased drastically from the starting Ti350 by 9 folds after annealing at 650 °C.

The N_2 physisorption analysis after in situ reduction and methanation was carried out on Ti350Ru350, Ti350Ru450, and Ti350Ru650. Generally, the textural properties of the catalysts after reduction and methanation remained nearly unchanged.

Table 4-5: Textural properties of mesoporous TiO_2 supported Ru-based catalysts.

Sample	SSA_{BET} (m^2g^{-1})	D_{pore} (nm)	V_{pore} (cm^3g^{-1})
Ti350	262	5.4	0.36
Ti350Ru350	166	6.7	0.28
Ti350Ru350-after test	156	6.6	0.26
Ti350Ru450	112	8.7	0.24
Ti350Ru450-after test	111	8.6	0.24
Ti350Ru550	69	11.0	0.19
Ti350Ru650	29	17.7	0.13
Ti350Ru650-after test	31	16.1	0.13

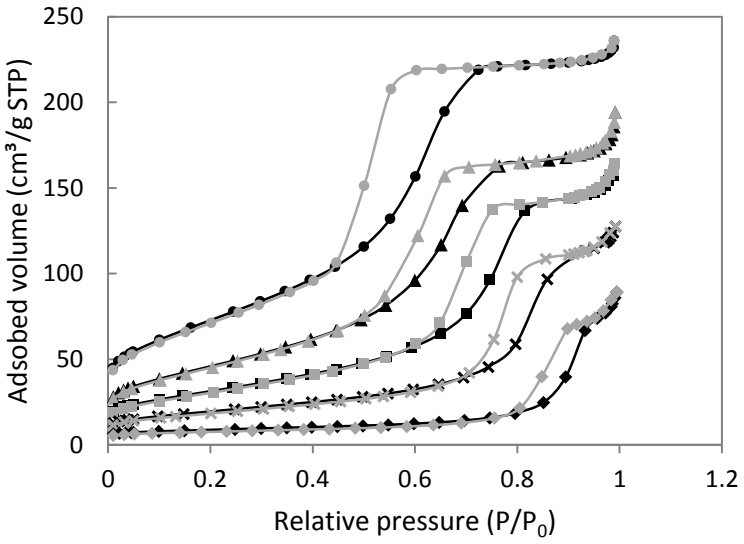

Figure 4-16: N_2 isotherms of Ti350 (●), Ti350Ru350 (▲), Ti350Ru450 (■), Ti35oRu550 (✖), and Ti350Ru650 (◆). Adsorption isotherm is in black and desorption isotherm is in grey.

FTIR-ATR analysis after RuO_2 deposition and further annealing is shown in Figure 4-17. The weak bands around 2980 cm^{-1} remained even after RuO_2 deposition and further annealing, which can be related to carbonaceous impurity. The weak bands in the 800 – 400 cm^{-1} range became more prevalent for the further annealed catalysts compared to Ti350. Specifically, the maxima of the peaks at 790 cm^{-1} and 440 cm^{-1} shifted towards lower wavenumber, which can be attributed to the strengthened TiO_2 network as previously discussed in the section 3.1 [178, 180].

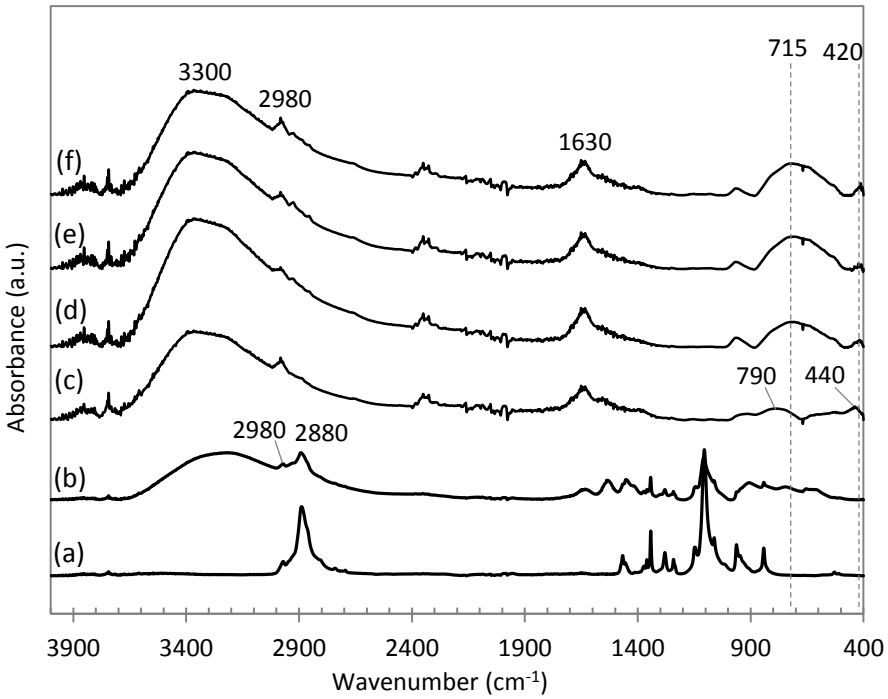

Figure 4-17: FTIR-ATR spectra of (a) F127, (b) fresh mesostructured sample, and 5x amplified spectra of (c) Ti350, (d) Ti350Ru350, (e) Ti350Ru400, and (f) Ti350Ru450; dotted lines are guide to the eyes.

The XRD patterns in Figure 4-18 show the further crystallization and growth of the anatase phase of the TiO_2 support with annealing in presence of RuO_2. Interestingly, the appearance of (110) and (101) rutile TiO_2 peaks was seen starting at the annealing temperature as low as 250 °C. As the epitaxial growth of RuO_2 on rutile TiO_2 was observed in chapter 1, the opposite phenomenon had occurred on nearly amorphous TiO_2 which was transformed into epitaxial rutile TiO_2 in close proximity to the RuO_2 phase. This phenomenon is also previously reported for the fabrication of RuO_2-TiO_2 films, for the growth of rutile TiO_2 layer using the RuO_2 as a seed layer

[187, 188]. In our system, it was verified that the rutile TiO_2 phase did not form without the presence of RuO_2, when the Ti350 was further annealed at 550 °C for 4 h with heating rate of 1 °C/min, at the same condition as Ti350Ru550 (XRD pattern not shown).

The peaks were deconvoluted to obtain more precise positions and widths of the peaks (Table 4-6). The deconvolution of the (110) and (101) RuO_2 peaks was only possible after annealing at 450 °C and higher temperatures due to the low intensity of the peaks. The evolution of peak positions for RuO_2 and rutile TiO_2 was represented as a difference between the (110) and (101) peak positions (Figure 4-19). Interestingly, the positions of RuO_2 peaks remained constant while the positions of rutile TiO_2 peaks, which was originally closer to RuO_2 peak positions, evolved towards the expected positions with increasing annealing temperature. This phenomenon is a proof that the rutile TiO_2 formation was indeed seeded by the presence of RuO_2 on nearly amorphous TiO_2. The deconvolution of XRD patterns in Figure 4-20 show the evolution of (101) TiO_2 peak position with increasing annealing temperature; the (101) TiO_2 peak position moves from the side of (101) RuO_2 peak position towards the theoretical (101) TiO_2 peak position, indicating that the epitaxial relation between (101) TiO_2 and (101) RuO_2 becomes weaker with increasing annealing temperature.

The Scherrer calculation resulted in the growth RuO_2 crystallite size with increased annealing temperature; 29 nm (Ti350Ru450), 38 nm (Ti350Ru550), to 68 nm (Ti350Ru650) for (110) RuO_2 and 12 nm (Ti350Ru350), 13 nm (Ti350Ru450), 12 nm (Ti350Ru550), to 22 nm (Ti350Ru650) for (101) RuO_2.

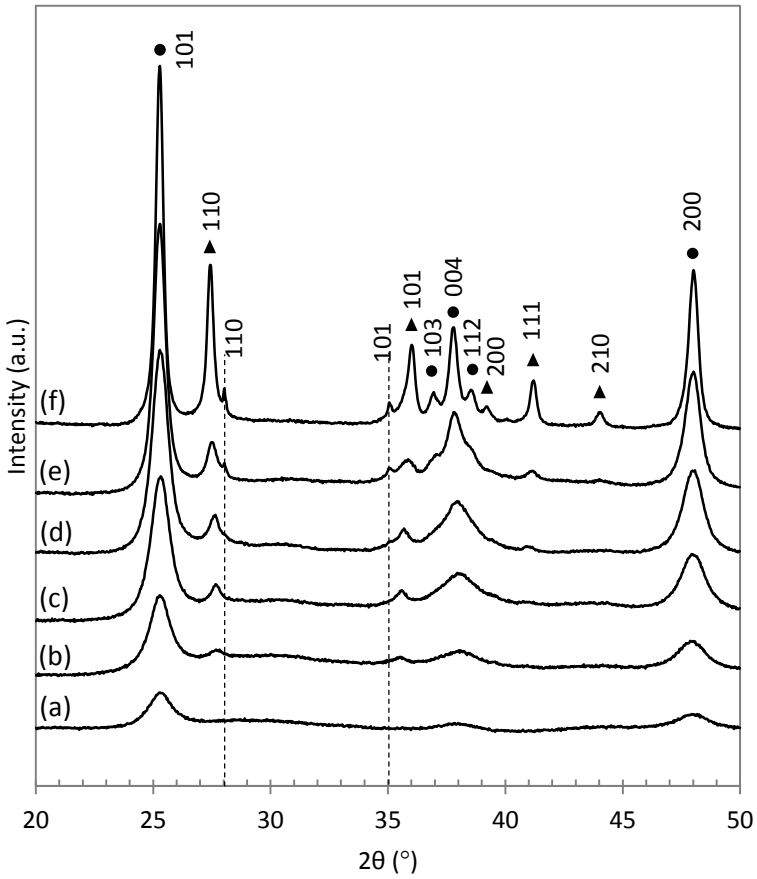

Figure 4-18: XRD patterns of (a) Ti350, (b) Ti350Ru250, (c) Ti350Ru350, (d) Ti350Ru450, (e) Ti350Ru550, and (f) Ti350Ru650; rutile TiO_2 (▲), anatase TiO_2 (●), and rutile RuO_2 (drawn as dotted lines) peak positions.

*Table 4-6: Positions (2ϑ) and widths (FWHM) main TiO_2 and RuO_2 peaks obtained after deconvolution.**

phase	hkl	Ti350Ru250		Ti350Ru350		Ti350Ru450		Ti350Ru550		Ti350Ru650	
		2 θ (°)	FWHM (°)	2 θ (°)	FWHM (°)	2 θ (°)	FWHM (°)	2 θ (°)	FWHM (°)	2 θ (°)	FWHM (°)
anatase	**101**	25.260	0.666	25.281	0.987	25.279	0.827	25.255	0.597	25.248	0.359
rutile	**110**	27.675	0.599	27.662	0.472	27.584	0.497	27.490	0.535	27.415	0.331
RuO_2	**110**					28.077	0.283	28.024	0.217	28.017	0.125
RuO_2	**101**			34.963	0.709	35.090	0.643	35.065	0.671	35.047	0.385
rutile	**101**	35.450	0.662	35.539	0.546	35.656	0.494	35.802	0.672	36.001	0.264
anatase	**103**	37.218	1.894	37.236	1.534	36.994	0.965	36.938	0.604	36.916	0.396
anatase	**004**	38.122	1.468	38.020	1.471	37.894	1.208	37.807	0.751	37.761	0.417
anatase	**112**	39.563	1.449	38.719	0.966	38.571	1.124	38.504	0.659	38.526	0.412
rutile	**200**			39.495	0.682	39.515	0.617	39.373	1.275	39.195	0.355

* RuO_2 peaks could not be deconvoluted for Ti350Ru250 (both 110 and 101) and Ti350Ru350 (110) due to the low crystallinity.

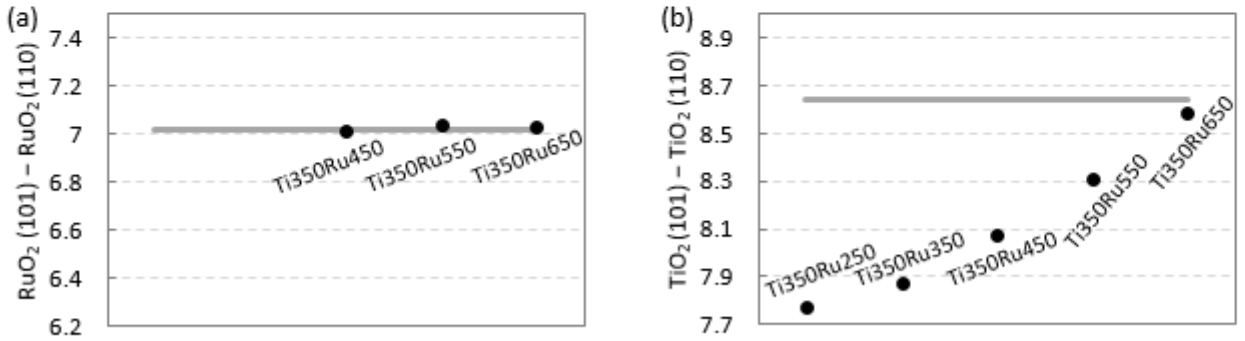

Figure 4-19: The difference between 101 and 110 peak positions for (a) RuO_2 and (b) rutile TiO_2. The grey lines represent the expected values based on ICDD 01-070-2662 for RuO_2 and ICDD 00-021-1276 for TiO_2.

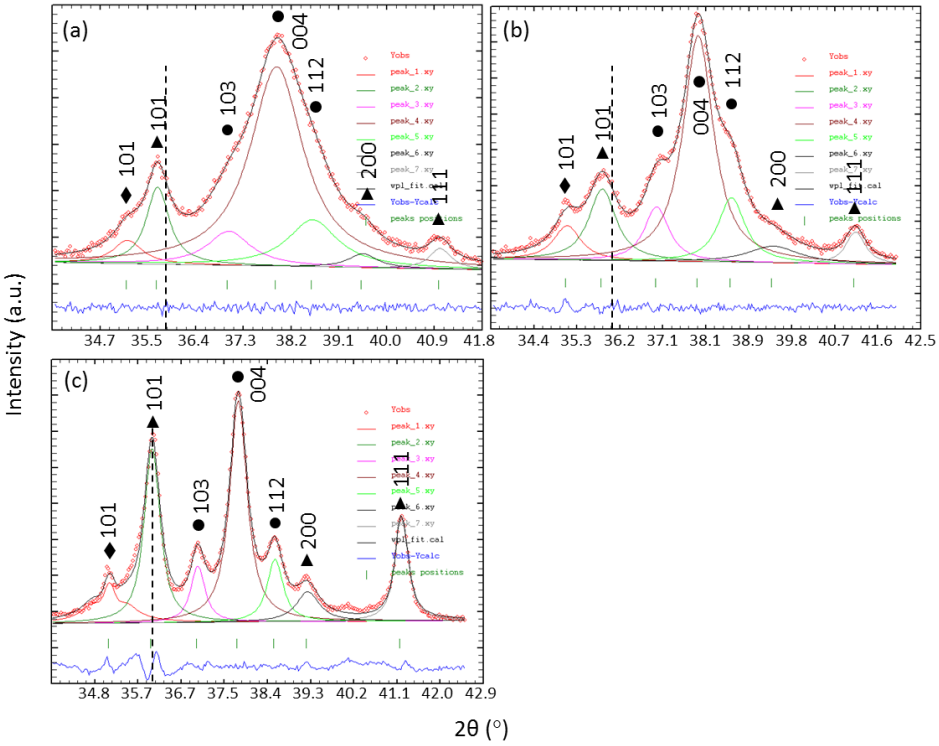

Figure 4-20: Deconvoluted RuO_2 (♦), rutile TiO_2 (▲), anatase TiO_2 (●) peaks in the 2θ range of 34° – 42°; (a) Ti350Ru450, (b) Ti350Ru550, (c) Ti350Ru650. Black dotted lines indicate theoretical (101) TiO_2 peak position.

The cross-sectional HRTEM analysis after methanation for Ru350Ti350 revealed that the Ru species successfully diffused inside the pores (Figure 4-21(a)). This suggests that the RuO_2 NPs were inside the pores prior to annealing and that Ru-species are likely to be inside the TiO_2 spheres formed by the aerosol droplets after annealing at all temperatures. The low crystalline mesoporous TiO_2 support is considered to have prevented the sintering of the Ru-species to certain degree thanks to the interaction between the TiO_2 and RuO_2 (i.e. RuO_2 inside the pores and stabilization via epitaxial lattice matching), although Ru aggregates up to about 40 nm were observed. The non-cross-sectional HRTEM image of Ru350Ti450 also showed that the Ru species are always present with TiO_2 support, but not separated from TiO_2 (Figure 4-21 (b)). Rutile TiO_2 phase was observed in close proximity to Ru species, confirming the XRD analysis.

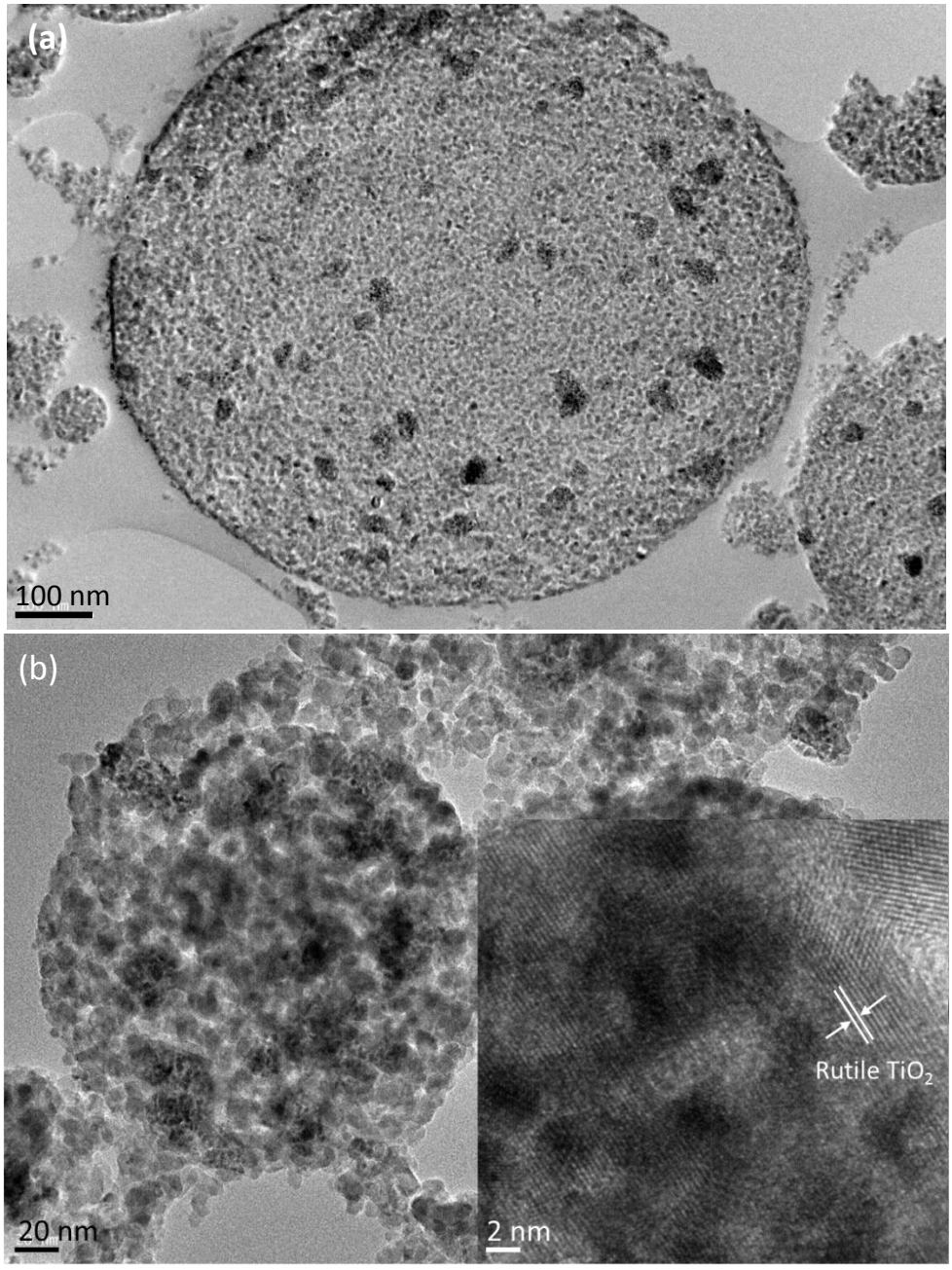

Figure 4-21: (a) Cross-sectional HRTEM image of Ti350Ru350 and (b) HRTEM image of Ti350Ru450. The inset shows a zoomed image showing the crystal planes of rutile TiO_2.

TPR experiments are carried out on Ti350Ru350, Ti350Ru450, and Ti350Ru500 to examine any relation to the increased (from Ti350Ru350 to Ti350Ru450) or decreased (from Ti450Ru450 to Ti350Ru550) catalytic activities. The shape of the reduction profile was different for the three catalysts as shown in Figure 4-22. The reduction peak around 125 °C for Ti350Ru350 is attributed to the reduction of $RuCl_3$ [189], which points out that Ru^{3+} species are still present after annealing at 350 °C. The global reduction event tends to shift towards higher temperatures with higher annealing temperature, which could be attributed to more difficult reducibility due to the stronger interaction between RuO_2 and TiO_2. Although TPR analysis do not directly reveal the difference in catalytic performances of these catalysts, it is anticipated that the Ru reduced from oxidized species results in higher catalytic activity. Furthermore, it is possible that there is an optimal degree of RuO_2-TiO_2 interactions.

Ru dispersion values of Ti350Ru450 and Ti350Ru550 were determined by H_2 chemisorption to obtain qualitative relation between Ru dispersion and the activity drop after annealing at 500 and above. The Ru dispersion was found to be 4.7% for Ti350Ru450 and 4.3% for Ti350Ru550. This means that the decrease in catalytic activity after annealing at 550 °C is not primarily due to Ru dispersion.

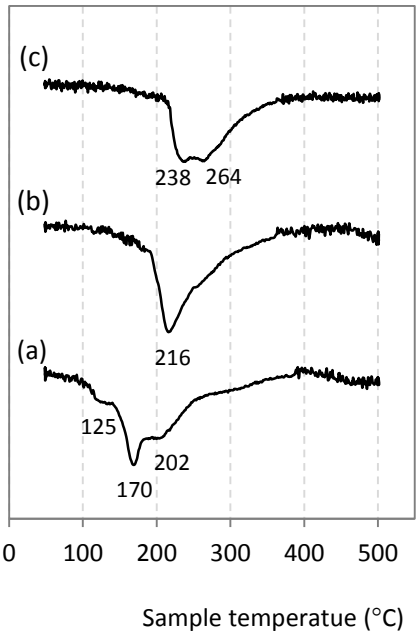

Figure 4-22: H_2-TPR of (a) Ti350Ru350, (b) Ti350Ru450, and (c) Ti350Ru500.

3.4. Measuring true intrinsic activity?

It is important to verify that the levels of activity correspond to the intrinsic activity of the catalysts and are not biased by physical (diffusion) or thermodynamic limitations.

Since activation energy (Ea) was always ~15 kcal/mol in the course of the thesis and also here in the vase of mesoporous supports, internal diffusion limitation can be excluded (lower activation energies – typically half of Ea from chemical kinetics– are expected in such case). Also, external limitations are avoided by selecting a relatively small particles size (and also lower activation energies (< 5 kcal/mol) are expected in such case). Catalysts are systematically ground and sieved in the 100-315 µm range. It was not verified experimentally that this range is indeed suitable in the conditions used here, but we rely on previous (unpublished) validations tests performed in the laboratory (thesis of Alejandro Karelovic), as well as on our practical know-how to consider that external diffusional limitations are unlikely.

In order to examine whether the activity is not underestimated by thermodynamic limitations – i.e. when approaching the equilibrium, the turnover slows down – a catalytic test was repeated with half the mass used for the initial catalytic test for Ti350Ru350. In these conditions, CO_2 conversion was exactly divided by two. In other words, the specific activity (or rate) was the same (Figure 4-23). This clarifies that the reported levels of activity truly correspond to intrinsic activity levels and are not biased by thermodynamic limitation. As a reminder, the equilibrium at 200 °C corresponds to ~ 100 % CO_2 conversion, while the rate measured here at 200 °C corresponds to 12.6 % (200 mg catalyst) and 6.7 % (100 mg catalyst) conversion.

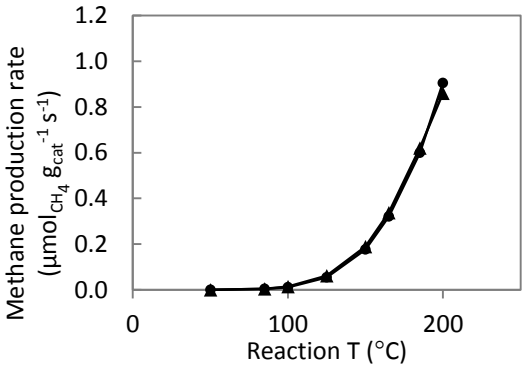

Figure 4-23: Comparison of methane production rates of Ti350Ru350 tested with different mass; 200 mg (●) and 100 mg (▲).

3.5. Effect of Ru incorporation method

Different catalyst preparation methods using Ti350 as a support are employed and compared. First, the catalyst was prepared by deposition of pre-synthesized RuO_2 NPs, as discussed earlier in this chapter. Second, the catalyst was prepared by wet impregnation of aqueous solution of dissolved $RuCl_3$ salt, which is widely used to prepare metal nanoparticles in preparation of supported catalysts. Third, the catalyst was prepared by incipient wetness impregnation of aqueous solution of $RuCl_3$ followed by microwave treatment to form RuO_2 particles. The incipient wetness impregnation, also called capillary impregnation or dry impregnation, is a commonly used technique in preparation of supported catalysts. In this method, the volume of the metal precursor dissolved in aqueous solution corresponding to the pore volume of the support is added and the solution is drawn into the pores by capillary action. The catalyst is then calcined to deposit the metal on the support.

In the current study, the catalyst prepared by incipient wetness impregnation of $RuCl_3$ solution was treated by microwave in the aim of forming RuO_2 particles with high energy in a short time without destroying the pore structure of the support. In doing so, first, the formation of RuO_2 phase was confirmed by XRD analysis (Figure 4-24) after treating a concentrated pure $RuCl_3$ solution ([Ru]= 0.6 M) in microwave at 200 °C for 30 min. The catalysts preparation was then proceeded by incipient wetness impregnation of $RuCl_3$ solution of same Ru concentration used to confirm the RuO_2 phase and immersing the resulting powder in toluene to ensure no diffusion of water outside of pore during the microwave treatment. However, since toluene does not absorb microwave radiation, a SiC bar was dropped in the toluene containing the catalyst to help raise and maintain the temperature during the microwave treatment.

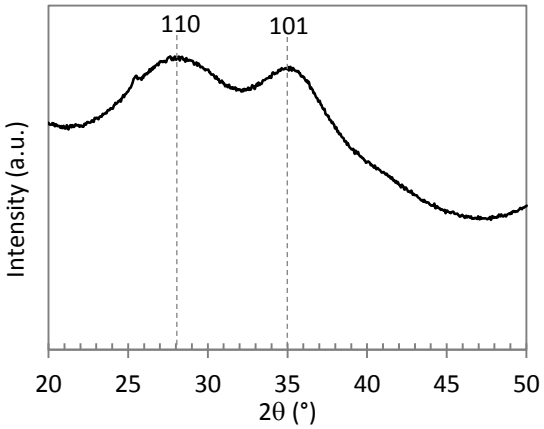

Figure 4-24: XRD pattern of RuO_2 prepared by microwave; dotted line indicates RuO_2 phase.

The textural properties of the catalysts prepared by different Ru incorporation methods are summarized in Table 4-7. The RuO_2 deposition (Ti350Ru450) and $RuCl_3$ wet impregnation (Ti350Ru450-WI) showed similar textural properties. The textural properties of the microwave treated catalyst after annealing at 450 °C (Ti350Ru450-MW), on the other hand, was relatively more disturbed.

For reference, the microwave treated catalysts before annealing (Ti350RuBA-MW) and after annealing at 350 °C (Ti350Ru350-MW) were also compared. The surface area and pore volume of the catalyst were found to be affected by the microwave reatment alone. This could be attributed to the growth of RuO_2 phase. After further annealing at 350 °C, the textural properties were greatly affected.

Table 4-7: Comparison of textural properties of catalysts prepared by different Ru incorporation methods.

Sample	SSA_{BET} (m^2g^{-1})	V_{pore} (cm^3g^{-1})	D_{pore} (nm)
Ti350	262	0.36	5.4
Ti350Ru450	112	0.24	8.7
Ti350Ru450-WI	114	0.23	8.1
Ti350Ru450-MW	87	0.24	10.9
Ti350Ru350-MW	103	0.25	9.6
Ti350RuBA-MW	211	0.30	5.6

The XRD patterns in Figure 4-25 showed that the growth of RuO_2 phase was apparent for Ti350Ru450-MW as un-shifted (110) and (101) RuO_2 peaks were observed (Figure 4-25 (d)). These peaks were less pronounced for Ti350Ru450 and

Ti350Ru450-WI. For Ti350-Ru450-WI, the (110) and (101) peak positions were in-between RuO_2 and rutile TiO_2 positions, which indicates the stabilized RuO_2 phase on rutile TiO_2 by formation of epitaxial phase.

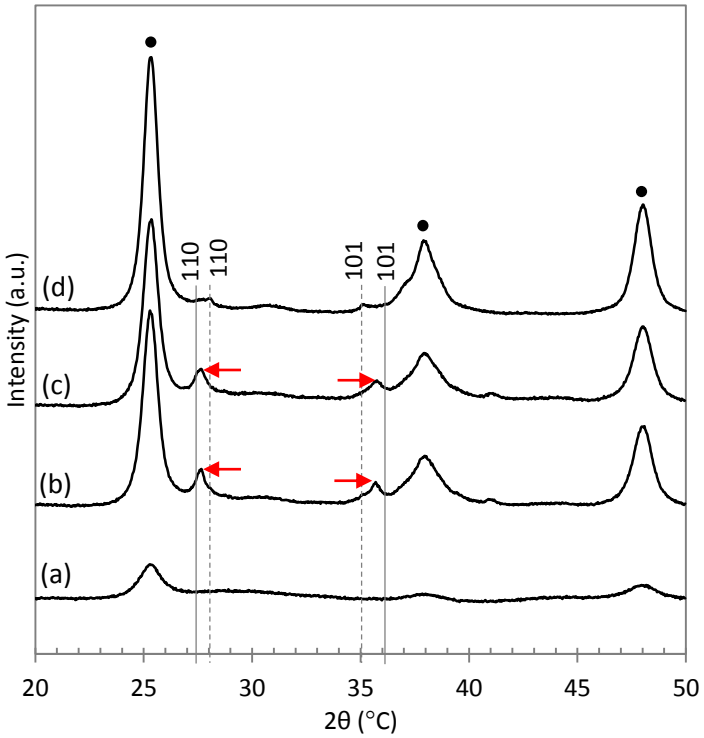

Figure 4-25: XRD patterns of (a) Ti350, (b) Ti350Ru450, (c) Ti350Ru450-WI, and (d) Ti350Ru450-MW; black dot (●) indicates anatase TiO_2 phase, solid grey line indicates rutile TiO_2 phase, and dotted line indicates RuO_2 phase.

The catalytic activities were compared as shown in Figure 4-26; Ti350Ru450 > Ti350Ru450-WI > Ti350Ru450-MW, in decreasing order.

As a reference, the catalytic activities of the microwave treated samples followed by annealing at lower temperatures than 450 °C (350 °C and 250 °C) were found to be lower than Ti350Ru450-MW (not shown). Furthermore, when the support, Ti350, was replaced by P25 and followed the same microwave treatment and annealing at 250, 350, and 450 °C, the catalytic activities of microwave treated RuO_2/P25 were indifferent from RuO_2/P25 prepared by deposition of RuO_2 nanoparticles (not shown). These observations show that the microwave-assisted preparation of catalysts is not beneficial. As far as the mesoporous TiO_2 (Ti350) was concerned as

a catalyst support, the deposition of pre-synthesized RuO_2 nanoparticles was superior at promoting the methane production rate.

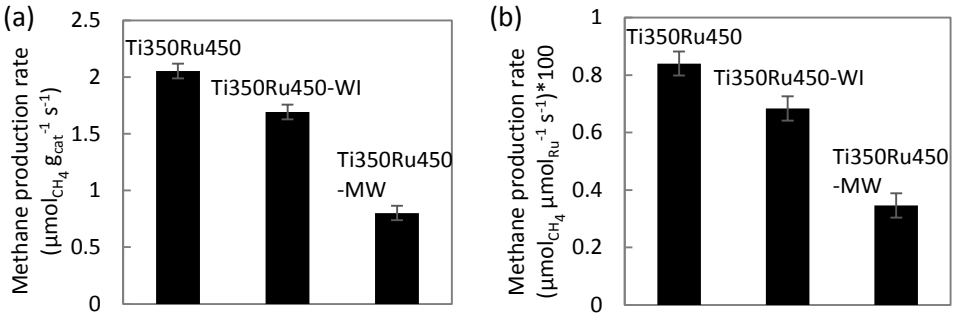

Figure 4-26: Comparison of methanation activities at 200 °C, represented in methane production rate (a) per gram of catalyst and (b) per mole of Ru.

Along with the catalytic performance represented in methane production rate, Ru dispersion values were found to be the highest for Ti350Ru450 and the lowest for Ti350Ru450-MW; the higher the methanation production rate, the higher the Ru dispersion is. Qualitatively, the lowest Ru dispersion of Ti350Ru450-MW could be attributed to the RuO_2 crystal formation as observed in XRD analysis, thereby resulting in agglomerated metallic Ru particles after reduction and methanation. As a result, the trend in TOF values were the opposite; the highest TOF for lowest Ru dispersion and vice versa.

Table 4-8: Ru dispersion and TOF values for the catalysts.

	Ti350Ru450	**Ti350Ru450-WI**	**Ti350Ru450-MW**
Ru dispersion (%)	10.1	5.5	1.5
TOF (s^{-1})	0.08	0.12	0.24

4. Conclusion

Mesostructured TiO_2 was successfully synthesized via the integration of aerosol-assisted self-assembly process and AcHE sol-gel chemistry. The resulting TiO_2 materials could be obtained with a good control of the textural properties upon removal of the organic template. Importantly, crystallization of amorphous TiO_2 to crystalline anatase phase was inevitable especially after calcination at 350 °C and higher temperatures. These modifications result in significant textural

modifications that are however controllable to a certain extent. The slow heating rate of 1 °C/min during calcination was found to be an important parameter to remove the residual organic template more efficiently. The mesoscopic order was maintained after calcination at 350 °C with well-defined pore size of 5 nm. It is however progressively disrupted as the calcination temperature increases.

The mesoporous TiO_2 materials were used as supports for RuO_2 nanoparticles to serve as a catalyst containing 2.2 wt. % Ru for CO_2 methanation. Ru-species were found inside the pores of TiO_2 support after in situ reduction and reaction. However, the high surface area (262 $m^2g^{-1}$and 132 m^2g^{-1}) of the mesoporous TiO_2 was found not to offer any additional advantage for low Ru loading of 2.2 wt.%. It is however envisaged to be beneficial at higher loadings in the dispersion of Ru-species.

The deposition of RuO_2 nanoparticles on low crystalline TiO_2 support promoted the growth of rutile phase TiO_2 at annealing temperature as low as 250 °C, due to the close structural similarities of RuO_2 and rutile TiO_2. The annealing of the partially oxidized Ru-species was again found to be an important activation step as the catalytic activity was at its maximum when annealed at 400 - 450 °C, which is in agreement with what was demonstrated in case of TiO_2-P25 support. Moreover, this means that the crystallinity of the initial TiO_2 support did not affect this "activation step".

The catalytic performance is envisaged to be strongly affected by the interaction between the Ru-species and support. As the reduction profile of the catalysts annealed at higher than 450 °C are different regardless of similar Ru dispersion, the difference in the catalytic activities after annealing at 450 °C or above could be related to the reducibility as well as the re-oxidizability of the Ru-species during the methanation reaction. Finally, the preparation of the catalysts by deposition of pre-synthesized RuO_2 nanoparticles was found to be more beneficial compared to wet impregnation of $RuCl_3$ solution or microwave treatment to form RuO_2 phase inside the pores of the support, thanks to the better dispersed Ru. The results confirm that higher Ru dispersion is beneficial for the production of methane (or the conversion of CO_2) but more agglomerated Ru species appear to be more active on a metal surface basis.

Chapter 5: Preparation of mesoporous Ti-Si and Ti-Al mixed oxides and their application as supports for Ru-based catalysts

1. Introduction

The previous chapter demonstrated that the mesoporous TiO_2 with high mesoporosity and surface area was successfully prepared via integration of aerosol-assisted self-assembly process and AcHE sol-gel chemistry. Yet, thermal stability of the initially amorphous mesoporous TiO_2 was not high enough to withstand the higher calcination temperature or the catalyst preparation process and led to the formation of TiO_2 crystallites at relatively low temperature, thereby destroying the mesoscopic order. Especially, the RuO_2 as an initial active phase of the mesoporous TiO_2 makes the preparation even more challenging due to the strong interaction between RuO_2 and TiO_2 as crystallization of these two phases progresses by thermal annealing. With an acknowledgement that TiO_2 is probably the most effective support for Ru-phases in CO_2 methanation [190, 191], it is also interesting, in the materials science point of view, to enhance the thermal stability of the mesoporous TiO_2. In this chapter, with a hypothesis that the Si- or Al-oxide species do not play any role as support materials in CO_2 methanation, the incorporation of Si and Al in the oxide network of Ti to prepare Ti-Si and Ti-Al mixed oxides using aerosol process is demonstrated. As previously reported in conventional sol-gel system [192-196], the introduction of Si or Al atoms is considered to hinder TiO_2 phase segregation and delay TiO_2 crystallization growth rate.

The versatility of the AcHE sol-gel system, aerosol process, and the combination of both in synthesis of wide range of multicomponent mesoporous materials has been previously demonstrated by several authors [54, 66, 173, 197]. As discussed in the previous chapter, the AcHE system allows the formation of stable metal oxo-

acetate particles by the acetate ligand bonded to the metal cores of the metal alkoxides [66]. As a result, the hydrolysis and condensation behaviours of the preformed precursor particles are controlled. This allows simultaneous controlling of the sol-gel chemistry of multicomponent mixtures of metal alkoxide precursors to form stable precursor nanoparticles with similar size. Furthermore, the AcHE sol-gel chemistry permits the rapid-evaporation of the aerosol and the process permits the coupling between much more reactive non-siliceous sol-gel chemistry and surfactant directed assembly. Consequently, the synthesis of homogeneous multicomponent mesoporous spheres is allowed, as demonstrated by Tsung et al [66].

In this chapter, the preparation and characterization of the Ti-Si and Ti-Al mixed oxides are demonstrated at two different mixing ratios of the metal alkoxide precursors. Although the application of these materials should not be limited to serve as catalyst supports for Ru-species, these mixed oxides are specifically used as supports for Ru-species to explore the effect of the support structure and the interaction between the support and the active Ru-phase. Furthermore, different incorporation methods of Ru-species (RuO_2 NPs deposition and $RuCl_3$ wet impregnation) in the mesoporous cavities are compared and related to the catalytic performance in CO_2 methanation.

2. Experimental summary

The mesoporous oxides were prepared via aerosol-assisted self-assembly process as described in the experimental summary in Chapter 4 (Pg. 125). The precursor solutions were prepared by dissolving Titanium (IV) butoxide ($Ti(OBu)_4$) and TEOS, or Aluminum tri-sec-butoxide ($Al(OBu)_3$), acetic acid, and hydrochloric acid (37 wt.%) in ethanol. The molar ratio of the components was metal precursor : acetic acid : HCl : EtOH : F127 = 1 : 4 : 1.2 : 40 : 0.01 (water from concentrated HCl gives metal to water ratio of 1 to 4). The separately prepared precursor solutions were mixed to yield Ti:Si or Ti:Al molar ratios of 9:1 (90%/10%) and 1:1. (50%/50%). The two solutions were mixed together when they became transparent and were then stirred for 1 h. Amphiphilic block copolymer F127 was then added and stirred vigorously for one more hour to obtain a transparent solution before the aerosol spray process.

After the aerosol process, the collected powder was calcined at 350 °C and 450 °C for 5 h with 1 °C/min heating rate in static air to remove the organic template. The resulting mixed oxides are denoted as TiSi91, TiSi55, TiAl91, and TiAl55 for 90%Ti-

10%Si, 50%Ti-50%Si, 90%Ti-10%Al, and 50%Ti-50%Al (At. % of the metal), respectively.

The catalysts were prepared with the 450 °C calcined mesoporous supports by deposition of pre-synthesized RuO_2 nanoparticles, exactly in the same way as detailed in the experimental section of chapter 4 (pg. 126). The calculated amount of mixed oxide was added to the calculated volume of RuO_2 nanoparticles colloidal suspension to yield 2.2 wt. % of Ru in the final catalyst and placed in an ultrasonic bath for 30 minutes operating at 40 kHz at room temperature. After ultrasonification, the excess water was removed by rotary evaporation under vacuum at 50° C. The resulting dried powder was annealed at 450 °C for 4 h with heating rate of 10 °C/min. The samples are not washed by water as it was previously shown that chlorine content levels off to zero after annealing with or without washing and that no impact on catalytic activity was observed on P25 supported catalysts (see Appendix B). The catalysts are denoted as TiSi91Ru450, TiSi55Ru450, TiAl91Ru450, and TiAl55Ru450.

To investigate any chemical effect from Si or Al, additional catalysts were prepared with deposition of pre-synthesized RuO_2 nanoparticles on commercial SiO_2, γ-Al_2O_3, as well as mechanical mixture of SiO_2 and γ-Al_2O_3, with rutile TiO_2 in an arbitrarily chosen ratio of SiO_2 or γ-Al_2O_3 : rutile TiO_2 = 4 : 1. The mechanical mixture was prepared by simply mixing the two different oxides vigorously using mortar and pestle before immersing the mixture into a colloidal solution of RuO_2 nanoparticles. The catalysts are denoted as Ru/SiO_2, Ru/Al_2O_3, Ru/SiO_2R, and Ru/ Al_2O_3R, respectively.

The catalyst preparation by deposition of RuO_2 nanoparticles is compared with wet impregnation of $RuCl_3$ solution. For wet impregnation, $RuCl_3$ were dissolved in water at [Ru] = 0.007 M (same concentration as RuO_2 NPs in suspension) and support was added to yield 2.2 wt. % of Ru in the final catalyst. The dried powder was obtained after rotary evaporation under vacuum at 50° C. and annealed at 450 °C for 4 h with heating rate of 10 °C/min.

3. Results and discussion

3.1. Mesoporous mixed oxides of Ti-Si and Ti-Al prepared by aerosol-assisted self-assembly process

The textural properties of the mixed oxides calcined at both 350 °C and 450 °C are summarized in Table 5-1. The specific surface areas were generally lower after

calcination at 450 °C, indicating sintering of the mixed oxides due to their thermal sensitivity. Yet, the specific surface areas of the mixed oxides were higher compared to the pure TiO_2, which implies that the thermal stability is higher due to the introduction of the Si and Al in the oxide network of Ti. The higher thermal stability of the mixed oxides is also demonstrated by the less disturbed pore volume and diameter compared to pure TiO_2, after calcination at 350 °C vs. 450 °C.

It is important to note that the specific surface areas of the mixed oxides containing less Ti contents were higher. This observation can be correlated to the shrinkage of the mixed oxide network; the smaller extent of shrinkage for the smaller content of Ti. It can be explained by the fact that titanium-rich system contains more water due to the more hygroscopic Ti^{4+}, resulting from its higher coordination number compared to Si^{4+} or Al^{3+} [192]. The higher thermal stability of the mixed oxides compared to pure TiO_2 can be thus related to their smaller extent of shrinkage.

The N_2 physisorption isotherms of all mixed oxides showed type IV, corresponding to typical mesoporous materials, as shown in Figure 5-1. The shape of the hysteresis could be attributed to type H2, typical for many porous materials of not uniformly distributed pore size and shape, which could be interconnecting pores (H2).

Table 5-1: Textural properties of mixed oxides after calcination.

Sample	Calcination T (°C)	SSA_{BET} (m^2g^{-1})	V_{pore} (cm^3g^{-1})	D_{pore} (nm)
TiSi91	350	330	0.42	5.0
	450	257	0.33	5.1
TiSi55	350	397	0.44	4.4
	450	375	0.42	4.5
TiAl91	350	355	0.46	5.2
	450	306	0.42	5.5
TiAl55	350	421	0.48	4.5
	450	357	0.49	5.5
Ti350*	350	262	0.36	5.4
Ti450*	450	132	0.23	6.8

*Pure mesoporous TiO_2 after calcination at 350 °C and 450 °C for comparison.

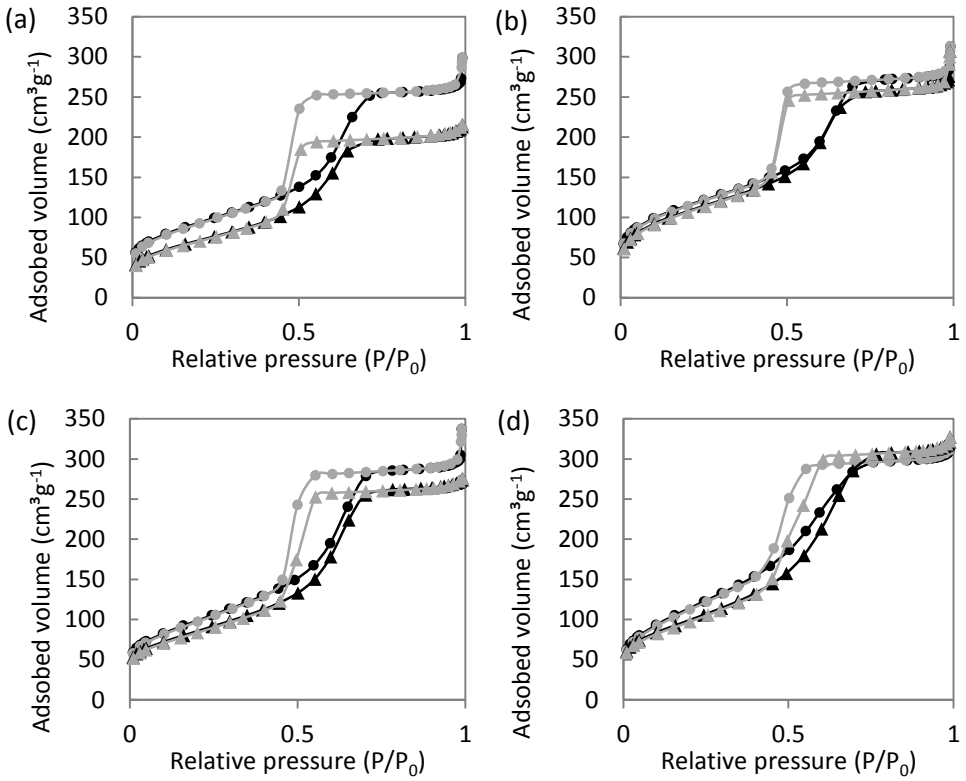

Figure 5-1: N_2 isotherms of (a) TiSi91, (b) TiSi55, (c) TiAl91, and (d) TiAl55, after calcination at 350 °C (●) and 450 °C (◢). Adsorption isotherm is in black and desorption isotherm is in grey.

The TEM analysis revealed that the mesostructure was preserved even after calcination at 450 °C, as shown in Figure 5-2 for Ti-Si mixed oxides and Figure 5-3 for Ti-Al mixed oxides, at both mixed ratios.

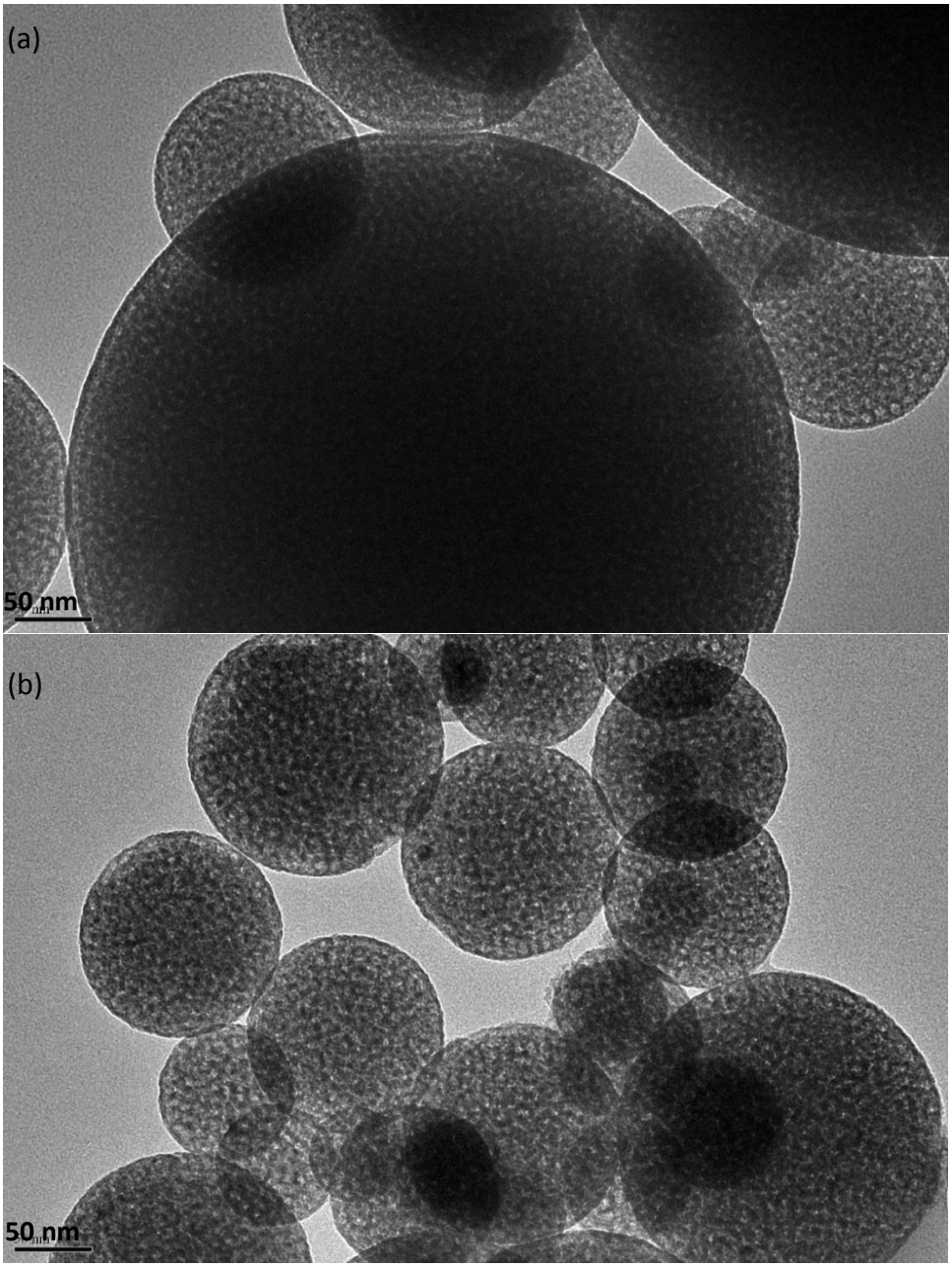

Figure 5-2: TEM images of (a) TiSi91 (b) TiSi55, calcined at 450 °C.

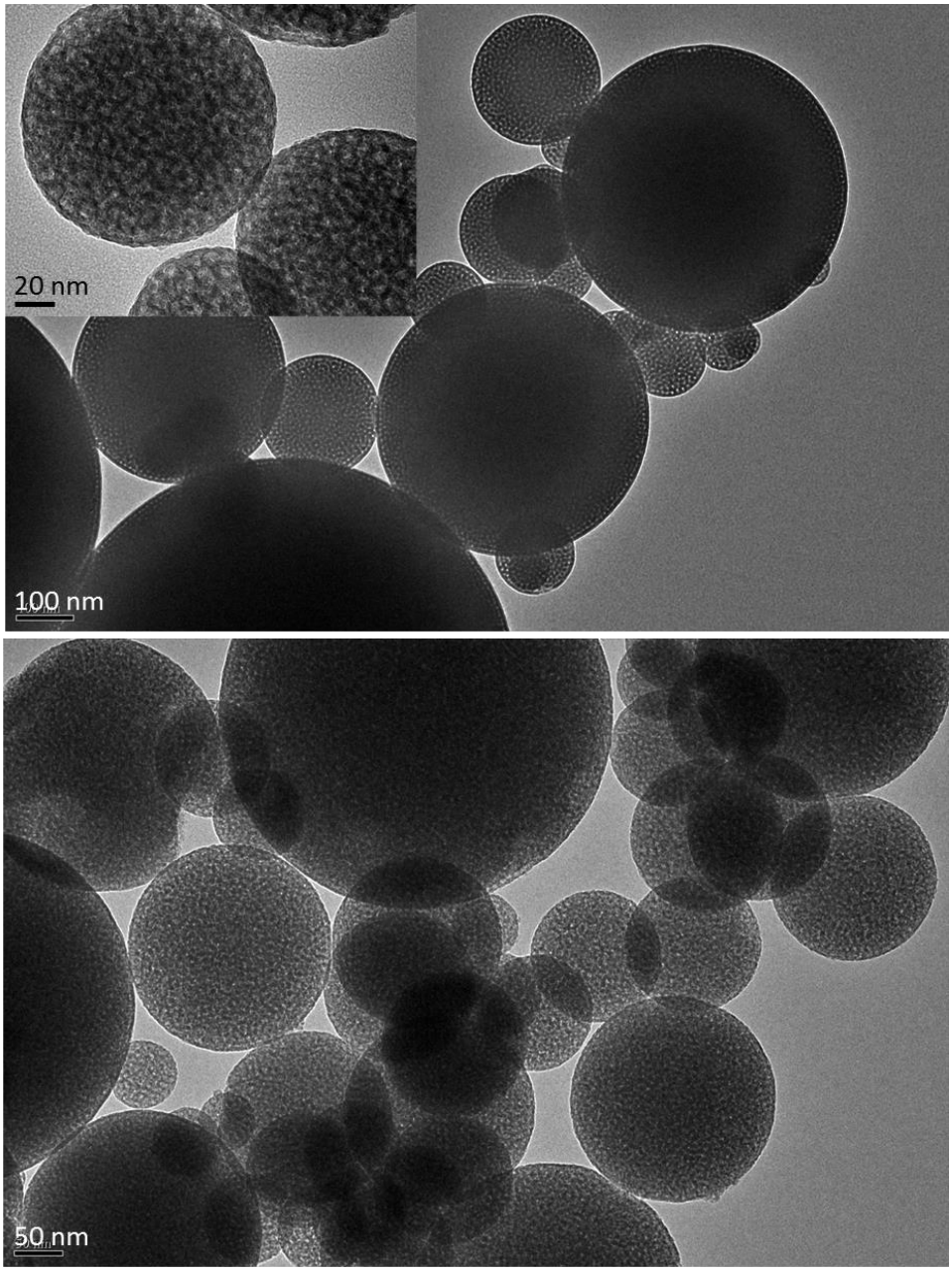

Figure 5-3: TEM images of (a) TiAl91 (b) TiAl55, calcined at 450 °C.

SAXS analysis showed correlation peaks for all samples before and after calcination, as shown in Figure 5-4. This confirms the TEM observation that the mesoscopic order in the fresh samples was maintained even after calcination at 450 °C. The shift in position of the scattering vector (q) towards higher value was observed after calcination for all samples, which corresponds to the smaller d-spacing due to the denser inorganic oxide network (Table 5-2). The d-spacing of all mixed oxides at the same processing condition (fresh or calcined) showed similar values; 11 – 12 nm for fresh samples and 8 – 9 nm for 350 and 450 °C calcined samples, although 450 °C calcined samples exhibited slightly smaller (by a few angstroms) d-spacing values. This points out that the condensation of the mixed oxides prepared by aerosol process is homogeneous regardless of the metal oxide precursor and that the mesostructure was effectively directed by F127.

The slight broadening of FWHM values after calcination at higher temperatures is attributed to the disturbance of the mesoscopic order resulting from the condensation of the mixed oxide network.

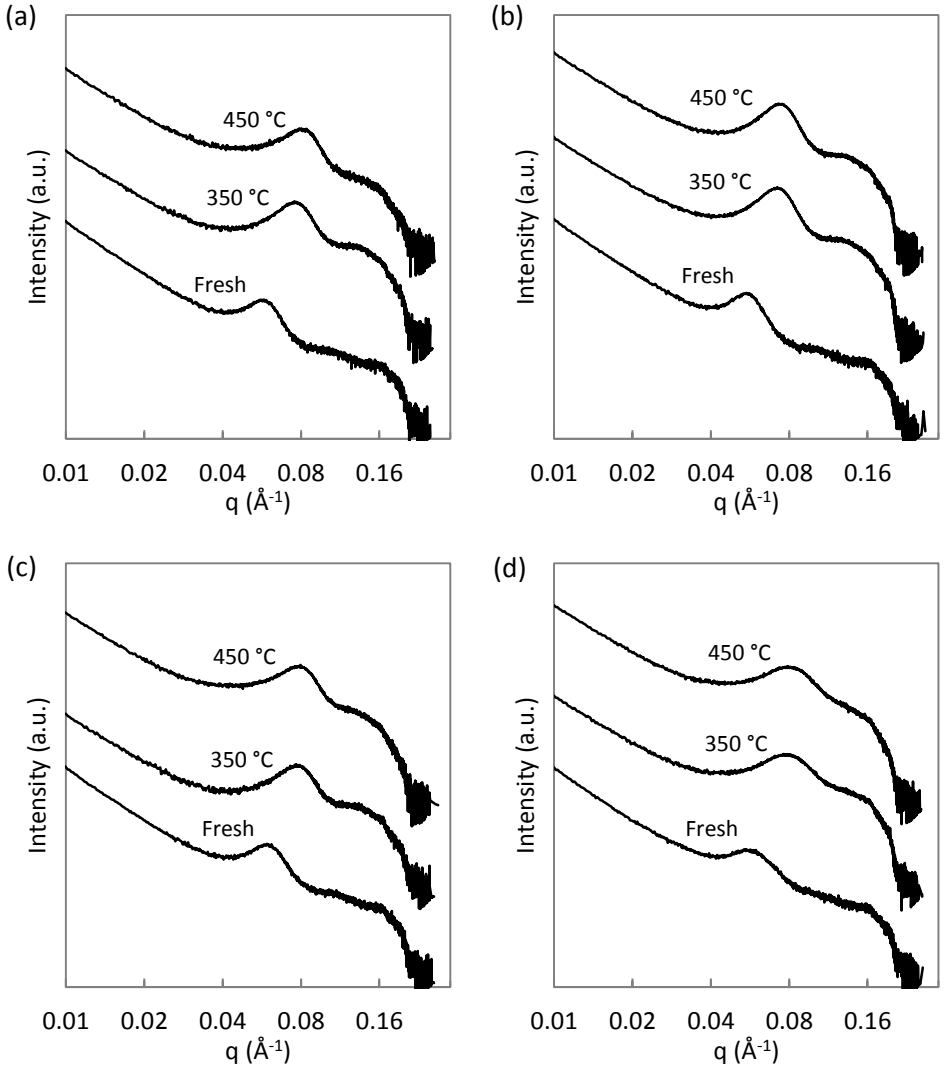

Figure 5-4: SAXS patterns of (a) TiSi91, (b) TiSi55, (c) TiAl91, and (d) TiAl55; bottom pattern: before calcination, middle pattern: after 350 °C calcination, top pattern: after 450 °C calcination.

Table 5-2: D-spacing, positions (q), and widths (FWHM) of the fitted correlation peaks.

Sample	Calcination T (°C)	D-spacing (Å)	Position, q ($Å^{-1}$)	FWHM ($Å^{-1}$)
TiSi91	Not calcined	111.9	0.056	0.015
	350	85.3	0.074	0.020
	450	79.8	0.079	0.021
TiSi55	Not calcined	116.9	0.054	0.012
	350	89.7	0.070	0.018
	450	87.5	0.071	0.019
TiAl91	Not calcined	108.1	0.058	0.015
	350	83.8	0.075	0.020
	450	82.5	0.076	0.021
TiAl55	Not calcined	115.5	0.055	0.020
	350	82.0	0.077	0.028
	450	80.0	0.079	0.029

The composition of mixed oxides supports was analyzed by ICP-AES and SEM-EDX for bulk and XPS for surface compositions. The obtained Ti/Si and Ti/Al ratios are shown in Table 5-3. The bulk analysis by both ICP-AES and SEM-EDX resulted in similar composition of Ti/Si and Ti/Al ratios; however, the ratios were higher than the nominal ratios. A possible explanation is that non-hydrolyzed Si and Al precursors were present in the aerosol precursor which have subsequently volatilized during the aerosol process. However, it is not likely because the reactivity gap between Si- and Al- precursors might have resulted in different Ti/Si and Ti/Al ratios. The plausible explanation couldn't be established at the moment. The compositions obtained by XPS analysis showed significantly lower Ti/Si and Ti/Al ratios. However, this XPS analysis result contradicts the results obtained by XRD and FTIR analysis on the homogeneity of the mixed oxides. Indeed, it is known that quantitative analysis by XPS is difficult for porous materials, thus any trustworthy interpretation couldn't be extracted.

Table 5-3: Ti/Si and Ti/Al ratios determined by ICP-AES, SEM-EDX, and XPS analysis compared to the nominal ratios.

Sample	Nominal	ICP-AES	SEM-EDX	XPS
TiSi91	9	15.5	15.5	4.4
TiSi55	1	1.7	1.8	
TiAl91	9	16.1	9.2	5.4
TiAl55	1	1.8	1.9	

The XRD patterns in Figure 5-5 show that all mesoporous mixed oxides calcined at 350 °C remained amorphous. This is contrary to the pure mesoporous TiO_2 calcined at 350 °C which showed anatase crystallization as discussed in Chapter 4. The crystallization of TiO_2, therefore, was effectively hindered by with the incorporation of Si and Al oxides in oxide network of Ti. For the mixed oxides containing lower content of Ti (TiSi55 and TiAl55), the TiO_2 crystallization was completely inhibited even after calcination at 450 °C. Indeed, for Ti-Si mixed oxide system, it was previously reported that Si atoms act as diffusion barrier for Ti atoms, if intimately mixed, which tends to delay the nucleation and growth of TiO_2 crystallites [192, 198-200]. On the other hand, when Ti contents in the mixed oxides are relatively higher, the anatase crystallization was observed, especially in case of TiSi91. The delay or absence of phase transition of TiO_2 suggests that Ti and Si or Al are homogeneously mixed in the oxide network [192, 199]. Furthermore, no crystalline solid solution of the binary $TiSiO_4$ or Al_2TiO_5 was observed, which indicates that the nucleation and growth mechanism of anatase TiO_2 for TiSi91 was achieved by the phase separation of TiO_2 from amorphous SiO_2 network (in case of TiSi91).

The crystallites of anatase TiO_2 are supported by the flexible amorphous SiO_2 phase located at the crystal boundaries [192, 196]. Therefore, the amorphous SiO_2 acts as a “glue” to hold the oxide network together. In addition, the TiO_2-SiO_2 interface is stabilized by formation of Ti-O-Si bonds playing the role of diffusion barrier for further crystal growth [192], which helps maintaining the mesostructure even after the formation of the anatase crystals as confirmed by TEM and SAXS analysis.

TiAl91, on the contrary to TiSi91, remained nearly amorphous. The suppressed growth of anatase TiO_2 phase at the same Ti content as TiSi91 indicates that the TiO_2 phase segregation from the Al_2O_3 was not achieved, unlike the case of TiO_2-SiO_2 mixed oxide system. It further suggests that the mixed oxides are not simply mixed oxides of two pure oxides, but solid solution of a single amorphous phase. The delay in the TiO_2 crystallization in the Ti-Al mixed oxide system is in agreement with previous findings [193, 201-203], where the possible formation of Ti-Al mixed oxide solid solution was demonstrated by the inhibition of TiO_2 phase transition at relatively high temperature at which pure TiO_2 is normally expected to go through the phase transition. Thus, the homogeneously mixed Ti-Al mixed oxide helps maintaining the mesostructure confirmed by TEM and XRD, while exhibiting higher specific surface area compared to Ti-Si mixed oxide.

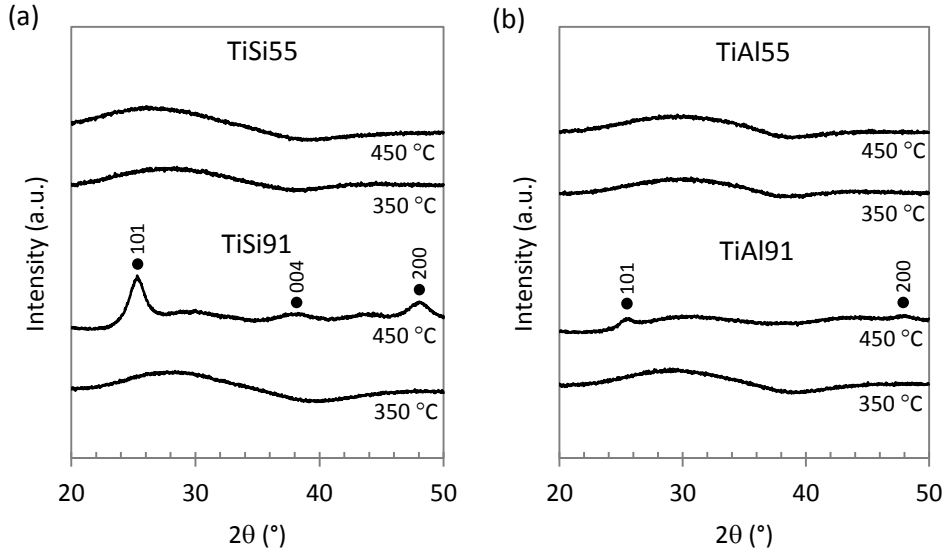

Figure 5-5: XRD patterns of (a) mesoporous TiO_2-SiO_2 and (b) mesoporous TiO_2-Al_2O_3; black dots (●) indicate anatase TiO_2 phases.

TGA was used to prove the efficiency of the removal of organic template, F127, for chosen samples, TiSi91 and TiAl91 (shown in Figure 5-6). Three heating rates are compared; 1, 5, and 10 °C/min; with 1 °C/min ramp, the sample was allowed to stay at 350 °C for 10 h. As already discussed in chapter 4, the decomposition temperature of the organic template was shifted towards lower temperature with slower heating rate, confirming the better efficiency of organic template removal with 1 °C/min heating rate for calcination.

The comparison of weight loss after calcination at 450 °C and 350 °C with 1 °C/min heating rate revealed that the weight loss was systematically greater for 350 °C calcined samples (Table 5-4). This indicates the presence of organic residue after calcination at 350 °C as well as further condensation of the mixed oxide network after calcination at 450 °C, as shown by the growth of anatase phase for the higher Ti content from XRD analysis.

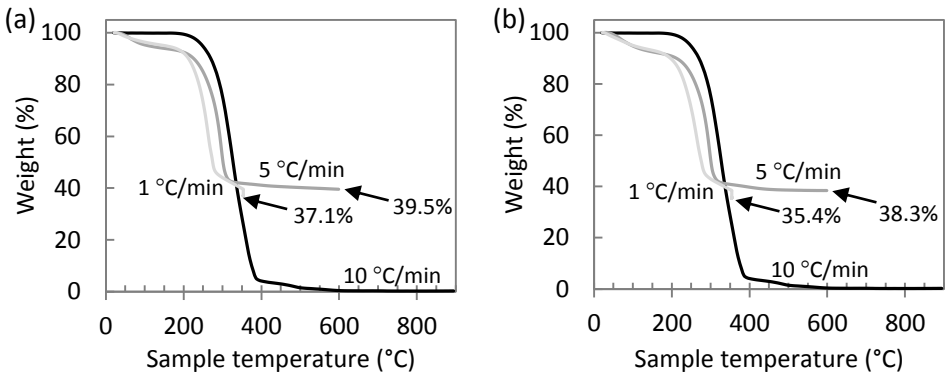

Figure 5-6: TGA curves showing sample weight loss for (a) fresh TiSi91 and (b) fresh TiAl91, in comparison to F127 with heating rate of 10 °C/min (black), fresh sample with heating rate of 5 °C/min (grey) up to 600 °C and 1 °C/min up to 350 °C, which was kept constant for 10 h (lighter grey).

Table 5-4: Weight loss after heating up to 600 °C (with 5 °C/min) of mesoporous mixed oxide samples after calcination at different temperatures.

Sample	Calcination T (°C)	Weight loss (%)
TiSi91	350	8.9
	450	6.2
TiSi55	350	12.6
	450	9.6
TiAl91	350	11.8
	450	9.8
TiAl55	350	15.5
	450	11.9

The complete removal of the organic templates after calcination at 450 °C was confirmed by FTIR analysis as shown in Figure 5-7 for Ti-Si oxides and 5-8 for Ti-Al oxides. The bands at 2970 cm^{-1} and 2880 cm^{-1} corresponding to C-H stretching vibration of PEO and at 1105 cm^{-1} corresponding to C-O-C stretching vibration of PPO blocks disappeared after calcination for both mixed oxides at both mixed ratios. The broad band around 3300 cm^{-1} and 1630-40 cm^{-1} is assigned to bending vibration af adsorbed water molecules [178, 204].

For Ti-Si mixed oxides (Figure 5-7), the band corresponding to Ti-O-Si was observed around 925 - 945 cm^{-1} [204-206]. Furthermore, the vibration frequencies

corresponding to Si-O-Si and Ti-O-Ti were observed at 1050 cm^{-1} and 760 – 790 cm^{-1}, respectively [206, 207]. The vibration frequency of Ti-O-Ti was also observed in 430 – 500 cm^{-1} range [178]. These observations confirm XRD results for TiO_2-SiO_2 phase separation and grain boundary formation, as well as the formation of Ti-O-Si bond at the grain boundary. For TiSi55 (Figure 5-7 (e)), the broadening of the Si-O-Si band around 1050 cm^{-1} or the appearance of shoulder at higher frequency around 1140 cm^{-1} was observed. This could be attributed to the longer or branched silica network which resulted in the broader and more complex absorption of Si-O-Si, showing more than one overlapping bands [205], resulting from the higher Si content in the mixed oxide.

For Ti-Al mixed oxides (Figure 5-8), the bands corresponding to Al bonding species were observed at 550, 800, and 900 cm^{-1} after calcination. The component at 550 cm^{-1} was attributed to the typical frequency of the strongest absorption in alumina, associated with the vibration of AlO_6 octahedra [202]. According to Ramirez et al. [202] and Moolenar et al. [208], the component near 800 cm^{-1} was assigned to AlO_3 stretching mode of an O_3Al-OH group on the surface. The higher frequency component at 900 cm^{-1}, was associated with stretching mode of AlO_4 tetrahedra [201, 209]. For TiAl91 with higher Ti content, the vibration frequency associated with Ti-O-Ti was observed at 440 cm^{-1}, which is in agreement with XRD analysis from which weak anatase TiO_2 phase was observed. The absence of the band corresponding to Ti-O-Ti of TiAl55 points to the homogeneity of Ti-Al mixed oxide. Ramirez et al. [201] observed the increase in the intensity near 550 cm^{-1} when subtracting the spectrum of pure γ-Al_2O_3 from that of Al-Ti mixed oxide. They reported that the intensity near 550 cm^{-1} could be assigned to the absorption of TiO_6 octahedra and that Ti can substitute partially for Al in the octahedral sites of alumina due to the relatively slight difference between the size of the Ti^{4+} (0.53 Å) and Al^{3+} (0.605 Å) cations. This again indicates the formation of Ti-Al oxide solid solution and confirms the amorphous nature of Ti-Al mixed oxides observed by XRD analysis.

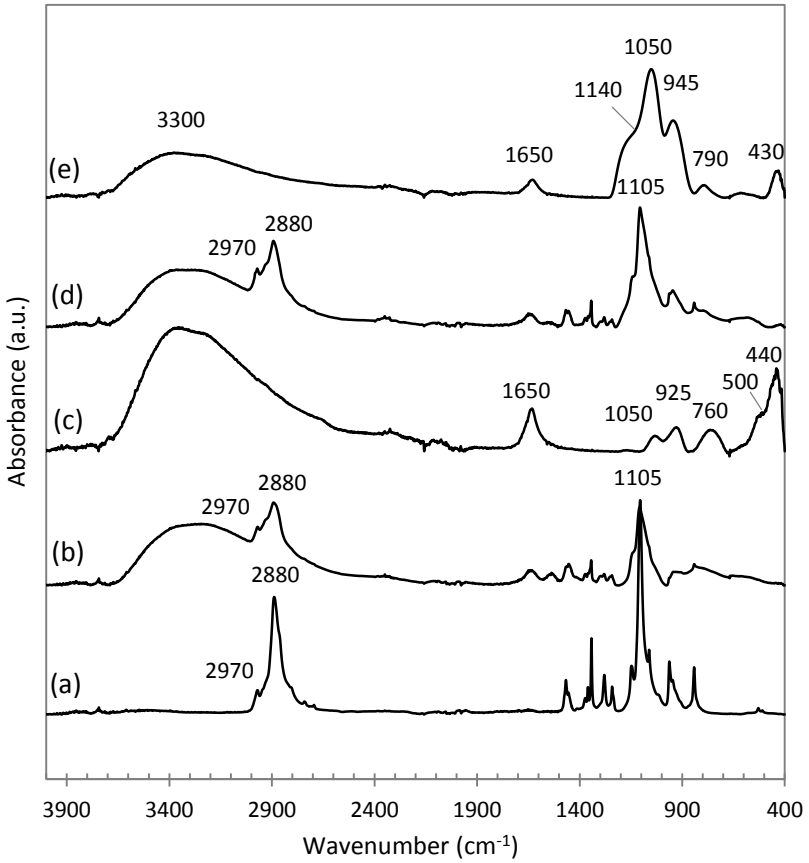

Figure 5-7: FTIR-ATR spectra of (a) F127, (b) fresh TiSi91, (c) 450 °C calcined TiSi91, (d) fresh TiSi55, and (e) 450 °C calcined TiSi55.

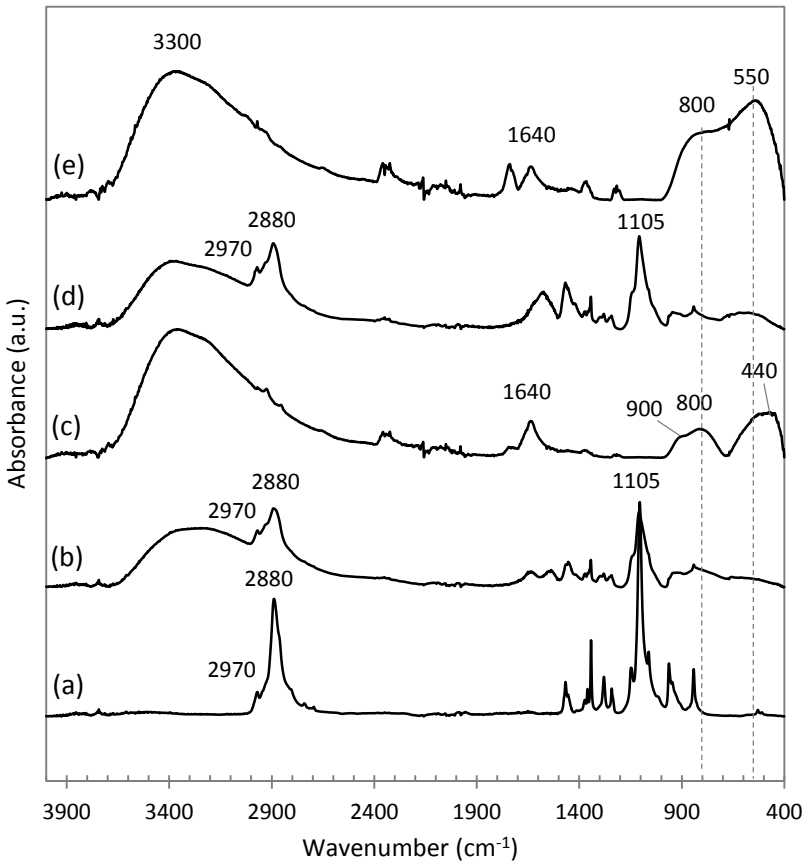

Figure 5-8: FTIR-ATR spectra of (a) F127, (b) fresh TiAl91, (c) 450 °C calcined TiAl91, (d) fresh TiAl55, and (e) 450 °C calcined TiAl55. Dotted lines are drawn at 800 cm^{-1} and 550 cm^{-1} to guide eyes.

3.2. Effect of the ratio of mixed oxides on Ru-based catalyst

The mixed oxide materials described above were used as supports to prepare Ru-based catalysts (2.2 wt. % Ru) by the deposition of pre-synthesized RuO_2 nanoparticles, followed by annealing at 450°C.

The mixed oxides calcined at 450 °C were chosen as supports in order to ensure the higher stability of the catalyst support, as the presence of mesostructure and thermal stability of these mixed oxides were proven by N_2 physisorption, TEM, SAXS, and XRD analysis.

3.2.1. Mesoporous Ti-Si mixed oxide support

For both ratios, the specific surface areas of the RuO_2 supported mixed oxides were lower compare to the starting supports. Accordingly, the pore volumes were also decreased and pore sizes were changed after annealing of RuO_2 supported catalysts. The change in the textural properties was due to the sintering of thermally unstable components in the catalysts, as shown in XRD patterns in Figure 5-9. However, the extent of the change in the textural properties are not significant for TiSi91Ru450 compared to TiSi91; the specific surface area was decreased by only 18 $m^2 g^{-1}$ (7% decrease). On the other hand, the change in the textural properties was significant for TiSi55Ru450 compared to TiSi55 (27 % decrease in SSA). The greater change in textural properties could be attributed to the densification and re-organization of amorphous Ti-Si mixed oxide network after undergoing an immersion in the highly acidic aqueous RuO_2 colloidal suspension and/or during annealing, whereas already crystallized TiSi91 was thermally and mechanically stronger, enough to withstand the next catalyst preparation steps. Indeed, the great modification of the pure mesoporous TiO_2 support after RuO_2 deposition was observed in chapter 4 (29% decrease in SSA for Ti450Ru450), due to more severe crystal growth of pure mesoporous TiO_2 support.

Table 5-5: Comparison of textural properties of Ti-Si mixed oxides before and after RuO_2 deposition.

Sample	SSA_{BET} (m^2g^{-1})	V_{pore} (cm^3g^{-1})	D_{pore} (nm)
TiSi91	257	0.33	5.1
TiSi91Ru450	239	0.28	4.7
TiSi55	375	0.42	4.5
TiSi55Ru450	273	0.29	3.7

The XRD patterns in Figure 5-9 show that, for TiSi91Ru450, the intensity of the anatase TiO_2 peaks nearly remained the same as TiSi91. Moreover, the growth of rutile TiO_2 phase was not observed. It is noteworthy that – unlike the case of pure titania supports – the anatase-to-rutile phase transition was inhibited even after annealing in presence of RuO_2 phase. It further indicates that the mesostructure of the Ti-Si mixed oxides was not totally destroyed, confirming the insignificant change in the textural properties. The inhibition of anatase-to-rutile TiO_2 phase transition was attributed to the presence of Si atoms which act as diffusion barrier for Ti atoms as well as formation of Ti-O-Si bond at the TiO_2-SiO_2 grain boundary. The Ti-Si mixed oxides support for TiSi55Ru450 remained completely amorphous even after RuO_2 deposition and annealing, which confirms the inhibition of TiO_2 phase transition due to the higher Si content resulting in the increased number of Ti-Si points of intimacy.

On the other hand, un-shifted RuO_2 crystallization was clearly observed for both TiSi91Ru450 and TiSi55Ru450, which indicates significant sintering and growth of RuO_2 crystals.

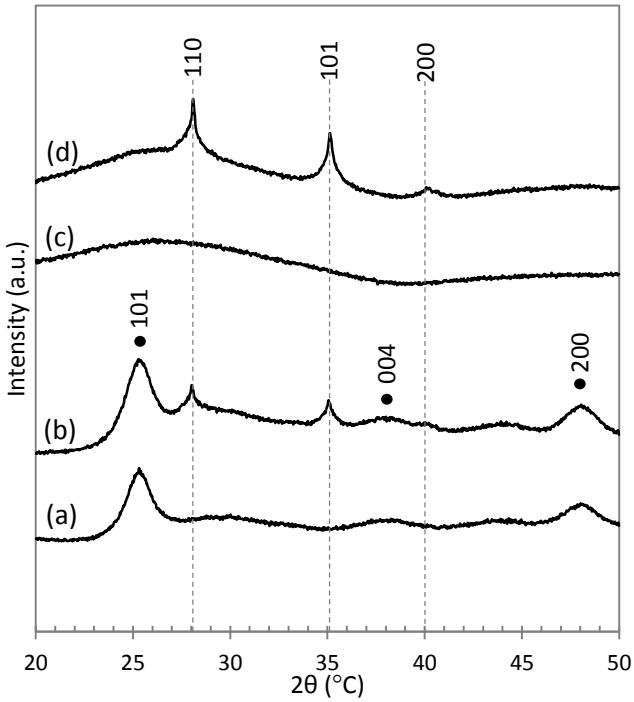

Figure 5-9: XRD patterns of (a) TiSi91, (b) TiSi91Ru450, (c) TiSi55, and (d) TiSi55Ru450; black dots (●) indicate anatase TiO_2 phases and dotted lines indicate RuO_2 phases.

The catalytic activities of TiSi91Ru450 and TiSi55Ru450 were found to be similar, as shown in Figure 5-10. The activities at 200 °C were within the error range of the repeatability of the testing apparatus for both representations of methane production rates, per gram of catalyst and per mole of Ru.

For practical reasons, H_2 chemisorption was carried out with an alternative method, based on volumetric titration and explained in the experimental section. No repetition was possible so the experimental error is not known. It must be noted that when reference catalysts were tested both by automated chemisorption apparatus (Micrometrics ASAP 2010C) and by manual pulse chemisorption apparatus (Micromeritics Pulse Chemisorb 2700), results were not fully consistent. Dispersion as calculated by Pulse Chemisorb 2700 was systematically much lower (approximately ~30% in relative) than that calculated by ASAP 2010C. In the present chapter, dispersion will be referred to as the value obtained by Pulse chemisorb 2700 and used only as a qualitative indication of the dispersion among the catalysts presented specifically in the present chapter. TOF will not be calculated and discussed on that basis and no comparison will be made with the catalysts presented elsewhere in the present thesis.

Both TiSi91Ru450 and TiSi55Ru450 exhibited low dispersion (1.9% and 3.0% respectively) and the Ti-rich catalyst seems to feature even lower dispersion as compared to the Ti-poor counterpart.

When compared to the pure TiO_2 supported catalyst, Ti450Ru450, the activities of Si-containing catalysts was significantly lower (Figure 5-10 (c)). The Ru dispersion on Ti450Ru450 was slightly higher (4.2%), however, more investigation is required to explain the high activity of pure TiO_2 supported catalyst.

In conclusion, the Ti-Si mixed ratio, in the range explored in this study, was not an important parameter for Ru-supported catalysts in CO_2 methanation. Rather, the TiSi91 and TiSi55 play a same role as supports for Ru species regardless of the Ti-Si mixed ratios for TiSi91Ru450 and TiSi55Ru450.

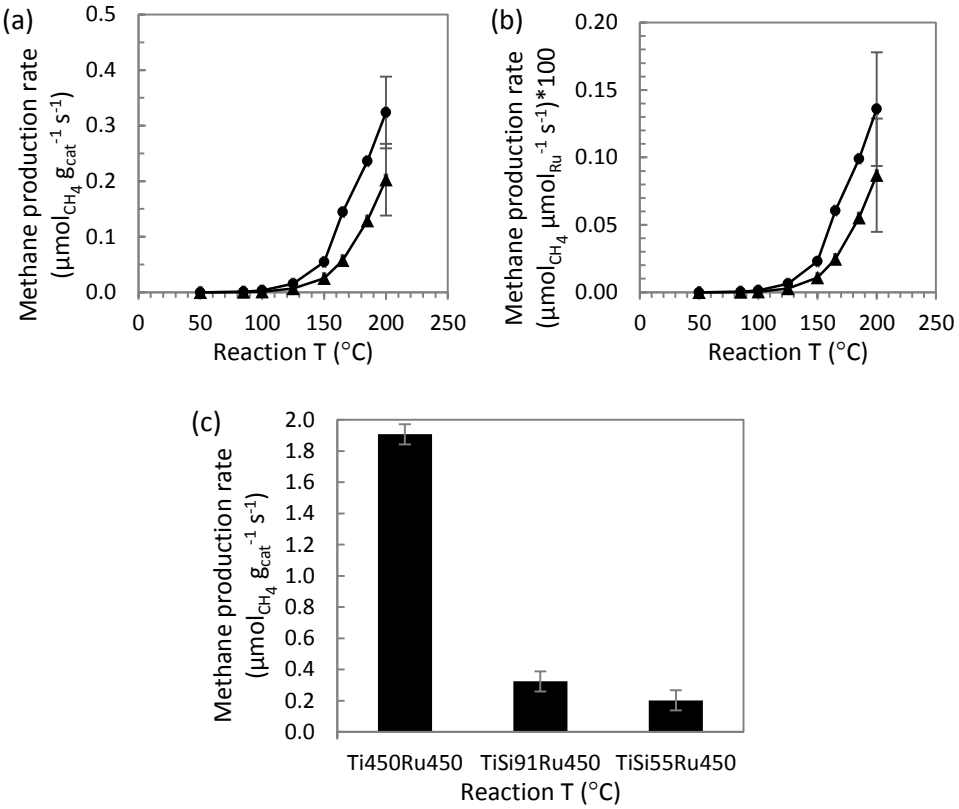

Figure 5-10: Catalytic activities of TiSi91Ru450 (●) and TiSi55Ru450 (▲) represented in methane production rate (a) per gram of catalyst, (b) per mole of Ru based on ICP-AES results of Ru content in the catalysts, and (c) activity comparison with pure mesoporous TiO_2 supported catalyst at 200 °C reaction temperature; error bars are included at 200 °C reaction temperature based on the error determined by repeatability test with RuO_2/TiO_2-P25 catalyst at 200 °C reaction temperature.

3.2.2. Mesoporous Ti-Al mixed oxide support

The textural properties of Ti-Al mixed oxide supports of two different Ti:Al ratios were modified after preparation of RuO_2 supported catalysts. BET surface area, pore volume and pore diameter values are summarized in in Table 5-6. The extent of the decrease in the SSA was slightly greater for TiAl91Ru450 (22%) compared to TiAl55Ru450 (20%). As seen in case of Ti-Si mixed oxide support, the modification in the textural properties is attributed to the growth of crystallites in the catalysts, as confirmed by XRD analysis (Figure 5-11).

For TiAl91Ru450, significant growth of anatase TiO_2 phase was observed compared to its support, TiAl91. The TiO_2 phase transition (amorphous-to-anatase) could have been facilitated after deposition of RuO_2 and annealing as anatase phase growth was already initiated for the pure support (TiAl91). The RuO_2 crystallization was also observed. Interestingly, the broadening on the shoulders of 110 and 101 RuO_2 peaks towards 110 and 101 rutile TiO_2 positions were observed (indicated by red arrows in Figure 5-11 (b)). This is attributed to the epitaxial formation of rutile TiO_2 phase, driven by RuO_2 crystallization.

This phenomenon, on the other hand, was not observed for TiAl55Ru450. Indeed, the TiO_2 phase separation and crystallization did not occur at all, which could be attributed to the greater homogeneity of Ti-Al mixing and more stable Ti-Al mixed oxide network, resulting from the better balanced Ti:Al ratio compared to TiAl91Ru450. For TiAl55Ru450, only RuO_2 crystallization was observed for 110, 101, and 200 planes. This indicates poor interaction between RuO_2 and its TiAl55 support which resulted in sintering of RuO_2 phase.

Table 5-6: Comparison of textural properties of Ti-Al mixed oxides before and after RuO_2 deposition.

Sample	SSA_{BET} (m^2g^{-1})	V_{pore} (cm^3g^{-1})	D_{pore} (nm)
TiAl91	306	0.42	5.5
TiAl91Ru450	240	0.36	5.9
TiAl55	357	0.49	5.5
TiAl55Ru450	286	0.47	3.7

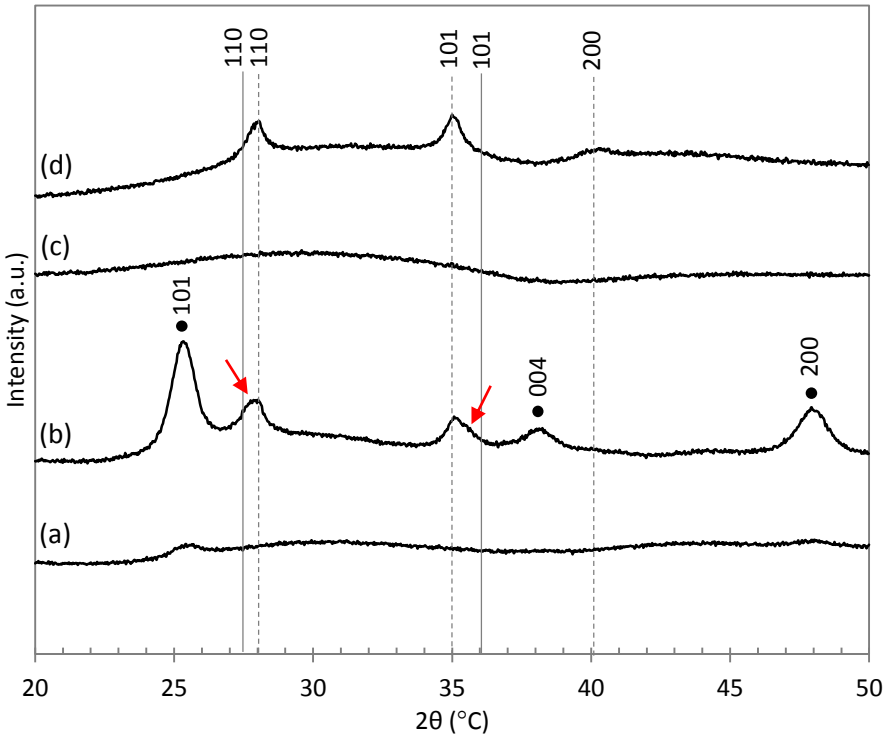

Figure 5-11: XRD patterns of (a) TiAl91, (b) TiAl91Ru450, (c) TiAl55, and (d) TiAl55Ru450; black dots (●) indicate anatase TiO_2 phases, dotted lines indicate RuO_2 phases, and red arrows indicate broadening on the shoulders of 110 and 101 RuO_2 peaks towards 110 and 101 rutile TiO_2 positions

The Ru dispersion as measured from Pulse Chemisorb 2700 was again relatively low (2.7 % for TiAl91Ru450 and 4.3 % for TiAl55Ru450). Consistently with XRD which showed similar RuO_2 peak intensities for both catalysts, dispersion values are in the same order of magnitude. The catalytic activity of TiAl91Ru450 was higher than that of TiAl55Ru450, as shown in Figure 5-12. Yet, compared to pure mesoporous TiO_2 supported catalyst (Ti450Ru450), the catalytic activities of the Al-containing supports are lower. This result is remarkable because characterization data point to a similar Ru phase but clear differences in the properties of the support. It appears that the Ru-species formed through the stabilized RuO_2 by epitaxial lattice matching with rutile phase TiO_2 support may play an important role in CO_2 methanation.

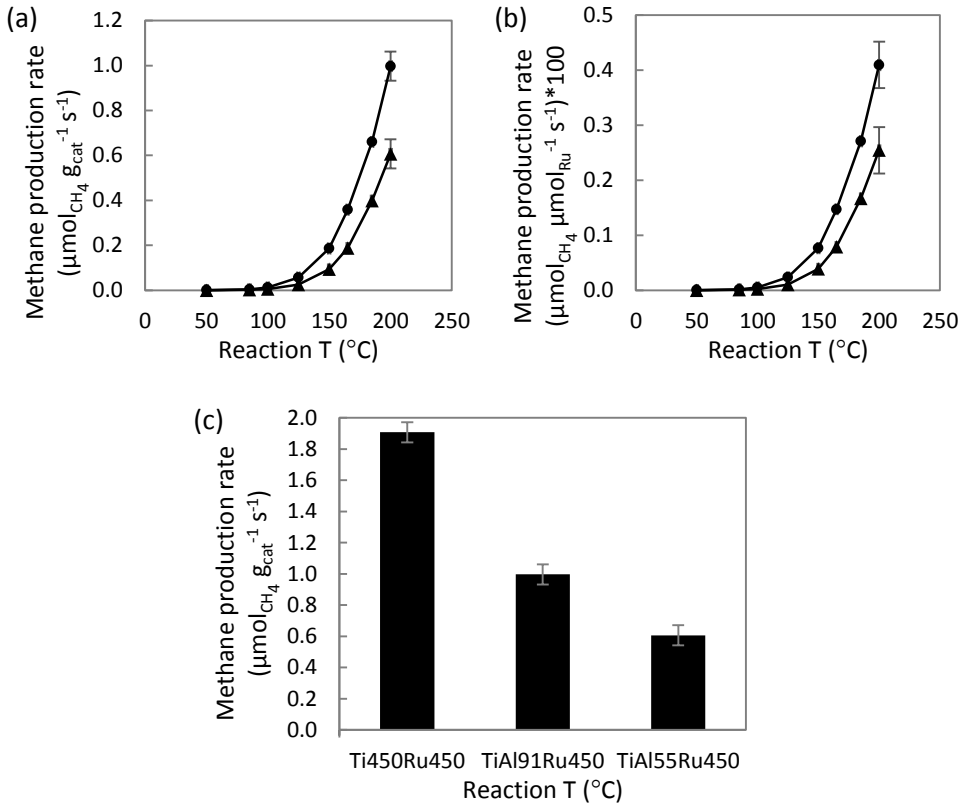

Figure 5-12: Catalytic activities of TiAl91 (●) and TiAl55 (◢) represented in methane production rate (a) per gram of catalyst, (b) per mole of Ru based on ICP-AES results of Ru content in the catalysts, and (c) activity comparison with pure mesoporous TiO_2 supported catalyst at 200 °C reaction temperature; error bars are included at 200 °C reaction temperature based on the error determined by repeatability test with RuO_2/TiO_2-P25 catalyst at 200 °C reaction temperature.

3.3. Effect of the nature of mixed oxides supports on Ru-based catalyst

This section re-presents the results reported in the previous section in order to provide an insight to the effect of the nature of mixed oxides as supports for Ru-phase. The discussion is focused from a different angle to compare two different mixed oxides, Ti-Si and Ti-Al, of one mixed ratio at a time. Thus, the comparison is made on TiSi91Ru450 vs. TiAl91Ru450 and TiSi55Ru450 vs. TiAl55Ru450.

The change in textural properties of the final catalysts compared to their initial supports are summarized in Table 5-7. It was observed that the decrease in specific surface area was greater for TiAl91Ru450 than it was for TiSi91Ru450. The change

in textural properties was closely correlated to the XRD analysis, shown in Figure 5-13. The crystallinity of initial TiSi91 remained nearly unchanged for TiSi91Ru450; the crystallinity of anatase TiO_2 phase was not further enhanced. On the other hand, the nearly amorphous TiAl91 showed a significant growth of anatase TiO_2 phase for TiAl91Ru450, thereby resulting in the greater change in textural properties.

This observation shows that, at this higher Ti content, the amorphous Ti-Al mixed oxide is less thermally stable thus more apt to phase transition compared to Ti-Si mixed oxide.

When Al or Si content was higher in the mixed oxides, the TiO_2 phase segregation was suppressed for both TiSi55Ru450 and TiAl55Ru450, as shown in Figure 5-14. It is attributed to the more abundant Ti-Si or Ti-Al contacts created by the higher contents of Si or Al in the mixed oxides, which act as diffusion barriers for Ti atoms to delay the nucleation and growth of TiO_2 crystallites. As a result, only RuO_2 crystallization was observed. The change in the textural properties in Si- or Al-rich system could be related to further densification of the mixed oxides to a certain degree.

The 110 and 101 RuO_2 peaks were clearly visible for all catalysts. Interestingly, for Si containing catalysts, un-shifted and very sharp RuO_2 peaks were observed, whereas the RuO_2 peaks in Al containing catalysts were broadened and slightly shifted towards the corresponding 110 and 101 rutile TiO_2 peaks. This suggests that the interaction between RuO_2 and Al containing support is greater.

Table 5-7: Change in textural properties of mesoporous mixed oxides supported catalysts compared to their initial support.

Sample	**Δ SSA_{BET} (m^2g^{-1}/%)**	**Δ V_{pore} (cm^3g^{-1}/%)**	**Δ D_{pore} (nm/%)**
TiSi91Ru450	18/7	0.05/15	0.4/8
TiAl91Ru450	66/22	0.06/14	0.4/7
TiSi55Ru450	102/27	0.13/30	0.8/18
TiAl55Ru450	71/20	0.02/4	1.8/33

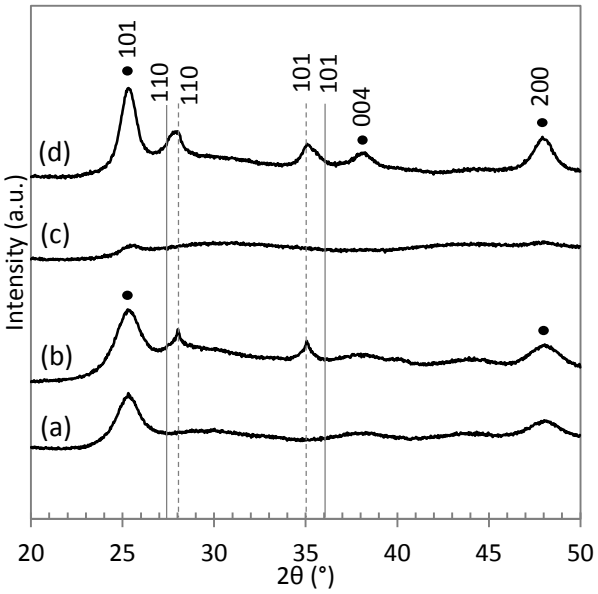

Figure 5-13: XRD patterns of (a) TiSi91, (b) TiSi91Ru450, (c) TiAl91, and (d) TiAl91Ru450; black dots (●) indicate anatase TiO_2 phase, dotted lines indicate RuO_2 phase, and solid lines indicate rutile TiO_2 phase.

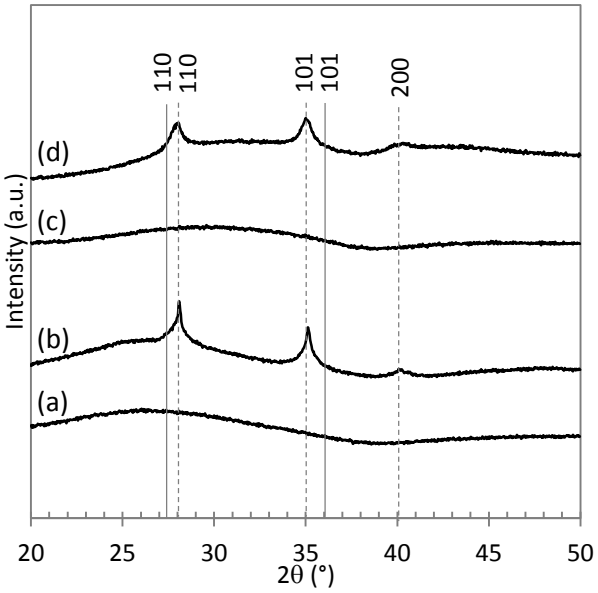

Figure 5-14: XRD patterns of (a) TiSi55, (b) TiSi55Ru450, (c) TiAl55, and (d) TiAl55Ru450; black dots (●) indicate anatase TiO_2 phase, dotted lines indicate RuO_2 phase, and solid lines indicate rutile TiO_2 phase.

The methanation activities of Ti-Al mixed oxide supported catalysts showed higher activities compared to Ti-Si mixed oxide at both mixed ratios, as shown in Figure 5-15.

Consistently, Ru dispersion values determined by H_2 chemisorption were systematically higher on Ti-Al mixed oxides support, and higher on pure TiO_2 support. Thus the lower stability of Ti-Al supports during catalyst preparation by immersing into aqueous colloidal suspension of RuO_2 nanoparticles appears to favor an easier TiO_2 phase segregation that is beneficial for the dispersion of Ru and the stabilization of more active Ru particles. The growth of anatase phase and even rutile phase through RuO_2 phase stabilization was observed on pure mesoporous TiO_2 as demonstrated in chapter 4.

TPR analysis shown in Figure 5-16 revealed that the main reduction peaks for Ti-Al mixed oxides were at higher temperatures compared to Ti-Si mixed oxides. It was observed that the temperatures of the main reduction peaks are similar for the mixed oxide of same nature. The significant difference in reduction temperature reveals that the nature of the RuO_2 species is different in the catalysts based on TiAl and TiSi supports respectively. RuO_2 in close interaction with pure TiO_2 (crystalline or at the onset of crystallization) was already shown to occur at relatively high temperature (The main reduction peak for RuO_2 on pure mesoporous TiO_2 was at 216 °C). Consistently with other characterization results, this is what is also observed for the catalysts based on Ti-Al blends, where the onset of TiO_2 crystallization is observed and where XRD peak position indicated epitaxial matching. In catalysts based on Ti-Si blends, reduction appears at lower temperature, indicative of particles that are not interacting strongly with the (mainly amorphous) support and are therefore more easily reduced.

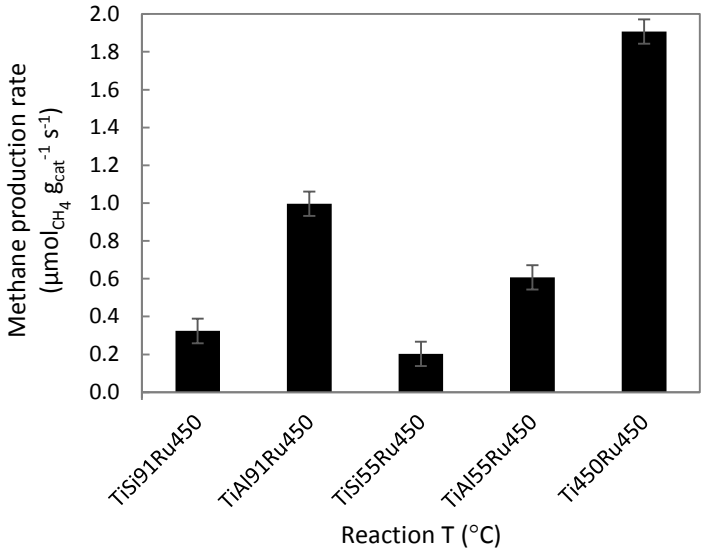

Figure 5-15: Comparison of methanation activities at 200 °C.

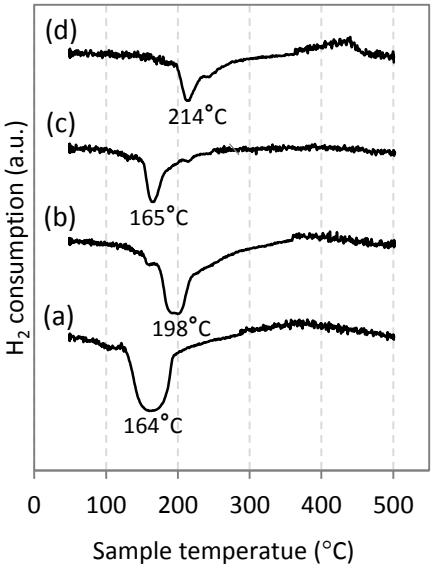

Figure 5-16: H_2 consumption by TPR analysis for (a) TiSi91Ru450, (b) TiAl91Ru450, (c) TiSi55Ru450, and (d) TiAl55Ru450.

Dispersion appears to be higher in Ti-Al blends as compared to Ti-Si blends. As discussed above, this can be explained by the fact that TiO_2 sintering is more intense in Ti-Al blends, while Ti-Si blends tend to remain rather amorphous. At the onset of TiO_2 crystallization, it appears that RuO_2 can develop specific interactions with the support (as attested by peak shift in XRD for TiAl-based catalysts) which can be responsible for a better dispersion. On the contrary, on the Ti-Si supports which either remain totally amorphous or poorly crystallized, no interaction is noticed and RuO_2 sinters more heavily.

Since we are looking at porous samples, another difference may arise from the location of the Ru species within the support. Cross-sectional TEM analysis was performed on TiSi91Ru450 and TiAl91Ru450 in an attempt to visualize the distribution of Ru (Figure 5- 7). For Ti-Al mixed oxides, the dispersion appeared to be rather homogeneous, with Ru particles clearly located inside of the porous particles. Comparatively, in chapter 4, Ru particles were also dispersed inside the pores of pure mesoporous TiO_2. Interestingly however, for Ti-Si mixed oxide, the Ru species were found exclusively outside of the pores of the support.

There are two possible causes for the Ru diffusion inside the porous particles. First, surface charge of the mesoporous oxide may have repulsive or attractive electrostatic interaction with RuO_2 nanoparticles. The isoelectric point (IEP) of the RuO_2 nanoparticles and the mixed oxides supports were compared. Since TiO_2 and SiO_2 domains separate in the Ti-Si mixed oxides, the IEP of the pure oxides were taken from literatures and they were found to be 3.8 – 6 for TiO_2 (anatase) and 1.7 – 3.5 for SiO_2 [210, 211]. The IEP of RuO_2 nanoparticles is ~5 and the pH of the aqueous medium of the RuO_2 colloidal suspension is ~2 [41]. Thus all components (TiO_2, SiO_2 and RuO_2) are positively charged when the mixed oxide support is immersed in the RuO_2 nanoparticles colloidal suspension. Therefore, there is an electrostatic repulsion, which could have prevented the diffusion of RuO_2 nanoparticles. However, the similar electrostatic repulsion is also present between RuO_2 nanoparticles and Al-Ti mixed oxide considering that Al_2O_3 has IEP of 7-8 (gamma alumina) and TiO_2 has IEP of 3.8 – 6. Against this logic though, our XRD analysis has shown that no grain boundary between Al_2O_3 and TiO_2 (TiAl19) was created. Thus, it indicates that IEP comparison between RuO_2 and the pure oxides, Al_2O_3 and TiO_2, does not represent the actual IEP of the well-mixed Al-Ti mixed oxide system. Sanchez et al. demonstrated that high homogeneity of Si-Zr mixed oxide can drastically shift the IEP to a significantly lower value (more acidic pH) compared to both SiO_2 and ZrO_2, not an intermediate value between SiO_2 and ZrO_2 [212]. This phenomenon can possibly occur in Al-Ti mixed oxide which may have neutralized

its surface in the RuO_2 nanoparticles colloidal suspension to better interact with the RuO_2 nanoparticles. Another possible explanation is the formation of inorganic crust (wall) around the outer surface of the spherical aerosol particles which, fully or partially blocks the porous network at the surface preventing the diffusion of RuO_2 nanoparticles. Indeed, a group of researchers at LCMCP demonstrated that SiO_2 crust around the aerosol-processed particles are correlated with the closure of hysteresis loop on desorption branch of N_2 physisorption isotherm at partial pressure $P/P_0 \sim 0.4$, lower than that of a mesoporous metal oxide that does not form the crust. Indeed, our Ti-Si mixed oxide showed the closure of hysteresis loop on desorption branch at $P/P_0 = 0.4$, as opposed to that of Ti-Al mixed oxide ($P/P_0 = 0.45$), which could be attributed to the presence of inorganic crust in Ti-Si mixed oxide.

This effect can possibly be the cause - or only an enhancing factor – of the phenomenon described in the previous paragraph. Indeed, the lack of matching between RuO_2 phase and the TiO_2 crystallites that tend to form upon annealing may simply be caused or worsened by the fact that RuO_2 are simply not distributed throughout the support but only outside of the TiSi particles.

On these mixed oxide supports, clear observation of crystallized Ru phase was made by XRD analysis (Figure 5-18). The crystalline Ru peaks were never observed for catalysts after in situ reduction and methanation on pure TiO_2 supports discussed in the previous chapters. The Ru crystallite sizes calculated by Scherrer formula (Table 5-8), on the other hand, were similar to those observed by TEM analysis on P25-TiO_2 support in Chapter 1. This means that isotropically grown crystalline Ru are present on mixed oxide supports. It can be hypothesized that certain facets of Ru are exposed on pure TiO_2 (which were not be detected by XRD analysis at the same condition), which promote the higher catalytic activity of pure TiO_2 (rutile phase, specifically) supported Ru species. However, this phenomenon is not fully understood at this point.

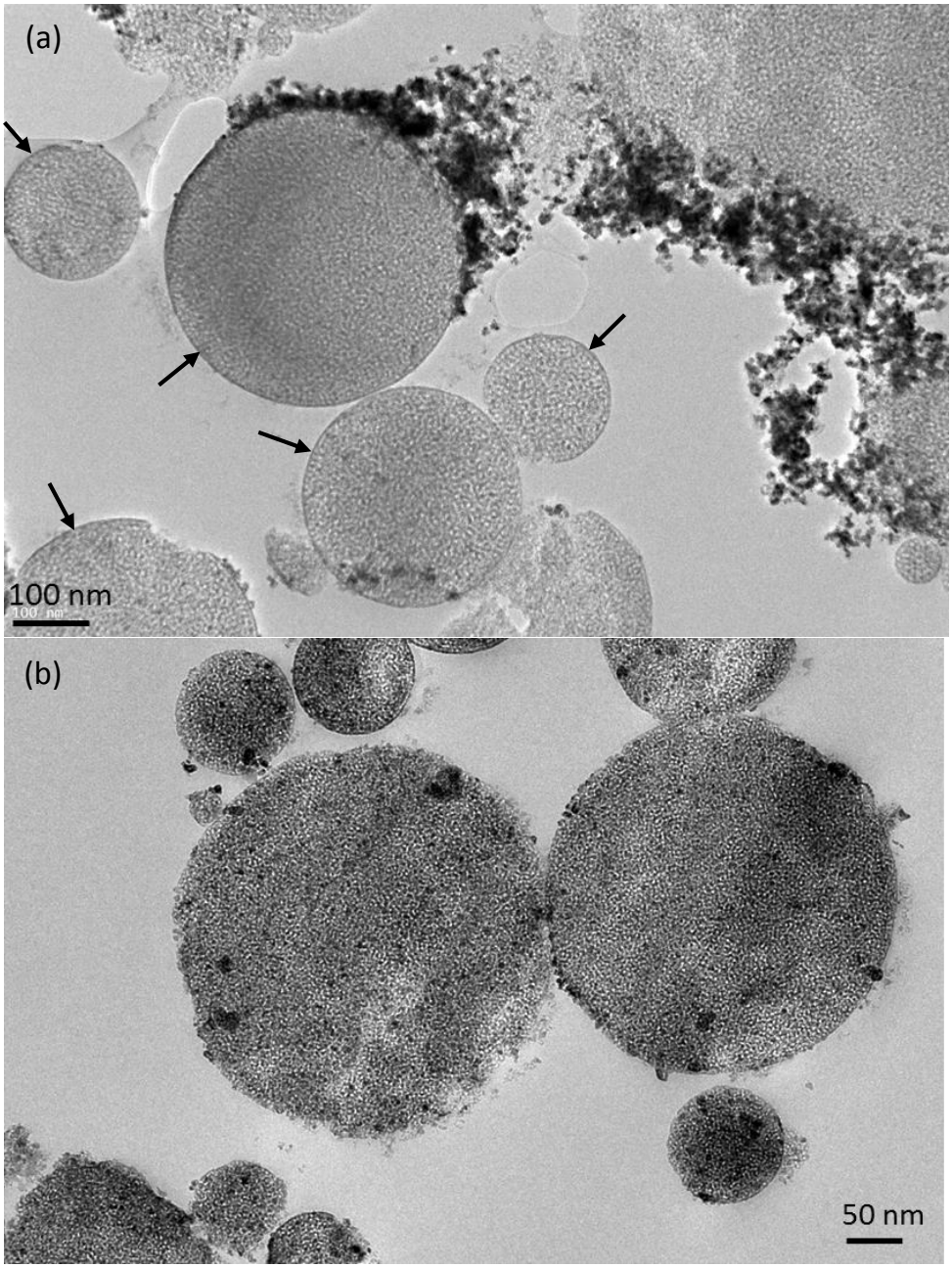

Figure 5-17: Cross-sectional TEM images of (a) TiSi91Ru450 and (b) TiAl91Ru450 after in situ reduction and methanation; black arrows represent "possible" existence of inorganic crust around the aerosol particles at the surface.

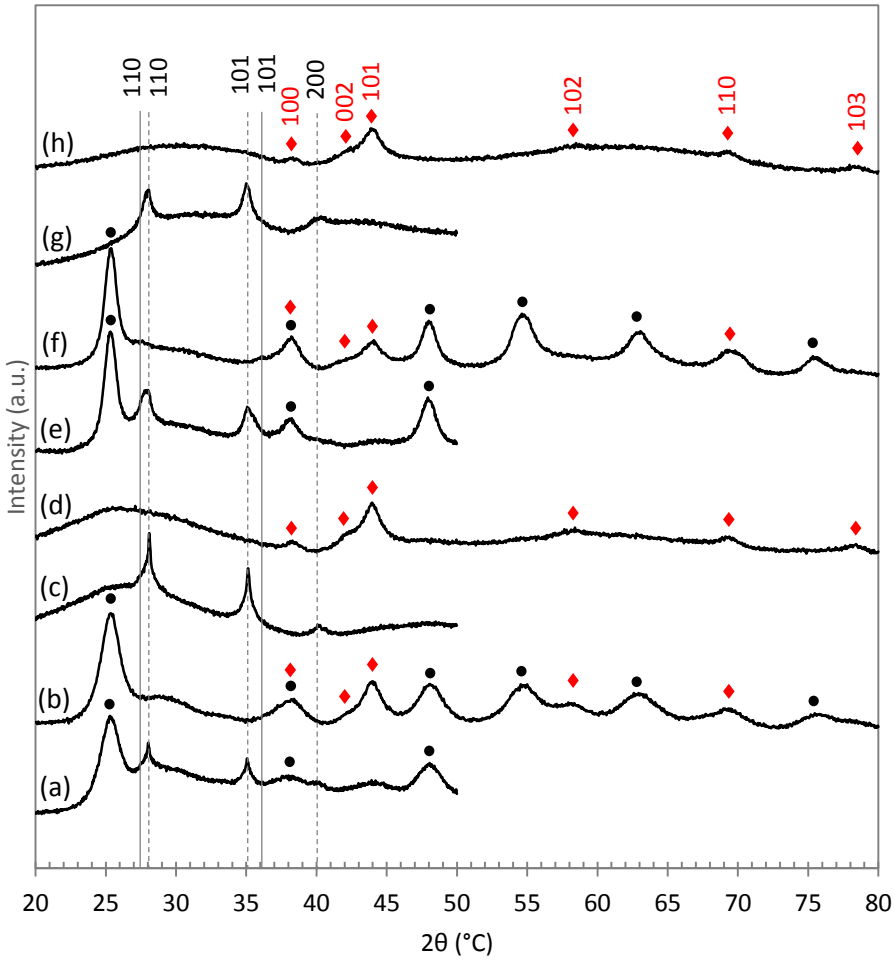

Figure 5-18: XRD patterns of (a) TiSi91Ru450, (b) TiSi91Ru450-spent, (c) TiSi55Ru450, (d) TiSi55Ru450-spent, (e) TiAl91Ru450, (f) TiAl91Ru450-spent, (g) TiAl55Ru450, and (h) TiAl55Ru450-spent; black dots (●) indicate anatase TiO_2 phase, red diamonds (♦) indicate metallic Ru phase, dotted lines indicate RuO_2 phase, and solid lines indicate rutile TiO_2 phase.

Table 5-8: Ru crystallites sizes calculated by Scherrer formula.

	TiSi91Ru450	TiAl91Ru450	TiSi55Ru450	TiAl55Ru450
Ru 002	-	-	3.3 nm	4.6 nm
Ru 101	4.8 nm	3.8 nm	5.9 nm	5.9 nm
Ru 102	3.4 nm	-	3.0 nm	3.2 nm
Ru 110	2.8 nm	4.8 nm	6.5 nm	9.7 nm
Average	3.7 nm	4.3 nm	4.7 nm	5.8 nm

3.4. Chemical effect from Al or Si?

The presence of silica or alumina in the support clearly impacts the catalytic activity. Especially in the case of TiSi supports, activity is lowered, due to a much lower interaction of the RuO_2 phase with the support upon annealing. The quality of alumina and silica alone as supports for Ru are avaluated here in an attempt to elucidate their effect in the mixed supports.

The SiO_2 supported Ru catalyst showed higher activity compared to Al_2O_3 supported Ru catalyst, as shown in Figure 5-19. This observation is contradictory to the catalytic activities of the mixed oxides discussed in the previous section (Figure 5-15), where the Si containing mixed oxides showed lower catalytic activity compared to Al containing mixed oxides. On the other hand, when SiO_2 or Al_2O_3 are mechanically mixed with rutile TiO_2 powder (20 % rutile by weight), the catalytic activities of both SiO_2- and Al_2O_3- containing catalysts resulted in the same catalytic activity, higher than SiO_2 or Al_2O_3 alone. Also, the methane production rates of Ru/SiO_2R and Ru/Al_2O_3R are in the same range as that of Ru/TiO_2-P25 (2.5 μmol_{CH4} g_{cat}^{-1} s^{-1}), which contains similar portion of rutile phase (20 %).

This observation points out that the catalytic activities are not affected by chemical nature of Si or Al. As demonstrated in the previous chapters, this implies that the interaction of the active Ru-phase and support originating from the structure of the support plays an important role. Furthermore, it suggests that the catalytic activities of the mixed oxide supported catalysts discussed in the previous sections are dependent on the altered crystalline structure of the support, but not on the nature of the support. In this regard, rutile TiO_2 structure is a promoter for the high catalytic activity for Ru supported catalysts in CO_2 methanation.

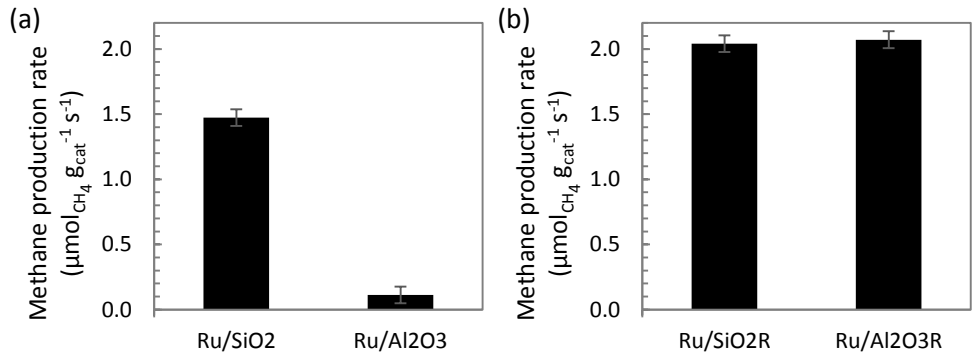

Figure 5-19: Comparison of catalytic activities for (a) Ru/SiO_2 and Ru/Al_2O_3, and (b) Ru/SiO_2R and Ru/Al_2O_3R, at 200 °C.

3.5. Effect of Ru incorporation method

The incorporation of RuO_2 nanoparticles into the pores of the mixed oxide supports was identified as a possible cause for the poor interaction between the partners and consequently for the relatively low activity of the catalysts. The method used to load the support with Ru is now investigated further, using TiSi91 and TiAl91. More precisely, deposition of pre-synthesized RuO_2 NPs method is compared to conventional wet impregnation using $RuCl_3$. .

The textural properties (Table 5-9) of the catalysts prepared by wet impregnation was not significantly different from the catalyst prepared by deposition of RuO_2 nanoparticles; only slight decrease in specific surface areas (21 m^2g^{-1}, 9%) was observed in case of Ti-Si mixed oxide while that of Ti-Al mixed oxide remained unchanged.

Table 5-9: Comparison of textural properties.

Sample	**SSA_{BET} (m^2g^{-1})**	**V_{pore} (cm^3g^{-1})**	**D_{pore} (nm)**
TiSi91Ru450	239	0.28	4.7
TiSi91Ru450-WI	218	0.25	4.5
TiAl91Ru450	240	0.36	5.9
TiAl91Ru450-WI	243	0.36	6.0

Accordingly, no significant further crystal growth in the catalysts were observed by XRD analysis (Figure 5-20). Interestingly, the shift of the RuO_2 peak toward 110 and 101 rutile TiO2 was not the same in the samples prepared by deposition and impregnation methods respectively. In the case of TiAl support, the slight shift discussed earlier in this chapter is much more evident here in the catalyst prepared by impregnation. In the case of TiSi support, while the peak was totally unshifted in the catalyst described earlier, a slight but clearly noticeable shift is observed in the case of the impregnation method (red arrows in Figure 5-20). This observation could be attributed to the formation of oxidized Ru species during the annealing step for the wet impregnation method, which could have facilitated the epitaxial lattice matching rutile TiO_2 growth with help of residual water in the catalyst. The mobility of initial Ru species to further oxidize is assumed to be higher in case of wet impregnation compared to pre-synthesized RuO_2 particles.

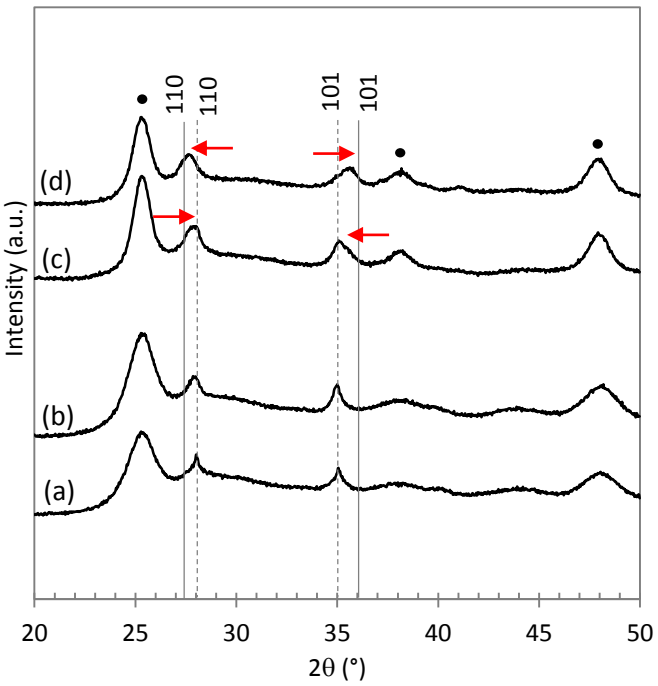

Figure 5-20: XRD patterns of (a) TiSi91Ru450, (b) TiSi91Ru450-WI, (c) TiAl91Ru450, and (d) TiSi91Ru450-WI; black dots (●) indicate anatase TiO_2 phase, dotted lines indicate RuO_2 phase, and solid lines indicate rutile TiO_2 phase. Red arrows point the location and shift direction of RuO_2 peaks.

Cross-sectional TEM analysis revealed that the wet impregnation method resulted in the Ru-species being located inside the pores of the support, whatever the nature of the latter as shown in Figure 5-21. Thus also for the TiSi support, the distribution throughout the support porosity is achieved in this case, unlike when the deposition of pre-formed RuO_2 nanoparticles was used as the preparation method. This indicates that dissolved $RuCl_3$ solution was able to diffuse inside the pores of Ti-Si mixed oxides while pre-synthesized 2 nm RuO_2 nanoparticles were prevented to diffuse through the possible electrostatic repulsion or crust of the aerosol particles. The catalytic activity of the TiSi91Ru450-WI showed significant improvement compared to that of TiSi91Ru450 prepared by RuO_2 deposition. The same trend was observed for TiAl91Ru450-WI and TiAl91Ru450. It must be highlighted that this result again points to the crucial role of the interaction of the RuO_2 phase with the TiO_2-based support upon annealing, for the development of more active catalysts. The catalysts that display this interaction (attested by the shift in the XRD peak position for RuO_2) are more active.

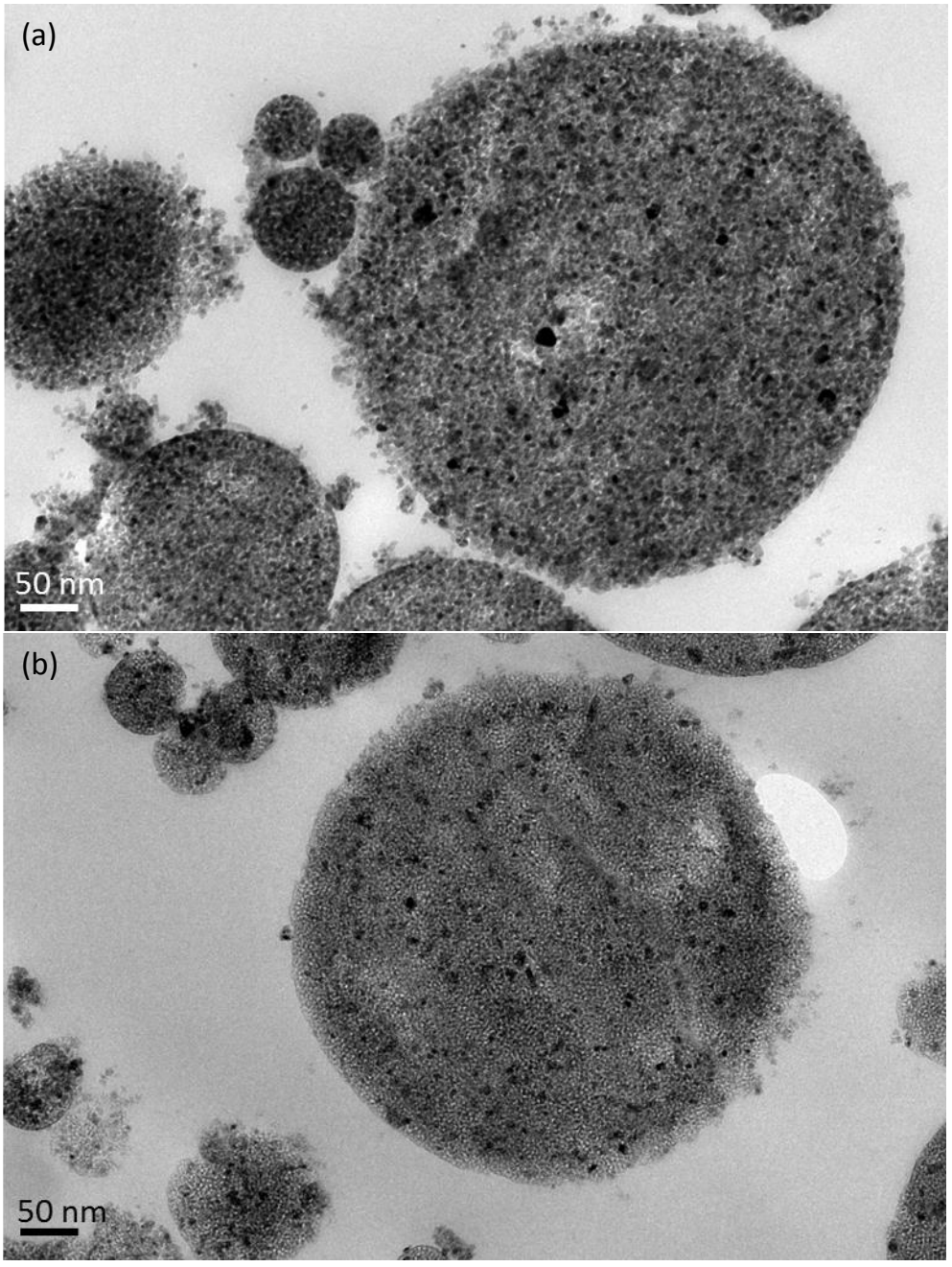

Figure 5-21: TEM images of (a) TiSi91Ru450-WI and (b) TiAl91Ru450-WI, after in situ reduction and methanation.

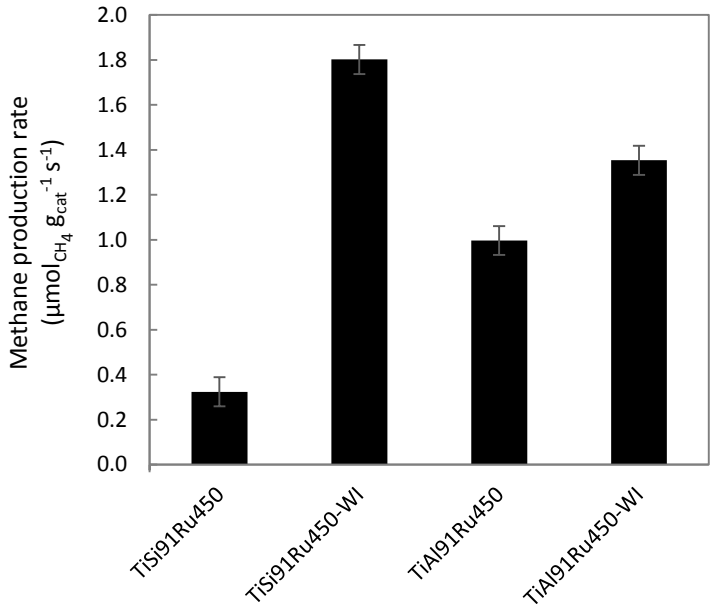

Figure 5-22: Comparison of methanation activities at 200 °C.

Figure 5-23 shows the XRD patterns of the wet-impregnated catalysts before and after (in situ reduction and) methanation. Two important phenomena are observed.

First, 110 and 101 rutile TiO_2 are formed after methanation for both catalysts (indicated by red arrows). This was not observed on catalysts prepared by the deposition method. Second, crystalline planes of metallic Ru crystallites were not detected for reduced wet-impregnated catalysts, in contrast to the catalysts prepared by deposition of RuO_2 nanoparticles (refer to Figure 5-18). The tiny bump at $2\theta \sim 44°$ corresponds to the strongest 101 Ru peak position, however, it is difficult to be identified as 101 Ru since it overlaps with 210 rutile TiO_2.

The first phenomenon could be explained by a hypothesis that, when the RuO_2 was reduced, the abundant metastable epitaxial rutile TiO_2 (110 and 101 d-spacing in between RuO_2 and rutile TiO_2) becomes stabilized by arranging itself to transform into a complete rutile structure, possibly facilitated by the exothermic reaction environment or by the fact that no interaction is further possible with the partner of the epitaxy (RuO_2 is reduced to Ru). The second phenomenon indicates the formation of smaller Ru particles as compared to the case of catalysts prepared by the deposition method, consistent with a better dispersion of the Ru precursors on

the support surface and a good interaction with the latter preventing heavy sintering.

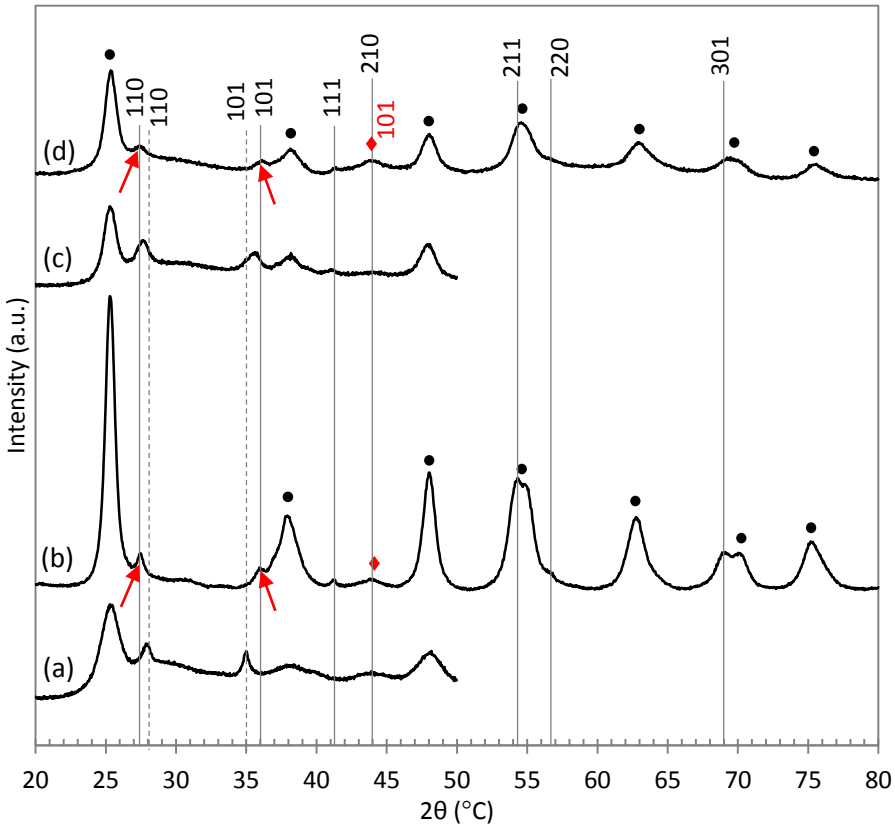

Figure 5-23: XRD patterns of (a) TiSi91Ru450-WI, (b) TiSi91Ru450-WI-spent, (c) TiAl91Ru450-WI, and (d) TiAl91Ru450-WI-spent; black dots (●) indicate anatase TiO_2 phases, red diamond (♦) indicates position of metallic Ru (101), dotted lines indicate RuO_2 phase, and solid lines indicate rutile TiO_2 phase. Red arrows emphasize the 110 and 101 rutile TiO_2 peaks.

H_2-TPR analysis showed that the main reduction events occurred at 230 °C and 243°C for TiSi91Ru450-WI and TiAl91Ru450-WI, respectively. Clearly, the reducing behaviour of the wet-impregnated catalysts was different from the RuO_2-deposited catalysts. This again points to a stronger interaction between the TiO_2 support and the RuO_2 species, which consequently become less reducible. Apart from dispersion effects largely discussed in this thesis, it is possible that the reducibility of the RuO_2 species stabilized on the catalysts is an additional decisive factor dictating

methanation activity. Further investigation (in situ techniques) would be needed to relate the oxidation state of Ru during reaction with methanation activity.

4. Conclusion

Mesoporous mixed oxides of Ti-Si and Ti-Al were successfully prepared at two different mixed ratios via integration of aerosol-assisted self-assembly process and AcHE sol-gel chemistry. The thermal stability of these mesoporous mixed oxides was greatly enhanced compared to pure mesoporous TiO_2; the mesostructure was maintained even after calcination at 450 °C. The improved thermal stability was strongly correlated to the delay in the crystallization temperature compared to the pure mesoporous TiO_2.

Nevertheless, the preparation of Ru supported catalyst – and more precisely the annealing step – disturbed the textural properties of the mixed oxides. Addition of small amount of Si or Al in the mixed oxide was sufficient to lower the tendency of TiO_2 to phase segregate. Indeed, TiO_2 phase segregation and texture collapse was much less pronounced than in the case of pure mesoporous TiO_2 support (Chapter 4), and the lower Ti content in the mixture inhibited the TiO_2 crystallization even in presence of RuO_2 nanoparticles.

In parallel, the interaction of the RuO_2 phase with the support was perturbed by the presence of the other oxide in the supports. The RuO_2 peak was shifted toward the position of TiO_2 rutile in the cases where TiO_2 tends to crystallize and the texture tends to collapse (especially in the case of Ti-Al mixed oxide support and at high Ti content). On the other hand crystalline RuO_2 was observed un-shifted in the catalysts that maintain their texture and their amorphous character (especially in the case of Ti-Si mixed support and at low Ti content).

The catalytic performances were not enhanced when the support structure could be preserved. On the contrary, higher catalytic activities were observed on the support that underwent severe modifications and exhibiting rutile structure (including shift or broadening of in RuO_2 peak positions towards rutile TiO_2 peak positions). This clearly occurs when the interaction of RuO_2 with the support is good. Furthermore, the improved catalytic activity was observed when Ru species are within the pores of the mesoporous mixed oxide particles. This Ru incorporation within the pores achieved by wet impregnation of $RuCl_3$ was shown to eliminate the electrostatic repulsion or physical barrier for the Ru-species to diffuse inside the pores.

Regarding the nature of the support compositions, it was demonstrated that Al_2O_3 and SiO_2 do not have any chemical effect on the catalytic activity, as mixing of Al_2O_3 or SiO_2 with a small amount of rutile TiO_2 as supports for Ru-species resulted in the same catalytic performance, much higher than that of pure Al_2O_3 or SiO_2 supported catalysts.

This study provides a useful insight that the catalytic performance is not directly dependant on the mixing ratio and nature of added element in the Ti-based support. More significantly, the formation of epitaxial rutile structure promotes the catalytic performance as a support for Ru-based catalyst and is envisaged to play a role in the reducibility, size, and dispersion of the Ru-species.

General Conclusion

This thesis is developed to provide an understanding of morphological factors of a chosen catalyst, Ru/TiO_2, which influence the catalytic performance in CO_2 methanation. Recycling of CO_2 originating from carbon-intensive energy sectors has a great environmental and industrial advantage, provided H_2 can be produced via renewable pathways. Thus, development of catalysts for CO_2 hydrogenation to CH_4 has been extensively studied on different metal-based catalytic systems in search for high selectivity and low temperature operation. Yet, fundamental understanding of the structure of catalysts that may influence the catalytic performance has been less exploited. Therefore, this thesis deals with necessary components to provide an insight to the catalysts' structure-performance relationship with an aim to contribute to careful design and development of catalysts of similar catalytic systems. It is envisaged that progress can be made in the case of various catalytic systems including CO_2 hydrogenation reactions as well as different catalytic reactions using Ru/TiO_2 or RuO_2/TiO_2 as catalysts.

Specific focus of this thesis work has been on crystallinity, composition, porosity, and textural properties of TiO_2 materials as supports for Ru-based nanoparticles. For systematic studies, calibrated RuO_2 nanoparticles of uniform size distribution (2nm) served as a primary source of active metallic Ru phase. The role of TiO_2 crystal structures on the morphology of Ru or RuO_2 nanoparticles was explored by extensive materials characterization techniques, mesoporous TiO_2-based materials were strategically synthesized to serve as new support materials for Ru-based catalysts, and the structures of these catalysts were related to the catalytic performance in CO_2 methanation. Several important parameters of the CO_2 methanation reaction was fixed constant to extract the information with regards to structure-performance relationship of the catalysts; reactant composition was set at stoichiometric molar ratio of $H_2/CO_2 = 4$, low reaction temperature was chosen and set at ≤ 200 °C. In these conditions, selectivity to CH_4 was always 100 %.

The TiO_2 crystal structure has shown to have an important impact on the morphology and location of Ru-species; the initially deposited RuO_2 nanoparticles

selectively migrated to and stabilized on rutile TiO_2 crystal phase. Subsequently, metallic Ru species are formed upon thermal reduction on the same location where they were initially present in an oxidized form. This RuO_2 migration phenomenon, initially driven by the applied energy (heat), was shown to be due to the strong interactions between the RuO_2 and rutile TiO_2, which lead to a transformation of RuO_2 nanoparticles to anisotropic epitaxial layers over the rutile TiO_2. The formation of epitaxial layer of RuO_2 over rutile TiO_2 was due to their lattice-matched interfacial structure. It is clearly demonstrated by X-ray diffraction. On the contrary, there was weak interactions between the RuO_2 and anatase TiO_2 phase which induced sintering and isotropic growth of large RuO_2 crystals. The mixed crystalline phases of rutile and anatase TiO_2 was shown to successfully modulate the interactions between the RuO_2 nanoparticles and the support, which resulted in well-dispersed RuO_2 phase. Consequently, the well-dispersed active Ru-species were formed which was found to be responsible for an improved catalytic performance in CO_2 methanation reaction.

The mixed crystalline phases of anatase and rutile TiO_2 indeed resulted in synergy in catalytic performance in CO_2 methanation, synergy being defined as a higher activity of the catalysts supported on mixed TiO_2 phases as compared to that of the weighted average of the catalysts supported on pure TiO_2 phases. Interestingly, the synergy was not originating from the co-existence of the anatase and rutile TiO_2 phases in the reaction but rather from the location of Ru-species affected by the co-existence of anatase and rutile TiO_2 phases. The migration of RuO_2 nanoparticles towards rutile TiO_2 phase during annealing led to the higher Ru dispersion and synergy in catalytic performance. It was ultimately demonstrated that the non-sintering rutile TiO_2 support is the best support for high catalytic activity due to the stabilized Ru-species resulting in high Ru dispersion.

The phenomenon of mobility and migration of RuO_2 nanoparticles towards rutile TiO_2 phases was attempted to be clarified by in situ study thanks to state-of-the-art environmental TEM analysis at atmospheric pressure. However, the preliminary experiments have demonstrated the challenges of in situ studies to mimic the real annealing conditions. Nevertheless, the combination of in situ and ex situ studies have shown that the mechanism of RuO_2 migration involves two possible phenomena: (i) local volatilization of RuO_2 species followed by re-deposition and (ii) surface diffusion of mobile molecular Ru species. We propose that these two phenomena co-exist, with one being predominant over the other depending on the environment. The stabilized RuO_2 species were demonstrated to be found on various crystallographic planes of isotropic rutile particles of TiO_2-P25.

Mesoporous TiO_2 with low crystallinity and high surface area as a new support material for Ru phases was successfully synthesized via integration of aerosol-assisted self-assembly process and acetic acid mediated sol-gel chemistry. The mesoporous TiO_2 exhibited high surface area and porosity as well as great versatility in the control of the textural properties. The deposition of RuO_2 nanoparticles on low crystalline TiO_2 support promoted the growth of rutile phase TiO_2 at annealing temperature as low as 250 °C, due to the close structural similarities of RuO_2 and rutile TiO_2. Interestingly, the catalytic performance is influenced by the formation of the (epitaxial) rutile phase. Indeed, the stability of Ru-phase and the Ru dispersion was affected by the interaction between the Ru-species and the support. The high specific surface area was found to be not beneficial for low metal loading (Ru = 2.2 wt. %). Yet, it is envisaged to be beneficial for higher metal loading.

The integration of aerosol-assisted self-assembly process and acetic acid mediated sol-gel chemistry allowed to prepare mesoporous multicomponent oxides; Ti-Si mixed oxides and Ti-Al mixed oxides were successfully prepared to serve as support materials for Ru-species. The incorporation of Si or Al oxide species enhanced thermal stability of the mesoporous TiO_2-based oxides. It was further demonstrated that the Si- or Al- oxide species do not play a direct role in CO_2 methanation. Rather, the epitaxial stabilization of RuO_2 species was anticipated to be the contributor to the higher catalytic activity. More thermally stable Ti-based mixed oxides were less prone to the rutile phase transformation and thus exhibited lower catalytic activities compared to the pure TiO_2 supported catalysts.

This thesis work demonstrates the importance of the morphological aspect of Ru/TiO_2 methanation catalysts in designing of efficient heterogeneous catalysts. It was found that RuO_2 stabilization on rutile TiO_2 is the key to better performance of Ru/TiO_2 methanation catalysts. The critical role of annealing step on RuO_2 morphology was demonstrated via migration, sintering, and epitaxial stabilization. The resulting RuO_2 morphology was found to influence the formation of active Ru phase which impacted the catalytic activity. Finally, rutile TiO_2 was shown to play a crucial role in the high catalytic performance.

This thesis work may provide future research prospects in several directions. First, determination of catalytic active sites can be explored. As this current study has shown the similar activation energy for all Ru/TiO_2 catalysts explored in this thesis, the nature of active sites should be similar. Thus, the number of active sites responsible for the catalytic performance could be evaluated. For instance, in situ

studies such as diffusion reflectance infrared spectroscopy (DRIFTS) can be conducted on the catalysts during or after CO adsorption. Indeed, Ru can adsorb CO in various conformations [213]. Linear or bridge type CO adsorption on Ru may provide an insight to the adsorbed CO species on different facets, edges, or steps of active Ru metal which then can be correlated to the CO_2 methanation performance. Second, the possible reaction mechanism as well as rate determining step can be investigated. To do so, in situ near-ambient-pressure X-ray photoelectron spectroscopy (NAP-XPS) may give an indication towards the surface adsorbed intermediate species. Furthermore, a comparison with different catalyst systems (i.e. Ru/TiO_2 catalyst with other CO_2 methanation catalysts) during the in situ analysis could reveal why one type of catalyst is better than the other. Third, the correlation between H_2 consumption and oxidation state could help deeper understanding of the relation between metal-support interactions (i.e. RuO_2-TiO_2) and the resulting catalytic performance. This current study has suggested that there could be an optimal reducibility of Ru oxide species for optimal catalytic performance. Quantitative analysis of H_2 consumption by temperature-programmed reduction (TPR) analysis could be correlated with the oxidation states of active species which may indicate the strength of RuO_2-TiO_2 interactions responsible for the optimal catalytic performance.

Towards industrial applications, it is suggested that rutile TiO_2 is potentially the best support for active Ru phase provided that the metallic Ru is formed through RuO_2-TiO_2 epitaxial stabilization and that the support does not sinter. Furthermore, for the improved catalytic performance, low crystalline mesoporous TiO_2 with high surface area is envisaged to serve as an efficient support for higher Ru loading. The facile epitaxial transformation of rutile TiO_2 in presence of RuO_2 may contribute to higher Ru dispersion on TiO_2 support with high surface area without severe concentration of Ru species as it is expected in case of high Ru loading on low surface area support.

Appendix

A. Characterization of pre-synthesized RuO_2 nanoparticles

The RuO_2 nanoparticles in colloidal suspension are well separated and dispersed in size. The average diameter of particles by TEM analysis are measured to be 2.0 $\pm$ 0.2 nm (Figure A-1). Crystalline rutile RuO2 structure is visible under electron beam (Figure A-2). The RuO_2 nanoparticles suspension is highly stable; initial pH = 2 does not evolve for months. Isoelectric point is estimated at 5.

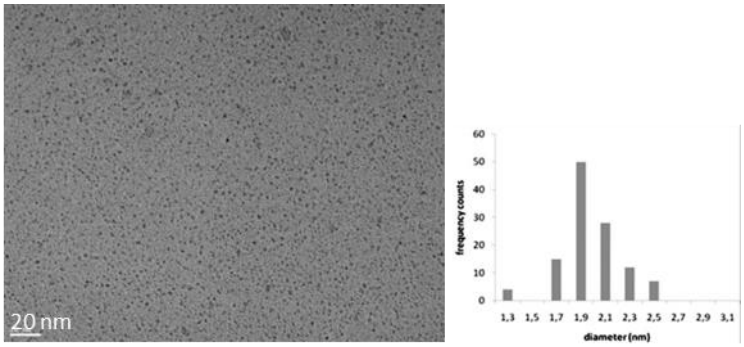

Figure A-1: TEM image of pre-synthesized RuO_2 nanoparticles and their size distribution measured by TEM.

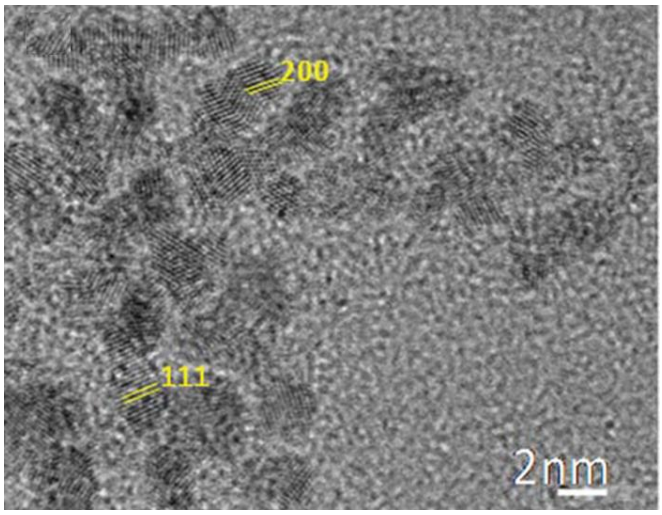

Figure A-2: HRTEM image of pre-synthesized RuO_2 nanoparticles showing rutile structure.

B. Chlorine content in catalysts

Table B-1 shows that washing catalysts (RuO_2/TiO2-P25) with water effectively lowers the surface chlorine content. However, the chlorine content levels off to zero percent after annealing at 450 °C no matter the catalyst is washed or not.

Table B-1: Atomic percentage (at. %) of chlorine in the catalysts measured by XPS after washing with water and after annealing at 450 °C.

	0x	**1x**	**3x**	**5x**
Washing with water	1.35	1.05	0.83	0.76
After annealing at 450 °C	0	0	0	0

The catalytic activities of non-washed (0x) and washed (3x) were the same (Figure B-1).

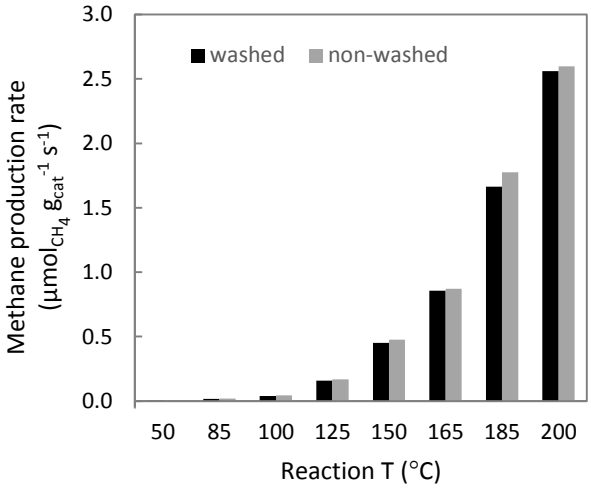

Figure B-1: Catalytic activities comparison of washed vs. non-washed catalysts after annealing at 450 °C.

C. TiO_2 particle size measured by TEM

The average particle sizes of initial TiO_2 supports measured from TEM images are 28 nm for P25, 6.3 nm for anatase TiO_2, and 11 (width) x 100 (length) nm for rutile TiO_2. The size histograms are shown in Figure C-1.

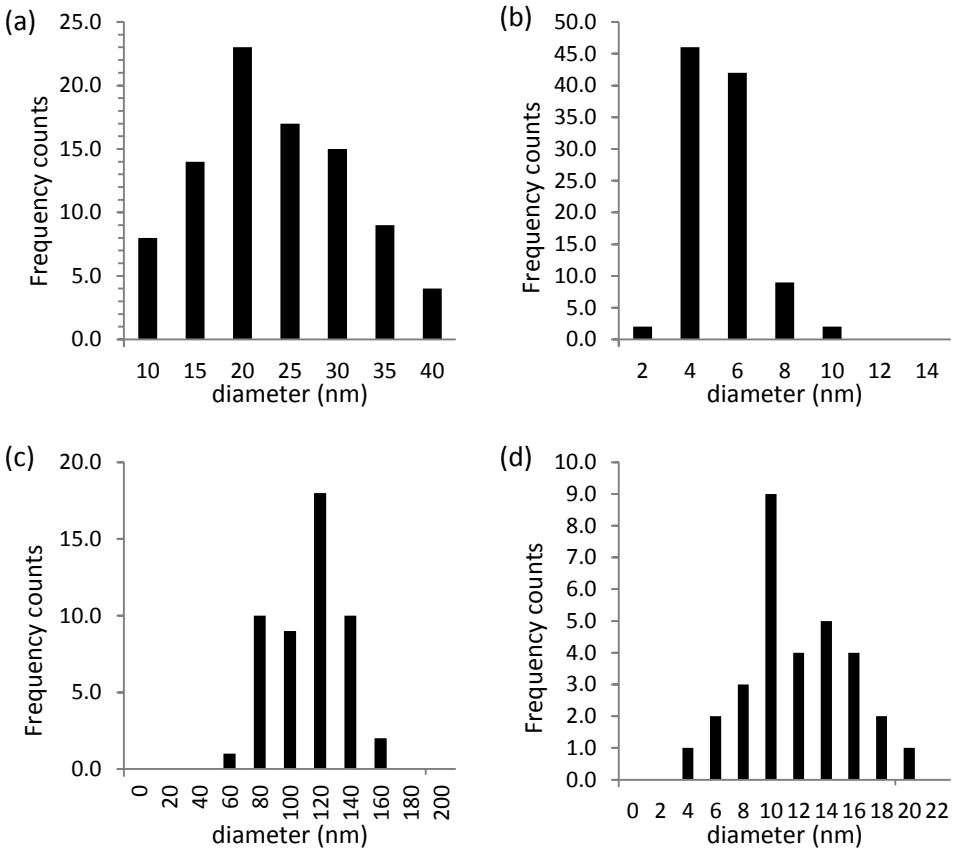

Figure C-1: Initial TiO_2 particle size measured by TEM; (a) P25, (b) anatase, (c) rutile length, and (d) rutile width.

D. CO_2 conversion and CH_4 yield

The catalytic activity is represented as methane production rate, CO_2 conversion, and CH_4 yield in Table D-1. For all catalysts studied, the selectivity to CH_4 was 100 % (confirmed by carbon balance).

Table D-1: Catalytic activity represented in different definitions.

Support	µmol (CH_4) $gcat^{-1}$ s^{-1}	X (CO_2)	Y (CH_4)
P25	2.57	27.4	33.2
Anatase	1.59	16.3	22.4
rutile	0.98	12.1	13.7

E. Catalytic activity vs. time

The catalytic activities of all catalysts studied in this thesis was stable at each reaction temperature over time. An example is shown in Figure E-1.

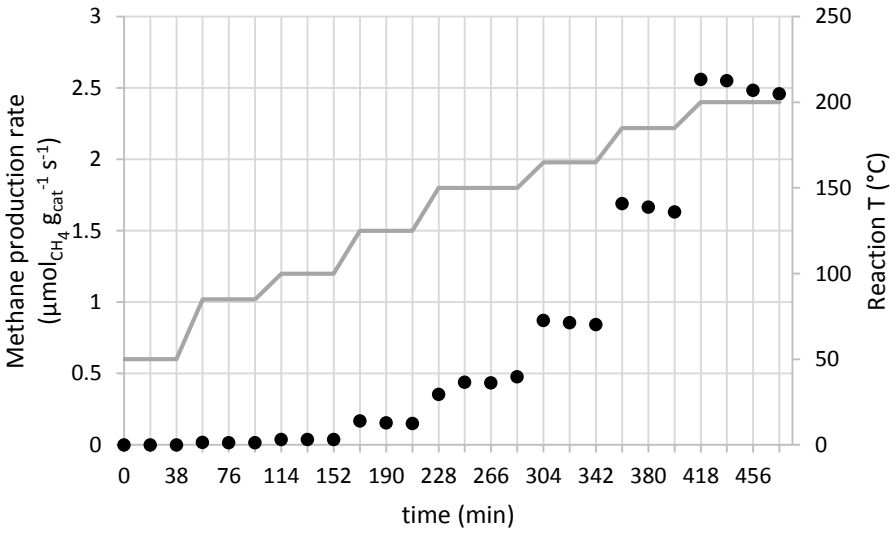

Figure E-1: Catalytic activity of Ru/TiO_2-P25-450 vs. time. Reaction temperature program is represented in grey line and the repeated catalytic activity measurements (every 19 min) are shown in black dots.

References

1. *World Energy Outlook Special Report 2015: Energy and Climate Change*, F. Birol, Editor. 2015, International Energy Agency: Paris.
2. *Climate Change 2014: Synthesis Report*, R.K.P.a.L.A.M. Core Writing Team, Editor. 2014, Intergovernmental Panel on Climate Change (IPCC): Geneva, Switzerland.
3. Wei, W. and G. Jinlong, *Methanation of carbon dioxide: an overview.* Frontiers of Chemical Science and Engineering, 2010. **5**(1): p. 2-10.
4. Riduan, S.N. and Y. Zhang, *Recent developments in carbon dioxide utilization under mild conditions.* Dalton Transactions, 2010. **39**(14): p. 3347-3357.
5. Wang, W., et al., *Recent advances in catalytic hydrogenation of carbon dioxide.* Chemical Society Reviews, 2011. **40**(7): p. 3703-3727.
6. Yang, H., et al., *Progress in carbon dioxide separation and capture: A review.* Journal of Environmental Sciences, 2008. **20**(1): p. 14-27.
7. Aziz, M.A.A., et al., *CO2 methanation over heterogeneous catalysts: recent progress and future prospects.* Green Chemistry, 2015. **17**(5): p. 2647-2663.
8. Ola, O., M. Mercedes Maroto-Valer, and S. Mackintosh, *Turning CO2 into Valuable Chemicals.* Energy Procedia, 2013. **37**: p. 6704-6709.
9. Mikkelsen, M., M. Jorgensen, and F.C. Krebs, *The teraton challenge. A review of fixation and transformation of carbon dioxide.* Energy & Environmental Science, 2010. **3**(1): p. 43-81.
10. Centi, G. and S. Perathoner, *Opportunities and prospects in the chemical recycling of carbon dioxide to fuels.* Catalysis Today, 2009. **148**(3–4): p. 191-205.
11. Over, H., *Surface Chemistry of Ruthenium Dioxide in Heterogeneous Catalysis and Electrocatalysis: From Fundamental to Applied Research.* Chemical Reviews, 2012. **112**(6): p. 3356-3426.
12. Rard, J.A., *Chemistry and thermodynamics of ruthenium and some of its inorganic compounds and aqueous species.* Chemical Reviews, 1985. **85**(1): p. 1-39.
13. Higgins, S., *Regarding ruthenium.* Nat Chem, 2010. **2**(12): p. 1100-1100.

14. Nguyen, S.T., R.H. Grubbs, and J.W. Ziller, *Syntheses and activities of new single-component, ruthenium-based olefin metathesis catalysts.* Journal of the American Chemical Society, 1993. **115**(21): p. 9858-9859.
15. Vougioukalakis, G.C. and R.H. Grubbs, *Ruthenium-Based Heterocyclic Carbene-Coordinated Olefin Metathesis Catalysts.* Chemical Reviews, 2010. **110**(3): p. 1746-1787.
16. Bond, G.G. and G. Webb, *Ruthenium and Osmium as Hydrogenation Catalysts.* Platinum Metals Review, 1962. **6**(1): p. 12-19.
17. Muhler, M., et al., *Ruthenium as catalyst for ammonia synthesis*, in *Studies in Surface Science and Catalysis*, W.N.D.E.I. Joe W. Hightower and T.B. Alexis, Editors. 1996, Elsevier. p. 317-326.
18. Grätzel, M., *Dye-sensitized solar cells.* Journal of Photochemistry and Photobiology C: Photochemistry Reviews, 2003. **4**(2): p. 145-153.
19. Chan, H.Y.H., C.G. Takoudis, and M.J. Weaver, *High-Pressure Oxidation of Ruthenium as Probed by Surface-Enhanced Raman and X-Ray Photoelectron Spectroscopies.* Journal of Catalysis, 1997. **172**(2): p. 336-345.
20. Lewerenz, H.J., S. Stucki, and R. Kötz, *Oxygen evolution and corrosion: XPS investigation on Ru and RuO2 electrodes.* Surface Science, 1983. **126**(1): p. 463-468.
21. Morgan, D.J., *Resolving ruthenium: XPS studies of common ruthenium materials.* Surface and Interface Analysis, 2015. **47**(11): p. 1072-1079.
22. Grillo, M.E., *Stability of corundum- versus rutile-type structures of ruthenium and rhodium oxides.* Physical Review B, 2004. **70**(18): p. 184115.
23. Over, H., *Ruthenium dioxide, a fascinating material for atomic scale surface chemistry.* Applied Physics A, 2002. **75**(1): p. 37-44.
24. Honkala, K., et al., *Ammonia Synthesis from First-Principles Calculations.* Science, 2005. **307**(5709): p. 555-558.
25. Hinrichsen, O., et al., *The microkinetics of ammonia synthesis catalyzed by cesium-promoted supported ruthenium.* Chemical Engineering Science, 1996. **51**(10): p. 1683-1690.
26. Abe, T., et al., *CO2 methanation property of Ru nanoparticle-loaded TiO2 prepared by a polygonal barrel-sputtering method.* Energy & Environmental Science, 2009. **2**(3): p. 315.
27. Seki, K., *Development of RuO2/Rutile-TiO2 Catalyst for Industrial HCl Oxidation Process.* Catalysis Surveys from Asia, 2010. **14**(3-4): p. 168-175.
28. Vadimsky, R.G., R.P. Frankenthal, and D.E. Thompson, *Ru and RuO2 as Electrical Contact Materials: Preparation and Environmental Interactions.* Journal of The Electrochemical Society, 1979. **126**(11): p. 2017-2023.
29. Assmann, J., et al., *On the Nature of the Active State of Supported Ruthenium Catalysts Used for the Oxidation of Carbon Monoxide: Steady-*

State and Transient Kinetics Combined with in Situ Infrared Spectroscopy†. The Journal of Physical Chemistry B, 2004. **108**(38): p. 14634-14642.
30. Bond, G.C., et al., *Effect of Various Pretreatments on the Structure and Properties of Ruthenium Catalysts.* Journal of Catalysis, 1996. **161**(1): p. 480-494.
31. Vogel, W., et al., *Ru Clusters Synthesized Chemically from Dissolved Carbonyl: In Situ Study of a Novel Electrocatalyst in the Gas Phase and in Electrochemical Environment.* The Journal of Physical Chemistry B, 2001. **105**(22): p. 5238-5243.
32. Rossi, L.M., et al., *Ruthenium dioxide nanoparticles in ionic liquids: synthesis, characterization and catalytic properties in hydrogenation of olefins and arenes.* Journal of the Brazilian Chemical Society, 2004. **15**: p. 901-910.
33. Iqbal, S., et al., *Ruthenium Nanoparticles Supported on Carbon: An Active Catalyst for the Hydrogenation of Lactic Acid to 1,2-Propanediol.* ACS Catalysis, 2015. **5**(9): p. 5047-5059.
34. Rachiero, G.P., U.B. Demirci, and P. Miele, *Facile synthesis by polyol method of a ruthenium catalyst supported on γ-Al2O3 for hydrolytic dehydrogenation of ammonia borane.* Catalysis Today, 2011. **170**(1): p. 85-92.
35. Li, H., et al., *Ultrasound-Assisted Polyol Method for the Preparation of SBA-15-Supported Ruthenium Nanoparticles and the Study of Their Catalytic Activity on the Partial Oxidation of Methane.* Langmuir, 2004. **20**(19): p. 8352-8356.
36. Chen, Y., K.Y. Liew, and J. Li, *Size-controlled synthesis of Ru nanoparticles by ethylene glycol reduction.* Materials Letters, 2008. **62**(6–7): p. 1018-1021.
37. Zawadzki, M. and J. Okal, *Synthesis and structure characterization of Ru nanoparticles stabilized by PVP or γ-Al2O3.* Materials Research Bulletin, 2008. **43**(11): p. 3111-3121.
38. Liang, C., et al., *Controlled synthesis of supported ruthenium catalysts for CO oxidation by organometallic chemical vapor deposition*, in *Studies in Surface Science and Catalysis*, M.D.D.E.D.V.S.H.P.A.J.J.A.M. E.M. Gaigneaux and P. Ruiz, Editors. 2006, Elsevier. p. 473-480.
39. Chang, K.-H. and C.-C. Hu, *Hydrothermal Synthesis of Hydrous Crystalline RuO2 Nanoparticles for Supercapacitors.* Electrochemical and Solid-State Letters, 2004. **7**(12): p. A466-A469.
40. Lin, Y., et al., *Synthesis of Ruthenium Dioxide Nanoparticles by a Two-Phase Route and Their Electrochemical Properties.* The Journal of Physical Chemistry C, 2008. **112**(42): p. 16219-16224.
41. Sassoye, C., et al., *A sustainable aqueous route to highly stable suspensions of monodispersed nano ruthenia.* Green Chemistry, 2011. **13**(11): p. 3230-3237.

42. Chen, X. and S.S. Mao, *Titanium Dioxide Nanomaterials: Synthesis, Properties, Modifications, and Applications.* Chemical Reviews, 2007. **107**(7): p. 2891-2959.
43. Bagheri, S., N. Muhd Julkapli, and S. Bee Abd Hamid, *Titanium Dioxide as a Catalyst Support in Heterogeneous Catalysis.* The Scientific World Journal, 2014. **2014**: p. 21.
44. Wetchakun, N., et al., *Influence of calcination temperature on anatase to rutile phase transformation in TiO2 nanoparticles synthesized by the modified sol–gel method.* Materials Letters, 2012. **82**(0): p. 195-198.
45. Hanaor, D.H. and C. Sorrell, *Review of the anatase to rutile phase transformation.* Journal of Materials Science, 2011. **46**(4): p. 855-874.
46. Choudhury, B. and A. Choudhury, *Local structure modification and phase transformation of TiO2 nanoparticles initiated by oxygen defects, grain size, and annealing temperature.* International Nano Letters, 2013. **3**(1): p. 1-9.
47. Tonomura, O., et al., *Band Engineering of Ru/Rutile-TiO2/Ru Capacitors by Doping Cobalt to Suppress Leakage Current.* Journal of The Electrochemical Society, 2011. **159**(1): p. G1-G5.
48. Oskam, G., et al., *The Growth Kinetics of TiO2 Nanoparticles from Titanium(IV) Alkoxide at High Water/Titanium Ratio.* The Journal of Physical Chemistry B, 2003. **107**(8): p. 1734-1738.
49. Livage, J. and C. Sanchez, *Sol-gel chemistry.* Journal of Non-Crystalline Solids, 1992. **145**: p. 11-19.
50. Livage, J., M. Henry, and C. Sanchez, *Sol-gel chemistry of transition metal oxides.* Progress in Solid State Chemistry, 1988. **18**(4): p. 259-341.
51. Barthez, J.M., et al., *Hydrolysis and Condensation of Transition Metal Alkoxide: Experiments and Simulations.* Journal of Sol-Gel Science and Technology, 1997. **8**(1-3): p. 83-88.
52. Barringer, E.A. and H.K. Bowen, *High-purity, monodisperse TiO2 powders by hydrolysis of titanium tetraethoxide. 1. Synthesis and physical properties.* Langmuir, 1985. **1**(4): p. 414-420.
53. Doeuff, S., et al., *Hydrolysis of titanium alkoxides: Modification of the molecular precursor by acetic acid.* Journal of Non-Crystalline Solids, 1987. **89**(1–2): p. 206-216.
54. Fan, J., S.W. Boettcher, and G.D. Stucky, *Nanoparticle Assembly of Ordered Multicomponent Mesostructured Metal Oxides via a Versatile Sol−Gel Process.* Chemistry of Materials, 2006. **18**(26): p. 6391-6396.
55. Debecker, D.P. and P.H. Mutin, *Non-hydrolytic sol-gel routes to heterogeneous catalysts.* Chemical Society Reviews, 2012. **41**(9): p. 3624-3650.

56. Gressel-Michel, E., D. Chaumont, and D. Stuerga, *From a microwave flash-synthesized TiO2 colloidal suspension to TiO2 thin films.* Journal of Colloid and Interface Science, 2005. **285**(2): p. 674-679.
57. Corradi, A.B., et al., *Conventional and Microwave-Hydrothermal Synthesis of TiO2 Nanopowders.* Journal of the American Ceramic Society, 2005. **88**(9): p. 2639-2641.
58. Dufour, F., et al., *Do TiO2 Nanoparticles Really Taste Better When Cooked in a Microwave Oven?* European Journal of Inorganic Chemistry, 2012. **2012**(16): p. 2707-2715.
59. Li, W., et al., *A Perspective on Mesoporous TiO2 Materials.* Chemistry of Materials, 2014. **26**(1): p. 287-298.
60. Wang, Y.-d., et al., *Synthesis and characterization of amorphous TiO2 with wormhole-like framework mesostructure.* Journal of Non-Crystalline Solids, 2003. **319**(1–2): p. 109-116.
61. Antonelli, D.M. and J.Y. Ying, *Synthesis of Hexagonally Packed Mesoporous TiO2 by a Modified Sol–Gel Method.* Angewandte Chemie International Edition in English, 1995. **34**(18): p. 2014-2017.
62. Cabrera, S., et al., *Enhanced surface area in thermally stable pure mesoporous TiO2.* Solid State Sciences, 2000. **2**(5): p. 513-518.
63. Yang, P., et al., *Generalized syntheses of large-pore mesoporous metal oxides with semicrystalline frameworks.* Nature, 1998. **396**(6707): p. 152-155.
64. Lu, Y., et al., *Aerosol-assisted self-assembly of mesostructured spherical nanoparticles.* Nature, 1999. **398**(6724): p. 223-226.
65. Boissiere, C., et al., *First in-situ SAXS studies of the mesostructuration of spherical silica and titania particles during spray-drying process.* Chemical Communications, 2003(22): p. 2798-2799.
66. Tsung, C.-K., et al., *A General Route to Diverse Mesoporous Metal Oxide Submicrospheres with Highly Crystalline Frameworks.* Angewandte Chemie International Edition, 2008. **47**(45): p. 8682-8686.
67. Grosso, D., et al., *Nanocrystalline Transition-Metal Oxide Spheres with Controlled Multi-Scale Porosity.* Advanced Functional Materials, 2003. **13**(1): p. 37-42.
68. Komaya, T., et al., *The Influence of Metal-Support Interactions on the Accurate Determination of Ru Dispersion for Ru/TiO2.* Journal of Catalysis, 1994. **149**(1): p. 142-148.
69. Wang, B., et al., *Remarkable crystal phase effect of Cu/TiO2 catalysts on the selective hydrogenation of dimethyl oxalate.* RSC Advances, 2015. **5**(37): p. 29040-29047.
70. Omotoso, T., S. Boonyasuwat, and S.P. Crossley, *Understanding the role of TiO2 crystal structure on the enhanced activity and stability of Ru/TiO2*

catalysts for the conversion of lignin-derived oxygenates. Green Chemistry, 2014. **16**(2): p. 645-652.
71. Kondratenko, E.V., et al., *Superior activity of rutile-supported ruthenium nanoparticles for HCl oxidation.* Catalysis Science & Technology, 2013. **3**(10): p. 2555.
72. Lin, Q., et al., *Crystal phase effects on the structure and performance of ruthenium nanoparticles for CO2 hydrogenation.* Catalysis Science & Technology, 2014. **4**(7): p. 2058-2063.
73. Tauster, S.J., S.C. Fung, and R.L. Garten, *Strong metal-support interactions. Group 8 noble metals supported on titanium dioxide.* Journal of the American Chemical Society, 1978. **100**(1): p. 170-175.
74. Caballero, A., et al., *In situ spectroscopic detection of SMSI effect in a Ni/CeO2 system: hydrogen-induced burial and dig out of metallic nickel.* Chemical Communications, 2010. **46**(7): p. 1097-1099.
75. Bowker, M., et al., *Model catalyst studies of the strong metal–support interaction: Surface structure identified by STM on Pd nanoparticles on TiO2(110).* Journal of Catalysis, 2005. **234**(1): p. 172-181.
76. de la Pena O'Shea, V.A., et al., *Direct evidence of the SMSI decoration effect: the case of Co/TiO2 catalyst.* Chemical Communications, 2011. **47**(25): p. 7131-7133.
77. Gao, J., et al., *Recent advances in methanation catalysts for the production of synthetic natural gas.* RSC Advances, 2015. **5**(29): p. 22759-22776.
78. Wei, W. and G. Jinlong, *Methanation of carbon dioxide: an overview.* Frontiers of Chemical Science and Engineering, 2011. **5**(1): p. 2-10.
79. Fechete, I. and J. Vedrine, *Nanoporous Materials as New Engineered Catalysts for the Synthesis of Green Fuels.* Molecules, 2015. **20**(4): p. 5638.
80. Ma, J., et al., *A short review of catalysis for CO2 conversion.* Catalysis Today, 2009. **148**(3–4): p. 221-231.
81. Falconer, J.L. and A.E. Zağli, *Adsorption and methanation of carbon dioxide on a nickel/silica catalyst.* Journal of Catalysis, 1980. **62**(2): p. 280-285.
82. Marwood, M., R. Doepper, and A. Renken, *In-situ surface and gas phase analysis for kinetic studies under transient conditions. The catalytic hydrogenation of CO2.* Applied Catalysis A: General, 1997. **151**(1): p. 223-246.
83. Weatherbee, G.D. and C.H. Bartholomew, *Hydrogenation of CO2 on group VIII metals.* Journal of Catalysis, 1982. **77**(2): p. 460-472.
84. Oki, S. and R. Mezaki, *Mechanistic structure of the water-gas shift reaction in the vicinity of chemical equilibrium.* The Journal of Physical Chemistry, 1973. **77**(13): p. 1601-1605.

85. Wagner, C., *Adsorbed Atomic Species as Intermediates in Heterogeneous Catalysis*, in *Advances in Catalysis*, H.P. D.D. Eley and B.W. Paul, Editors. 1970, Academic Press. p. 323-381.
86. Jacquemin, M., A. Beuls, and P. Ruiz, *Catalytic production of methane from CO2 and H2 at low temperature: Insight on the reaction mechanism.* Catalysis Today, 2010. **157**(1–4): p. 462-466.
87. Fujita, S.-i., et al., *Mechanisms of methanation of carbon dioxide and carbon monoxide over nickel/alumina catalysts.* Applied Catalysis A: General, 1993. **104**(1): p. 87-100.
88. Peebles, D.E., D.W. Goodman, and J.M. White, *Methanation of carbon dioxide on nickel(100) and the effects of surface modifiers.* The Journal of Physical Chemistry, 1983. **87**(22): p. 4378-4387.
89. Choe S. J., K.H.J., Kim S. J., Park S. B. Park D. H, and Huh D. S., *Adsorbed Carbon Formation and Carbon Hydrogenation for CO2 Methanation on the Ni (111) surface: ASED-MO study.* Bulletin of the Korean Chemical Society, 2006. **26**: p. 1682-1688.
90. Akamaru, S., et al., *Density functional theory analysis of methanation reaction of CO2 on Ru nanoparticle supported on TiO2 (1 0 1).* Applied Catalysis A: General, 2014. **470**(0): p. 405-411.
91. Panagiotopoulou, P., D.I. Kondarides, and X.E. Verykios, *Mechanistic aspects of the selective methanation of CO over Ru/TiO2 catalyst.* Catalysis Today, 2012. **181**(1): p. 138-147.
92. Loveless, B.T., et al., *CO Chemisorption and Dissociation at High Coverages during CO Hydrogenation on Ru Catalysts.* Journal of the American Chemical Society, 2013. **135**(16): p. 6107-6121.
93. Solymosi, F. and M. Pásztor, *Analysis of the IR-spectral behavior of adsorbed CO formed in H2 + CO2 surface interaction over supported rhodium.* Journal of Catalysis, 1987. **104**(2): p. 312-322.
94. Trovarelli, A., C. de Leitenburg, and G. Dolcetti, *CO and CO2 hydrogenation under transient conditions over Rh-CeO2: novel positive effects of metal-support interaction on catalytic activity and selectivity.* Journal of the Chemical Society, Chemical Communications, 1991(7): p. 472-473.
95. Tada, S., et al., *Ni/CeO2 catalysts with high CO2 methanation activity and high CH4 selectivity at low temperatures.* International Journal of Hydrogen Energy, 2012. **37**(7): p. 5527-5531.
96. Vesselli, E., et al., *Carbon Dioxide Hydrogenation on Ni(110).* Journal of the American Chemical Society, 2008. **130**(34): p. 11417-11422.
97. Sharma, S., et al., *CO2 methanation on Ru-doped ceria.* Journal of Catalysis, 2011. **278**(2): p. 297-309.

98. Sane S, B.J., Damon J P, Masson J., *Raney metal catalysts. I: Comparative properties of Raney nickel proceeding from Ni-Al intermetallic phases.* Applied Catalysis, 1984. **9**(1): p. 69-83.
99. Riani, P., et al., *Unsupported versus alumina-supported Ni nanoparticles as catalysts for steam/ethanol conversion and CO2 methanation.* Journal of Molecular Catalysis A: Chemical, 2014. **383–384**: p. 10-16.
100. Graça, I., et al., *CO2 hydrogenation into CH4 on NiHNaUSY zeolites.* Applied Catalysis B: Environmental, 2014. **147**: p. 101-110.
101. Ocampo, F., et al., *Effect of Ce/Zr composition and noble metal promotion on nickel based CexZr1−xO2 catalysts for carbon dioxide methanation.* Applied Catalysis A: General, 2011. **392**(1–2): p. 36-44.
102. Aldana, P.A.U., et al., *Catalytic CO2 valorization into CH4 on Ni-based ceria-zirconia. Reaction mechanism by operando IR spectroscopy.* Catalysis Today, 2013. **215**: p. 201-207.
103. Hattori, H., *Solid base catalysts: generation of basic sites and application to organic synthesis.* Applied Catalysis A: General, 2001. **222**(1–2): p. 247-259.
104. Zhi, G., et al., *Effect of La2O3 modification on the catalytic performance of Ni/SiC for methanation of carbon dioxide.* Catalysis Communications, 2011. **16**(1): p. 56-59.
105. Zhu, H., et al., *Catalytic Methanation of Carbon Dioxide by Active Oxygen Material CexZr1−xO2 Supported Ni□Co Bimetallic Nanocatalysts.* AIChE Journal, 2013. **59**(7): p. 2567-2576.
106. Eckle, S., et al., *Influence of the catalyst loading on the activity and the CO selectivity of supported Ru catalysts in the selective methanation of CO in CO2 containing feed gases.* Catalysis Today, 2012. **181**(1): p. 40-51.
107. Karelovic, A. and P. Ruiz, *CO2 hydrogenation at low temperature over Rh/γ-Al2O3 catalysts: Effect of the metal particle size on catalytic performances and reaction mechanism.* Applied Catalysis B: Environmental, 2012. **113-114**: p. 237-249.
108. Kowalczyk, Z., et al., *Supported ruthenium catalysts for selective methanation of carbon oxides at very low COx/H2 ratios.* Applied Catalysis A: General, 2008. **342**(1–2): p. 35-39.
109. Xu, J., et al., *CO2 Methanation over TiO2 - Al2O3 Binary Oxides Supported Ru Catalysts.* Chinese Journal of Chemical Engineering, 2015.
110. Li, D., et al., *Hydrogenation of CO2 over sprayed Ru/TiO2 fine particles and strong metal–support interaction.* Applied Catalysis A: General, 1999. **180**(1–2): p. 227-235.
111. Batenburg, K.J., et al., *3D imaging of nanomaterials by discrete tomography.* Ultramicroscopy, 2009. **109**(6): p. 730-740.
112. Zürner, A., et al., *Discrete tomography of demanding samples based on a modified SIRT algorithm.* Ultramicroscopy, 2012. **115**: p. 41-49.

113. Patterson, A.L., *The Scherrer formula for x-ray particle-size determination.* Phys. Rev., 1939. **56**: p. 978-82.
114. Over, H., et al., *On the origin of the Ru-3d5/2 satellite feature from RuO2(1 1 0).* Surface Science, 2002. **504**(0): p. L196-L200.
115. Okal, J., et al., *The use of hydrogen chemisorption for the determination of Ru dispersion in Ru/γ-alumina catalysts.* Applied Catalysis A: General, 2007. **319**: p. 202-209.
116. Goodwin Jr, J.G., *Characterization of highly dispersed Ru catalysts by chemisorption.* Journal of Catalysis, 1981. **68**(1): p. 227-232.
117. Cuenya, B.R., *Synthesis and catalytic properties of metal nanoparticles: Size, shape, support, composition, and oxidation state effects.* Thin Solid Films, 2010. **518**(12): p. 3127-3150.
118. Campelo, J.M., et al., *Sustainable preparation of supported metal nanoparticles and their applications in catalysis.* ChemSusChem, 2009. **2**(1): p. 18-45.
119. Xiang, G., et al., *Size effects in atomic-level epitaxial redistribution process of RuO(2) over TiO(2).* Scientific Reports, 2012. **2**: p. 801.
120. Mahata, N., et al., *Phenol hydrogenation over palladium supported on magnesia: Relationship between catalyst structure and performance.* Physical Chemistry Chemical Physics, 2001. **3**(13): p. 2712-2719.
121. Venezia, A.M., et al., *Relationship between Structure and CO Oxidation Activity of Ceria-Supported Gold Catalysts.* The Journal of Physical Chemistry B, 2005. **109**(7): p. 2821-2827.
122. Tada, S., et al., *Study of RuNi/TiO2 catalysts for selective CO methanation.* Applied Catalysis B: Environmental, 2013. **140-141**: p. 258-264.
123. Chen, M.S. and D.W. Goodman, *Structure–activity relationships in supported Au catalysts.* Catalysis Today, 2006. **111**(1–2): p. 22-33.
124. Liu, J., *Advanced Electron Microscopy of Metal–Support Interactions in Supported Metal Catalysts.* ChemCatChem, 2011. **3**(6): p. 934-948.
125. Bell, A.T., *The Impact of Nanoscience on Heterogeneous Catalysis.* Science, 2003. **299**(5613): p. 1688-1691.
126. Martins, J., et al., *CO2 hydrogenation with shape-controlled Pd nanoparticles embedded in mesoporous silica: Elucidating stability and selectivity issues.* Catalysis Communications, 2015. **58**(0): p. 11-15.
127. Van Santen, R.A., *Complementary Structure Sensitive and Insensitive Catalytic Relationships.* Accounts of Chemical Research, 2008. **42**(1): p. 57-66.
128. Zhang, Y. and T. Ren, *Silica supported ruthenium oxide nanoparticulates as efficient catalysts for water oxidation.* Chemical Communications, 2012. **48**(89): p. 11005-7.

129. Campbell, C.T., *Catalyst-support interactions: Electronic perturbations.* Nature Chemistry, 2012. **4**(8): p. 597-598.
130. Thampi, K.R., J. Kiwi, and M. Gratzel, *Methanation and photo-methanation of carbon dioxide at room temperature and atmospheric pressure.* Nature, 1987. **327**(6122): p. 506-508.
131. Lunde, P.J. and F.L. Kester, *Carbon Dioxide Methanation on a Ruthenium Catalyst.* Industrial & Engineering Chemistry Process Design and Development, 1974. **13**(1): p. 27-33.
132. Karelovic, A. and P. Ruiz, *Mechanistic study of low temperature CO2 methanation over Rh/TiO2 catalysts.* Journal of Catalysis, 2013. **301**(0): p. 141-153.
133. Erdöhelyi, A., M. Pásztor, and F. Solymosi, *Catalytic hydrogenation of CO2 over supported palladium.* Journal of Catalysis, 1986. **98**(1): p. 166-177.
134. Solymosi, F., A. Erdöhelyi, and T. Bánsági, *Methanation of CO2 on supported rhodium catalyst.* Journal of Catalysis, 1981. **68**(2): p. 371-382.
135. Henderson, M.A. and S.D. Worley, *An infrared study of the hydrogenation of carbon dioxide on supported rhodium catalysts.* The Journal of Physical Chemistry, 1985. **89**(8): p. 1417-1423.
136. Urasaki, K., et al., *Effect of Support Materials on the Selective Methanation of CO over Ru Catalysts.* Topics in Catalysis, 2010. **53**(7-10): p. 707-711.
137. Lin, Q., et al., *RuO2/rutile-TiO2: a superior catalyst for N2O decomposition.* Journal of Materials Chemistry A, 2014. **2**(15): p. 5178-5181.
138. Debecker, D.P., et al., *Total oxidation of propane with a nano-RuO2/TiO2 catalyst.* Applied Catalysis A: General, 2014. **481**: p. 11-18.
139. Balaraju, M., et al., *Surface and structural properties of titania-supported Ru catalysts for hydrogenolysis of glycerol.* Applied Catalysis A: General, 2010. **384**(1–2): p. 107-114.
140. Cassaignon, S. and O. Durupthy, Private communications, Chimie de la Matière Condensée de Paris Collège de France, 2012.
141. Wang, A., et al., *Synthesis and Characterization of Ruthenium-Titanium Composite Oxide and a Platinum Catalyst Supported on It.* Chinese Journal of Catalysis, 2009. **30**(3): p. 179-181.
142. Hanaor, D.A.H. and C.C. Sorrell, *Review of the anatase to rutile phase transformation.* J. Mater. Sci., 2011. **46**(4): p. 855-874.
143. Pillai, S.C., et al., *Synthesis of High-Temperature Stable Anatase TiO2 Photocatalyst.* The Journal of Physical Chemistry C, 2007. **111**(4): p. 1605-1611.
144. Fernández, C., et al., *Effect of the size and distribution of supported Ru nanoparticles on their activity in ammonia synthesis under mild reaction conditions.* Applied Catalysis A: General, 2014. **474**(0): p. 194-202.

145. Chiu, C.-c., et al., *C-O cleavage of aromatic oxygenates over ruthenium catalysts. A computational study of reactions at step sites.* Physical Chemistry Chemical Physics, 2015. **17**(23): p. 15324-15330.
146. Diebold, U., *The surface science of titanium dioxide.* Surface Science Reports, 2003. **48**(5–8): p. 53-229.
147. Fisher, I.A. and A.T. Bell, *A Comparative Study of CO and CO2Hydrogenation over Rh/SiO2.* Journal of Catalysis, 1996. **162**(1): p. 54-65.
148. Solymosi, F., T. Bánsági, and A. Erdöhelyi, *Infrared study of the reaction of adsorbed formate ion with H2 on supported Rh catalysts.* Journal of Catalysis, 1981. **72**(1): p. 166-169.
149. McKeown, D.A., et al., *Structure of Hydrous Ruthenium Oxides: Implications for Charge Storage.* The Journal of Physical Chemistry B, 1999. **103**(23): p. 4825-4832.
150. Vannice, M.A., *The catalytic synthesis of hydrocarbons from H2CO mixtures over the group VIII metals.* Journal of Catalysis, 1976. **44**(1): p. 152-162.
151. Burch, R. and A.R. Flambard, *Strong metal-support interactions in nickel/titania catalysts: The importance of interfacial phenomena.* Journal of Catalysis, 1982. **78**(2): p. 389-405.
152. Sachtler, W.M.H. and M. Ichikawa, *Catalytic site requirements for elementary steps in syngas conversion to oxygenates over promoted rhodium.* The Journal of Physical Chemistry, 1986. **90**(20): p. 4752-4758.
153. Rietveld, H.M., *A profile refinement method for nuclear and magnetic structures.* Journal of Applied Crystallography, 1969. **2**(2): p. 65-71.
154. Rodríguez-Carvajal, J., *Recent advances in magnetic structure determination by neutron powder diffraction.* Physica B: Condensed Matter, 1993. **192**(1–2): p. 55-69.
155. Allard, L.F., et al., *Novel MEMS-Based Gas-Cell/Heating Specimen Holder Provides Advanced Imaging Capabilities for In Situ Reaction Studies.* Microsc. Microanal., 2012. **18**(4): p. 656-666.
156. Gai, P.L. and E.D. Boyes, *Advances in atomic resolution in situ environmental transmission electron microscopy and 1Å aberration corrected in situ electron microscopy.* Microscopy Research and Technique, 2009. **72**(3): p. 153-164.
157. Benavidez, A.D., et al., *Environmental Transmission Electron Microscopy Study of the Origins of Anomalous Particle Size Distributions in Supported Metal Catalysts.* ACS Catalysis, 2012. **2**(11): p. 2349-2356.
158. Xiang, G., et al., *Size effects in atomic-level epitaxial redistribution process of RuO2 over TiO2.* Sci. Rep., 2012. **2**: p. srep00801, 6 pp.

159. Ji, L., J. Lin, and H.C. Zeng, *Thermal Processes of Volatile RuO2 in Nanocrystalline Al2O3 Matrixes Involving γ→α Phase Transformation.* Chemistry of Materials, 2001. **13**(7): p. 2403-2412.
160. Garisto, F., *MODELLING THE OXIDATION OF DEFECTED FUEL ELEMENT.* AECL-9552, 1988. **International Atomic Energy Agency**
161. Bell, W.E. and M. Tagami, *High-temperature chemistry of the ruthenium-oxygen system.* J. Phys. Chem., 1963. **67**(11): p. 2432-6.
162. Schaefer, H., A. Tebben, and W. Gerhardt, *Chemistry of the platinum metals. V. Equilibriums with Ru(s), RuO2(s), RuO3(g), and RuO4(g).* Z. Anorg. Allg. Chem., 1963. **321**: p. 41-55.
163. Colomer, M.T. and M.J. Velasco, *Rutile-type dense ceramics fabricated by pressureless sintering of Ti1−xRuxO2 powders prepared by sol–gel.* Journal of the European Ceramic Society, 2007. **27**(6): p. 2369-2376.
164. Gandhi, H.S., H.K. Stepien, and M. Shelef, *Optimization of ruthenium-containing, stabilized, nitric oxide reduction catalysts.* Mater. Res. Bull., 1975. **10**(8): p. 837-45.
165. Gandhi, H.S., H.K. Stepien, and M. Shelef, *Optimization of ruthenium-containing, stabilized, nitric oxide reduction catalysts.* Materials Research Bulletin, 1975. **10**(8): p. 837-845.
166. Paquez, X., et al., *Resistant RuO2/SiO2 Absorbing Sol–Gel Coatings for Solar Energy Conversion at High Temperature.* Chemistry of Materials, 2015. **27**(7): p. 2711-2717.
167. Hansen, T.W., et al., *Sintering of Catalytic Nanoparticles: Particle Migration or Ostwald Ripening?* Accounts of Chemical Research, 2013. **46**(8): p. 1720-1730.
168. Yoshida, K., Bright, A., Tanaka, N., *Direct Observation of the Initial Process of Ostwald Ripening using Spherical Aberration-Corrected Transmission Electron Microscopy.* J. Electron Microsc. 2012, 2012. **61**: p. 99–103.
169. Simonsen, S.B., et al., *Direct Observations of Oxygen-induced Platinum Nanoparticle Ripening Studied by In Situ TEM.* Journal of the American Chemical Society, 2010. **132**(23): p. 7968-7975.
170. Brinker, C.J. and G.W. Scherer, *Sol-Gel Science*. 1990: Academic Press.
171. Ward, D.A. and E.I. Ko, *Preparing Catalytic Materials by the Sol-Gel Method.* Industrial & Engineering Chemistry Research, 1995. **34**(2): p. 421-433.
172. Alothman, Z., *A Review: Fundamental Aspects of Silicate Mesoporous Materials.* Materials, 2012. **5**(12): p. 2874.
173. Boissiere, C., et al., *Aerosol Route to Functional Nanostructured Inorganic and Hybrid Porous Materials.* Advanced Materials, 2011. **23**(5): p. 599-623.
174. Ciriminna, R., et al., *The Sol–Gel Route to Advanced Silica-Based Materials and Recent Applications.* Chemical Reviews, 2013. **113**(8): p. 6592-6620.

175. Schubert, U., *Chemical modification of titanium alkoxides for sol-gel processing.* Journal of Materials Chemistry, 2005. **15**(35-36): p. 3701-3715.
176. Glisoni, R.J. and A. Sosnik, *Novel Poly(Ethylene Oxide)-b-Poly(Propylene Oxide) Copolymer-Glucose Conjugate by the Microwave-Assisted Ring Opening of a Sugar Lactone.* Macromolecular Bioscience, 2014. **14**(11): p. 1639-1651.
177. Socrates, G., *Infrared and Raman Characteristic Group Frequencies, Tables and Charts.* John Wiley & Sons, Chichester, UK, 2001.
178. Musić, S., et al., *Chemical and micro structural properties of TiO2 synthesized by sol-gel procedure.* Materials Science and Engineering: B, 1997. **47**(1): p. 33-40.
179. Castellano, F.N., et al., *Spectroscopic and excited-state properties of titanium dioxide gels.* Chemistry of Materials, 1994. **6**(11): p. 2123-2129.
180. Burgos, M. and M. Langlet, *The sol-gel transformation of TIPT coatings: a FTIR study.* Thin Solid Films, 1999. **349**(1–2): p. 19-23.
181. Izutsu, H., et al., *Structure and properties of TiO2-SiO2 prepared by sol-gel method in the presence of tartaric acid.* Materials Research Bulletin, 1997. **32**(9): p. 1303-1311.
182. Phillippi, C.M. and S.R. Lyon, *Longitudinal-Optical Phonons in TiO2(Rutile) Thin-Film Spectra.* Physical Review B, 1971. **3**(6): p. 2086-2087.
183. D. Vasconcelos, V.C., E. Nunes, A. Sabioni, M. Gasparon and W. Vasconcelos, *Infrared Spectroscopy of Titania Sol-Gel Coatings on 316L Stainless Steel.* Materials Sciences and Applications, 2011. **2**(10): p. 1375-1382.
184. Sing, K.S.W., et al., *Reporting Physisorption Data for Gas/Solid Systems*, in *Handbook of Heterogeneous Catalysis*. 2008, Wiley-VCH Verlag GmbH & Co. KGaA.
185. Mason, G., *The effect of pore space connectivity on the hysteresis of capillary condensation in adsorption—desorption isotherms.* Journal of Colloid and Interface Science, 1982. **88**(1): p. 36-46.
186. Mason, G., *A Model of Adsorption-Desorption Hysteresis in which Hysteresis is Primarily Developed by the Interconnections in a Network of Pores.* Proceedings of the Royal Society of London A: Mathematical, Physical and Engineering Sciences, 1983. **390**(1798): p. 47-72.
187. Fröhlich, K., et al., *Growth of High-Dielectric-Constant TiO2 Films in Capacitors with RuO2 Electrodes.* Electrochemical and Solid-State Letters, 2008. **11**(6): p. G19-G21.
188. Wang, X. and R.G. Gordon, *High-Quality Epitaxy of Ruthenium Dioxide, RuO2, on Rutile Titanium Dioxide, TiO2, by Pulsed Chemical Vapor Deposition.* Crystal Growth & Design, 2013. **13**(3): p. 1316-1321.

189. Komanoya, T., et al., *Catalysis and characterization of carbon-supported ruthenium for cellulose hydrolysis.* Applied Catalysis A: General, 2011. **407**(1–2): p. 188-194.
190. Prairie, M.R., et al., *A fourier transform infrared spectroscopic study of C02 methanation on supported ruthenium.* Journal of Catalysis, 1991. **129**(1): p. 130-144.
191. Highfield, J.G., et al., *Catalyst Characterization and in situ FTIR Studies of Carbon Dioxide Methanation Over Ruthenium Supported on Titania*, in *Studies in Surface Science and Catalysis*, A.Z. Claudio Morterra and C. Giacomo, Editors. 1989, Elsevier. p. 469-479.
192. Louis, B., et al., *Understanding Crystallization of Anatase into Binary SiO2/TiO2 Sol−Gel Optical Thin Films: An in Situ Thermal Ellipsometry Analysis.* The Journal of Physical Chemistry C, 2011. **115**(7): p. 3115-3122.
193. Jung, Y.-S., et al., *Synthesis of alumina–titania solid solution by sol–gel method.* Journal of Physics and Chemistry of Solids, 2008. **69**(5–6): p. 1464-1467.
194. Molina, T., et al., *Dispersion and reaction sintering of alumina–titania mixtures.* Materials Research Bulletin, 2012. **47**(9): p. 2469-2474.
195. Ahmed, M.A. and M.F. Abdel-Messih, *Structural and nano-composite features of TiO2–Al2O3 powders prepared by sol–gel method.* Journal of Alloys and Compounds, 2011. **509**(5): p. 2154-2159.
196. Faustini, M., et al., *Ultraporous Nanocrystalline TiO2-based Films: Synthesis, Patterning and Application as Anti-Reflective, Self-Cleaning, Superhydrophilic Coatings.* Nanoscale, 2015.
197. Boettcher, S.W., et al., *Harnessing the Sol–Gel Process for the Assembly of Non-Silicate Mesostructured Oxide Materials.* Accounts of Chemical Research, 2007. **40**(9): p. 784-792.
198. Machida, M., et al., *The effect of SiO2 addition in super-hydrophilic property of TiO2 photocatalyst.* Journal of Materials Science, 1999. **34**(11): p. 2569-2574.
199. Smitha, V.S., et al., *Sol–gel route to synthesize titania-silica nano precursors for photoactive particulates and coatings.* Journal of Sol-Gel Science and Technology, 2010. **54**(2): p. 203-211.
200. Almeida, R. and E. Christensen, *Crystallization Behavior of SiO2-TiO2 Sol-Gel Thin Films.* Journal of Sol-Gel Science and Technology, 1997. **8**(1-3): p. 409-413.
201. Gutiérrez-Alejandre, A., et al., *Characterization of alumina–titania mixed oxide supports: Part II: Al2O3-based supports.* Microporous and Mesoporous Materials, 1998. **23**(5–6): p. 265-275.

202. Gutiérrez-Alejandre, A., et al., *Characterization of alumina-titania mixed oxide supports I. TiO2-based supports.* Microporous Materials, 1997. **12**(1–3): p. 79-91.
203. Yamaguchi, O. and Y. Mukaida, *Formation and Transformation of TiO2 (Anatase) Solid Solution in the System TiO2—Al2O3.* Journal of the American Ceramic Society, 1989. **72**(2): p. 330-333.
204. Murashkevich, A.N., et al., *Infrared absorption spectra and structure of TiO2-SiO2 composites.* Journal of Applied Spectroscopy, 2008. **75**(5): p. 730-734.
205. Launer, P.J., *Infrared analysis of organosilicon compounds: Spectra-structure correlations.* 1987: p. 100-103.
206. Zeitler, V.A. and C.A. Brown, *The Infrared Spectra of Some Ti-O-Si, Ti-O-Ti and Si-O-Si Compounds.* The Journal of Physical Chemistry, 1957. **61**(9): p. 1174-1177.
207. Jongsomjit, B., S. Ngamposri, and P. Praserthdam, *Catalytic Activity During Copolymerization of Ethylene and 1-Hexene via Mixed TiO2/SiO2-Supported MAO with rac-Et[Ind]2ZrCl2 Metallocene Catalyst.* Molecules, 2005. **10**(6): p. 672.
208. Moolenaar, R.J., J.C. Evans, and L.D. McKeever, *Structure of the aluminate ion in solutions at high pH.* The Journal of Physical Chemistry, 1970. **74**(20): p. 3629-3636.
209. Tarte, P., *Infra-red spectra of inorganic aluminates and characteristic vibrational frequencies of AlO4 tetrahedra and AlO6 octahedra.* Spectrochimica Acta Part A: Molecular Spectroscopy, 1967. **23**(7): p. 2127-2143.
210. Suttiponparnit, K., et al., *Role of Surface Area, Primary Particle Size, and Crystal Phase on Titanium Dioxide Nanoparticle Dispersion Properties.* Nanoscale Res Lett, 2011. **6**(1): p. 27.
211. Kosmulski, M., *Chemical Properties of Material Surfaces* Journal of the American Chemical Society, 2001. **124**(6): p. 1127-1127.
212. Colilla, M., et al., *Advanced Drug Delivery Vectors with Tailored Surface Properties Made of Mesoporous Binary Oxides Submicronic Spheres.* Chemistry of Materials, 2010. **22**(5): p. 1821-1830.
213. Kazuyuki Nakai, K.N., *Pulse chemisorption measurement <Metal dispersion measurement>*. 2003.

List of scientific communications

Publications

Selective CO_2 methanation on Ru/TiO_2 catalyst: unraveling the decisive role of the TiO_2 support crystal structure
Ara Kim, Clément Sanchez, Gilles Patriarche, Ovidiu Ersen, Simona Moldovan, Andreas Wisnet, Capucine Sassoye, Damien Debecker
(Written, to be submitted)

Synthesis of monolithic meso–macroporous silica and carbon with tunable pore size
Ara Kim, Robert Black, Yong Jae Hyun, Linda F. Nazar, Eric Prouzet
Chemical Communications, 2012, 48, 4335–4337

Vacuum-assisted aerosol deposition of a low-dielectric-constant periodic mesoporous organosilica film
Wendong Wang, Daniel Grozea, Ara Kim, Douglas D. Perovic, Geoffrey A. Ozin
Advanced Materials, 2010, 22, 99–102

Conferences

Selective CO_2 methanation on Ru/TiO_2 catalyst: unraveling the decisive role of the TiO_2 crystal structure
Ara Kim, Clément Sanchez, Damien Debecker, Capucine Sassoye
Poster, The 1st European Summer School on Catalyst Preparation, Vogüé, France, May 2014

Vacuum-assisted aerosol preparation of mesoporous Ru/TiO2catalysts for CO_2 methanation
Ara Kim, Capucine Sassoye, Clément Sanchez, Damien Debecker
Poster, The 11th International Symposium on the "Scientific Bases for the Preparation of Heterogeneous Catalysts" (PREPA 11), Louvain-la-Neuve, Belgium, July 2014

Effect of TiO_2 crystal structures as supports for RuO_2 nanoparticles in CO_2 methanation

Ara Kim, Capucine Sassoye, Clément Sanchez, Damien Debecker

Oral and poster, The 8th International Conference on Environmental Catalysis (ICEC 2014), Asheville, USA, August 2014

Structure-performance relationship in the design of Ru/TiO_2 catalyst for CO_2 methanation

Ara Kim, Capucine Sassoye, Clément Sanchez, Damien Debecker

Oral, The 249th ACS National Meeting & Exposition, Denver, USA, March 2015